

Superradiant Atomic Beam Laser

by

Haonan Liu

B.S., Physics, University of Richmond, 2016

B.A., Mathematics, University of Richmond, 2016

M.S., University of Colorado Boulder, 2019

A thesis submitted to the
Faculty of the Graduate School of the
University of Colorado in partial fulfillment
of the requirements for the degree of
Doctor of Philosophy
Department of Physics

2021

Committee Members:

Murray J. Holland, Chair

Ana Maria Rey

James K. Thompson

Jun Ye

Josh Combes

Liu, Haonan (Ph.D., Physics)

Superradiant Atomic Beam Laser

Thesis directed by Prof. Murray J. Holland

Steady-state superradiant lasers are a promising candidate for next-generation ultracoherent light sources. In this thesis, we propose a new type of superradiant laser based on a hot atomic beam traversing an optical cavity. We show that the theoretical minimum linewidth and maximum power are competitive with the best ultracoherent clock lasers. Also, our system operates naturally in a continuous wave modality, which has been elusive for superradiant lasers so far. Unlike many existing proposals for ultracoherent lasers, our design is simple and rugged. This makes it a potential candidate for the first widely accessible ultracoherent laser, as well as the first to realize sought-after applications of ultracoherent lasers in challenging environments.

Aside from metrological usefulness, the superradiant atom beam laser system is of fundamental interest in terms of various superradiant phase transitions. To this end, we theoretically analyze the system for three different configurations: (i) For a thermal atomic beam interacting with a resonant cavity mode, we derive a semiclassical model and determine the onset of superradiant emission and its stability. We find two different superradiant phases; a steady-state superradiant phase and a multi-component superradiant phase. In the latter case we observe sidebands in the frequency spectrum that can be calculated using a stability analysis of the amplitude mode of the collective dipole. We show that both superradiant phases are robust against free-space spontaneous emission and T_2 dephasing processes. (ii) For a collimated atomic beam interacting with an off-resonant cavity mode, we derive an analytical formula for the cavity pulling coefficient. We find that the pulling is small if the cavity linewidth is much larger than the collective linewidth of the atomic beam. This regime is desired for building stable lasers because the emission frequency is robust against cavity length fluctuations. Furthermore, we find polychromatic emission regimes, where the spectrum has several frequency components while the light output is still superradiant. (iii) For

a slanted collimated atomic beam passing through a cavity that is on resonance, we find that the atoms undergo superradiant emission when the collective linewidth exceeds the transit-time broadening. We find steady-state superradiance providing the tilt of the atomic beam is sufficiently small. However, if the atoms travel more than half a wavelength along the cavity axis during one transit time we predict a dynamical phase transition to a new bistable superradiant regime. In this phase the atoms undergo collective spontaneous emission with a frequency that can be either blue or red detuned from the free-space atomic resonance. We show that the linewidth of the emitted light exhibits features of a critical scaling close to the phase boundaries.

Dedication

给父亲，母亲，小姨，姥姥，和奶奶。谁言寸草心，报得三春晖。

To GQ, for everything.

Acknowledgements

It has been five memorable and fun years at JILA and CU Boulder. I would like to express my most sincere gratitude to my advisor Murray J. Holland, who has always been kind, supportive, and understanding. The insightful discussions, the countless lunches on the “hill”, and the share of love for skiing and hiking, have all become the most valuable memory of my time at the Holland group. I offer my special thanks to John (Jinx) Cooper. Thank you Jinx for helping me become a better physicist with your patient guidance. I shall never forget our “2pm-whiteboard-equation-deriving” sessions. Thanks to Travis L. Nicholson, who is always encouraging and has the best ideas. Thank you Travis for showing me the experimental side of the quantum optical world. Thanks to Simon B. Jäger without whom I would have had a much tougher time becoming a PhD. A good leader and a good friend, Simon constantly impresses me with his passion, concentration, and remarkable erudition. Thanks to Athreya Shankar, Liang-Ying Chih, John P. Bartolotta, and Jarrod Reilly for making the best Holland group. Thanks to James K. Thompson, Ana Maria Rey, Jun Ye, Graeme Smith, and Florian Schreck for helpful discussions. Thanks to David Tieri, Minghui Xu, Peiru He, Baochen Wu, Chun-Chia Chen, Victor Colussi, John Wilson, Gage W. Harmon, Arnon Goldberg, Shayne Bennetts, and Sheng Zhou for useful discussions. Thanks to my undergraduate advisors Emory (Ted) F. Bunn and Ovidiu Lipan for keeping supporting me. Thanks to Jeanne Nijhowne, Jim McKown, and other staff members of the physics department and JILA for making life so much easier for us.

I could never have made this far without the support of family and friends. Thanks Mom, Dad, Aunt, and my dear Grandmas. I made it. I am deeply indebted to GQ, who is the savior of

my world. Thanks Aunt Jialin Su for guiding me and caring for me. Thanks to my uncles, aunts, and cousins for your everlasting support. Friendship has been a major source of my energy to accomplish the PhD. Special thanks to Dan (Eva) Zhou. Thank you Eva for being the best friend ever. Thanks to Yifei Ni, Guan Gui, Xi Chen, Nianchen Han, Sihang Wei, Zekun Lyv, Lin Zhu, Yu Zhang, Xu Zheng, Chen Tang, Tong Chen, Danyi Chen, Bannong Zhang, Jingwen (Ada) Liao, Huiling Shao, Congxin Xu, Juekun Wen, Jieyi Ding, and many others for tolerating my whims and accompanying me along the way.

I cannot express how much love I have for Colorado, for the snow, for the mountains, and most importantly, for the memories I have had with all of you. Thank you all. Thank you.

Contents

Chapter	
1 Introduction	1
2 Background	4
2.1 Canonical quantization of electrodynamics	4
2.1.1 Classical Lagrangian of electrodynamics	5
2.1.2 Hamiltonian and canonical quantization	11
2.1.3 Quantization volume	14
2.1.4 Mode functions	16
2.2 Jaynes-Cummings model	18
2.2.1 Long-wavelength approximation	18
2.2.2 The $\hat{\mathbf{p}} \cdot \hat{\mathbf{A}}$ interaction and dipole representation	19
2.2.3 Two-level, single-mode, and rotating-wave approximation	23
3 Open Quantum Systems	28
3.1 Master equation	29
3.1.1 Quantum optics approach	29
3.1.2 Quantum information approach	34
3.2 Heisenberg-Langevin equations	36
3.3 Equivalence between master equation and Heisenberg-Langevin equations	43
3.3.1 Master equation to Langevin equations	44

3.3.2	Langevin equations to master equation	46
3.4	Prescription for decoherence	47
3.4.1	Free-space spontaneous emission	47
3.4.2	T_2 dephasing	48
3.4.3	Cavity decay	49
3.5	Summary	50
4	Theory of Superradiant Atomic Beam Laser	51
4.1	From Dicke superradiance to steady-state cavity superradiance	51
4.2	Steady-state superradiance laser	54
4.3	Superradiant atomic beam laser	56
4.3.1	Model	56
4.3.2	Heisenberg-Langevin equations	57
4.3.3	Adiabatic elimination	60
4.3.4	Superradiant equations	62
4.4	Semiclassical c -number equations	64
4.4.1	Rules for c -number equations	66
4.4.2	c -number Langevin equations	68
5	Rugged mHz-Linewidth Superradiant Laser Driven by a Hot Atomic Beam	75
5.1	Introduction	75
5.2	Formalism	77
5.3	Results	80
5.4	Sample design constraints	86
5.4.1	First example: $2\pi \times 400$ Hz line of ^{40}Ca	87
5.4.2	Second example: $2\pi \times 7.5$ kHz line of ^{88}Sr	88
5.5	Conclusion	88

6	Superradiant Emission of a Thermal Atomic Beam into an Optical Cavity	90
6.1	Introduction	90
6.2	Derivation of the model	92
6.2.1	System and master equation	92
6.2.2	Elimination of the cavity field	93
6.2.3	Parameter regime and c -number approximations	94
6.2.4	Phase-space density description	96
6.3	Mean-field analysis	98
6.3.1	Non-superradiant phase (NSR)	99
6.3.2	Steady-state superradiant phase (SSR)	101
6.4	Analytical estimates for the linewidth	107
6.4.1	Linewidth in the NSR phase	108
6.4.2	Linewidth in the SSR phase	111
6.4.3	Discussion and limitations	114
6.5	A thermal beam traversing the cavity	115
6.5.1	NSR phase	115
6.5.2	SSR phase	118
6.5.3	Transition from SSR to NSR	122
6.5.4	Transition from SSR to MCSR	124
6.5.5	Spontaneous emission and T_2 dephasing	129
6.6	Conclusions	135
7	Collective Emission of an Atomic Beam into an Off-Resonant Cavity Mode	137
7.1	Introduction	137
7.2	Theoretical model	140
7.2.1	Master equation formalism	140
7.2.2	Heisenberg-Langevin equations	141

7.2.3	Semiclassical description	142
7.2.4	Density description	143
7.3	Stationary states of the system	144
7.3.1	The non-superradiant solution	145
7.3.2	The superradiant solution	145
7.3.3	Perturbative solution for $\chi \ll 1$: Cavity pulling	149
7.4	Stability in the bad cavity regime	151
7.4.1	Stability of the non-superradiant configuration	151
7.4.2	Stability of the superradiant configuration	153
7.5	An atomic beam with a single velocity traversing an off-resonant optical cavity . . .	156
7.5.1	Non-superradiant phase	156
7.5.2	Superradiant phase	158
7.5.3	Numerical study	160
7.5.4	Cavity pulling	168
7.6	Conclusion	170
8	Regular and Bistable Steady-State Superradiant Phases of an Atomic Beam Traversing an Optical Cavity	172
8.1	Introduction	172
8.2	Model	174
8.2.1	Parameter regime and quantum mechanical description	175
8.2.2	Semiclassical description of the atomic degrees of freedom	176
8.3	Onset of superradiance	178
8.4	Superradiant phases	182
8.4.1	Regular SSR and bistable SSR	183
8.4.2	Intensity and emission frequency	185
8.4.3	Mode hopping probability	190

8.4.4	The linewidth	192
8.5	Discussion and conclusion	200
9	Summary and Outlook	202
	Bibliography	204
	Appendix	
A	Fourier Series and Fourier Transform	215
A.1	Fourier series	215
A.2	Fourier transform	216
A.3	Kronecker and Dirac delta functions	217
B	Separation of Center-of-Mass Motion with External Fields	219
B.1	Two-body system	219
B.2	Three-body system	220
B.3	$(N + 1)$ -body system	222
C	Pauli Matrix Relations	225
D	Rotating Frames and Interaction Pictures	226
D.1	Closed systems	226
D.1.1	Rotating frames	226
D.1.2	Interaction pictures	228
D.2	Open systems	232
D.2.1	Master equation	232
D.2.2	Heisenberg-Langevin equation	235
E	Derivation of Lindblad Master Equation	237

Tables

Table

5.1	Sample model parameters for the superradiant beam laser utilizing the $2\pi \times 400$ Hz transition line of ^{40}Ca	87
5.2	Sample model parameters for the superradiant beam laser utilizing the $2\pi \times 7.5$ kHz transition line of ^{88}Sr	88

Figures

Figure

- 4.1 Source: Ref. [52]. Comparison between the general characteristics of ordinary fluorescence and superradiance experiments. (a) Ordinary spontaneous emission is essentially isotropic with an exponentially decaying intensity (time constant τ_{sp}). (b) Superradiance is anisotropic with an emission occurring in a short burst of duration $\sim \tau_{\text{sp}}/N$ 52
- 4.2 Source: Ref. [128] (notations and captions have been adapted). The superradiant phase transition for the Dicke model with a single mode. Here, g describes the atom-photon coupling. The order parameter for the phase transition is $\langle \hat{a} \rangle / \sqrt{N}$, where $\langle \hat{a} \rangle$ is the mean field amplitude and N is the atom number. When the coupling parameter g is bigger than the critical coupling g_c , the order parameter $\langle \hat{a} \rangle / \sqrt{N}$ becomes non-zero with two opposite phases which correspond to the symmetry breaking equilibria of the free energy F 53
- 4.3 Source: Ref. [101] (notations and captions have been adapted). (Left) Power as a function of pump rate w and atom number N . The rapid buildup of power above threshold w can be seen as well as the decrease of emitted power for too strong a pump. The dashed line shows the boundary of the region of collective emission. (Right) Linewidth vs w and N . The white dashed lines indicate (from left to right) the spontaneous decay rate, the inhomogeneous relaxation rate $1/T_2$, and the maximum pump rate w_{max} 55

- 5.1 The superradiant beam laser. The atomic beam is generated from an effusive source, like a commercial effusion cell. After emerging from the source (upper right), the atoms are prepared by pumping lasers (blue arrows) in a metastable state prior to entering the cavity (lower left). Inset: The minimal atomic structure needed for the superradiant beam laser to operate. In this three-level scheme, atoms are rapidly prepared in a metastable state $|e\rangle$ by pumping (blue) on a broad transition. Lasing (red) occurs on the long-lived $|g\rangle \leftrightarrow |e\rangle$ transition. Real atomic systems may require more complex pumping schemes. 76
- 5.2 (a) Mean-field calculations of the linewidth in units of the transit time broadening $1/\tau$, as a function of the Doppler width $\delta_D\tau$ and $\Phi\tau^2\Gamma_c$. Here $\Phi\tau^2\Gamma_c$ is the number of collective lifetimes that elapse during the transit time τ . The black dashed line is the phase transition threshold for steady-state superradiance, above which mean-field calculations predict a zero linewidth. (b) The linewidth in units of Γ_c as a function of the Doppler width for $\Phi\tau^2\Gamma_c = 20$. The markers are simulation results using Eqs. (5.1)–(5.3) with $\Phi = 1000/\tau$ and $\Gamma_c = 0.02/\tau$. For every data point, we calculated 100 trajectories each with a simulation time of $T = 2000\tau$. This numerical simulation is compared with the mean-field theory, which is analytic. Inset: Below the phase transition, simulations show an ultranarrow linewidth of order Γ_c , which is 50 times smaller than transit time broadening for these simulation parameters. (c) Simulation results of the linewidth in units of Γ_c as a function of $\Phi\tau^2\Gamma_c$. For every data point, we calculated 100 trajectories each with a simulation time of $T = 200\tau$ and $\Phi = 500/\tau$ 79
- 5.3 The output power of the superradiant beam laser. The markers are c -number simulation results. For every data point, we calculated 100 trajectories each with a simulation time of $T = 200\tau$ and $\Phi = 500/\tau$. For $\delta_D\tau = 0.2\pi$, both the mean-field and simulation results peak at $\Phi\tau^2\Gamma_c \approx 20$ with $P = 0.7\hbar\omega\Phi$ 81

- 5.4 Simulation results of the second-order time correlation function $g^{(2)}(0)$ compared to the mean-field prediction. For each data point, we calculated 100 trajectories each with a simulation time of $T = 200$ with $\Phi = 500$, $\tau = 1$, and $\delta_D\tau = 0.2\pi$ 83
- 5.5 The cavity pulling coefficient \wp at $\delta_D\tau = 0.2\pi$. A small cavity pulling makes the laser frequency insensitive to environmental noise, such as vibrations. The markers are c -number simulation results with $\kappa = 1000/\tau$ and $\omega_c - \omega_a = 100/\tau$. For every data point, we calculated 100 trajectories each with a simulation time of $T = 100\tau$. As N increases, the simulation results approach the mean-field calculation. 85
- 6.1 Schematic of the system (a) and the atom-cavity coupling (b). We consider a beam of two-level atoms in the excited state $|e\rangle$ traversing an optical cavity of loss rate κ with a given velocity distribution. The x and z axes are chosen perpendicular and parallel to the cavity axis. The atomic beam is much broader than the optical wavelength λ so that the atoms experience different phases of the cavity mode (blue and red denote different signs of the cavity mode function). The excited state $|e\rangle$ of the atomic dipoles (b) couples to the ground state $|g\rangle$ via photon emission into the cavity with coupling $g\eta(\mathbf{x})$. The function $\eta(\mathbf{x})$ is the mode function of the cavity. . . 91
- 6.2 Schematic of the stationary collective dipole in the J^x - J^y plane. Its mean length is given by J_0^{\parallel} as defined in Eq. (6.55). The dynamics of its length fluctuations, δJ^{\parallel} , we interpret as a Higgs mode, and the dynamics of its phase fluctuations, δJ^{\perp} , as a Goldstone mode (see Sec. 6.3.2.2). 102
- 6.3 The zero ν_0 of $D(\nu)$ from Eq. (6.116) with the largest real part as a function of the Doppler width δ_D and of the collective linewidth NT_c , all in units of $1/\tau$. In the region where $\nu_0 > 0$ (shown as white region) the state of the atomic beam is unstable and the beam of excited dipoles will undergo superradiant emission. The solid black line indicates the transition where $\nu_0 = 0$ [Eq. (6.118)]. 116

- 6.4 The absolute value of the g_1 function [Eq. (6.77)] normalized by $|g_1(0)|$ as a function of time t in units of τ for (a) $\delta_D\tau = 0.1$, $N\Gamma_c\tau = 4$ and (b) $\delta_D\tau = 10$, $N\Gamma_c\tau = 20$. The g_1 function is calculated by numerically integrating Eqs. (6.20)–(6.23) using Eqs. (6.114)–(6.115) over a total time $t_{\text{sim}} = 200\tau$ with $N = 2000$ atoms, and averaging over 100 trajectories. For the calculation of g_1 we have chosen $t_0 = 10\tau$. The red dashed line is an exponential fit $\propto \exp(ct)$ of the tail with an exponent $c\tau \approx -1.9$ (a) and $c\tau \approx -6.5$ (b), respectively. The values of ν_0 (see Fig. 6.3) for the same parameters are $\nu_0\tau = -1.8$ (a), and $\nu_0\tau = -6.2$ (b). 119
- 6.5 The real part $\text{Re}(\nu_0)$ (a) and the absolute value of the imaginary part $|\text{Im}(\nu_0)|$ (b) in units of $1/\tau$ of the zero ν_0 with the largest real part of the Higgs dispersion relation [Eq. (6.69)] as a function of the Doppler width δ_D and the collective linewidth $N\Gamma_c$ in units of $1/\tau$. The parameter region where the Higgs mode is unstable, $\text{Re}(\nu_0) > 0$, is marked as gray area and bounded by a dashed black line. We call this phase multi-component superradiant (MCSR). The solid black line, given by Eq. (6.118), marks the transition from SSR to the NSR phase (see also Fig. 6.3). Subplots (c) and (d) show the value of the collective dipole j_0^{\parallel} [Eq. (6.123)] and the linewidth Γ [Eq. (6.110)] in units of Γ_c , respectively. They are shown as a function of the same parameters as subplots (a) and (b) for the parameter regime where the Higgs mode is stable. For all calculations we have used Eq. (6.114) and Eq. (6.115). 121

- 6.6 (a) The normalized collective dipole correlation $\langle J^* J \rangle / N^2$, (b) the linewidth Γ in units of the collective linewidth $N\Gamma_c$, and (c) the linewidth in units of the single-atom linewidth Γ_c as a function of the Doppler width δ_D in units of $1/\tau$. The different markers correspond to different intracavity atom number N as described in the inset of subplot (a). The linewidth is calculated by fitting the g_1 function using $t_0 = 10\tau$ to an exponential $\propto \exp(-\Gamma t/2)$ over a time interval of length $t_f = 20\tau$. The solid line in subplot (a) is the value of $(j_0^{\parallel})^2/4$ calculated from Eq. (6.123). The linewidths in (b) visible as solid line are $-2\nu_0$, where ν_0 is the zero with the largest real part of the dispersion relation in Eq. (6.116). In (c) the solid line gives the solution of Eq. (6.110) calculated using Eq. (6.121) for given values of j_0^{\parallel} . The red dashed vertical lines mark the transition from SSR to the NSR phase. We have chosen $N\Gamma_c\tau = 20$ with a simulation time of $t_{\text{sim}} = 200\tau$ and a total number of trajectories $200000/N$ for corresponding N 123
- 6.7 The collective dipole correlation $\langle J^* J \rangle / N^2$ (a) and the value of $g_2(0) - 1$ [Eq. (6.125)] (b) as a function of δ_D in units of $1/\tau$. The different symbols indicate different intracavity atom numbers N [see inset of subplot (a)]. The solid line in subplot (a) is the value of $(j_0^{\parallel})^2/4$ calculated from Eq. (6.123). Subplot (c) shows the intensity spectrum $|S_2(\omega)|$ defined in Eq. (6.126) as a function of ω and δ_D in units of $1/\tau$. The value of $|S_2(\omega)|$ is normalized for every δ_D by the maximum $|S_2^{\text{max}}| \equiv \max_{\omega} |S_2(\omega)|$ and calculated for $N = 4000$. The red vertical dashed lines indicate the threshold from SSR to MCSR and from the MCSR to the SSR phases [see Fig.6.5(a)]. The red horizontal solid lines in subplot (c) are the values of $\pm \text{Im}(\nu_0)$ corresponding to the zero ν_0 of Eq. (6.69) with the largest real part. For the calculation of g_2 we have used $t_0 = 10\tau$ and for the calculation of $S_2(\omega)$ and integration time of $t_f = 20\tau$. All simulations were performed with $N\Gamma_c\tau = 50$ and with a simulation time of $t_{\text{sim}} = 200\tau$. For every N we have averaged over $200000/N$ trajectories. 125

- 6.8 The spectrum $|S_1(\omega)|$ [Eq. (6.127)] plotted for $\delta_D\tau = 3$ (a), $\delta_D\tau = 4.5$ (b), $\delta_D\tau = 6$ (c) as a function of ω in units of $1/\tau$. The different lines correspond to different intracavity atom numbers N as shown in the inset of subplot (a). The spectrum is normalized for every δ_D by the maximum $|S_1^{\max}| \equiv \max_{\omega}|S_1(\omega)|$. The red vertical lines in (b) correspond to $\pm \text{Im}(\nu_0)$ where ν_0 is the zero of Eq. (6.69) with the largest real part. The red vertical lines in (c) correspond to $\pm \text{Im}(\nu_0)/2$. Subplot (d) shows the spectrum $|S_1(\omega)|$ as a function of δ_D and ω in units of τ for $N = 4000$. The red dashed horizontal line marks the threshold from the SSR to MCSR regime. The circles on this line are the values of $\pm \text{Im}(\nu_0)$ for the given parameters. All simulations were performed with $N\Gamma_c\tau = 50$, with a simulation time of $t_{\text{sim}} = 200\tau$ and averaged over $200000/N$ trajectories. The spectra are calculated using $t_0 = 10\tau$ and $t_f = 20\tau$. 128
- 6.9 The spectrum $|S_1(\omega)|$ [Eq. (6.127)] (a) and the intensity spectrum $|S_2(\omega)|$ [Eq. (6.126)] (b) as a function of $N\Gamma_c$ and ω in units of $1/\tau$. Both spectra are normalized for every δ_D by the maximum $|S_n^{\max}| \equiv \max_{\omega}|S_n(\omega)|$ with $n \in \{1, 2\}$. The red dashed horizontal line in (a) marks the threshold between the SSR and the MCSR phase and the circles are the values of $\pm \text{Im}(\nu_0)$. Here, ν_0 is the zero of Eq. (6.69) with the largest real part. The red solid vertical lines are given by $\pm \text{Im}(\nu_0)/2$. In subplot (b) the red lines show the values of $\pm \text{Im}(\nu_0)$. For all results in subplots (a) and (b) we have used $N = 4000$, $t_0 = 10\tau$, $t_f = 20\tau$, and averaged over 50 trajectories. Subplot (c) shows the squared effective Rabi frequency [Eq. (6.128)] in units of $1/\tau^2$ as a function of the collective linewidth $N\Gamma_c$ in units of $1/\tau$. The data are shown for various values of N (see inset). The black solid line shows the result obtained from Eq. (6.123) and the red vertical dashed line shows the transition from SSR to MCSR. All simulations are performed for $\delta_D\tau = 6$ 130

- 6.10 The normalized collective dipole correlation $\langle J^*J \rangle / N^2$ (a) and the linewidth Γ in units of the single-atom linewidth Γ_c (b) as a function of transit-time broadening τ^{-1} in units of $N\Gamma_c$. The black circles are simulation results using Eqs. (6.130)–(6.132). We have fixed $\delta_D / (N\Gamma_c) = \pi \times 10^{-2}$, $\gamma_1 / (N\Gamma_c) = 10^{-2}$, $\gamma_2 / (N\Gamma_c) = 5 \times 10^{-3}$, and the intracavity atom number $N = 2000$. The linewidth is calculated by fitting the g_1 function using $t_0 = 10\tau$ to an exponential $\propto \exp(-\Gamma t/2)$ over a varying t_f . All the simulations were performed with $t_{\text{sim}} = 100\tau$ and averaged over 100 trajectories. The gray plus symbols are simulation results using the same parameters except for $\gamma_1 = 0 = \gamma_2$. The gray dashed lines are analytical solutions, giving in (a) the value of $(j_0^{\parallel})^2/4$ using Eq. (6.123), and in (b) the linewidth Eq. (6.110) calculated using Eq. (6.121) with corresponding values of j_0^{\parallel} , respectively. 132
- 6.11 Simulation results of the real part of $g_1(t)$ normalized by $\text{Re}[g_1(0)]$ for $\delta_D\tau = 4.5$ (a) and $\delta_D\tau = 6.0$ (b). For the black solid lines we have used $N\Gamma_c\tau = 50$, $\gamma_1 = 0.05\tau^{-1}$ with $N = 4000$ and $t_{\text{sim}} = 200$. The g_1 function is calculated using $t_0 = 10\tau$ and averaged over 50 trajectories. For the gray dashed lines we have used the same parameters except for $\gamma_1 = 0$. These dashed lines are the real parts of the g_1 functions that are used to calculate the spectra shown in Figs. 6.8(b) and 6.8(c). 134
- 7.1 (a) Atoms enter the cavity in the excited state $|e\rangle$ and can emit photons into a single cavity mode. Photons leak out through the cavity output mirror with rate κ . (b) Each atom is represented as an optical dipole of transition frequency ω_a coupled to the cavity mode of frequency ω_c . The coupling $g\eta(\mathbf{x})$ depends on the position \mathbf{x} of the atom, where g is the vacuum Rabi frequency or Jaynes-Cummings coupling coefficient and $\eta(\mathbf{x})$ is the mode function. The cavity-atom detuning frequency is given by $\Delta = \omega_c - \omega_a$ 139

- 7.2 Sketch of the Bloch sphere where the dipole density can be mapped on a point of the sphere (here visible as the blue arrow) with radius $\rho(\mathbf{p})$ depending solely on the momentum \mathbf{p} . The angles K and ϕ depend on position \mathbf{x} , momentum \mathbf{p} , and time t . 146
- 7.3 (a) The real component $\text{Re}(\nu_0)$ and (b) the imaginary component $\text{Im}(\nu_0)$ of the zero ν_0 with the largest real component of $D(\nu)$ in Eq. (7.92). They are plotted as a function of the detuning Δ in units of $\kappa/2$ and the collective linewidth $N\Gamma_c$ in units of $1/\tau$. The black solid line is determined by $\text{Re}(\nu_0) = 0$ above which we expect superradiant emission. 157
- 7.4 Bloch vectors parametrized according to Eqs. (7.76)–(7.78) where we have combined Eqs. (7.98) and (7.99) to calculate ω and J_0^\parallel and then Eqs. (7.93), (7.95), and (7.97) to calculate $K(x)$ and $\psi(x)$. The black solid lines are the traces of the Bloch vectors for $-w \leq x \leq w$. We have used $N\Gamma_c\tau = 10$ and four different values of $\Delta/(\kappa/2)$ [see titles of subplots (a)–(d)] for the numerical values used. 159
- 7.5 The normalized collective dipole $j_0^\parallel = J_0^\parallel/N$ (a) and the frequency ω in units of $1/\tau$ (a) as a function of $\Delta/(\kappa/2)$ and the collective linewidth $N\Gamma_c$ in units of $1/\tau$. The results are calculated using Eq. (7.98) and Eq. (7.99). The black dashed line is the boundary of the gray area where the superradiant configuration transitions to a multicomponent superradiant regime. This has been determined using the solution of j_0^\parallel and ω to find zeros of the dispersion relation in Eq. (7.89). 161

- 7.6 (a) The cavity output power $\kappa\langle\hat{a}^\dagger\hat{a}\rangle$ in units of N/τ [see Eq. (7.101)] and (b) the value of $g_2(0) - 1$ [see Eq. (7.102)] as functions of $\Delta/(\kappa/2)$ for various values of N [see inset of subplot (a)]. (c) The spectrum $|S(\nu)|$ [see Eq. (7.103)] normalized for every value of $\Delta/(\kappa/2)$ by the maximum $S^{\max} = \max_\nu |S(\nu)|$ as a function of ν in units of $1/\tau$ and of $\Delta/(\kappa/2)$ obtained by numerically integrating Eqs. (7.63)–(7.65) for $N = 4000$. For all simulations we have used $N\Gamma_c\tau = 20$. The black solid line in subplot (a) is calculated from the solution j_0^{\parallel} obtained from Eqs. (7.98) and (7.99). The vertical red dashed lines mark the analytical threshold between the superradiant and non-superradiant emission regimes. For (c) we have used $t_0 = 10\tau$ and $t_{\text{cut}} = 20\tau$. The red solid line in (c) in the superradiant regime is the frequency ω calculated using Eqs. (7.98) and (7.99). The red solid line in (c) in the non-superradiant regime is $\text{Im}(\nu_0)$ where ν_0 is the zero of Eq. (7.73) with the largest real part. All simulations have been performed for a total time $T = 200\tau$ and averaged over $100000/N$ different initializations. 163
- 7.7 (a) The cavity output power $\kappa\langle\hat{a}^\dagger\hat{a}\rangle$ in units of N/τ [see Eq. (7.101)] and (b) the value of $g_2(0) - 1$ [see Eq. (7.102)] as functions of $\Delta/(\kappa/2)$ for various values of N [see inset of subplot (a)]. (c) The spectrum $|S(\nu)|$ [see Eq. (7.103)] normalized for every value of $\Delta/(\kappa/2)$ by the maximum $S^{\max} = \max_\nu |S(\nu)|$ as a function of ν in units of $1/\tau$ and of $\Delta/(\kappa/2)$ obtained by numerically integrating Eqs. (7.63)–(7.65) for $N = 4000$. For all simulations we have used $N\Gamma_c\tau = 50$. The black solid line in subplot (a) is calculated from the solution j_0^{\parallel} obtained from Eq. (7.98) and Eq. (7.99). The vertical red dashed lines border the multicomponent regime. For subplot (c) we have taken the values $t_0 = 10\tau$ and $t_{\text{cut}} = 20\tau$. The red solid line in (c) in the superradiant regime is the frequency ω calculated using Eq. (7.98) and Eq. (7.99). The red circles in (c) at the phase thresholds are the values of $\omega \pm \text{Im}(\nu_1)$, where ν_1 is the zero of Eq. (7.89) with the largest real part. All simulations have been performed for a total time $T = 200\tau$ and averaged over $100000/N$ different initializations. . . . 165

- 7.8 The same quantities as shown in Fig. 7.7 but for a fixed value of $\Delta/(\kappa/2) = 1.5$ and as a function of $N\Gamma_c\tau$. The vertical red dashed line marks the transition from the stationary to the polychromatic superradiant regime and the red circles in (c) at the phase threshold are the values of $\omega \pm \text{Im}(\nu_1)$. The remaining parameters are the same as in Fig. 7.7. 167
- 7.9 (a) The cavity pulling coefficient \wp defined in Eq. (7.61) as a function of the cavity linewidth κ and the collective decay $N\Gamma_c$, both in units $1/\tau$. For the calculation of \wp we have solved Eq. (7.60) using the solution of Eq. (7.98) for $f = 0$. (b) The cavity pulling coefficient \wp normalized by $1/(\kappa\tau)$ as a function of $N\Gamma_c$ in units $1/\tau$. For the derivation we have calculated $\wp = \omega/\Delta$ that is independent of Δ in the limit $\kappa\tau \gg 1$ where the cavity field can be eliminated. 169
- 8.1 (a) Atoms are preexcited and pass through a lossy optical cavity. (b) Two-level atoms resonantly exchange photons with the cavity mode with a spatially dependent coupling $g\eta(\mathbf{x})$ 173
- 8.2 The resulting phase diagram describing the light emission for different values of the Doppler shift, $k_c v_z$, and the collective linewidth, $N\Gamma_c$, both in units of the inverse transit time, $1/\tau$. For small values of $N\Gamma_c\tau$ we find no superradiant emission. For sufficiently large values of $N\Gamma_c\tau$, regimes of either regular steady-state superradiance (SSR) or bistable SSR are observed depending on the magnitude of $k_c v_z\tau$ 181

- 8.3 The spectrum $S(\omega)$, defined in Eq. (8.31), as a function of the frequency ω in units of $1/\tau$ in the SSR phase for $k_c v_z \tau = 2\pi \times 0.3$ (a) and in the bistable SSR phase $k_c v_z \tau = 2\pi \times 0.8$ (b). For the simulation we used $N\Gamma_c \tau = 30$, $N = 800$, and a total integration time of $t_0 + T = t_{\text{sim}} = 2000\tau$. The spectra are calculated using 500 independent initializations and after a time $t_0 = 10\tau$ (after which the system is well described as being in steady state). The two insets in subplot (b) show the averaged spectrum of the trajectories that correspond to a negative frequency $\omega\tau \approx -4.46$ (238 trajectories) and positive frequency $\omega\tau \approx 4.46$ (262 trajectories). 184
- 8.4 The phase difference $\Delta\varphi(t)$, defined in Eq. (8.32), as a function of time in units of τ for $N = 800$. The time window is defined by $t_0 = 10\tau$ and $t_1 = 1700\tau$, and the total simulation time is $t_{\text{sim}} = 2000\tau$. For the simulations we used 500 trajectories and the parameters $k_c v_z \tau = 2\pi \times 0.8$ and $N\Gamma_c \tau = 30$ 186
- 8.5 The collective dipole $\langle J^* J \rangle / N^2$, subplots (a–c), and the frequency of the light ω in units of $1/\tau$, subplots (b–d), as functions of $k_c v_z \tau$. Subplots (a–b), and (c–d) show results for $N\Gamma_c \tau = 20$ and $N\Gamma_c \tau = 30$, respectively. The circles and stars correspond to numerical simulations of Eqs. (8.5)–(8.8), and the solid lines represent analytical solutions for $N \rightarrow \infty$. The vertical gray dashed lines show the transition from regular SSR to bistable SSR. The numerical values of ω from the simulations in subplots (b) and (d) have been calculated by fitting $g_1(t)$ (Eq. (8.64)) to $\cos(\omega t + \phi_0)e^{-\Gamma t/2}$ and $t_0 = 10\tau$. Here, ω , Γ and ϕ_0 are fitting parameters. The simulations are performed with $N = 800$, an integration time of $t_{\text{sim}} = 100\tau$, and 400 initializations. 189

- 8.6 The jump probability P_{jump} , defined in Eq. (8.45), for different values of $k_c v_z \tau$ for $N\Gamma_c \tau = 20$ (a) and $N\Gamma_c \tau = 30$ (b). For the simulations we used $t_{\text{sim}} = 100\tau$, $N = 800$, and $\mathcal{T} = 400$ and started the analysis after $t_0 = 10\tau$, after which, to good approximation, the system had reached the stationary state. The value of $\Delta\varphi(t)$ for each trajectory is calculated according to Eq. (8.32) without the time average for $t_1 \rightarrow t_0$. According to the definitions given in the text prior to Eq. (8.45), we have used $t_{\text{max}} = 90\tau$ that we split into $M = 20$ bins. The gray dashed vertical line shows the threshold between the regular SSR and the bistable SSR phases, i.e., $k_c v_z \tau = \pi$. 191
- 8.7 The linewidth Γ in units $1/(N\tau)$ as functions of $k_c v_z \tau$ for $N\Gamma_c \tau = 20$ (a) and $N\Gamma_c \tau = 30$ (b). The circles and stars correspond to numerical simulations, and the solid lines represent the result of Eq. (8.63) for $N \rightarrow \infty$. The vertical gray dashed lines show the transition from regular SSR to bistable SSR. The values of Γ have been calculated by fitting g_1 (Eq. (8.64)) with $\cos(\omega t + \phi_0)e^{-\Gamma t/2}$ and $t_0 = 10\tau$. The simulations are performed with $N = 800, 400$ trajectories, and an integration time of $t_{\text{sim}} = 100\tau$ 196
- 8.8 The linewidth Γ in units of $1/\tau$ as a function of the intracavity atom number N for $N\Gamma_c \tau = 30$. The blue circles, green crosses, and red stars correspond to different values of $k_c v_z \tau$ (see legend) at the threshold, in the SSR phase, and in the bistable SSR phase. The blue dashed, green dashed-dotted, and red dotted lines are linear fits according to $\Gamma\tau \propto N^\alpha$ with $\alpha = -0.30$, $\alpha = -1.03$, and $\alpha = -1.06$, respectively. For every N we average over $4.8 \times 10^5/N$ trajectories with a simulation time $t_{\text{sim}} = 100\tau$. Every point is calculated using the fit as described in the caption of Fig. 8.7. . . . 198

Chapter 1

Introduction

The study of collective effects in atomic and molecular ensembles with cavity-mediated interactions is a very active research topic in quantum gas physics. Ongoing research focuses on the simulation and exploration of many-body systems [8, 125, 53, 157, 108] and also their application to metrology that takes advantage of the collective behavior [135, 90, 113, 50, 118].

An example of such a collective effect is superradiance, which describes the collective light emission enhanced by the build-up of macroscopic coherence in the ensemble of atomic or molecular dipoles. Originally, superradiance was predicted for free-space systems, that is, when the interparticle distance is smaller than the optical wavelength [32, 52]. However, this condition can be overcome by trapping the light in a confined volume, such as an optical cavity, and maintaining the condition of strong coupling of the particles to a single lossy resonator mode. More explicitly, superradiance in this case requires the cavity linewidth to be large compared to the collective linewidth of the dipoles. This results in a situation in which the coherence is stored in the atomic dipoles while the cavity mode is overdamped.

The superradiant laser [101, 12] takes advantage of this effect and relies on a stable coherent collective dipole. This laser has the potential to produce light with an ultranarrow linewidth [101, 100] that reflects the extremely high quality factor of the electronic transition [115, 116]. In addition, recent studies have analyzed such systems as manifestation of phase synchronization [166, 172, 161], connected them to time crystals [49, 62, 156, 7, 18, 73, 75], and discussed them as candidates for active optical clocks [25, 168].

A number of previous superradiant laser proposals and current experiments suggest trapping the atoms inside of the cavity [101, 12, 100, 99, 95, 80, 29, 170, 87, 136, 169] with potential continuous incoherent repumping as its energy source. However, this is typically not easy to realize due to the need for closed transitions and external fields to trap the atoms. Furthermore, these additional complexities will usually lead to radiative heating of the atomic cloud and also to atom loss.

Another approach to achieve superradiant lasing is to couple a beam of moving atomic dipoles to a single resonator mode [153, 92, 70]. In this case the atoms can be precooled and prepared in the excited state before entering the cavity. This spatially separates the quantum state preparation stage from the collective emission that occurs while atoms travel through the cavity volume. Such designs are less prone to the adverse effects of radiative heating and atom loss due to the finite lifetime of trapped atom systems. This may allow for an alternative pathway towards truly continuous-wave superradiant lasing in the optical domain [92].

In this thesis, we study in detail the *superradiant atomic beam laser* model. The remaining of the thesis is structured as follows. In Chap. 2, we derive the Jaynes-Cummings model for a moving atom interacting with a single mode cavity. In Chap. 3, we derive the quantum master equation and the corresponding Heisenberg-Langevin equations. We show their equivalence given a heat bath of harmonic oscillators in vacuum. In Chap. 4, we lay out the theoretical foundation to study cavity superradiant systems. We derive the Heisenberg-Langevin equations for the superradiant beam laser system in the “bad cavity” limit. Moreover, we provide the detailed form of the corresponding c -number Langevin equations, which are used to numerically simulate the superradiant atomic beam laser system under various configurations in Chap. 5–8. In Chap. 5, we propose the superradiant beam laser from an experimental point of view, focusing on its potential as a candidate to be the first rugged ultracoherent laser. In Chaps. 6 we study the same model from a theoretical point of view and analyze multiple superradiant phase transitions including a multicomponent superradiant phase. In Chap. 7, we introduce a finite cavity detuning and discuss the various superradiant phases as well as calculating the cavity pulling coefficient. In Chap. 8, we examine the regular and bistable

superradiant phases given a slanted atomic beam of a single velocity. In Chap. 9, we conclude our discussion and talk about future research direction.

Chapter 2

Background

In this chapter, we review the background of modern quantum optics. Starting from the canonical quantization of electrodynamics, we first derive the quantized Hamiltonian of the coupled system of moving particles and electromagnetic fields. We then focus on systems that are confined in a certain quantization volume such as an optical cavity, which are normally called the cavity quantum electrodynamics systems, or *cavity QED systems*. With the long-wavelength and rotating-wave approximations, we derive the Jaynes-Cummings model of a two-level atom coupled to a single cavity mode.

All of the analysis in this thesis is non-relativistic.

2.1 Canonical quantization of electrodynamics

Quantum optics studies the quantum nature of interactions between individual quanta of electromagnetic fields, the “photons”, and ensembles of charged particles such as neutral atoms, ions, and molecules. Such interactions are classically described by Maxwell’s equations and the Lorentz force equation in electrodynamics. In this section, we start from these classical equations, and then follow the route of Dirac’s *canonical quantization* [35, 34] to derive the quantized Hamiltonian of the coupled system of photons and charged particles. For a more detailed derivation and discussions, we refer the readers to Ref. [27, 28].

It should be noted here that historically this quantization process is sometimes called “second quantization”. While “first quantization” refers to the canonical quantization of classical particles

into quantum wave functions, the term “second quantization” has been used to describe the canonical quantization of classical electromagnetic fields into a sum of quantum harmonic oscillators. From modern point of view, this is more of a misnomer. We are not quantizing electromagnetism “twice” as the name “second” suggests, but only quantizing classical fields instead of classical particles. On the other hand, “second quantization” is now mostly used in the formalism of quantum field theory. In that context, the term refers to the “second” quantization of a system of already quantized particles from a Hilbert space with symmetric or antisymmetric tensor algebra into a Fock space, where a vacuum state and occupation states are defined.¹ Although the results of the quantization in electromagnetism and quantum field theory are similar—a Fock space, we will avoid using the term “second quantization” in the remaining of this thesis and instead call it canonical quantization.

2.1.1 Classical Lagrangian of electrodynamics

Classical Maxwell’s equations in vacuum have the form

$$\nabla \cdot \mathbf{E}(t, \mathbf{r}) = \frac{\rho(t, \mathbf{r})}{\varepsilon_0}, \quad (2.1)$$

$$\nabla \cdot \mathbf{B}(t, \mathbf{r}) = 0, \quad (2.2)$$

$$\nabla \times \mathbf{E}(t, \mathbf{r}) = -\dot{\mathbf{B}}(t, \mathbf{r}), \quad (2.3)$$

$$\nabla \times \mathbf{B}(t, \mathbf{r}) = \mu_0 \mathbf{J}(t, \mathbf{r}) + \mu_0 \varepsilon_0 \dot{\mathbf{E}}(t, \mathbf{r}), \quad (2.4)$$

where $\mathbf{E}(t, \mathbf{r})$ and $\mathbf{B}(t, \mathbf{r})$ are the electric and magnetic field vectors, $\rho(t, \mathbf{r}) = \sum_j q_j \delta[\mathbf{r} - \mathbf{r}_j(t)]$ is the charge density for point charges q_j , $\mathbf{J}(t, \mathbf{r}) = \sum_j q_j \dot{\mathbf{r}}_j(t) \delta[\mathbf{r} - \mathbf{r}_j(t)]$ is the current density, and ε_0 and μ_0 are the electric and magnetic vacuum permittivities, satisfying $\varepsilon_0 \mu_0 c^2 = 1$, with c the speed of light. Here $\delta(\mathbf{r})$ is the Dirac delta function. We have used Newton’s notation $\dot{\mathbf{r}}_j(t)$ to denote the total derivative $\frac{d\mathbf{r}_j}{dt}$, and the notation $\dot{\mathbf{B}}(t, \mathbf{r})$ to denote the partial derivative $\frac{\partial \mathbf{B}}{\partial t}$, etc. It should be clear whether this notation means total or partial derivative within a given context.

¹As Edward Nelson said, “first quantization is a mystery, but second quantization is a functor.”

In essence, Eq. (2.2) and Eq. (2.3) only characterize the self-coupling structure of the fields, and are immediately satisfied if we introduce the electric potential $\phi(t, \mathbf{r})$ and vector potential $\mathbf{A}(t, \mathbf{r})$ and define

$$\mathbf{E}(t, \mathbf{r}) = -\nabla\phi(t, \mathbf{r}) - \dot{\mathbf{A}}(t, \mathbf{r}), \quad (2.5)$$

$$\mathbf{B}(t, \mathbf{r}) = \nabla \times \mathbf{A}(t, \mathbf{r}). \quad (2.6)$$

On the other hand, Eq. (2.1) and Eq. (2.4) describe the change of the fields due to the interaction with matter. These two equations, combined with the Newton-Lorentz equation

$$m_j \ddot{\mathbf{r}}_j = q_j [\mathbf{E}(\mathbf{r}_j) + \dot{\mathbf{r}}_j \times \mathbf{B}(\mathbf{r}_j)], \quad (2.7)$$

which describes the dynamics of point charges with mass m_j in the fields, give the classical picture of the coupling between matter and fields.

We now present the classical “standard Lagrangian” [27] for the system of electromagnetic fields and particles. With the definitions in Eqs. (2.5)–(2.6), we define

$$L = \sum_j \frac{1}{2} m_j \dot{\mathbf{r}}_j^2 + \frac{\varepsilon_0}{2} \int d^3\mathbf{r} (\mathbf{E}^2 - c^2 \mathbf{B}^2) + \sum_j q_j [\dot{\mathbf{r}}_j \cdot \mathbf{A}(\mathbf{r}_j) - \phi]. \quad (2.8)$$

It is straightforward to check that the Euler-Lagrangian equations of the standard Lagrangian L in Eq. (2.8) leads to Eq. (2.1), Eq. (2.4), and Eq. (2.7).

Now, in order to apply canonical quantization, we need to derive the Hamiltonian corresponding to the Lagrangian. But before finding the canonical momentum and thereby proceeding, it is extremely useful to examine and reduce the number of dynamical variables. Taking \mathbf{E} and \mathbf{B} as functions of \mathbf{A} and ϕ , there are eight field dynamical variables at each point in space in Eq. (2.8), i.e., $\{\mathbf{A}(\mathbf{r}), \phi(\mathbf{r}), \dot{\mathbf{A}}(\mathbf{r}), \dot{\phi}(\mathbf{r})\}$. However, in the Maxwell-Lorentz equations, there are only six field dynamical variables, i.e., $\{\mathbf{E}(\mathbf{r}), \mathbf{B}(\mathbf{r})\}$. Therefore, there are two redundant variables in Eq. (2.8). Noticing that $\dot{\phi}$ does not appear in Eq. (2.8), we are led to eliminate ϕ as well, since its canonical

momentum is zero ². Rewriting Eq. (2.8) as

$$L = \sum_j \frac{1}{2} m_j \dot{\mathbf{r}}_j^2 + \int d^3\mathbf{r} \mathcal{L}_{\text{EM}}, \quad (2.9)$$

where

$$\mathcal{L}_{\text{EM}} = \frac{\varepsilon_0}{2} (\mathbf{E}^2 - c^2 \mathbf{B}^2) + \mathbf{J} \cdot \mathbf{A} - \rho \phi \quad (2.10)$$

is the Lagrangian density of electromagnetic fields, we have

$$\begin{aligned} 0 &= \frac{\partial L}{\partial \dot{\phi}} = \frac{d}{dt} \left(\frac{\partial L}{\partial \dot{\phi}} \right) = \frac{\partial L}{\partial \phi} \\ &= \frac{\partial \mathcal{L}_{\text{EM}}}{\partial \phi} - \nabla \cdot \left(\frac{\partial \mathcal{L}_{\text{EM}}}{\partial \nabla \phi} \right) \\ &= -\rho(\mathbf{r}) - \varepsilon_0 \nabla^2 \phi(t, \mathbf{r}) - \varepsilon_0 \nabla \cdot \dot{\mathbf{A}}(t, \mathbf{r}). \end{aligned} \quad (2.11)$$

Here we have used the Euler-Lagrangian equation for ϕ and the derivative of the functional. We have also used the notation $\frac{\partial}{\partial \mathbf{v}} = \left(\frac{\partial}{\partial v_x}, \frac{\partial}{\partial v_y}, \frac{\partial}{\partial v_z} \right)^T$ for any vector \mathbf{v} .

It is immediately obvious that we can solve for ϕ from Eq. (2.11) conveniently by going into the corresponding Fourier space (or the reciprocal space as referred to by Cohen-Tannoudji in Ref. [27]) of the real space, i.e.,

$$0 = -\tilde{\rho}(\mathbf{k}) + \varepsilon_0 k^2 \tilde{\phi}(t, \mathbf{k}) - \varepsilon_0 i \mathbf{k} \cdot \frac{\partial \tilde{\mathbf{A}}(t, \mathbf{k})}{\partial t}, \quad (2.12)$$

and therefore

$$\tilde{\phi}(t, \mathbf{k}) = \frac{1}{k^2} \left[\frac{\tilde{\rho}(\mathbf{k})}{\varepsilon_0} + i \mathbf{k} \cdot \frac{\partial \tilde{\mathbf{A}}(t, \mathbf{k})}{\partial t} \right], \quad (2.13)$$

with $k = |\mathbf{k}|$. Here, we have used the following definition of the Fourier transform in three dimensions ³

$$\tilde{f}(\mathbf{k}) = \frac{1}{(2\pi)^{3/2}} \int d^3\mathbf{r} f(\mathbf{r}) e^{-i\mathbf{k} \cdot \mathbf{r}}, \quad (2.14)$$

$$f(\mathbf{r}) = \frac{1}{(2\pi)^{3/2}} \int d^3\mathbf{k} \tilde{f}(\mathbf{k}) e^{i\mathbf{k} \cdot \mathbf{r}}, \quad (2.15)$$

²Actually, it is not even possible to canonically quantize the system from the standard Lagrangian without reducing ϕ , since its conjugate momentum is identically zero.

³See Appx. A for further discussions on conventions for Fourier transform.

where $f(\mathbf{r})$ can be any function defined on real space, and $\tilde{f}(\mathbf{k})$ is then its counterpart in Fourier space.

We can now derive the reduced Lagrangian density in Fourier space. To do this, we first rewrite Eq. (2.9) as

$$L = \sum_j \frac{1}{2} m_j \dot{\mathbf{r}}_j^2 + \int d^3\mathbf{k} \left[\frac{\varepsilon_0}{2} \left(|\tilde{\mathbf{E}}|^2 - c^2 |\tilde{\mathbf{B}}|^2 \right) + \tilde{\mathbf{J}}^* \cdot \tilde{\mathbf{A}} - \tilde{\rho}^* \tilde{\phi} \right], \quad (2.16)$$

where we have used Plancherel's theorem. Notice that, in Fourier space, the degrees of freedom have doubled in number because $\tilde{\mathbf{A}}$, $\tilde{\phi}$, $\tilde{\mathbf{J}}$, and $\tilde{\rho}$ are now complex. However, since $\mathbf{A}(\mathbf{r})$ is real, $\tilde{\mathbf{A}}(\mathbf{k})$ is a Hermitian function satisfying $\tilde{\mathbf{A}}(-\mathbf{k}) = \tilde{\mathbf{A}}^*(\mathbf{k})$. Likewise, $\tilde{\phi}$, $\tilde{\mathbf{J}}$, and $\tilde{\rho}$ also satisfy similar Hermitian constraints. Therefore if we know the values of these functions in half of the Fourier space, or the reciprocal half space, we know them in the whole Fourier space. This leads us to rewrite the standard Lagrangian L again as

$$L = \sum_j \frac{1}{2} m_j \dot{\mathbf{r}}_j^2 + \int d^3\mathbf{k} \overline{\mathcal{L}}, \quad (2.17)$$

where the notation $\int d^3\mathbf{k}$ means the integral over the reciprocal half space, and

$$\overline{\mathcal{L}} = \varepsilon_0 \left(|\tilde{\mathbf{E}}|^2 - c^2 |\tilde{\mathbf{B}}|^2 \right) + 2 \operatorname{Re} \left\{ \tilde{\mathbf{J}}^* \cdot \tilde{\mathbf{A}} - \tilde{\rho}^* \tilde{\phi} \right\}. \quad (2.18)$$

In Fourier space, Eqs. (2.5)–(2.6) become

$$\tilde{\mathbf{E}} = -i\mathbf{k}\tilde{\phi} - \frac{\partial \tilde{\mathbf{A}}}{\partial t}, \quad (2.19)$$

$$\tilde{\mathbf{B}} = i\mathbf{k} \times \tilde{\mathbf{A}}. \quad (2.20)$$

Using Eq. (2.13) to eliminate $\tilde{\phi}$ in Eq. (2.19) yields

$$\tilde{\mathbf{E}} = -i \frac{\mathbf{k}}{\varepsilon_0 k^2} \tilde{\rho} - \frac{\partial \tilde{\mathbf{A}}^\perp}{\partial t}. \quad (2.21)$$

Here, we define the longitudinal component of the vector potential $\tilde{\mathbf{A}}$ as $\tilde{\mathbf{A}}^\parallel = \frac{\mathbf{k} \cdot \tilde{\mathbf{A}}}{k^2} \mathbf{k}$ and the transverse component as $\tilde{\mathbf{A}}^\perp = \tilde{\mathbf{A}} - \tilde{\mathbf{A}}^\parallel$.

Now, substituting Eq. (2.13), Eq. (2.20), and Eq. (2.21) into Eq. (2.18), we have the reduced Lagrangian density $\overline{\mathcal{L}}$ in the reciprocal half space

$$\overline{\mathcal{L}} = -\frac{|\tilde{\rho}|^2}{\varepsilon_0 k^2} + \varepsilon_0 \left(\left| \frac{\partial \tilde{\mathbf{A}}^\perp}{\partial t} \right|^2 - c^2 k^2 |\tilde{\mathbf{A}}^\perp|^2 \right) + 2 \operatorname{Re} \{ \tilde{\mathbf{J}}^* \cdot \tilde{\mathbf{A}}^\perp \} + \overline{\mathcal{L}}^\parallel, \quad (2.22)$$

where

$$\overline{\mathcal{L}}^\parallel = 2 \operatorname{Re} \{ \tilde{\mathbf{J}}^* \cdot \tilde{\mathbf{A}}^\parallel \} + \frac{2}{k^2} \operatorname{Im} \left\{ \tilde{\rho}^* \frac{\partial \tilde{\mathbf{A}}^\parallel}{\partial t} \cdot \mathbf{k} \right\} \quad (2.23)$$

is the longitudinal Lagrangian density.

At this point, we have already expressed the reduced Lagrangian density in terms of the dynamical variables $\left\{ \tilde{\mathbf{A}}, \frac{\partial \tilde{\mathbf{A}}}{\partial t} \right\}$ only. It is possible to directly find the Hamiltonian using the Legendre transform and then to impose the canonical quantization rules. However, a careful examination on the longitudinal Lagrangian density $\overline{\mathcal{L}}^\parallel$ is not only useful for simplification of the derivation, but also helpful to understand the gauge invariance underlying both the classical and quantum electrodynamics.

It is obvious from Eq. (2.22) that the longitudinal components of the fields appear only in $\overline{\mathcal{L}}^\parallel$. The Euler-Lagrangian equation for $\tilde{\mathbf{A}}^\parallel$ yields

$$\frac{\partial \tilde{\rho}}{\partial t} = -i \tilde{\mathbf{J}} \cdot \mathbf{k} \quad (2.24)$$

which is nothing other than charge conservation. The fact that Eq. (2.24) is independent of $\tilde{\mathbf{A}}^\parallel$ means that $\tilde{\mathbf{A}}^\parallel$ is not a real dynamical variable and can take any value. This is manifest if we substitute Eq. (2.24) back into $\overline{\mathcal{L}}^\parallel$ and thereby note that

$$\overline{\mathcal{L}}^\parallel = \frac{\partial}{\partial t} \frac{2 \operatorname{Im} \{ \tilde{\rho}^* \tilde{A}^\parallel \}}{k}, \quad (2.25)$$

which gives

$$L = \sum_j \frac{1}{2} m_j \dot{\mathbf{r}}_j^2 - \int d^3 \mathbf{k} \frac{|\tilde{\rho}|^2}{\varepsilon_0 k^2} + \int d^3 \mathbf{k} \left[\varepsilon_0 \left(\left| \frac{\partial \tilde{\mathbf{A}}^\perp}{\partial t} \right|^2 - c^2 k^2 |\tilde{\mathbf{A}}^\perp|^2 \right) + 2 \operatorname{Re} \{ \tilde{\mathbf{J}}^* \cdot \tilde{\mathbf{A}}^\perp \} \right] + \frac{dF}{dt}, \quad (2.26)$$

where

$$F = 2 \operatorname{Im} \int d^3 \mathbf{k} \frac{\tilde{\rho}^* \tilde{A}^{\parallel}}{k} \quad (2.27)$$

determines the gauge choice, with $\tilde{A}^{\parallel} = \frac{\tilde{\mathbf{A}}^{\parallel} \cdot \mathbf{k}}{k}$. Since $\frac{dF}{dt}$ is a total derivative with respect to time, and the longitudinal field $\tilde{\mathbf{A}}^{\parallel}$ only appears in F , we know that the dynamics of the system is invariant with our free selection of the gauge function F . If we choose the Coulomb gauge, i.e.,

$$\tilde{\mathbf{A}}^{\parallel} = 0, \quad (2.28)$$

then $F = 0$, and we arrive at the standard Lagrangian

$$L_{\text{coul}} = \sum_j \frac{1}{2} m_j \dot{\mathbf{r}}_j^2 - V_{\text{coul}} + \int d^3 \mathbf{k} \overline{\mathcal{L}}_{\text{coul}}, \quad (2.29)$$

where

$$V_{\text{coul}} = \int d^3 \mathbf{k} \frac{|\tilde{\rho}(\mathbf{k})|^2}{\varepsilon_0 k^2} = \frac{1}{8\pi\varepsilon_0} \iint d^3 \mathbf{r} d^3 \mathbf{r}' \frac{\rho(\mathbf{r})\rho(\mathbf{r}')}{|\mathbf{r} - \mathbf{r}'|} \quad (2.30)$$

is the non-retarded Coulomb energy (including the diverging self energy) and

$$\overline{\mathcal{L}}_{\text{coul}} = \varepsilon_0 \left(\left| \frac{\partial \tilde{\mathbf{A}}^{\perp}}{\partial t} \right|^2 - c^2 k^2 |\tilde{\mathbf{A}}^{\perp}|^2 \right) + 2 \operatorname{Re} \{ \tilde{\mathbf{J}}^* \cdot \tilde{\mathbf{A}}^{\perp} \} \quad (2.31)$$

is the Lagrangian density in Coulomb gauge.

It is also natural to express the standard Lagrangian in real space, where we have

$$L_{\text{coul}} = \sum_j \frac{1}{2} m_j \dot{\mathbf{r}}_j^2 - V_{\text{coul}} + \int d^3 \mathbf{r} \mathcal{L}_{\text{coul}}, \quad (2.32)$$

and

$$\mathcal{L}_{\text{coul}} = \frac{\varepsilon_0}{2} \left(|\dot{\mathbf{A}}|^2 - c^2 |\nabla \times \mathbf{A}|^2 \right) + \mathbf{J} \cdot \mathbf{A} \quad (2.33)$$

with the Coulomb gauge condition $\nabla \cdot \mathbf{A} = 0$.

In the next section, we will continue to work in Fourier space and use Eq. (2.29) to find the corresponding Hamiltonian for the fields. There are several benefits. First, it is intrinsically easy to work in Fourier space since the space derivatives have been turned into multiplications using the

substitution rule $\nabla \rightarrow i\mathbf{k}$. Second, the physical meaning of the longitudinal and transverse modes of the fields is clearer in Fourier space, since they are defined with respect to the wavevector \mathbf{k} . Third, since there are no derivatives with respect to \mathbf{k} , the Lagrangian density $\overline{\mathcal{L}}$ is now strictly local in \mathbf{k} . As a result, contributions of various modes of the field appear explicitly, which makes it easy to separate the nonrelativistic modes, i.e., long-wavelength modes, and make the dipole approximation, as we will see later.

2.1.2 Hamiltonian and canonical quantization

From the standard Lagrangian in the Coulomb gauge introduced in Eqs. (2.29)–(2.33), we can identify the canonical momenta as follows,

$$\mathbf{p}_j = \frac{\partial L_{\text{coul}}}{\partial \dot{\mathbf{r}}_j} = m_j \dot{\mathbf{r}}_j + q_j \mathbf{A}(\mathbf{r}_j), \quad (2.34)$$

$$\tilde{\boldsymbol{\Pi}}(\mathbf{k}) = \left[\frac{\partial L_{\text{coul}}}{\partial \left(\frac{\partial \tilde{\mathbf{A}}^\perp}{\partial t} \right)} \right]^* = \varepsilon_0 \frac{\partial \tilde{\mathbf{A}}^\perp(\mathbf{k})}{\partial t}. \quad (2.35)$$

Here, the definition with the complex conjugate in Eq. (2.35) is to make sure of the self-consistency such that $\tilde{\boldsymbol{\Pi}}(\mathbf{k})$ is the Fourier transform of the momentum $\boldsymbol{\Pi}(\mathbf{r}) = \varepsilon_0 \frac{\partial \mathbf{A}(\mathbf{r})}{\partial t}$ and is therefore conjugate with the field $\mathbf{A}(\mathbf{r})$. Also, the definition of $\tilde{\boldsymbol{\Pi}}(\mathbf{k})$ can be easily generalized to the full Fourier space by imposing $\tilde{\boldsymbol{\Pi}}^*(\mathbf{k}) = \tilde{\boldsymbol{\Pi}}(-\mathbf{k})$.

We can now use the Legendre transform to construct the Hamiltonian from the Lagrangian L in Coulomb gauge, which yields

$$H = \sum_j \frac{1}{2m_j} [\mathbf{p}_j - q_j \mathbf{A}(\mathbf{r}_j)]^2 + \varepsilon_0 \int d^3\mathbf{k} \left[\frac{|\tilde{\boldsymbol{\Pi}}(\mathbf{k})|^2}{\varepsilon_0^2} + c^2 k^2 |\tilde{\mathbf{A}}^\perp(\mathbf{k})|^2 \right] + V_{\text{coul}}, \quad (2.36)$$

and in real space

$$H = \sum_j \frac{1}{2m_j} [\mathbf{p}_j - q_j \mathbf{A}(\mathbf{r}_j)]^2 + \frac{\varepsilon_0}{2} \int d^3\mathbf{r} \left[\frac{|\boldsymbol{\Pi}(\mathbf{r})|^2}{\varepsilon_0^2} + c^2 |\nabla \times \mathbf{A}^\perp(\mathbf{r})|^2 \right] + V_{\text{coul}} \quad (2.37)$$

with $\mathbf{A}(\mathbf{r})$ satisfying the Coulomb condition $\nabla \cdot \mathbf{A} = 0$.

As the last step of the canonical quantization, we promote the dynamical variables in the

Hamiltonian H into quantum operators (denoted by $\hat{\cdot}$) that act on the Hilbert space, and introduce their commutation relations.

For the particle position and momentum, we promote

$$\left\{ (r_j)_\alpha, (p_k)_\beta \right\} \rightarrow \left\{ (\hat{r}_j)_\alpha, (\hat{p}_k)_\beta \right\} \quad (2.38)$$

with the commutation relations

$$\left[(\hat{r}_j)_\alpha, (\hat{p}_k)_\beta \right] = i\hbar\delta_{jk}\delta_{\alpha\beta}, \quad (2.39)$$

where j, k stand for particle indices, and $\alpha, \beta \in \{x, y, z\}$ stand for Cartesian components. The operators $(\hat{r}_j)_\alpha$ and $(\hat{p}_k)_\beta$ are Hermitian since both the particle position and momentum are physical observables. The functions δ_{jk} and $\delta_{\alpha\beta}$ are Kronecker delta functions. All the other combinations of the commutations are zero.

Since at each point \mathbf{k} in the reciprocal half space there are two independent complex components in the transverse field $\tilde{\mathbf{A}}^\perp$ (corresponding to the two polarizations), we promote the field dynamical variables

$$\left\{ \tilde{A}_\varepsilon^\perp(\mathbf{k}), \tilde{\Pi}_{\varepsilon'}(\mathbf{k}') \right\} \rightarrow \left\{ \hat{A}_\varepsilon(\mathbf{k}), \hat{\Pi}_{\varepsilon'}(\mathbf{k}') \right\} \quad (2.40)$$

with the commutation relations [27]

$$\left[\hat{A}_\varepsilon(\mathbf{k}), \hat{\Pi}_{\varepsilon'}^\dagger(\mathbf{k}') \right] = i\hbar\delta(\mathbf{k} - \mathbf{k}')\delta_{\varepsilon\varepsilon'}, \quad (2.41)$$

where \mathbf{k} and \mathbf{k}' are vectors in the reciprocal half space. All the other combinations of commutations are zero. Here $\varepsilon \in \{1, 2\}$ stands for the two transverse directions orthogonal to \mathbf{k} , so we can write $\hat{A}_\varepsilon(\mathbf{k}) = \boldsymbol{\varepsilon} \cdot \hat{\mathbf{A}}(\mathbf{k})$ with $\boldsymbol{\varepsilon}$ the corresponding unit vector. The newly promoted field operators and their conjugates satisfy the Hermitian constraints $\hat{A}_\varepsilon(-\mathbf{k}) = \hat{A}_\varepsilon^\dagger(\mathbf{k})$, $\hat{\Pi}_\varepsilon(-\mathbf{k}) = \hat{\Pi}_\varepsilon^\dagger(\mathbf{k})$. We have dropped the \perp notation for field operators, but one should keep in mind that only the transverse fields contribute. The field operators and their conjugates commute with the operators for particles introduced in Eq. (2.38).

With the introduction of the quantum operators and commutation relations, we can write down the promoted quantum Hamiltonian from Eq. (2.36)

$$\hat{H} = \sum_j \frac{1}{2m_j} \left[\hat{\mathbf{p}}_j - q_j \hat{\mathbf{A}}(\hat{\mathbf{r}}_j) \right]^2 + \varepsilon_0 \int d^3\mathbf{k} \sum_\varepsilon \left[\frac{\hat{\Pi}_\varepsilon^\dagger(\mathbf{k}) \hat{\Pi}_\varepsilon(\mathbf{k})}{\varepsilon_0^2} + \omega^2 \hat{A}_\varepsilon^\dagger(\mathbf{k}) \hat{A}_\varepsilon(\mathbf{k}) \right] + \hat{V}_{\text{coul}}, \quad (2.42)$$

where $\omega = c|\mathbf{k}|$ is the angular frequency corresponding to the wave vector \mathbf{k} , and \hat{V}_{coul} is the quantum version of the Coulomb potential energy Eq. (2.30). Notice that the ordering of operators is arbitrary here since only products of commuting operators exist in Eq. (2.42).

Formally, this concludes the canonical quantization description. However, similar to the approach developed for simple harmonic oscillators, it is useful to express the generalized position and momentum in terms of creation and annihilation operators [27]. In our case, we define

$$\hat{a}_\varepsilon(\mathbf{k}) = \sqrt{\frac{\varepsilon_0}{2\hbar\omega}} \left[\omega \hat{A}_\varepsilon(\mathbf{k}) + \frac{i}{\varepsilon_0} \hat{\Pi}_\varepsilon(\mathbf{k}) \right], \quad (2.43)$$

$$\hat{a}_\varepsilon^\dagger(\mathbf{k}) = \sqrt{\frac{\varepsilon_0}{2\hbar\omega}} \left[\omega \hat{A}_\varepsilon^\dagger(\mathbf{k}) - \frac{i}{\varepsilon_0} \hat{\Pi}_\varepsilon^\dagger(\mathbf{k}) \right], \quad (2.44)$$

with the commutation relations

$$\left[\hat{a}_\varepsilon(\mathbf{k}), \hat{a}_{\varepsilon'}^\dagger(\mathbf{k}') \right] = \delta_{\varepsilon\varepsilon'} \delta(\mathbf{k} - \mathbf{k}'). \quad (2.45)$$

All the other commutators are zero. One can check that Eqs. (2.43)–(2.44) and Eq. (2.45) are consistent with Eq. (2.41). Moreover, the commutation relations in Eq. (2.45) hold not only for \mathbf{k} and \mathbf{k}' in the reciprocal half space, but also in the whole Fourier space as results from Eq. (2.45) and the Hermitian constraints. Therefore the new field operator $\hat{a}_\varepsilon(\mathbf{k})$ is truly independent in the whole Fourier space. It is therefore more convenient to express the Hamiltonian using the operators $\hat{a}_\varepsilon(\mathbf{k})$ and $\hat{a}_\varepsilon^\dagger(\mathbf{k})$.

From Eq. (2.44) we have

$$\hat{a}_\varepsilon^\dagger(-\mathbf{k}) = \sqrt{\frac{\varepsilon_0}{2\hbar\omega}} \left[\omega \hat{A}_\varepsilon^\dagger(-\mathbf{k}) - \frac{i}{\varepsilon_0} \hat{\Pi}_\varepsilon^\dagger(-\mathbf{k}) \right] = \sqrt{\frac{\varepsilon_0}{2\hbar\omega}} \left[\omega \hat{A}_\varepsilon(\mathbf{k}) - \frac{i}{\varepsilon_0} \hat{\Pi}_\varepsilon(\mathbf{k}) \right], \quad (2.46)$$

which combined with Eq. (2.43) gives

$$\hat{A}_\varepsilon(\mathbf{k}) = \sqrt{\frac{\hbar}{2\omega\varepsilon_0}} \left[\hat{a}_\varepsilon(\mathbf{k}) + \hat{a}_\varepsilon^\dagger(-\mathbf{k}) \right], \quad (2.47)$$

$$\hat{\Pi}_\varepsilon(\mathbf{k}) = -i \sqrt{\frac{\hbar\omega\varepsilon_0}{2}} \left[\hat{a}_\varepsilon(\mathbf{k}) - \hat{a}_\varepsilon^\dagger(-\mathbf{k}) \right]. \quad (2.48)$$

Substituting Eqs. (2.47)–(2.48) into the Hamiltonian in Eq. (2.42) and keeping track of the ordering of operators, we have the final expression for the quantum electrodynamics Hamiltonian

$$\hat{H} = \sum_j \frac{1}{2m_j} \left[\hat{\mathbf{p}}_j - q_j \hat{\mathbf{A}}(\hat{\mathbf{r}}_j) \right]^2 + \int d^3\mathbf{k} \frac{\hbar\omega}{2} \sum_\varepsilon \left[\hat{a}_\varepsilon^\dagger(\mathbf{k}) \hat{a}_\varepsilon(\mathbf{k}) + \hat{a}_\varepsilon(\mathbf{k}) \hat{a}_\varepsilon^\dagger(\mathbf{k}) \right] + \hat{V}_{\text{coul}} \quad (2.49)$$

$$= \sum_j \frac{1}{2m_j} \left[\hat{\mathbf{p}}_j - q_j \hat{\mathbf{A}}(\hat{\mathbf{r}}_j) \right]^2 + \int d^3\mathbf{k} \hbar\omega \sum_\varepsilon \left[\hat{a}_\varepsilon^\dagger(\mathbf{k}) \hat{a}_\varepsilon(\mathbf{k}) + \frac{1}{2} \delta(0) \right] + \hat{V}_{\text{coul}}, \quad (2.50)$$

where we have chosen the normal ordering in Eq. (2.50). Both ω and \sum_ε depend on \mathbf{k} .

2.1.3 Quantization volume

So far we have derived the canonically quantized Hamiltonian for electrodynamics in free space. One may notice that the vacuum energy term in Eq. (2.50) contains an IR (infrared) diverging $\delta(0)$ term. This is a well-known problem for directly quantizing electromagnetism in infinite space, which can be seen by rewriting $\delta(0) \propto \int \exp[-i(\mathbf{k} - \mathbf{k}) \cdot \mathbf{r}] d^3\mathbf{r} = \int d^3\mathbf{r} \rightarrow \infty$. This formal divergence is remedied in the following manner. In any realistic physical setup, we anticipate a finite space volume, called a *quantization volume*. This finite region together with appropriate boundary conditions provides a lower cutoff for the wave vector \mathbf{k} or field frequency $\omega_{\mathbf{k}}$.

We therefore will first consider a finite box quantization volume $V = L^3$ in real space. To model infinite space, one just needs to take the limit $L \rightarrow \infty$. By imposing periodic boundary conditions of the field variables in the volume V that is constrained by $x, y, z \in \left[-\frac{L}{2}, \frac{L}{2}\right]$, we define the Fourier conjugates of any function $f(\mathbf{r})$ using the following definitions

$$\tilde{f}_{\mathbf{k}} = \frac{1}{V} \int_V d^3\mathbf{r} f(\mathbf{r}) e^{-i\mathbf{k} \cdot \mathbf{r}}, \quad (2.51)$$

$$f(\mathbf{r}) = \sum_{\mathbf{k}} \tilde{f}_{\mathbf{k}} e^{i\mathbf{k} \cdot \mathbf{r}}, \quad (2.52)$$

where \mathbf{k} is given by $k_\alpha = \frac{2\pi n_\alpha}{L}$, $n_\alpha \in \mathbb{Z}$ for $\alpha \in \{x, y, z\}$.

It is easy to see that we are merely replacing the Fourier transform introduced in Eqs. (2.14)–(2.15) by a Fourier series. We have chosen the convention for the Fourier series in such a way that the dimension of $\tilde{f}_{\mathbf{k}}$ is the same as that of $f(\mathbf{r})$, which differs by a three-dimensional volume from

the dimension of $\tilde{f}(\mathbf{k})$ as defined in Eq. (2.14). Thus within a finite volume V , all the results that we have derived in the previous section follow, except that we need to replace $\int d^3\mathbf{k} \rightarrow V \sum_{\mathbf{k}}$, $\delta(\mathbf{k} - \mathbf{k}') \rightarrow \frac{\delta_{\mathbf{k}\mathbf{k}'}}{V}$, and $\tilde{f}(\mathbf{k}) \rightarrow \tilde{f}_{\mathbf{k}}$, where f refers to all the variables to which we have applied the Fourier transform.

The resulting Hamiltonian analogous to Eq. (2.42) is thus

$$\hat{H} = \sum_j \frac{1}{2m_j} \left[\hat{\mathbf{p}}_j - q_j \hat{\mathbf{A}}(\hat{\mathbf{r}}_j) \right]^2 + \varepsilon_0 V \sum_{\mathbf{k}, \varepsilon} \left[\frac{\hat{\Pi}_{\mathbf{k}, \varepsilon}^\dagger \hat{\Pi}_{\mathbf{k}, \varepsilon}}{\varepsilon_0^2} + \omega_{\mathbf{k}}^2 \hat{A}_{\mathbf{k}, \varepsilon}^\dagger \hat{A}_{\mathbf{k}, \varepsilon} \right] + \hat{V}_{\text{coul}}, \quad (2.53)$$

where $\omega_{\mathbf{k}} = c|\mathbf{k}|$. The commutation relations are

$$\left[\hat{A}_{\mathbf{k}, \varepsilon}, \hat{\Pi}_{\mathbf{k}', \varepsilon'} \right] = \frac{i\hbar}{V} \delta_{\mathbf{k}\mathbf{k}'} \delta_{\varepsilon\varepsilon'}. \quad (2.54)$$

We prefer to remove the spatial dimensions when introducing the field operators $\hat{a}_{\mathbf{k}, \varepsilon}$ and $\hat{a}_{\mathbf{k}, \varepsilon}^\dagger$ following Eqs. (2.43)–(2.44). Thus we choose the prefactors in such a way that

$$\hat{A}_{\mathbf{k}, \varepsilon} = \sqrt{\frac{\hbar}{2\omega_{\mathbf{k}}\varepsilon_0 V}} \left(\hat{a}_{\mathbf{k}, \varepsilon} + \hat{a}_{-\mathbf{k}, \varepsilon}^\dagger \right), \quad (2.55)$$

$$\hat{\Pi}_{\mathbf{k}, \varepsilon} = -i \sqrt{\frac{\hbar\omega_{\mathbf{k}}\varepsilon_0}{2V}} \left(\hat{a}_{\mathbf{k}, \varepsilon} - \hat{a}_{-\mathbf{k}, \varepsilon}^\dagger \right). \quad (2.56)$$

Here the field operators $\hat{a}_{\mathbf{k}, \varepsilon}$ and $\hat{a}_{\mathbf{k}, \varepsilon}^\dagger$ are dimensionless, with the bosonic commutation relations

$$\left[\hat{a}_{\mathbf{k}, \varepsilon}, \hat{a}_{\mathbf{k}', \varepsilon'} \right] = \left[\hat{a}_{\mathbf{k}, \varepsilon}^\dagger, \hat{a}_{\mathbf{k}', \varepsilon'}^\dagger \right] = 0, \quad (2.57)$$

$$\left[\hat{a}_{\mathbf{k}, \varepsilon}, \hat{a}_{\mathbf{k}', \varepsilon'}^\dagger \right] = \delta_{\varepsilon\varepsilon'} \delta_{\mathbf{k}\mathbf{k}'}. \quad (2.58)$$

The resulting Hamiltonian is given by

$$\hat{H} = \sum_j \frac{1}{2m_j} \left[\hat{\mathbf{p}}_j - q_j \hat{\mathbf{A}}(\hat{\mathbf{r}}_j) \right]^2 + \sum_{\mathbf{k}, \varepsilon} \frac{\hbar\omega_{\mathbf{k}}}{2} \left(\hat{a}_{\mathbf{k}, \varepsilon}^\dagger \hat{a}_{\mathbf{k}, \varepsilon} + \hat{a}_{\mathbf{k}, \varepsilon} \hat{a}_{\mathbf{k}, \varepsilon}^\dagger \right) + \hat{V}_{\text{coul}} \quad (2.59)$$

$$= \sum_j \frac{1}{2m_j} \left[\hat{\mathbf{p}}_j - q_j \hat{\mathbf{A}}(\hat{\mathbf{r}}_j) \right]^2 + \sum_{\mathbf{k}, \varepsilon} \hbar\omega_{\mathbf{k}} \left(\hat{a}_{\mathbf{k}, \varepsilon}^\dagger \hat{a}_{\mathbf{k}, \varepsilon} + \frac{1}{2} \right) + \hat{V}_{\text{coul}}. \quad (2.60)$$

Comparing Eq. (2.50) and Eq. (2.60), we see that a theory with a finite quantization volume avoids the IR divergence of energy.

From now on, we will always consider the Hamiltonian in Eq. (2.60), and refer to $\hat{a}_{\mathbf{k},\varepsilon}$ and $\hat{a}_{\mathbf{k},\varepsilon}^\dagger$ defined by Eqs. (2.57)–(2.58) as the field operators, or simply the fields. This definition is nice because the field operators are now equivalent to the annihilation and creation operators for simple harmonic oscillators. Also the quantization volume V does not show up explicitly in the Hamiltonian.

Before we end our discussion of canonical quantization, we would like to comment on the significance of the Hamiltonian operator in Eq. (2.60). Physically, Eq. (2.60) is equivalent to saying that the quantum nature of the electromagnetic fields is nothing other than that arising from quantum simple harmonic oscillators. Each independent oscillator corresponds to a transverse mode of the field. The study of interactions between matter and light is thus transformed into the study of interactions between particle states and field Fock states. The operator $\hat{a}_{\mathbf{k},\varepsilon}^\dagger$ creates a particle of energy $\hbar\omega_{\mathbf{k}}$ and polarization ε , called a “photon”, and $\hat{a}_{\mathbf{k},\varepsilon}$ destroys one. In quantum field theory, this idea is further generalized such that the particle states also become Fock states.

2.1.4 Mode functions

From Eqs. (2.51)–(2.52) and Eq. (2.55) we can write down the vector potential $\hat{\mathbf{A}}(\mathbf{r})$ in real space

$$\hat{\mathbf{A}}(\mathbf{r}) = \sum_{\mathbf{k},\varepsilon} \hat{A}_\varepsilon(\mathbf{k}) e^{i\mathbf{k}\cdot\mathbf{r}} \boldsymbol{\varepsilon} = \sum_{\mathbf{k},\varepsilon} \sqrt{\frac{\hbar}{2\omega_{\mathbf{k}}\varepsilon_0 V}} \left[\hat{a}_{\mathbf{k},\varepsilon} e^{i\mathbf{k}\cdot\mathbf{r}} + \hat{a}_{\mathbf{k},\varepsilon}^\dagger e^{-i\mathbf{k}\cdot\mathbf{r}} \right] \boldsymbol{\varepsilon}. \quad (2.61)$$

Here we can always switch from $\sum_{\mathbf{k},\varepsilon} \hat{a}_{-\mathbf{k},\varepsilon}^\dagger e^{i\mathbf{k}\cdot\mathbf{r}}$ to $\sum_{\mathbf{k},\varepsilon} \hat{a}_{\mathbf{k},\varepsilon}^\dagger e^{-i\mathbf{k}\cdot\mathbf{r}}$ because terms with wavevectors \mathbf{k} of opposite signs must coexist in the summation so that the fields can propagate forward and backward.

In general, the quantization volume does not need to be a box. In fact, different geometries with different boundary conditions will correspond to different Fourier expansions of $\hat{\mathbf{A}}(\mathbf{r})$. This leads us to define the *mode function* of the fields within a finite volume.

Consider electromagnetic fields propagating inside a cavity of a certain shape and with corresponding boundary conditions. We assume no sources in the cavity, and choose the Coulomb

gauge with $\phi = 0$ (this is sometimes called the radiation gauge). In classical electromagnetism one can derive the wave equation for $\mathbf{A}(\mathbf{r})$

$$\nabla^2 \mathbf{A} - \frac{1}{c^2} \frac{\partial^2 \mathbf{A}}{\partial t^2} = 0 \quad (2.62)$$

by substituting Eqs. (2.5)–(2.6) into Eq. (2.3). Separation of spatial and temporal variables in \mathbf{A} leads to the solution

$$\mathbf{A}(\mathbf{r}, t) = \int d\omega A_0(\omega) e^{-i\omega t} [\mathbf{u}(\mathbf{r}) + \mathbf{u}^*(\mathbf{r})]. \quad (2.63)$$

Here $A_0(\omega)$ is the field amplitude for frequency ω , and $\mathbf{u}(\mathbf{r})$ is called the *mode function* that must satisfy the homogeneous Helmholtz equation

$$\nabla^2 \mathbf{u}(\mathbf{r}) + k^2 \mathbf{u}(\mathbf{r}) = 0, \quad (2.64)$$

where $k = \omega/c$ is the norm of the wavevector \mathbf{k} . For different wavevectors \mathbf{k}, \mathbf{k}' and different polarizations $\varepsilon, \varepsilon'$ (two for each \mathbf{k} in the Coulomb gauge as we have seen before), we can define the orthonormal mode functions $\mathbf{u}_{\mathbf{k},\varepsilon}(\mathbf{r})$ that satisfy the orthonormality condition

$$\int_V d^3\mathbf{r} \mathbf{u}_{\mathbf{k},\varepsilon}(\mathbf{r}) \cdot \mathbf{u}_{\mathbf{k}',\varepsilon'}^*(\mathbf{r}) = \delta_{\varepsilon\varepsilon'} \delta_{\mathbf{k}\mathbf{k}'}. \quad (2.65)$$

As an example, the solution to the Helmholtz equation for a box of volume $V = L^3$ with periodic boundary conditions is

$$\mathbf{u}_{\mathbf{k},\varepsilon}(\mathbf{r}) = \frac{1}{\sqrt{V}} e^{i\mathbf{k}\cdot\mathbf{r}} \boldsymbol{\varepsilon} \quad (2.66)$$

Thus we can rewrite Eq. (2.61) as

$$\hat{\mathbf{A}}(\mathbf{r}) = \sum_{\mathbf{k},\varepsilon} \sqrt{\frac{\hbar}{2\omega_{\mathbf{k}}\varepsilon_0}} \left[\hat{a}_{\mathbf{k},\varepsilon} \mathbf{u}_{\mathbf{k},\varepsilon}(\mathbf{r}) + \hat{a}_{\mathbf{k},\varepsilon}^\dagger \mathbf{u}_{\mathbf{k},\varepsilon}^*(\mathbf{r}) \right]. \quad (2.67)$$

If the geometry and boundary conditions of the quantization volume are different, as in the case of some cavities where the fields travel among highly conducting walls, we will need to solve for the eigensolutions of the mode functions, called eigenmodes. For typical cavity QED systems, we assume the fields will always propagate with the eigenmodes of the cavity. From the perspective

of the Fourier series, eigenmodes can be as simple as plane waves as we have seen for the periodic box, or can be a superposition of standing waves (a set of Fourier terms) in the cavity ⁴. In the latter case, however, the form of Eq. (2.67) remains the same, except that the summation over \mathbf{k} now means summing over the eigenmodes, and the field operators $\hat{a}_{\mathbf{k},\varepsilon}$ and $\hat{a}_{\mathbf{k},\varepsilon}^\dagger$ will correspond to the specific modes.

In the next section, we use Eq. (2.67) to derive the Jaynes-Cummings model.

2.2 Jaynes-Cummings model

In this section, we make some approximations and assumptions to simplify the form of the Hamiltonian derived in Eq. (2.60). Specifically, we derive the famous *Jaynes-Cummings Hamiltonian* [64, 77, 103, 147] that describes the coupling between a two-level atom and a single cavity mode. As the simplest fully quantum model for the atom-field interaction, the Jaynes-Cummings model serves as the foundation of our treatment of cavity QED systems for the quantum systems studied in this thesis.

2.2.1 Long-wavelength approximation

As mentioned earlier, the field of quantum optics studies interactions between photons and atoms (or molecules), which are composed of electrons and nuclei. Typically, the length scale of bounded nuclei-electron systems is on the order of Bohr radii ($\simeq 10^{-10}$ m), which is much smaller than the field wavelength λ in the optical ($\lambda \gtrsim 10^{-7}$ m) or microwave domain ($\lambda \gtrsim 10^{-3}$ m). Therefore, it is reasonable to ignore the variations of the field over the spatial extension of an atom. In other words, the *long-wavelength approximation* assumes that the electrons and the nucleus of the same atom observe the same field. From another point of view, long wavelengths also correspond to an upper bound on \mathbf{k} , which restricts our theory to low-energy fields. For this reason we also refer to long-wavelength modes as non-relativistic modes.

⁴For cylindrical or spherical geometries, it is more convenient to use cylindrical or spherical harmonics in place of Fourier series.

For simplicity, from now on we will study the interaction between a single neutral atom ⁵ and quantized fields in a cavity. This means that in Eq. (2.60) the summation over particles \sum_j now sums over the electrons and the nucleus of a single atom, and the term \hat{V}_{coul} describes the atomic internal Coulomb potential. The field $\hat{\mathbf{A}}(\hat{\mathbf{r}}_j)$ that interacts with the atom is found in Eq. (2.67), where $\sum_{\mathbf{k},\varepsilon}$ now sums over cavity eigenmodes. The long-wavelength approximation means that we can expand the spatial dependence $e^{i\mathbf{k}\cdot\mathbf{r}}$ in the mode function $\mathbf{u}_{\mathbf{k},\varepsilon}(\mathbf{r})$ as

$$e^{i\mathbf{k}\cdot\mathbf{r}} = e^{i\mathbf{k}\cdot\mathbf{R}} e^{i\mathbf{k}\cdot(\mathbf{r}-\mathbf{R})} \approx e^{i\mathbf{k}\cdot\mathbf{R}} [1 + i\mathbf{k}\cdot(\mathbf{r}-\mathbf{R}) + \dots], \quad (2.68)$$

where \mathbf{R} represents the position of the atom ⁶. To zeroth order, we then have $e^{i\mathbf{k}\cdot\mathbf{r}} \rightarrow e^{i\mathbf{k}\cdot\mathbf{R}}$ and $\hat{\mathbf{A}}(\mathbf{r}) = \hat{\mathbf{A}}(\mathbf{R})$. As we will see later, this approximation leads to atomic dipole transitions. For this reason, the long-wavelength approximation is often called the electric dipole approximation. Keeping higher order terms of $e^{i\mathbf{k}\cdot\mathbf{r}}$ will correspond to multipole transitions that can have higher order effects.

2.2.2 The $\hat{\mathbf{p}} \cdot \hat{\mathbf{A}}$ interaction and dipole representation

Before applying the long-wavelength approximation to our system, it is useful to first simplify the terms involving $\hat{\mathbf{A}}(\mathbf{r})$. Expanding the first term of the Hamiltonian in Eq. (2.60) yields

$$\hat{H} = \sum_j \frac{\hat{\mathbf{p}}_j^2}{2m_j} + \hat{V}_{\text{coul}} + \hat{H}_I + \hat{H}_A + \hat{H}_R, \quad (2.69)$$

where

$$\hat{H}_I = - \sum_j \frac{q_j}{2m_j} \left[\hat{\mathbf{p}}_j \cdot \hat{\mathbf{A}}(\hat{\mathbf{r}}_j) + \hat{\mathbf{A}}(\hat{\mathbf{r}}_j) \cdot \hat{\mathbf{p}}_j \right], \quad (2.70)$$

$$\hat{H}_A = \sum_j \frac{q_j^2}{2m_j} \hat{\mathbf{A}}^2(\hat{\mathbf{r}}_j), \quad (2.71)$$

$$\hat{H}_R = \sum_{\mathbf{k}} \hbar\omega_{\mathbf{k}} \left(\hat{a}_{\mathbf{k},\varepsilon}^\dagger \hat{a}_{\mathbf{k},\varepsilon} + \frac{1}{2} \right), \quad (2.72)$$

⁵See Complement A_{IV} of Ref. [27] for a discussion on charged systems like ions.

⁶See next subsection for a clear physical meaning of \mathbf{R} .

are identified as above, representing the atom-field interaction term, the $\hat{\mathbf{A}}^2$ term, and the free radiation term of the Hamiltonian, respectively. We now examine these terms in greater detail.

In an arbitrary gauge, the operators $\hat{\mathbf{p}}_j$ and $\hat{\mathbf{A}}(\hat{\mathbf{r}}_j)$ in the \hat{H}_I term do not generally commute. However, they do commute in the specific choice of the Coulomb gauge $\hat{\nabla}_j \cdot \hat{\mathbf{A}}(\hat{\mathbf{r}}_j) = 0$, which is what we choose. To see this, we use the chain rule in the position basis and get

$$\hat{\mathbf{p}} \cdot \hat{\mathbf{A}} = \left(-i\hbar\hat{\nabla}\right) \cdot \hat{\mathbf{A}} = \left(-i\hbar\hat{\nabla} \cdot \hat{\mathbf{A}}\right) + \hat{\mathbf{A}} \cdot \left(-i\hbar\hat{\nabla}\right) = \hat{\mathbf{A}} \cdot \hat{\mathbf{p}}. \quad (2.73)$$

Therefore, the \hat{H}_I term becomes

$$\hat{H}_I = - \sum_j \frac{q_j}{m_j} \hat{\mathbf{p}}_j \cdot \hat{\mathbf{A}}(\hat{\mathbf{r}}_j) \quad (2.74)$$

The \hat{H}_A term is usually small and can be ignored. The relative orders of magnitude can be approximated as the following. Comparing \hat{H}_A and \hat{H}_I , we have

$$\frac{q_j^2 \hat{\mathbf{A}}^2}{q_j \hat{\mathbf{p}}_j \cdot \hat{\mathbf{A}}} \approx \frac{q_j |\hat{\mathbf{A}}|}{|\hat{\mathbf{p}}_j|} \quad (2.75)$$

which is small for low-energy fields such as visible light and microwaves. We can also compare \hat{H}_A and \hat{H}_R , yielding

$$\frac{\sum_j q_j^2 \hat{A}_\varepsilon(\mathbf{k})^2 / (2m_j)}{\hbar\omega_{\mathbf{k}} \left[\hat{a}_{\mathbf{k},\varepsilon}^\dagger \hat{a}_{\mathbf{k},\varepsilon} + \frac{1}{2} \right]} = \frac{\sum_j \frac{q_j^2}{2m_j} \frac{\hbar}{2\omega_{\mathbf{k}}\varepsilon_0 V} \left(\hat{a}_\varepsilon^\dagger + \hat{a}_\varepsilon \right)^2}{\hbar\omega_{\mathbf{k}} \left[\hat{a}_\varepsilon^\dagger \hat{a}_\varepsilon + \frac{1}{2} \right]} \lesssim \frac{\frac{(N+1)e^2}{2m_e} \frac{\hbar}{2\omega_{\mathbf{k}}\varepsilon_0 V}}{\hbar\omega_{\mathbf{k}}} \propto \frac{(N+1)a_0^3}{V} \left(\frac{\text{Ry}}{\hbar\omega_{\mathbf{k}}} \right)^2 \quad (2.76)$$

where m_e is the electron mass, N is the total number of particles in the atom, $a_0 = \frac{4\pi\hbar^2\varepsilon_0}{m_e e^2}$ is the Bohr radius, and $\text{Ry} = \frac{m_e e^4}{8\varepsilon_0^2 \hbar^2} \approx 13.6 \text{ eV}$ is the Rydberg unit of energy [71]. Thus for fields with low radiation intensity, the \hat{H}_A term can be safely ignored if the dimension of the quantization Volume is much larger than the Bohr radius, which is true if we treat the quantization volume as the cavity volume for example.

We mention here that we have derived the Hamiltonian by quantizing a classical theory. Therefore the terms that have no classical counterparts, such as spin-field interactions, will not show up in Eq. (2.60). For this reason, Eq. (2.60) is called a minimal-coupling Hamiltonian. One may as well start directly from the Dirac equation or Pauli equation and get an extra term in the

Hamiltonian that describes the interaction between the spin operators $\hat{\mathbf{S}}_j$ and the fields, which has the form

$$\hat{H}_S = - \sum_j \mathcal{G}_j \frac{q_j}{2m_j} \hat{\mathbf{S}}_j \cdot \hat{\mathbf{B}}, \quad (2.77)$$

where \mathcal{G}_j is the g -factor of particle j . Comparing \hat{H}_S with \hat{H}_I , i.e.,

$$\frac{\mathcal{G}_j q_j \hat{\mathbf{S}}_j \cdot \hat{\mathbf{B}}(\mathbf{k})}{q_j \hat{\mathbf{p}}_j \cdot \hat{\mathbf{A}}(\mathbf{k})} \approx \frac{\hbar |\hat{\mathbf{k}}|}{|\hat{\mathbf{p}}_j|}, \quad (2.78)$$

we see that \hat{H}_S can be ignored given low radiation intensities, similar to the argument to ignore \hat{H}_A . This is in general a very good approximation for the systems that we study. For fields of higher energy, one needs a complete quantum field theory.

With the discussions above, we now ignore the small terms \hat{H}_A and \hat{H}_S and make the zeroth order long-wavelength approximation $\hat{\mathbf{A}}(\mathbf{r}) = \hat{\mathbf{A}}(\mathbf{R})$ in \hat{H}_I in Eq. (2.74), yielding

$$\hat{H} = \sum_j \frac{\hat{\mathbf{p}}_j^2}{2m_j} + \hat{V}_{\text{coul}} - \sum_j \frac{q_j}{m_j} \hat{\mathbf{p}}_j \cdot \hat{\mathbf{A}}(\hat{\mathbf{R}}) + \sum_{\mathbf{k}} \sum_{\varepsilon} \hbar \omega_{\mathbf{k}} \left[\hat{a}_{\mathbf{k},\varepsilon}^\dagger \hat{a}_{\mathbf{k},\varepsilon} + \frac{1}{2} \right]. \quad (2.79)$$

Notice that we have not given the position operator $\hat{\mathbf{R}}$ a clear physical meaning, nor have we restricted the motion of the atom. It would be ideal if we could identify $\hat{\mathbf{R}}$ as the center of mass of the atom, and separate the atomic energy into an external kinetic part \hat{H}_{ext} and an internal part \hat{H}_{int} . It turns out that this separation is possible for an atom. Let $\hat{\mathbf{R}} = \frac{\sum_j m_j \hat{\mathbf{r}}_j}{M}$ and $\hat{\mathbf{P}} = \sum_j \hat{\mathbf{p}}_j$ be the position and momentum of the center of mass, with $M = \sum_j m_j$ the total atomic mass. We can then rewrite Eq. (2.79) as

$$\begin{aligned} \hat{H} &= \frac{\hat{\mathbf{P}}^2}{2M} + \sum_j \frac{\hat{\mathcal{P}}_j^2}{2\mu_j} + \hat{V}_{\text{coul}} - \sum_j \frac{e}{\mu_j} \hat{\mathcal{P}}_j \cdot \hat{\mathbf{A}}(\hat{\mathbf{R}}) + \sum_{\mathbf{k}} \hbar \omega_{\mathbf{k}} \left[\hat{a}_{\mathbf{k},\varepsilon}^\dagger \hat{a}_{\mathbf{k},\varepsilon} + \frac{1}{2} \right] \\ &= \hat{H}_{\text{ext}} + \hat{H}_{\text{int}} + \hat{H}_I + \hat{H}_R, \end{aligned} \quad (2.80)$$

where μ_j and $\hat{\mathcal{P}}_j$ are the reduced mass and momentum of the j th ‘‘relative’’ particle needed to separate the motion of the center of mass, and e is the elementary charge. In Eq.(2.80) we have introduced

$$\hat{H}_{\text{ext}} = \frac{\hat{\mathbf{P}}^2}{2M} \quad (2.81)$$

as the kinetic energy of the atom, and

$$\hat{H}_{\text{int}} = \sum_j \frac{\hat{\mathcal{P}}_j^2}{2\mu_j} + \hat{V}_{\text{coul}} \quad (2.82)$$

as the internal energy of the atom. Here the Coulomb potential \hat{V}_{coul} , from Eq. (2.30), is a function that only depends on the absolute values of the relative positions of the electrons and the nucleus. Therefore \hat{V}_{coul} can also be expressed as a function of the positions $|\hat{\mathcal{R}}_j|$ of the relative particles. Since $\left[\left(\hat{\mathcal{P}}_j \right)_\alpha, \left(\hat{\mathcal{P}}_k \right)_\beta \right] = i\hbar \delta_{jk} \delta_{\alpha\beta}$, for $\alpha, \beta \in \{x, y, z\}$, the term \hat{H}_{int} can be thought of as the Hamiltonian of an isolated system composed of particles with mass μ_j in potential \hat{V}_{coul} . In these coordinates, the interaction Hamiltonian \hat{H}_I can be rewritten as

$$\hat{H}_I = - \sum_j \frac{e}{\mu_j} \hat{\mathcal{P}}_j \cdot \hat{\mathbf{A}}(\hat{\mathbf{R}}). \quad (2.83)$$

We refer the readers to Appx. B for a detailed derivation of Eq. (2.80) and the corresponding analysis.

Equation (2.80) is obviously non-relativistic. To good approximation, we have separated the Hamiltonian into four different parts: the atomic external (kinetic) energy, the atomic internal energy, the atomic-field coupling energy, and the field free energy. If the atom is forced to be at rest, for example trapped in the Lamb-Dicke regime [163], then $\hat{\mathbf{P}} \equiv 0$, and the interaction will only change the internal degrees of freedom of the atom. If the atom is free to move, then the motion of the atom is coupled to the atom-field interactions, which means that optomechanical forces should be considered. However, in the case that the atom's kinetic energy is far larger than the recoil energy of the field photons, we can assume that the atom's kinetic energy is held constant. We will see in Chap. 4 that these three situations correspond to different superradiant setups, and the last one is exactly the approximation we make for the superradiant beam laser system.

The Hamiltonian \hat{H}_{int} is often well known and extensively studied. Therefore, we can use its

eigenbasis and rewrite Eq. (2.80) as

$$\begin{aligned}
\hat{H} &= \hat{H}_{\text{int}} - \sum_j \frac{e}{\mu_j} \hat{\mathcal{P}}_j \cdot \hat{\mathbf{A}}(\hat{\mathbf{R}}) + \hat{H}_{\text{ext}} + \hat{H}_{\text{R}} \\
&= \hat{H}_{\text{int}} - \sum_j \frac{ie}{\hbar} [\hat{H}_{\text{int}}, \hat{\mathcal{R}}_j] \cdot \hat{\mathbf{A}}(\hat{\mathbf{R}}) + \hat{H}_{\text{ext}} + \hat{H}_{\text{R}} \\
&= \sum_{n,n'} |n\rangle\langle n'| \left[E_n \delta_{nn'} - \frac{i(E_n - E_{n'})}{\hbar} \langle n | \left(\sum_j e^{\hat{\mathcal{R}}_j} \right) |n'\rangle \cdot \hat{\mathbf{A}}(\hat{\mathbf{R}}) \right] + \hat{H}_{\text{ext}} + \hat{H}_{\text{R}} \\
&= \sum_{n,n'} |n\rangle\langle n'| \left[E_n \delta_{nn'} - \frac{i(E_n - E_{n'})}{\hbar} \mathbf{d}_{nn'} \cdot \hat{\mathbf{A}}(\hat{\mathbf{R}}) \right] + \hat{H}_{\text{ext}} + \hat{H}_{\text{R}}, \tag{2.84}
\end{aligned}$$

where we have used

$$\hat{\mathcal{P}}_j = \frac{i\mu_j}{\hbar} [\hat{H}_{\text{int}}, \hat{\mathcal{R}}_j] \tag{2.85}$$

and the eigenbasis $|n\rangle$ of \hat{H}_{int} such that $\hat{H}_{\text{int}} |n\rangle = E_n |n\rangle$ with E_n the eigenstates of \hat{H}_{int} . We have also introduced the dipole matrix element

$$\mathbf{d}_{nn'} = \langle n | \left(\sum_j e^{\hat{\mathcal{R}}_j} \right) |n'\rangle. \tag{2.86}$$

Notice that because $[\hat{H}_{\text{int}}, \hat{\mathcal{P}}] = 0$ where $\hat{\mathcal{P}}$ is the parity operator, $|n\rangle$ is also an eigenstate of $\hat{\mathcal{P}}$. Thus the diagonal dipole matrix elements \mathbf{d}_{nn} are zero. The fact that the $\mathbf{d} \cdot \hat{\mathbf{A}}$ term vanishes when $n = n'$ also directly follows from Eq. (2.84) since $E_n - E_{n'} = 0$ when $n = n'$.

2.2.3 Two-level, single-mode, and rotating-wave approximation

In Eq. (2.84) we have written \hat{H}_{int} in terms of its eigenbasis. For further simplification, we make the *two-level approximation*, which assumes that the Hilbert space \hat{H}_{int} lives in is two-dimensional, or equivalently, only two eigenstates of \hat{H}_{int} are considered during the interaction process with the fields. This simple model turns out to contain rich physics. Experimentally, the two-level approximation is valid when the atom decays or gets repumped rapidly from other levels back to the two energy levels we consider, or when the transitions to other levels are highly suppressed.

Within the two-level approximation, we can label the lower level as the ground state $|g\rangle$, and the higher level as the excited state $|e\rangle$. We define the energy difference between these two levels as $\hbar\omega_a$, where ω_a is called the atomic transition frequency, or the rest-frame atomic transition frequency, since we have separated the center-of-mass motion from \hat{H}_{int} . In matrix representation, these states have the form

$$|e\rangle = \begin{pmatrix} 1 \\ 0 \end{pmatrix}, \quad |g\rangle = \begin{pmatrix} 0 \\ 1 \end{pmatrix}. \quad (2.87)$$

Clearly,

$$|e\rangle = \hat{\sigma}^+ |g\rangle, \quad |g\rangle = \hat{\sigma}^- |e\rangle, \quad (2.88)$$

where

$$\hat{\sigma}^+ = |e\rangle\langle g| = \begin{pmatrix} 0 & 1 \\ 0 & 0 \end{pmatrix}, \quad \hat{\sigma}^- = |g\rangle\langle e| = \begin{pmatrix} 0 & 0 \\ 1 & 0 \end{pmatrix}. \quad (2.89)$$

We choose the energy reference point such that $E_g = -\frac{\hbar\omega_a}{2}$ and $E_e = \frac{\hbar\omega_a}{2}$, which allows us to represent \hat{H}_{int} as

$$\hat{H}_{\text{int}} = \frac{\hbar\omega_a}{2} \begin{pmatrix} 1 & 0 \\ 0 & -1 \end{pmatrix} = \frac{\hbar\omega_a}{2} \hat{\sigma}^z, \quad (2.90)$$

where

$$\hat{\sigma}^z = |e\rangle\langle e| - |g\rangle\langle g| = \begin{pmatrix} 1 & 0 \\ 0 & -1 \end{pmatrix}. \quad (2.91)$$

We also give the other Pauli matrices

$$\hat{\sigma}^x = \hat{\sigma}^+ + \hat{\sigma}^- = \begin{pmatrix} 0 & 1 \\ 1 & 0 \end{pmatrix}, \quad \hat{\sigma}^y = i(\hat{\sigma}^- - \hat{\sigma}^+) = \begin{pmatrix} 0 & -i \\ i & 0 \end{pmatrix} \quad (2.92)$$

here for future use. One can refer to Appx. C for useful properties of the Pauli matrices.

For most cavity QED problems, the simplest interaction is between two-level atoms and a *single cavity mode*. From Eq. (2.67) we obtain the expression of \mathbf{A} for a single cavity mode and

polarization

$$\hat{\mathbf{A}}(\hat{\mathbf{R}}) = \sqrt{\frac{\hbar}{2\omega_c\epsilon_0}} \left[\hat{\mathbf{a}}\mathbf{u}(\hat{\mathbf{R}}) + \hat{\mathbf{a}}^\dagger\mathbf{u}^*(\hat{\mathbf{R}}) \right], \quad (2.93)$$

where ω_c is the frequency of the single-mode field (“c” stands for “cavity” since we will be studying cavity QED systems). The radiation part of the Hamiltonian is thus

$$\hat{H}_R = \hbar\omega_c\hat{\mathbf{a}}^\dagger\hat{\mathbf{a}}, \quad (2.94)$$

where we remove the constant $\frac{1}{2}\hbar\omega_c$ term from the Hamiltonian.

With the two-level approximation and the single cavity mode chosen above, Eq. (2.84) becomes

$$\begin{aligned} \hat{H} &= \frac{\hbar\omega_a}{2}\hat{\sigma}^z - \sqrt{\frac{\hbar}{2\omega_c\epsilon_0}}i\omega_a(\hat{\sigma}^+\mathbf{d}_{eg} - \hat{\sigma}^-\mathbf{d}_{ge}) \cdot \left[\hat{\mathbf{a}}\mathbf{u}(\hat{\mathbf{R}}) + \hat{\mathbf{a}}^\dagger\mathbf{u}^*(\hat{\mathbf{R}}) \right] + \hat{H}_{\text{ext}} + \hat{H}_R, \\ &= \frac{\hbar\omega_a}{2}\hat{\sigma}^z + \frac{\hbar}{2} \left[g(\hat{\mathbf{R}})\hat{\sigma}^+\hat{\mathbf{a}} + g^*(\hat{\mathbf{R}})\hat{\sigma}^-\hat{\mathbf{a}}^\dagger \right] + \frac{\hbar}{2} \left[g'(\hat{\mathbf{R}})\hat{\sigma}^+\hat{\mathbf{a}}^\dagger + g'^*(\hat{\mathbf{R}})\hat{\sigma}^-\hat{\mathbf{a}} \right] + \hat{H}_{\text{ext}} + \hat{H}_R, \end{aligned} \quad (2.95)$$

where we have defined for any position \mathbf{r}

$$g(\mathbf{r}) = -i\omega_a\sqrt{\frac{2}{\hbar\omega_c\epsilon_0}}\mathbf{d}_{eg} \cdot \mathbf{u}(\mathbf{r}), \quad (2.96)$$

$$g'(\mathbf{r}) = -i\omega_a\sqrt{\frac{2}{\hbar\omega_c\epsilon_0}}\mathbf{d}_{eg} \cdot \mathbf{u}^*(\mathbf{r}). \quad (2.97)$$

It is often convenient to separate the spatial mode function from $g(\mathbf{r})$ such that

$$g(\mathbf{r}) = g\eta(\mathbf{r}), \quad (2.98)$$

where g is a constant and the spatial mode $\eta(\mathbf{r})$ is normalized such that $|\eta|_{\text{max}} = 1$. For example, in the periodic box case, for the mode function Eq. (2.66) we have

$$g = -i\omega_a\sqrt{\frac{2}{\hbar\omega_c\epsilon_0V}}\mathbf{d}_{eg} \cdot \boldsymbol{\varepsilon}, \quad (2.99)$$

which is called the single-photon vacuum Rabi frequency. Here V is the quantization volume, and $\boldsymbol{\varepsilon}$ is the unit polarization vector of the mode function $\mathbf{u}(\mathbf{r})$. Since at any given \mathbf{r} , we can choose the phase of the dipole matrix element such that $g(\mathbf{r})$ is real, we will take $g(\mathbf{r})$ to be real from now on.

One may notice that the form of g in Eq. (2.99) that is derived in Coulomb gauge is different from the usual form of the vacuum Rabi frequency derive in the electric dipole gauge (which corresponds to a $\hat{\mathbf{d}} \cdot \hat{\mathbf{E}}$ interaction), where

$$|g| = \sqrt{\frac{2\omega_c}{\hbar\varepsilon_0 V}} |\mathbf{d}_{eg} \cdot \boldsymbol{\varepsilon}|, \quad (2.100)$$

which is different from Eq. (2.99) by $\frac{\omega_c}{\omega_a}$. The reason is quite subtle and we refer the readers to Refs. [141, 147, 158] for detailed discussions. The general idea is that measurable physical quantities should always be gauge-invariant, as well as the energy conservation law. The difference is obviously reconciled in the resonant situation $\omega_a = \omega_c$. When $\omega_a \neq \omega_c$, the dipole matrix elements represent intermediate transitions in a larger multi-photon process. The physical results of the whole process is always gauge-invariant. After all, the theory we have derived is a low-energy non-relativistic approximation of the QED theory.

In Eq. (2.95), we can also ignore the non-resonant terms proportional to $\hat{\sigma}^+ \hat{a}^\dagger$ and $\hat{\sigma}^- \hat{a}$. This is called the *rotating-wave approximation* or *secular approximation* [52]. To see this, we switch to the interaction picture ⁷ defined by

$$\hat{U} = \exp \left[-\frac{i}{\hbar} \left(\hat{H}_{\text{int}} + \hat{H}_{\text{R}} \right) t \right] \quad (2.101)$$

where \hat{H}_{int} and \hat{H}_{R} are given in Eq. (2.90) and (2.94). In this picture, using the Baker-Campbell-Hausdorff formula [131] we see that the time dependence of non-resonant terms is

$$\hat{\sigma}^+ \hat{a}^\dagger \sim e^{i(\omega_a + \omega_c)t}, \quad \hat{\sigma}^- \hat{a} \sim e^{-i(\omega_a + \omega_c)t}, \quad (2.102)$$

while the time dependence of resonant terms is

$$\hat{\sigma}^+ \hat{a} \sim e^{i(\omega_a - \omega_c)t}, \quad \hat{\sigma}^- \hat{a}^\dagger \sim e^{-i(\omega_a - \omega_c)t}. \quad (2.103)$$

Since we have already made the two-level approximation, we have assumed that the transition to other levels than the chosen excited and ground states are highly suppressed, which implies $|\omega_a - \omega_c| \ll \omega_a + \omega_c$ or $|\Delta| \ll \omega_a + \omega_c$, where $\Delta = \omega_c - \omega_a$ is the cavity detuning. For this reason,

⁷See Appx. D for further discussions on interaction pictures.

the two-level and rotating-wave approximations should always be considered simultaneously. In the optical domain, the high frequency $\omega_a + \omega_c$ usually corresponds to femtosecond timescales that can be coarsened-grained with our assumption. In our later treatment of the superradiant laser where the detuning Δ can vary, we still assume $\Delta \ll \omega_c$ so that the rotating-wave approximation is valid.

In the end, with all the approximations made, we derive the Jaynes-Cummings model for a moving two-level atom interacting with a single cavity mode

$$\hat{H} = \frac{\hat{\mathbf{P}}^2}{2M} + \frac{\hbar\omega_a}{2}\hat{\sigma}^z + \hbar\omega_c\hat{a}^\dagger\hat{a} + \frac{\hbar g}{2}\eta(\hat{\mathbf{R}})\left(\hat{\sigma}^+\hat{a} + \hat{\sigma}^-\hat{a}^\dagger\right). \quad (2.104)$$

Chapter 3

Open Quantum Systems

So far we have been considering purely coherent processes, meaning that in the Schrödinger picture (SP) the time evolution of the system density operator $\hat{\rho}$ follows the von Neumann equation

$$\frac{d\hat{\rho}}{dt} = \frac{1}{i\hbar} [\hat{H}, \hat{\rho}], \quad (3.1)$$

or in the Heisenberg picture (HP) the time evolution of the observable \hat{O} (and other operators except for the density operator) follows the Heisenberg equation ¹

$$\frac{d\hat{O}}{dt} = -\frac{1}{i\hbar} [\hat{H}, \hat{O}]. \quad (3.2)$$

Systems that follow such coherent time evolutions are called closed systems. However, sometimes we are more interested in sub-systems (with few degrees of freedom) that are embedded in a larger environment (with many degrees of freedom). Under such circumstances, although the combined system of the sub-systems and the environment (or the reservoir, the heat bath, etc.) is still closed, the dynamics of the sub-systems themselves after tracing out the environment is not coherent. We call these sub-systems *open quantum systems*. As we will see, the incoherence implies extra terms in Eq. (3.1) leading to the *master equation*, and in Eq. (3.2) leading to the *Heisenberg-Langevin equations*. For clarity, from now on we will always use the term “system” to refer to the sub-system that we are interested in.

In this chapter, we first derive the master equation for the most general physical setup. Specifically, we follow two different approaches: one from a classic quantum optics point of view [28,

¹Here we assume that \hat{O} is not explicitly dependent on time.

43, 42, 103, 147, 158, 19, 96] and the other from a more modern quantum information point of view [120, 96]. For the same interaction Hamiltonian, we also derive the Heisenberg-Langevin equations, which can also be strictly formulated as the quantum stochastic differential equations [42, 43]. We show the equivalence between the master equation description and the Heisenberg-Langevin description given a heat bath composed of harmonic oscillators. In the end, we give a prescription for the forms of the master equation and the Heisenberg-Langevin equations for general cavity QED systems under the effect of various noise sources.

3.1 Master equation

3.1.1 Quantum optics approach

Consider a physical process that is described by the Hamiltonian

$$\hat{H} = \hat{H}_S + \hat{H}_E + \hat{V}, \quad (3.3)$$

where \hat{H}_S , \hat{H}_E , and \hat{V} are the Hamiltonians of the system, the environment, and the interaction between them, respectively. In the SP, the total density matrix of the system and the environment $\hat{\rho}$ satisfies the von Neumann equation (3.1). Our goal is to derive the time evolution of the reduced density matrix of the system $\hat{\rho}_S = \text{Tr}_E[\hat{\rho}]$.

For convenience, we now transform from the SP into the interaction picture (IP) defined by $\hat{H}_0 = \hat{H}_S + \hat{H}_E$ and $\hat{U} = \exp\left[-\frac{i}{\hbar}\hat{H}_0 t\right]$,² yielding

$$\frac{d\hat{\rho}^I}{dt} = \frac{1}{i\hbar}[\hat{V}^I, \hat{\rho}^I], \quad (3.4)$$

where $\hat{\rho}^I = \hat{U}^\dagger \hat{\rho} \hat{U}$ and $\hat{V}^I = \hat{U}^\dagger \hat{V} \hat{U}$ are the total density matrix and the interaction Hamiltonian in the IP, respectively.³ Using the cyclic property of the partial trace, we get

$$\hat{\rho}_S = \text{Tr}_E[\hat{\rho}] = \text{Tr}_E[\hat{U} \hat{\rho}^I \hat{U}^\dagger] = \text{Tr}_E[\hat{U}_S \hat{\rho}^I \hat{U}_S^\dagger] = \hat{U}_S \text{Tr}_E[\hat{\rho}^I] \hat{U}_S^\dagger \equiv \hat{U}_S \hat{\rho}_S^I \hat{U}_S^\dagger, \quad (3.5)$$

²We assume that \hat{H}_0 is time-independent.

³When the system itself is composed of sub-systems and their couplings, we can also define the IP without those couplings, thus leaving coherent coupling terms on the right hand side of Eq. (3.4) which are carried over through the whole calculation until being merged into \hat{H}_S in Eq. (3.20).

where $\hat{U}_S = \exp\left[-\frac{i}{\hbar}\hat{H}_S t\right]$ is the unitary defined by \hat{H}_S , and $\hat{\rho}_S^I = \text{Tr}_E[\hat{\rho}^I]$ is the reduced system density matrix in the IP. We thus turn our problem into finding the time evolution of $\hat{\rho}_S^I$.

Formally integrating Eq. (3.4) from 0 to t for two iterations, we get

$$\hat{\rho}^I(t) = \hat{\rho}^I(0) + \frac{1}{i\hbar} \int_0^t dt' \left[\hat{V}^I(t'), \hat{\rho}^I(0) \right] + \frac{1}{(i\hbar)^2} \int_0^t dt' \int_0^{t'} dt'' \left[\hat{V}^I(t'), \left[\hat{V}^I(t''), \hat{\rho}^I(t'') \right] \right], \quad (3.6)$$

which can be differentiated with respect to t to get

$$\frac{d}{dt} \hat{\rho}^I(t) = \frac{1}{i\hbar} \left[\hat{V}^I(t), \hat{\rho}^I(0) \right] + \frac{1}{(i\hbar)^2} \int_0^t dt' \left[\hat{V}^I(t), \left[\hat{V}^I(t'), \hat{\rho}^I(t') \right] \right]. \quad (3.7)$$

Tracing over the environment yields

$$\frac{d}{dt} \hat{\rho}_S^I(t) = \frac{1}{i\hbar} \text{Tr}_E \left[\hat{V}^I(t), \hat{\rho}^I(0) \right] + \frac{1}{(i\hbar)^2} \int_0^t dt' \text{Tr}_E \left[\hat{V}^I(t), \left[\hat{V}^I(t'), \hat{\rho}^I(t') \right] \right]. \quad (3.8)$$

To simplify the right hand side, we make the following approximations:

- (1) Decoupled initial conditions.

We assume that the system and the environment are decoupled at time $t = 0$, which means

$$\hat{\rho}^I(0) = \hat{\rho}(0) = \hat{\rho}_S(0) \otimes \hat{\rho}_E(0). \quad (3.9)$$

- (2) Weak-coupling approximation (Born approximation).

We assume that the environment is so large that its density matrix (and statistical properties) is unchanged by interacting with the system, i.e.,

$$\hat{\rho}_E(t) \approx \hat{\rho}_E(0) \equiv \hat{\rho}_E, \quad (3.10)$$

which implies the factorization of $\hat{\rho}^I(t)$ such that ⁴

$$\hat{\rho}^I(t) \approx \hat{\rho}_S^I(t) \otimes \hat{\rho}_E. \quad (3.11)$$

⁴This is a strong approximation. A weaker version for interaction terms of form $\hat{V}^I = \sum \hat{X}_S \hat{Y}_E$ would be the requirement $\text{Tr}_E \left[\hat{Y}_E(t), \left[\hat{Y}_E(t'), \hat{\rho}^I(t') \right] \right] \approx \hat{\rho}_S^I(t') \otimes \text{Tr}_E \left[\hat{Y}_E(t), \left[\hat{Y}_E(t'), \hat{\rho}_E \right] \right]$. Physically this means that the bath correlations are not changed by the interaction.

With the two approximations above, we have from Eq. (3.8)

$$\begin{aligned} \frac{d}{dt}\hat{\rho}_S^I(t) &\approx \frac{1}{i\hbar}\text{Tr}_E\left[\hat{V}^I(t), \hat{\rho}_S(0) \otimes \hat{\rho}_E\right] + \frac{1}{(i\hbar)^2} \int_0^t dt' \text{Tr}_E\left[\hat{V}^I(t), \left[\hat{V}^I(t'), \hat{\rho}_S^I(t') \otimes \hat{\rho}_E\right]\right] \\ &\approx \frac{1}{(i\hbar)^2} \int_0^t dt' \text{Tr}_E\left[\hat{V}^I(t), \left[\hat{V}^I(t'), \hat{\rho}_S^I(t') \otimes \hat{\rho}_E\right]\right], \end{aligned} \quad (3.12)$$

where we have assumed $\text{Tr}_E\left[\hat{V}^I\hat{\rho}_E\right] = 0$. The last approximation implies that \hat{V}^I has no diagonal terms in the eigenbasis representation of \hat{H}_E , which is either true, or can be satisfied by redefining \hat{H}_S and \hat{H}_E to include the diagonal terms [42, 96].

(3) Markov approximation.

In order to simplify the right hand side, we make the ‘‘Markov approximation’’, which assumes that the correlation time of the bath is much shorter than the time scale of the evolution of $\hat{\rho}_S^I(t)$, or equivalently, that the environment has short memory. If that is the case, then the trace over the environment will lead to Dirac delta functions in time, resulting in the approximation $\hat{\rho}_S^I(t') \approx \hat{\rho}_S^I(t)$ inside the correlations of the environment operators on the right hand side. The name ‘‘Markov approximation’’ comes from its classical analogy, since it yields a first-order differential equation from which it is sufficient to determine $\hat{\rho}_S^I(t + dt)$ given $\hat{\rho}_S^I(t)$. As C. Gardiner and P. Zoller comment [42],

‘‘... The Markov property is a highly desirable property from a mathematical point of view, because a whole structure of measurement theory can be built around it in a compact and self-contained way. The elegance of this structure leads to the formulation in the abstract of the concept of the quantum Markov process as a branch of mathematics. Nevertheless, it is important to remember that it is an assumption, based on the existence of short correlation times in the heat bath, and the use of perturbation theory.’’

(C. Gardiner & P. Zoller — *Quantum Noise*, 3rd edition)

With the Markov approximation, we end up with

$$\begin{aligned} \frac{d}{dt}\hat{\rho}_S^I &= -\frac{1}{\hbar^2} \int_0^t dt' \text{Tr}_E\left[\hat{V}^I(t), \left[\hat{V}^I(t'), \hat{\rho}_S^I(t) \otimes \hat{\rho}_E\right]\right], \\ &= -\frac{1}{\hbar^2} \int_0^\infty ds \text{Tr}_E\left[\hat{V}^I(t), \left[\hat{V}^I(t-s), \hat{\rho}_S^I(t) \otimes \hat{\rho}_E\right]\right], \end{aligned} \quad (3.13)$$

where we have set the lower integral limit to $-\infty$ since t is much larger than the correlation timescale, and changed the variable $t' \rightarrow t - s$.

Equation (3.13) is called the Redfield master equation for open quantum systems [122]. It is as far as we can get without an explicit form of the interaction Hamiltonian. To simplify this form of the master equation and to relate it to the Heisenberg-Langevin equations, let us consider a general form of the interaction Hamiltonian \hat{V} by assuming it to be a sum of direct products of system and environment operators, i.e.,

$$\hat{V} = \hbar \sum_j \Omega_j \left(\hat{\mathcal{O}}_S \right)_j \otimes \hat{E}_j, \quad (3.14)$$

where Ω_j is the coupling strength of dimension frequency, and $\left(\hat{\mathcal{O}}_S \right)_j$ and \hat{E}_j are some dimensionless system and environment operators that take part in the coupling.

Equation (3.14) is general in terms of the system and environment operators $\left(\hat{\mathcal{O}}_S \right)_j$ and \hat{E}_j . In fact, we can go even further by expanding $\left(\hat{\mathcal{O}}_S \right)_j$ in the basis composed of the eigenoperators of \hat{H}_S . Consider the superoperator $\mathcal{H}_S \left[\hat{\mathcal{O}}_S \right] \equiv \left[\hat{H}_S, \hat{\mathcal{O}}_S \right]$ that maps any system operator $\hat{\mathcal{O}}_S$ to the commutator between \hat{H}_S and $\hat{\mathcal{O}}_S$. Since the eigenvectors ⁵ of \mathcal{H}_S form a complete basis, we can express $\hat{\mathcal{O}}_S$ as

$$\hat{\mathcal{O}}_S = \sum_m c_m \hat{S}_m + d_m \hat{S}_m^\dagger, \quad (3.15)$$

where c_m and d_m are some coefficients, and the eigenoperators \hat{S}_m by definition fulfill

$$\mathcal{H}_S \left[\hat{S}_m \right] = \left[\hat{H}_S, \hat{S}_m \right] = -\hbar\omega_m \hat{S}_m, \quad (3.16)$$

$$\mathcal{H}_S \left[\hat{S}_m^\dagger \right] = \left[\hat{H}_S, \hat{S}_m^\dagger \right] = \hbar\omega_m \hat{S}_m^\dagger. \quad (3.17)$$

Therefore, in Eq. (3.14), we can expand $\left(\hat{\mathcal{O}}_S \right)_j$ in terms of $\left(\hat{S}_m \right)_j$ and $\left(\hat{S}_m^\dagger \right)_j$. After combining the summations over j and m to a single summation over k , and absorbing c_m and d_m into Ω_k , we

⁵The eigenvectors of the superoperator \mathcal{H}_S and the eigenoperators of \hat{H}_S both refer to the operators \hat{S}_m and \hat{S}_m^\dagger introduced in Eqs. (3.16)–(3.17). See Refs. [42, 96].

obtain

$$\hat{V} = \hbar \sum_k \left(\Omega_k \hat{S}_k \otimes \hat{E}_k^\dagger + \Omega_k^* \hat{S}_k^\dagger \otimes \hat{E}_k \right), \quad (3.18)$$

where we have used the fact that \hat{V} is Hermitian. Notice that here the index k sums over all the possible couplings j and all the eigenfrequencies ω_m for each j .

We now give several examples to help understand this construction. Suppose the system is a two-level atom. Then by Eq. (2.90), $\hat{H}_S = \frac{1}{2} \hbar \omega_a \hat{\sigma}^z$. For $\hat{O}_S = \hat{\sigma}^\pm$, we see that $\hat{\sigma}^\pm$ are already both eigenvectors of \mathcal{H}_S since $[\hat{H}_S, \hat{\sigma}^\pm] = \pm \hbar \omega_a \hat{\sigma}^\pm$. Therefore Eq. (3.18) follows. If the system is a single cavity mode, then by Eq. (2.94), $\hat{H}_S = \hbar \omega_c \left(\hat{a}^\dagger \hat{a} + \frac{1}{2} \right)$. For $\hat{O}_S = \hat{a}$ or \hat{a}^\dagger , these operators also satisfy $[\hat{H}_S, \hat{a}] = -\hbar \omega_c \hat{a}$ and $[\hat{H}_S, \hat{a}^\dagger] = \hbar \omega_c \hat{a}^\dagger$. The generalization to more complex systems with multiple eigenfrequencies is straightforward.

With the interaction Hamiltonian given in Eq. (3.18), in the IP, we then have

$$\begin{aligned} \hat{V}^I(t) &= \hbar \sum_k \Omega_k \left(e^{\frac{i}{\hbar} \hat{H}_S t} \hat{S}_k e^{-\frac{i}{\hbar} \hat{H}_S t} \right) \otimes \hat{E}_k^{I,\dagger}(t) + \text{h.c.} \\ &= \hbar \sum_k \Omega_k e^{-i\omega_k t} \hat{S}_k \otimes \hat{E}_k^{I,\dagger}(t) + \Omega_k^* e^{i\omega_k t} \hat{S}_k^\dagger \otimes \hat{E}_k^I(t), \end{aligned} \quad (3.19)$$

where we have used the Baker-Campbell-Hausdorff formula. Equation (3.19) provides a very general yet explicit form of the interaction Hamiltonian. By expanding the commutators in the Redfield master equation (3.13) and substituting in Eq. (3.19), we obtain multiple terms that depend on the system operators and time correlations of the environment operators. Due to the long algebra, we refer the readers to Appx. E for a detailed calculation of these terms. As a result, we obtain the Lindblad master equation in the SP, i.e.,

$$\frac{d}{dt} \hat{\rho}_S = \frac{1}{i\hbar} \left[\hat{H}_S + \sum_k \hbar \left(\epsilon_k \hat{S}_k \hat{S}_k^\dagger + \delta_k \hat{S}_k^\dagger \hat{S}_k \right), \hat{\rho}_S \right] + \sum_k \Gamma_k \mathcal{L} \left[\hat{S}_k \right] \hat{\rho}_S + \sum_k G_k \mathcal{L} \left[\hat{S}_k^\dagger \right] \hat{\rho}_S, \quad (3.20)$$

where

$$G_k = |\Omega_k|^2 \int_{-\infty}^{\infty} ds e^{-i\omega_k s} \left\langle \hat{E}_k^{I,\dagger}(s) \hat{E}_k \right\rangle, \quad (3.21)$$

$$\Gamma_k = |\Omega_k|^2 \int_{-\infty}^{\infty} ds e^{-i\omega_k s} \left\langle \hat{E}_k \hat{E}_k^{I,\dagger}(s) \right\rangle, \quad (3.22)$$

are the power spectra of the coupling for the normal and anti-normal orderings of the environment operators. The terms proportional to ϵ_k and δ_k correspond to small shifts in system energy levels that are called the Stark and Lamb shifts and are usually neglected.⁶ We have defined the Lindbladian superoperator as

$$\mathcal{L}[\hat{S}]\hat{\rho} = \frac{1}{2}\left(2\hat{S}\hat{\rho}\hat{S}^\dagger - \hat{S}^\dagger\hat{S}\hat{\rho} - \hat{\rho}\hat{S}^\dagger\hat{S}\right) \quad (3.23)$$

for the system operator \hat{S} and density matrix $\hat{\rho}$.

It is easy to tell that, by writing down the correlations of the environment operators as in Eqs. (3.21)–(3.22), we have assumed a stationary heat bath, which means that the correlations $\langle \hat{E}_k^{\text{I}\dagger}(t+s)\hat{E}_k^{\text{I}}(t) \rangle$ are not functions of t . Moreover, if we consider a heat bath at vacuum and identify operators \hat{E} and \hat{E}^\dagger as the bosonic annihilation and creation operators, which is a good approximation for many cavity QED experiments located in vacuum, then $G_k = 0$, and the only extra terms left are the Γ_k terms that describe the dissipation of the open quantum system caused by vacuum fluctuations. With these assumptions, we have the final form of the Lindblad master equation

$$\frac{d}{dt}\hat{\rho}_S(t) = \frac{1}{i\hbar}[\hat{H}_S, \hat{\rho}_S(t)] + \sum_k \Gamma_k \mathcal{L}[\hat{S}_k]\hat{\rho}_S(t), \quad (3.24)$$

The operator \hat{S}_k is called the quantum jump operator since it describes an incoherent “jump” of the quantum state caused by coupling to the environment. The summation over k can be understood as the summation over k different decoherent sources each generated by the quantum jump \hat{S}_k . Here, the independence of these decoherent sources is a result of the weak coupling approximation, which suggests that since the environment is not affected by the coupling to the system, we can treat the total effect of all the decoherence terms as a superposition of them.

3.1.2 Quantum information approach

In the previous section we have derived the master equation (3.24) from a quantum optics point of view. We mentioned that a measurement theory can be constructed from the Markov

⁶See Appx. E for further discussions on the coefficients ϵ_k and δ_k .

approximation. In this section, we follow that path and derive the master equation following J. Preskill's notes [120]. Due to limited space, we will not start from the basic definitions in quantum information theory such as quantum channels and Kraus operators. One is recommended to read Refs. [120, 42, 112, 96] for deeper understanding.

As we have discussed above, it is not obvious that there should be a first-order differential equation that describes the decoherence in an open quantum system. Such descriptions are only possible with the Markov approximation, where the system density matrix $\hat{\rho}_S(t + dt)$ is completely determined by $\hat{\rho}_S(t)$. Therefore, in terms of quantum information theory, our question naturally becomes how to find the most general way to map density matrices to density matrices. Consider the following relation between $\hat{\rho}_S(t + dt)$ and $\hat{\rho}_S(t)$

$$\hat{\rho}_S(t + dt) = \mathcal{E}_{dt}[\hat{\rho}_S(t)] = [\hat{\mathbb{1}} + \mathcal{L}dt]\hat{\rho}_S(t), \quad (3.25)$$

where $\hat{\mathbb{1}}$ is the identity matrix, \mathcal{E}_{dt} is a quantum channel, or a trace-preserving completely positive map, and \mathcal{L} is the Liouvillian operator that gives

$$\frac{d}{dt}\hat{\rho}_S = \mathcal{L}[\hat{\rho}_S]. \quad (3.26)$$

Our goal is to find the Liouvillian.

Expanding \mathcal{E}_{dt} into its operator-sum representation, we obtain

$$\mathcal{E}_{dt}[\hat{\rho}_S(t)] = \sum_k \hat{M}_k \hat{\rho}_S(t) \hat{M}_k^\dagger \quad (3.27)$$

for $k \in \{0, 1, 2, \dots\}$, where \hat{M}_k is the k th Kraus operator.

For closed systems, Eq. (3.27) is just

$$\hat{\rho}_S(t + dt) = \mathcal{E}_{dt}[\hat{\rho}_S(t)] = \hat{\rho}_S(t) + \frac{1}{i\hbar} [\hat{H}_S, \hat{\rho}_S(t)] dt, \quad (3.28)$$

which is equivalent to the von Neumann equation (3.1). In other words, up to first order in dt ,

$$\begin{cases} \hat{M}_0 = \hat{\mathbb{1}} + \frac{1}{i\hbar} \hat{H}_S dt \\ \hat{M}_k = 0, \quad k > 0 \end{cases}. \quad (3.29)$$

For open systems, without loss of generality, we can write

$$\left\{ \begin{array}{l} \hat{M}_0 = \hat{\mathbb{1}} + \left(\frac{1}{i\hbar} \hat{H}_S + \hat{K} \right) dt \\ \hat{M}_k = \sqrt{\Gamma_k} \hat{S}_k \sqrt{dt}, \quad k > 0 \end{array} \right. , \quad (3.30)$$

where \hat{K} is Hermitian, Γ_k is the decay rate of the k th decoherent source, and \hat{S}_k is the k th jump operator. Both \hat{S}_k and \hat{K} are zeroth order in dt . Up to the first order in dt , we obtain from the completeness of Kraus operators

$$\hat{\mathbb{1}} = \sum_{k=0} \hat{M}_k^\dagger \hat{M}_k = \hat{\mathbb{1}} + dt \left(2\hat{K} + \sum_{k>0} \Gamma_k \hat{S}_k^\dagger \hat{S}_k \right), \quad (3.31)$$

and thus

$$\hat{K} = -\frac{1}{2} \sum_{k>0} \Gamma_k \hat{S}_k^\dagger \hat{S}_k. \quad (3.32)$$

Substituting back into Eq. (3.26), we have

$$\frac{d}{dt} \hat{\rho}_S = \mathcal{L}[\hat{\rho}_S] = \frac{1}{i\hbar} [\hat{H}_S, \hat{\rho}_S] + \sum_k \Gamma_k \mathcal{L}[\hat{S}_k] \hat{\rho}_S \quad (3.33)$$

Therefore, the Liouvillian of a Lindblad master equation is the generator of a quantum channel that maps the system density operator back to itself. Notice that although Eq. (3.33) has the same form as Eq. (3.24), it actually has a broader interpretation since we have not specified the physical meanings of Γ_k and \hat{S}_k . In other words, Eq. (3.33) contains the G_k terms in Eq. (3.20) if we let $\Gamma_k \rightarrow G_k$ and $\hat{S}_k \rightarrow \hat{S}_k^\dagger$. Thus although the derivation of the master equation from measurement theory reveals the mathematical origin of the structure of the Lindbladian superoperator, we still need a physical derivation to interpret it.

3.2 Heisenberg-Langevin equations

The quantum master equation describes the time evolution of the system density operator $\hat{\rho}_S$ in the SP. Equivalently, one would expect a set of differential equations for the time evolution of observables and other operators in the HP. Indeed, there exist such equations, which are called

the Heisenberg-Langevin equations, or if formulated strictly, the quantum stochastic differential equations [42]. In this section, we formally derive the Heisenberg-Langevin equations in a general physical setup where we model the environment as harmonic oscillators.

In the HP, consider the same Hamiltonian as in Eq. (3.3),

$$\hat{H} = \hat{H}_S + \hat{H}_E + \hat{V}.$$

We still do not specify the form of the system Hamiltonian \hat{H}_S . However, we assume that the heat bath is now composed of harmonic oscillators, i.e.,

$$\hat{H}_E = \hbar \sum_k \int_{-\infty}^{\infty} d\omega \omega \hat{E}_k^\dagger(\omega) \hat{E}_k(\omega), \quad (3.34)$$

where $\hat{E}_k(\omega)$ and $\hat{E}_k^\dagger(\omega)$ are bosonic annihilation and creation operators that satisfy

$$\left[\hat{E}_k(\omega), \hat{E}_{k'}^\dagger(\omega') \right] = \delta_{kk'} \delta(\omega - \omega'). \quad (3.35)$$

With this heat bath model, we write the interaction Hamiltonian \hat{V} as

$$\hat{V} = \hbar \sum_k \int_{-\infty}^{\infty} d\omega \left[\Omega_k(\omega) \hat{S}_k \hat{E}_k^\dagger(\omega) + \Omega_k^*(\omega) \hat{S}_k^\dagger \hat{E}_k(\omega) \right], \quad (3.36)$$

where \hat{S}_k and \hat{S}_k^\dagger are eigenoperators of \hat{H}_S .⁷ Compared to Eq. (3.18), we have removed the \otimes sign since in the HP all the operators (system or environment) act on the combined Hilbert space of the system and environment. The dimensions of the coupling strength $\Omega_k(\omega)$ and \hat{E}_k have changed since we assume a continuous spectra for the environment. The commutation relation (3.35) implies that different eigenoperators of \hat{H}_S interact with different environment operators independently, which is a result of the weak coupling approximation.

There are several comments to be made on the form of \hat{H}_E and \hat{V} . In general, although it seems that we have a stronger condition here than in the derivation of the master equation (since we have a specific form of the heat bath), we will see later that this condition is not as strong as it appears because often the Lindblad master equation implicitly assumes a heat bath

⁷See Sec. 3.1 for a clear definition.

composed of harmonic oscillators, or at least with the statistical properties of harmonic oscillators. We will also see that if we specify the environment as harmonic oscillators in vacuum (thermal or white), which is approximately true for the systems we consider later, the master equation and Heisenberg-Langevin equations can be derived from each other.

Essentially, an interaction Hamiltonian \hat{V} as Eq. (3.36) implies the rotating-wave approximation, since we have ignored the $\hat{S}_k \hat{E}_k(\omega)$ and $\hat{S}_k^\dagger \hat{E}_k^\dagger(\omega)$ terms. As argued in Sec. 2.2.3, this approximation is valid as long as $|\omega_k - \omega| \ll \omega_k + \omega$, where ω_k is the frequency of the system operator \hat{S}_k as defined in Eq. (3.16). Since we have assumed a continuous spectra for the heat bath, the rotating-wave approximation also means that only the resonant terms with $\omega_k \approx \omega$ contribute, therefore allowing us to extend the lower limit of the integral in Eq. (3.36) and Eq. (3.34) from 0 to $-\infty$. This extension is crucial to define the quantum white noise and formulate a Markovian description of the time evolution of system operators.

We now derive the Heisenberg-Langevin equations using Eq. (3.36). In the HP, the time evolution of any system operator \hat{O}_S other than the density operator follows the Heisenberg equation (3.2). Our goal is to express this Heisenberg equation of \hat{O}_S using system operators and some quantum stochastic operators that carry the statistical properties of the environment. Using Eqs. (3.34) and (3.36) in the Heisenberg equation (3.2), we obtain

$$\begin{aligned} \frac{d}{dt} \hat{O}_S &= -\frac{1}{i\hbar} [\hat{H}_S, \hat{O}_S] - \frac{1}{i\hbar} [\hat{V}, \hat{O}_S] \\ &= -\frac{1}{i\hbar} [\hat{H}_S, \hat{O}_S] + i \sum_k \int_{-\infty}^{\infty} d\omega \left\{ \Omega_k(\omega) \hat{E}_k^\dagger(\omega) [\hat{S}_k, \hat{O}_S] + \Omega_k^*(\omega) [\hat{S}_k^\dagger, \hat{O}_S] \hat{E}_k(\omega) \right\} \end{aligned} \quad (3.37)$$

and

$$\frac{d}{dt} \hat{E}_k(\omega) = -\frac{1}{i\hbar} [\hat{H}_E, \hat{E}_k(\omega)] - \frac{1}{i\hbar} [\hat{V}, \hat{E}_k(\omega)] = -i\omega \hat{E}_k(\omega) - i\Omega_k(\omega) \hat{S}_k. \quad (3.38)$$

Solving Eq. (3.38) exactly, we have

$$\hat{E}_k(\omega, t) = \hat{E}_k(\omega, 0) e^{-i\omega t} - i\Omega_k(\omega) \int_0^t dt' e^{-i\omega(t-t')} \hat{S}_k(t'), \quad (3.39)$$

where $\hat{E}_k(\omega, 0)$ is the initial value of $\hat{E}_k(\omega, t)$ at $t = 0$. Substituting Eq. (3.39) into Eq. (3.37), we

obtain

$$\frac{d}{dt}\hat{\mathcal{O}}_S = -\frac{1}{i\hbar}[\hat{H}_S, \hat{\mathcal{O}}_S] + \sum_k \left\{ [\hat{S}_k^\dagger, \hat{\mathcal{O}}_S] \hat{X}_k - \hat{X}_k^\dagger [\hat{S}_k, \hat{\mathcal{O}}_S] \right\} + \sum_k \left\{ [\hat{S}_k^\dagger, \hat{\mathcal{O}}_S] \hat{Y}_k - \hat{Y}_k^\dagger [\hat{S}_k, \hat{\mathcal{O}}_S] \right\}, \quad (3.40)$$

where we have defined

$$\hat{X}_k = \int_0^t dt' \hat{S}_k(t') \int_{-\infty}^{\infty} d\omega |\Omega_k(\omega)|^2 e^{-i\omega(t-t')}, \quad (3.41)$$

$$\hat{Y}_k = i \int_{-\infty}^{\infty} d\omega e^{-i\omega t} \Omega_k^*(\omega) \hat{E}_k(\omega, 0), \quad (3.42)$$

which satisfy

$$\hat{X}_k + \hat{Y}_k = i \int_{-\infty}^{\infty} d\omega \Omega_k^*(\omega) \hat{E}_k(\omega, t). \quad (3.43)$$

Notice that although $\hat{E}_k(\omega, t)$ commutes with any system operator, operators \hat{X}_k and \hat{Y}_k in general do not commute with system operators.

So far, we have implicitly made the rotating-wave approximation when choosing the forms of \hat{H}_E and \hat{V} . After that our derivations have been exact. We now make the Markov approximation, which states that the heat bath has a short memory so that the system operator $\hat{\mathcal{O}}_S(t+dt)$ is only determined by $\hat{\mathcal{O}}_S(t)$. This is done by keeping the stationary values of the integral in Eq. (3.41) and assuming

$$|\Omega_k(\omega)|^2 = \frac{\Gamma_k}{2\pi}, \quad (3.44)$$

which yields

$$\begin{aligned} \hat{X}_k &\approx \int_0^t dt' \hat{S}_k(t') \frac{\Gamma_k}{2\pi} \int_{-\infty}^{\infty} d\omega e^{-i\omega(t-t')}, \\ &= \int_0^t dt' \hat{S}_k(t') \Gamma_k \delta(t-t'), \\ &= \frac{\Gamma_k}{2} \hat{S}_k(t), \end{aligned} \quad (3.45)$$

where the $\frac{1}{2}$ factor in the last line comes from the integral of $\delta(t-t')$ over $t' \in [0, t]$. Indeed, the approximation made in Eq. (3.44) eliminates all the $\hat{S}_k(t')$ terms for $t' < t$, and is sometimes

also called the first Markov approximation [42]. Physically Eq. (3.44) means that the coupling rate $|\Omega_k(\omega)|^2$ is independent of the frequency ω , which is a somewhat strong but still a good approximation over the frequency domain of interest near the resonant frequency of the system ω_k . This is a consequence of the rotating-wave approximation again. One can also compare Eq. (3.44) with Eq. (3.22) to see that Eq. (3.44) is indeed a stronger version of Markov approximation since it assumes a delta-correlated heat bath in time that corresponds to a short memory.

We now consider the operator \hat{Y}_k ⁸, which can be modeled by quantum white noise. Strictly speaking, to do so one needs to define the quantum Wiener process and then construct a theory on Ito and Stratonovich quantum stochastic differential equations [42, 43]. However, for simplicity, here we directly examine the commutation and statistical properties of \hat{Y}_k and make approximations as needed.

From Eqs. (3.35), (3.42), and (3.44), we obtain the commutation relation as

$$\begin{aligned}
[\hat{Y}_k(t), \hat{Y}_{k'}^\dagger(t')] &= \int_{-\infty}^{\infty} \int_{-\infty}^{\infty} d\omega d\omega' e^{-i\omega t} e^{i\omega' t'} \Omega_k^*(\omega) \Omega_{k'}(\omega') [\hat{E}_k(\omega, 0), \hat{E}_{k'}^\dagger(\omega', 0)] \\
&= \int_{-\infty}^{\infty} \int_{-\infty}^{\infty} d\omega d\omega' e^{-i\omega t} e^{i\omega' t'} \Omega_k^*(\omega) \Omega_{k'}(\omega') \delta_{kk'} \delta(\omega - \omega') \\
&= \delta_{kk'} \frac{\Gamma_k}{2\pi} \int_{-\infty}^{\infty} d\omega e^{-i\omega(t-t')} \\
&= \Gamma_k \delta_{kk'} \delta(t - t').
\end{aligned} \tag{3.46}$$

We next calculate the statistical moments of operators \hat{Y}_k and \hat{Y}_k^\dagger . To do this, we need to first specify the initial conditions of the heat bath. Here we make the same decoupled initial condition approximation as in Eq. (3.9) by assuming that the system and environment are completely decoupled at $t = 0$. In the calculations below, we only take the ensemble average with respect to the environment. Due to the decoupled density matrices, this is actually a stronger condition than averaging over the system plus the environment. The first moment is

$$\langle \hat{Y}_k(t) \rangle_{\text{E}} = i \int_{-\infty}^{\infty} d\omega e^{-i\omega t} \Omega_k^*(\omega) \text{Tr}_{\text{E}} [\hat{\rho}_{\text{E}}(0) \hat{E}_k(\omega, 0)] = 0, \tag{3.47}$$

⁸Operator \hat{Y}_k is usually referred to as the input field in the literature [42].

where we assume the ensemble average of the random initial value $\hat{E}_k(\omega, 0)$ to be zero. The second order correlations between \hat{Y}_k and \hat{Y}_k^\dagger are

$$\begin{aligned} \langle \hat{Y}_{k'}^\dagger(t') \hat{Y}_k(t) \rangle_{\text{E}} &= \int_{-\infty}^{\infty} \int_{-\infty}^{\infty} d\omega' d\omega e^{i\omega't'} e^{-i\omega t} \Omega_{k'}(\omega') \Omega_k^*(\omega) \langle \hat{E}_{k'}^\dagger(\omega', 0) \hat{E}_k(\omega, 0) \rangle_{\text{E}} \\ &= \int_{-\infty}^{\infty} \int_{-\infty}^{\infty} d\omega' d\omega e^{i\omega't'} e^{-i\omega t} \Omega_{k'}(\omega') \Omega_k^*(\omega) \bar{N}_k(\omega) \delta_{kk'} \delta(\omega - \omega') \\ &= \delta_{kk'} \frac{\Gamma_k}{2\pi} \int_{-\infty}^{\infty} d\omega e^{-i\omega(t-t')} \bar{N}_k(\omega) \\ &= \Gamma_k \bar{N}_k \delta_{kk'} \delta(t - t'), \end{aligned} \quad (3.48)$$

$$\langle \hat{Y}_k(t) \hat{Y}_{k'}^\dagger(t') \rangle_{\text{E}} = \Gamma_k (\bar{N}_k + 1) \delta_{kk'} \delta(t - t'), \quad (3.49)$$

where we have assumed a constant density of reservoir quanta $\bar{N}_k(\omega) \equiv \bar{N}_k$ that corresponds to an ideal quantum white noise source. If $\bar{N}_k(\omega)$ follows a thermal distribution, i.e., $\bar{N}_k(\omega) = \left[\exp\left(\frac{\hbar\omega}{k_{\text{B}} T_k}\right) - 1 \right]^{-1}$, where k_{B} is the Boltzmann constant and T_k is the temperature, Eqs. (3.48)–(3.49) will still be a good approximation although the delta-correlation is weaker. However, in order to interpret $\bar{N}_k(\omega)$ as a source of noise we do need it to have a broad bandwidth. If $\bar{N}_k(\omega)$ is a delta function, for instance, then it no longer represents a noise but a coherent drive.

Suppose we take the vacuum condition of the heat bath by letting $\bar{N}_k = 0$ (white) or $T = 0$ (thermal). Then the only noise left is due to the vacuum fluctuations. Under the vacuum condition, with Eqs. (3.47)–(3.49), we define the vacuum quantum white noise operator

$$\xi_k(t) = \frac{\hat{Y}_k(t)}{\sqrt{\Gamma_k}} \quad (3.50)$$

such that ⁹

$$\langle \hat{\xi}_k(t) \rangle_{\text{E}} = 0, \quad (3.51)$$

$$\langle \hat{\xi}_{k'}^\dagger(t') \hat{\xi}_k(t) \rangle_{\text{E}} = 0, \quad (3.52)$$

$$\langle \hat{\xi}_k(t) \hat{\xi}_{k'}^\dagger(t') \rangle_{\text{E}} = \delta_{kk'} \delta(t - t'), \quad (3.53)$$

$$\left[\hat{\xi}_k(t), \hat{\xi}_{k'}^\dagger(t') \right] = \delta_{kk'} \delta(t - t'). \quad (3.54)$$

⁹The fact that we can define the quantum white noise with its first and second order moments means that we implicitly assume a Gaussian noise model.

Substituting Eq. (3.45) and (3.50) into Eq. (3.40), we obtain the Heisenberg-Langevin equation for any system operator \hat{O}_S

$$\frac{d}{dt}\hat{O}_S = -\frac{1}{i\hbar}[\hat{H}_S, \hat{O}_S] + \sum_k \hat{D}_k + \sum_k \hat{F}_k, \quad (3.55)$$

where \hat{D}_k is called the drift operator that has the form

$$\hat{D}_k = \frac{\Gamma_k}{2} \left([\hat{S}_k^\dagger, \hat{O}_S] \hat{S}_k + \hat{S}_k^\dagger [\hat{O}_S, \hat{S}_k] \right) = \Gamma_k \bar{\mathcal{L}}[\hat{S}_k] \hat{O}_S, \quad (3.56)$$

where we have defined the superoperator $\bar{\mathcal{L}}[\hat{S}] \hat{O}$ as

$$\bar{\mathcal{L}}[\hat{S}] \hat{O} = \frac{1}{2} \left(2\hat{S}^\dagger \hat{O} \hat{S} - \hat{S}^\dagger \hat{S} \hat{O} - \hat{O} \hat{S}^\dagger \hat{S} \right) \quad (3.57)$$

for system operators \hat{S} and \hat{O} . Notice the difference between the superoperator $\bar{\mathcal{L}}$ and \mathcal{L} defined in Eq. (3.23).

The operator \hat{F}_k is called the noise or diffusion operator, which can be written as

$$\hat{F}_k = \sqrt{\Gamma_k} \left([\hat{S}_k^\dagger, \hat{O}_S] \hat{\xi}_k + \hat{\xi}_k^\dagger [\hat{O}_S, \hat{S}_k] \right) \quad (3.58)$$

with the correlation ¹⁰

$$\langle \hat{F}_k(t) \hat{F}_{k'}(t') \rangle = \Gamma_k \langle [\hat{S}_k^\dagger, \hat{O}_S] [\hat{O}_S, \hat{S}_k] \rangle \delta_{kk'} \delta(t - t'). \quad (3.59)$$

Equation (3.59) shows that there is no correlation between different noise sources. Thus for an open quantum system that is subject to several decoherence sources, we can treat each one of them separately and then add the resulting drift and noise operators together. We can also define the noise correlation between two different system operators \hat{O}_μ and \hat{O}_ν , which yields

$$\langle \hat{F}_{\mu k}(t) \hat{F}_{\nu k'}(t') \rangle = (2M_k)_{\mu\nu} \delta_{kk'} \delta(t - t'), \quad (3.60)$$

where

$$(2M_k)_{\mu\nu} \equiv \Gamma_k \langle [\hat{S}_k^\dagger, \hat{O}_\mu] [\hat{O}_\nu, \hat{S}_k] \rangle \quad (3.61)$$

¹⁰The strict proof of this correlation is non-trivial and is not presented here.

is called the diffusion matrix between operators \hat{O}_μ and \hat{O}_ν caused by the k th noise or decoherent source, which gets its name from the classical Langevin theory.

We identify \hat{S}_k as the jump operator of the k th noise source as introduced in Eq. (3.24), and Γ_k as the corresponding decay rate. Again, both the master equation and Heisenberg-Langevin equation approaches are valid only under the decoupled initial condition, rotating-wave, weak-coupling, and Markov approximations. With these approximations, each channel of decoherence corresponds to an independent noise contribution that does not affect any of the other noisy sources.

3.3 Equivalence between master equation and Heisenberg-Langevin equations

We have argued that with the harmonic oscillator model of the heat bath, the master equation description and the Heisenberg-Langevin equation description of the same open quantum system are equivalent. In this section, we prove this claim. For simplicity, we assume the heat bath to be vacuum, which corresponds to a zero temperature for thermal modes, or zero energy quanta for white noise. Also we only consider one noise channel. Then the master equation (3.24) and the Heisenberg-Langevin equation (3.55) become ¹¹

$$\frac{d}{dt}\hat{\rho}(t) = \frac{1}{i\hbar}[\hat{H}, \hat{\rho}(t)] + \frac{\Gamma}{2} [2\hat{S}\hat{\rho}(t)\hat{S}^\dagger - \hat{S}^\dagger\hat{S}\hat{\rho}(t) - \hat{\rho}(t)\hat{S}^\dagger\hat{S}], \quad (3.62)$$

$$\begin{aligned} \frac{d}{dt}\hat{O}(t) = & -\frac{1}{i\hbar}[\hat{H}(t), \hat{O}(t)] + \frac{\Gamma}{2} [2\hat{S}^\dagger(t)\hat{O}(t)\hat{S}(t) - \hat{S}^\dagger(t)\hat{S}(t)\hat{O}(t) - \hat{O}(t)\hat{S}^\dagger(t)\hat{S}(t)] \\ & + \sqrt{\Gamma} \left\{ [\hat{S}^\dagger(t), \hat{O}(t)]\hat{\xi}(t) + \hat{\xi}^\dagger(t)[\hat{O}(t), \hat{S}(t)] \right\}, \end{aligned} \quad (3.63)$$

where we use the time dependence to label the picture, and have dropped the S notation since all the operators except for ξ and ξ^\dagger are now system operators. The generalization to multiple noise sources and non-vacuum is straightforward.

¹¹Keep in mind that the master equation is in the SP and the Heisenberg-Langevin equation is in the HP.

3.3.1 Master equation to Langevin equations

Suppose we are given the master equation (3.62). For any operator $\hat{\mathcal{O}}$, we now use the master equation to find the drift \hat{D} and diffusion \hat{F} of its corresponding Heisenberg-Langevin equation

$$\frac{d}{dt}\hat{\mathcal{O}}(t) = -\frac{1}{i\hbar}\left[\hat{H}(t), \hat{\mathcal{O}}(t)\right] + \hat{D}(t) + \hat{F}(t) \quad (3.64)$$

with $\langle \hat{F}(t) \rangle = 0$. Here we directly write out the coherent part of the Heisenberg-Langevin equation which originates from the Heisenberg equation (3.2).

The expectation value of $\hat{\mathcal{O}}$ is picture-independent, i.e.,

$$\langle \hat{\mathcal{O}} \rangle = \text{Tr}\left[\hat{\rho}(t)\hat{\mathcal{O}} \otimes \hat{\rho}_{\text{E}}\right] = \text{Tr}\left[\hat{\rho}\hat{\mathcal{O}}(t)\right] = \langle \hat{\mathcal{O}}(t) \rangle, \quad (3.65)$$

where we have traced out the environment due to the weak-coupling approximation¹². Taking the time derivative, we then have

$$\frac{d}{dt}\langle \hat{\mathcal{O}} \rangle = \text{Tr}\left[\frac{d\hat{\rho}(t)}{dt}\hat{\mathcal{O}}\right] = \text{Tr}\left[\hat{\rho}\frac{d\hat{\mathcal{O}}(t)}{dt}\right] = \left\langle \frac{d\hat{\mathcal{O}}(t)}{dt} \right\rangle. \quad (3.66)$$

We focus on the relation

$$\text{Tr}\left[\frac{d\hat{\rho}(t)}{dt}\hat{\mathcal{O}}\right] = \left\langle \frac{d\hat{\mathcal{O}}(t)}{dt} \right\rangle. \quad (3.67)$$

Using Eq. (3.62), the left hand side (LHS) of Eq. (3.67) becomes

$$\begin{aligned} \text{LHS} &= \frac{1}{i\hbar}\text{Tr}\left\{\left[\hat{H}, \hat{\rho}(t)\right]\hat{\mathcal{O}}\right\} + \frac{\Gamma}{2}\text{Tr}\left\{\left[2\hat{S}\hat{\rho}(t)\hat{S}^\dagger - \hat{S}^\dagger\hat{S}\hat{\rho}(t) - \hat{\rho}(t)\hat{S}^\dagger\hat{S}\right]\hat{\mathcal{O}}\right\} \\ &= -\frac{1}{i\hbar}\left\langle\left[\hat{H}(t), \hat{\mathcal{O}}(t)\right]\right\rangle + \frac{\Gamma}{2}\left\langle 2\hat{S}^\dagger(t)\hat{\mathcal{O}}(t)\hat{S}(t) - \hat{S}^\dagger(t)\hat{S}(t)\hat{\mathcal{O}}(t) - \hat{\mathcal{O}}(t)\hat{S}^\dagger(t)\hat{S}(t) \right\rangle, \end{aligned} \quad (3.68)$$

where we have used the cyclic property of the trace and changed pictures. This leads to the important property

$$\text{Tr}\left\{\hat{\mathcal{O}}\mathcal{L}\left[\hat{S}\right]\hat{\rho}(t)\right\} = \text{Tr}\left\{\hat{\rho}\bar{\mathcal{L}}\left[\hat{S}(t)\right]\hat{\mathcal{O}}(t)\right\}. \quad (3.69)$$

¹²Here actually we can define $\hat{\rho}(t) = \text{Tr}_{\text{E}}\left[\hat{U}^\dagger(t)\hat{\rho}_{\text{S}} \otimes \hat{\rho}_{\text{E}}\hat{U}(t)\right]$ without using any approximation, where $\hat{U}(t)$ is the unitary that transforms from the SP to the HP.

The right hand side (RHS) of Eq. (3.67) from Eq. (3.64) is

$$\text{RHS} = -\frac{1}{i\hbar} \left\langle \left[\hat{H}(t), \hat{\mathcal{O}}(t) \right] \right\rangle + \left\langle \hat{D}(t) \right\rangle. \quad (3.70)$$

Comparing the left and right hand sides, we identify

$$\left\langle \hat{D}(t) \right\rangle = \frac{\Gamma}{2} \left\langle 2\hat{S}^\dagger(t)\hat{\mathcal{O}}(t)\hat{S}(t) - \hat{S}^\dagger(t)\hat{S}(t)\hat{\mathcal{O}}(t) - \hat{\mathcal{O}}(t)\hat{S}^\dagger(t)\hat{S}(t) \right\rangle. \quad (3.71)$$

Since Eq. (3.71) is true for any operator $\hat{\mathcal{O}}$, we can remove the expectation value operator and get

$$\hat{D}(t) = \frac{\Gamma}{2} \left[2\hat{S}^\dagger(t)\hat{\mathcal{O}}(t)\hat{S}(t) - \hat{S}^\dagger(t)\hat{S}(t)\hat{\mathcal{O}}(t) - \hat{\mathcal{O}}(t)\hat{S}^\dagger(t)\hat{S}(t) \right], \quad (3.72)$$

which agrees with Eq. (3.63).

It remains to show that we can get the correct noise terms \hat{F} and \hat{F}^\dagger from the master equation (3.62), where \hat{F}^\dagger is defined from the Hermitian conjugate of Eq. (3.64). Since we implicitly assume Gaussian noise, and the first moments (expectation values) of the noise operators \hat{F} and \hat{F}^\dagger are zero, it is sufficient to derive the second order moments. Using the Einstein relation¹³

$$\left\langle \hat{F}_\mu(t)\hat{F}_\nu(t) \right\rangle = \left\langle \frac{d}{dt} \left[\hat{\mathcal{O}}_\mu(t)\hat{\mathcal{O}}_\nu(t) \right] \right\rangle + \frac{1}{i\hbar} \left\langle \left[\hat{H}(t), \hat{\mathcal{O}}_\mu(t)\hat{\mathcal{O}}_\nu(t) \right] \right\rangle - \left\langle \hat{D}_\mu(t)\hat{\mathcal{O}}_\nu(t) \right\rangle - \left\langle \hat{\mathcal{O}}_\mu(t)\hat{D}_\nu(t) \right\rangle \quad (3.73)$$

for operators $\hat{\mathcal{O}}_\mu(t), \hat{\mathcal{O}}_\nu(t) \in \left\{ \hat{\mathcal{O}}(t), \hat{\mathcal{O}}^\dagger(t) \right\}$ together with Eq.(3.67), (3.69), and (3.72), we obtain

$$\begin{aligned} \left\langle \hat{F}_\mu(t)\hat{F}_\nu(t) \right\rangle &= \left\langle \bar{\mathcal{L}}[\hat{S}(t)] \left[\hat{\mathcal{O}}_\mu(t)\hat{\mathcal{O}}_\nu(t) \right] \right\rangle - \left\langle \hat{D}_\mu(t)\hat{\mathcal{O}}_\nu(t) \right\rangle - \left\langle \hat{\mathcal{O}}_\mu(t)\hat{D}_\nu(t) \right\rangle \\ &= \text{Tr} \left[\hat{\mathcal{O}}_\mu\hat{\mathcal{O}}_\nu\mathcal{L}[\hat{S}] \hat{\rho}(t) \right] - \left\langle \hat{D}_\mu\hat{\mathcal{O}}_\nu \right\rangle - \left\langle \hat{\mathcal{O}}_\mu\hat{D}_\nu \right\rangle \\ &= \Gamma \left\langle \left[\hat{S}^\dagger, \hat{\mathcal{O}}_\mu \right] \left[\hat{\mathcal{O}}_\nu, \hat{S} \right] \right\rangle, \\ &= \Gamma \left\langle \left[\hat{S}^\dagger(t), \hat{\mathcal{O}}_\mu(t) \right] \left[\hat{\mathcal{O}}_\nu(t), \hat{S}(t) \right] \right\rangle, \end{aligned} \quad (3.74)$$

which agrees with Eq. (3.61). Therefore we have successfully derived the Heisenberg-Langevin equations from the master equation. The fact that we get the correct diffusion matrix means that the master equation treatment and the Heisenberg-Langevin treatment agree to at least the second

¹³See Appx. F for the derivation of the Einstein relation.

order moments of the quantum noise. Given the quantum white noise model which is fundamentally a Gaussian theory, it might even be sufficient to say that the master equation can give rise to the exact noise terms given in Eq. (3.58) since we only care about the second order moments, although a strict mathematical proof is needed. In fact, if we specify the heat bath as the same harmonic oscillator model in the derivation of the master equation as in the Heisenberg-Langevin case, and make the same approximations on the density of quanta (thermal, white, etc.), then the equivalence between the two descriptions will be exact.

3.3.2 Langevin equations to master equation

Suppose we are given the Langevin equation (3.63) which applies to any system operator \hat{O} . From Eq. (3.66), we focus on the relation

$$\text{Tr} \left[\frac{d\hat{\rho}(t)}{dt} \hat{O} \right] = \text{Tr} \left[\hat{\rho} \frac{d\hat{O}(t)}{dt} \right]. \quad (3.75)$$

Using the property (3.69), we then have

$$\begin{aligned} \text{Tr} \left[\frac{d\hat{\rho}(t)}{dt} \hat{O} \right] &= -\frac{1}{i\hbar} \text{Tr} \left\{ \hat{\rho} \left[\hat{H}(t), \hat{O}(t) \right] \right\} + \Gamma \text{Tr} \left\{ \hat{\rho} \bar{\mathcal{L}} \left[\hat{S}(t) \right] \hat{O}(t) \right\} \\ &= \frac{1}{i\hbar} \text{Tr} \left\{ \left[\hat{H}, \hat{\rho}(t) \right] \hat{O} \right\} + \Gamma \text{Tr} \left\{ \mathcal{L} \left[\hat{S} \right] \hat{\rho}(t) \hat{O} \right\}. \end{aligned} \quad (3.76)$$

Since Eq. (3.76) applies to any system operator \hat{O} , we can remove the $\text{Tr} [\dots \hat{O}]$ operator and derive the master equation (3.62).

It is clear that the derivation from the Heisenberg-Langevin equations to the master equation is shorter than the other way around since there are no noise terms to derive. The reason is that, as we have seen from the Einstein relations (3.73), the diffusion matrix and the drift terms governed by the superoperator $\bar{\mathcal{L}}$ (which is transformed to the Lindbladian superoperator \mathcal{L} in the master equation) are self-consistent, which can be taken as the manifestation of the quantum fluctuation-dissipation theorem. With the form of the Lindbladian superoperator \mathcal{L} , the noise terms are implicitly determined. The derivation is shorter also because we have chosen a heat bath composed of harmonic oscillators in the Heisenberg-Langevin case. Therefore it is no surprising that the Heisenberg-Langevin equations are immediately sufficient to derive the master equation.

3.4 Prescription for decoherence

In the previous sections, we have derived the quantum master equation and Heisenberg-Langevin equations from a very general perspective. In this section, we give some concrete examples of different decoherent processes that are common for cavity QED systems, including free-space spontaneous (T_1) emission and T_2 dephasing of a two-level atom, as well as cavity decay through the mirrors. The resulting terms in the corresponding master equation and Heisenberg-Langevin equations can be used as the prescription for these decoherent processes when we introduce the many body superradiant cavity QED systems.

We consider a Jaynes-Cummings system composed a single two-level atom interacting with a single cavity mode. Then the system Hamiltonian is given by Eq. (2.104). For simplicity, we suppose the atom is trapped at the antinode of the cavity mode so that its external energy is a constant and can be removed from the Hamiltonian. The resulting system Hamiltonian is

$$\hat{H}_S = \frac{\hbar\omega_a}{2}\hat{\sigma}^z + \hbar\omega_c\hat{a}^\dagger\hat{a} + \frac{\hbar g}{2}(\hat{\sigma}^+\hat{a} + \hat{a}^\dagger\hat{\sigma}^-). \quad (3.77)$$

As a reminder, in Eq. (3.77), ω_a is the atomic transition frequency, ω_c is the cavity frequency, and g is the single-photon vacuum Rabi frequency. We now discuss the effect of different decoherent sources.

3.4.1 Free-space spontaneous emission

As the name suggests, free-space spontaneous emission is an effect of the atom that couples to the free-space modes other than the cavity modes. If the free space modes are in vacuum, then due to vacuum fluctuations, the atom will spontaneously decay from the excited state $|e\rangle$ to the ground state $|g\rangle$ [162]. This process can be described using the theory of open quantum systems as we have previously developed in this chapter.

- (1) Jump operator.

The jump operator for free-space spontaneous emission is $\hat{\sigma}^-$. Notice that this is true only

if we ignore the atomic motion so that photon recoil does not cause external momentum recoil [109].

As argued in footnote 3 of Sec. 3.1.1, for a system Hamiltonian with coherent coupling terms like $(\hat{\sigma}^+ \hat{a} + \hat{a}^\dagger \hat{\sigma}^-)$ as occurs in Eq. (3.77), in the derivation of the master equation we assign as the free Hamiltonian

$$\hat{H}_0 = \frac{\hbar\omega_a}{2} \hat{\sigma}^z + \hbar\omega_c \hat{a}^\dagger \hat{a} + \hat{H}_E. \quad (3.78)$$

Then we see $\hat{\sigma}^-$ is an eigenoperator of \hat{H}_0 since

$$[\hat{H}_0, \hat{\sigma}^-] = \left[\frac{\hbar\omega_a}{2} \hat{\sigma}^z, \hat{\sigma}^- \right] = -\hbar\omega_a \hat{\sigma}^-. \quad (3.79)$$

The jump operator $\hat{\sigma}^-$ corresponds to the incoherent coupling between the atom and vacuum modes in vicinity of the eigenfrequency ω_a .

(2) Lindblad master equation.

The incoherent coupling caused by $\hat{\sigma}^-$ is described by the term $\gamma_1 \mathcal{L}[\hat{\sigma}^-] \hat{\rho}$, where γ_1 is specified as the free-space spontaneous emission rate. Historically the spontaneous emission process is also called T_1 decay, where $T_1 \propto 1/\gamma_1$.

(3) Heisenberg-Langevin equations.

For any operator $\hat{\mathcal{O}}$, the drift term is given by $\hat{D} = \gamma_1 \bar{\mathcal{L}}[\hat{\sigma}^-] \hat{\mathcal{O}}$, and the noise term is given by $\hat{F} = \sqrt{\gamma_1} \left([\hat{\sigma}^+, \hat{\mathcal{O}}] \hat{\xi} + \hat{\xi}^\dagger [\hat{\mathcal{O}}, \hat{\sigma}^-] \right)$ where $\hat{\xi}$ and $\hat{\xi}^\dagger$ are quantum white noise terms satisfying $\langle \hat{\xi}(t) \hat{\xi}^\dagger(t') \rangle = \delta(t - t')$.

3.4.2 T_2 dephasing

The T_2 dephasing process describes the damping of the diagonal terms of the atomic density matrix. Physically such dephasing is caused by the general coupling between atomic internal states and the free-space modes. For a many body system this often represents a homogeneous dephasing process.

(1) Jump operator.

The jump operator for T_2 dephasing is $\hat{\sigma}^z$. This is most easily understood from the point of view of the dephasing channel language in quantum information [120]. Notice that it is easy to see that $[\hat{H}_0, \hat{\sigma}^z] = 0$, meaning the dephasing is indistinguishable from the free evolution.

(2) Lindblad master equation.

The incoherent coupling caused by $\hat{\sigma}^z$ is described by the term $\frac{\gamma_2}{4}\mathcal{L}[\hat{\sigma}^z]\hat{\rho}$, where $\gamma_2 = \frac{2}{T_2}$ is the rescaled T_2 dephasing rate. This definition is consistent with standard literature [165].

(3) Heisenberg-Langevin equations.

For any operator \hat{O} , the drift term is given by $\hat{D} = \frac{\gamma_2}{4}\bar{\mathcal{L}}[\hat{\sigma}^z]\hat{O}$, and the noise term is given by $\hat{F} = \frac{\sqrt{\gamma_2}}{2}\left([\hat{\sigma}^z, \hat{O}]\hat{\xi} + \hat{\xi}^\dagger[\hat{O}, \hat{\sigma}^z]\right)$ where $\hat{\xi}$ and $\hat{\xi}^\dagger$ are quantum white noise terms satisfying $\langle\hat{\xi}(t)\hat{\xi}^\dagger(t')\rangle = \delta(t-t')$.

3.4.3 Cavity decay

Cavity decay is important in cavity QED systems since it generates the measurable output fields. In terms of an open quantum system such as Eq. (3.77), cavity decay describes the incoherent coupling between the cavity mode and the vacuum heat bath. Most cavity QED systems we study are “high- Q ” systems, where Q stands for the quality factor of the cavity that is defined as $Q = \omega_c/\kappa$ with κ the cavity decay rate. For current experiments on atom-photon interactions in the optical domain, the Q -factor can be as high as 10^8 , corresponding to $\kappa \simeq 1$ MHz [104, 71].

(1) Jump operator.

The jump operator for cavity decay is \hat{a} , which represents losing one photon from the cavity to the environment. It is straightforward to see that $[\hat{H}_0, \hat{a}] = -\hbar\omega_c\hat{a}$.

(2) Lindblad master equation.

The incoherent coupling caused by \hat{a} is described by the term $\kappa\mathcal{L}[\hat{a}]\hat{\rho}$.

(3) Heisenberg-Langevin equations.

For any operator \hat{O} , the drift term is given by $\hat{D} = \kappa \bar{\mathcal{L}}[\hat{a}]\hat{O}$, and the noise term is given by $\hat{F} = \kappa \left([\hat{a}^\dagger, \hat{O}]\hat{\xi} + \hat{\xi}^\dagger [\hat{O}, \hat{a}] \right)$ where $\hat{\xi}$ and $\hat{\xi}^\dagger$ are quantum white noise terms satisfying $\langle \hat{\xi}(t)\hat{\xi}^\dagger(t') \rangle = \delta(t - t')$.

3.5 Summary

Before we end our discussion of open quantum systems, we comment on the advantages of using Heisenberg-Langevin equations rather than the master equation. First, the Heisenberg point of view allows us to easily compare the dynamics of quantum variables and their classical counterparts, if any. Second, the observables are themselves operators. Therefore, it is more intuitive to directly study the dynamics of the observables and their associated statistics in the HP rather than in the SP. Last, many of the semiclassical approaches, especially the c -number Langevin equations and the mean-field theory we use in this thesis, are directly applicable to the Heisenberg-Langevin equations. In fact, due to numerical considerations, the Heisenberg-Langevin equations are actually the only choice we have when we simulate an atomic beam traveling in and out of the cavity. We will introduce these c -number methods in the next chapter.

Chapter 4

Theory of Superradiant Atomic Beam Laser

In the previous chapters we have derived the Jaynes-Cummings model of a moving two-level atom interacting with a single cavity mode. We have also shown the equivalence between the quantum master equation and Heisenberg-Langevin equations for open quantum systems and presented a prescription for various decoherent sources. In this chapter, we combine these building blocks together to investigate a very general cavity QED system, the Tavis-Cummings model, in presence of several forms of dissipation including cavity decay, atomic spontaneous emission, and T_2 dephasing. Specifically, in the so-called “bad cavity” limit, the intracavity atomic dipoles can spontaneously synchronize, resulting in a macroscopic atomic dipole that collectively emits through the cavity. We call such phenomena cavity superradiance, and such devices superradiant lasers.

4.1 From Dicke superradiance to steady-state cavity superradiance

Superradiance in the context of quantum optics was first discussed by Dicke in 1954 (see Fig. 4.1) [32]. When the length scale L of an ensemble of N excited two-level atoms in free space is smaller than the corresponding wavelength λ of the atomic transition, instead of spontaneously emitting individually, the atoms will collectively emit in a fashion that can be N times faster, N times stronger, and in a well-defined direction that depends on the geometry of the ensemble. This effect is called *Dicke superradiance*, or *collective spontaneous emission* [17, 4, 52].

The mechanism of Dicke superradiance can be understood by considering the Dicke model [32, 140, 151, 51, 30]. As an extension of Dicke’s original work, the Dicke model describes the interaction

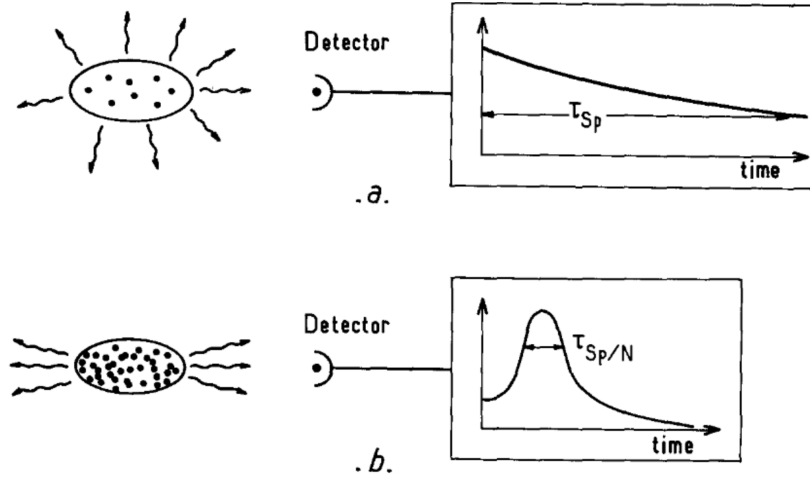


Figure 4.1: Source: Ref. [52]. Comparison between the general characteristics of ordinary fluorescence and superradiance experiments. (a) Ordinary spontaneous emission is essentially isotropic with an exponentially decaying intensity (time constant τ_{sp}). (b) Superradiance is anisotropic with an emission occurring in a short burst of duration $\sim \tau_{sp}/N$.

of N two-level systems (atoms in our case) and a single mode of the field. The atoms are assumed to be indistinguishable, which allows for the use of Dicke states [52, 45, 164, 65]. For free-space Dicke superradiance, this condition corresponds to the Dicke limit $L \ll \lambda$. In the thermodynamic limit $N \rightarrow \infty$, and in absence of dissipation, it has been shown that the system will spontaneously break the \mathbb{Z}_2 (parity) symmetry and transit into a superradiant phase when the atom-field coupling reaches a critical value (see Fig. 4.2) [57, 159, 128]. At the superradiant phase transition, the individual oscillators (atomic dipoles) constructively interfere (phase lock, synchronize, etc.), and this cooperative behavior can be seen as the formation of a macroscopic collective dipole. The spontaneous emission of this collective dipole then causes all the $\mathcal{O}(N)$ superradiant effects as considered in Dicke superradiance. Microscopically, dipole-dipole correlations are established and propagated as a result of the collective Lamb shift [81, 148, 6, 41, 52, 139] via vacuum fluctuations.

The simplest experimental realization of the Dicke model is through cavity superradiance, i.e., superradiance in cavity QED systems, where the Dicke limit $L \ll \lambda \simeq 10^{-7}$ m for optical wavelengths can be relaxed by using mode-selective high- Q cavities. With these high-performance cavities, the single-mode approximation is valid, and atoms at distances far larger than λ from each

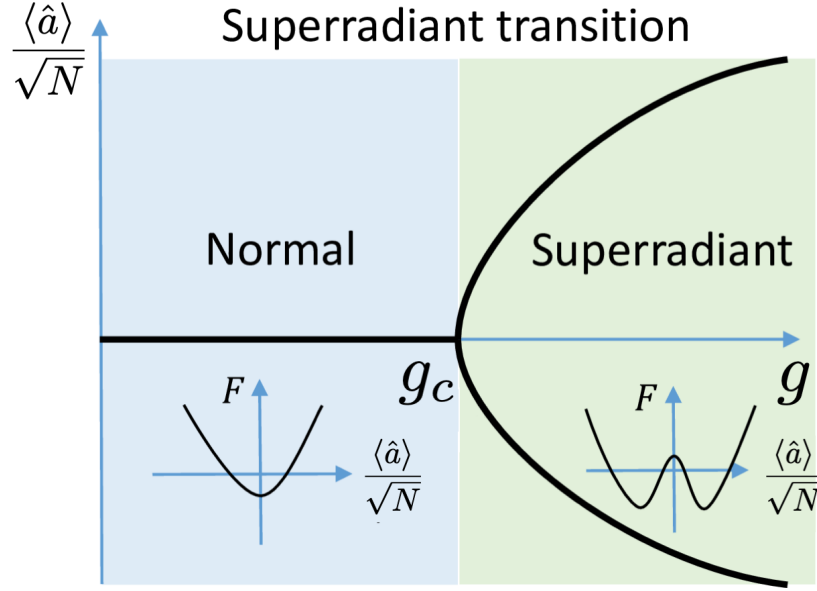


Figure 4.2: Source: Ref. [128] (notations and captions have been adapted). The superradiant phase transition for the Dicke model with a single mode. Here, g describes the atom-photon coupling. The order parameter for the phase transition is $\langle \hat{a} \rangle / \sqrt{N}$, where $\langle \hat{a} \rangle$ is the mean field amplitude and N is the atom number. When the coupling parameter g is bigger than the critical coupling g_c , the order parameter $\langle \hat{a} \rangle / \sqrt{N}$ becomes non-zero with two opposite phases which correspond to the symmetry breaking equilibria of the free energy F .

other can communicate coherently through the cavity field. In cavity setups, pulsed superradiant lasers have been built, and Dicke-type superradiant peaks have been observed [115, 116, 5, 113, 87, 136]. However, the observation of continuous superradiant emission is challenging because of the weak coupling and a no-go theorem [111] that prohibits a superradiant phase in conventional equilibrium cavity QED. Remarkably these obstacles can be overcome by introducing external pumping, which results in non-equilibrium superradiant phase transitions [33, 8]. Such transitions can also happen with other kinds of dissipation, as shown in Chaps. 5–8 of this thesis. Meanwhile, the steady-state output of cavity superradiance resulting from continuous pumping also makes continuous-wave (CW) superradiance possible.

In the remainder of the thesis, we will focus on steady-state cavity superradiance. Specifically, we discuss the design of a novel ultra-linewidth CW laser called the steady-state superradiant laser [101, 12, 92].

4.2 Steady-state superradiance laser

The original proposal for a steady-state superradiant laser [101, 100, 99] considers a system composed of N two-level atoms interacting with a single mode of a high- Q cavity. The atoms are trapped at the antinodes of the standing wave in the Lamb-Dicke regime [163], which means that we can ignore the external motion of the atoms. The coherent interaction between the atoms and the cavity is given by the *Tavis-Cummings model* [151, 152], i.e.,

$$\hat{H} = \frac{\hbar\omega_a}{2} \sum_{j=1}^N \hat{\sigma}_j^z + \hbar\omega_c \hat{a}^\dagger \hat{a} + \frac{\hbar g}{2} \sum_{j=1}^N \left(\hat{\sigma}_j^+ \hat{a} + \hat{a}^\dagger \hat{\sigma}_j^- \right), \quad (4.1)$$

which is a many body generalization of the Jaynes-Cummings model introduced in Eq. (3.77). Here, ω_a is the atomic transition frequency, ω_c is the cavity frequency, and g is the single-photon vacuum Rabi frequency. The operators $\hat{\sigma}_j^z$ and $\hat{\sigma}_j^\pm$ are the atomic pseudospin operators for atom j , while operators \hat{a} and \hat{a}^\dagger are the cavity fields.

The decoherence of the system comes from four different sources, namely the cavity decay, the free-space spontaneous emission, the T_2 dephasing, and the incoherent repumping. The corresponding decoherent terms in the master equation or the Heisenberg-Langevin equations for the first three sources can be directly written down following the prescription given in Sec. 3.4. The incoherent repumping can be understood as an effective spontaneous absorption process that incorporates pumping atoms from the ground state $|g\rangle$ to an auxiliary state that rapidly decays to the excited state $|e\rangle$. Therefore, analogous to spontaneous emission, the repumping process is well approximated by assuming a jump operator $\hat{\sigma}_j^+$ for each individual atom j . Physically, this incoherent repump serves as the energy source of the CW behavior of the superradiant laser.

We can now write down the master equation for the steady-state superradiant laser

$$\frac{d\hat{\rho}}{dt} = \frac{1}{i\hbar} [\hat{H}, \hat{\rho}] + \kappa \mathcal{L}[\hat{a}] \hat{\rho} + \sum_{j=1}^N \left(\gamma_1 \mathcal{L}[\hat{\sigma}_j^-] \hat{\rho} + \frac{\gamma_2}{4} \mathcal{L}[\hat{\sigma}_j^z] \hat{\rho} + w \mathcal{L}[\hat{\sigma}_j^+] \hat{\rho} \right), \quad (4.2)$$

where κ is the cavity decay rate or cavity linewidth, γ_1 is the free-space spontaneous rate, γ_2 is the T_2 dephasing rate, and w is the effective repumping rate. The parameter regime considered here is the superradiant or “bad cavity” regime, which assumes that $\kappa \gg \sqrt{N}g, \gamma_1, \gamma_2$, where $\sqrt{N}g$

is the collective coupling rate. In this regime, given enough intracavity atoms N , the system can go through a superradiant phase transition when the repumping rate matches the collective decay rate, while both dominating over the other decay rates, i.e., $\gamma_1, \gamma_2 \ll w \sim N\Gamma_c \ll \kappa$. Here we have introduced the cavity-assisted single-atom decay rate $\Gamma_c = \frac{g^2}{\kappa} = \mathcal{C}\gamma_1$ (for zero detuning), with \mathcal{C} the dimensionless cavity cooperativity parameter.

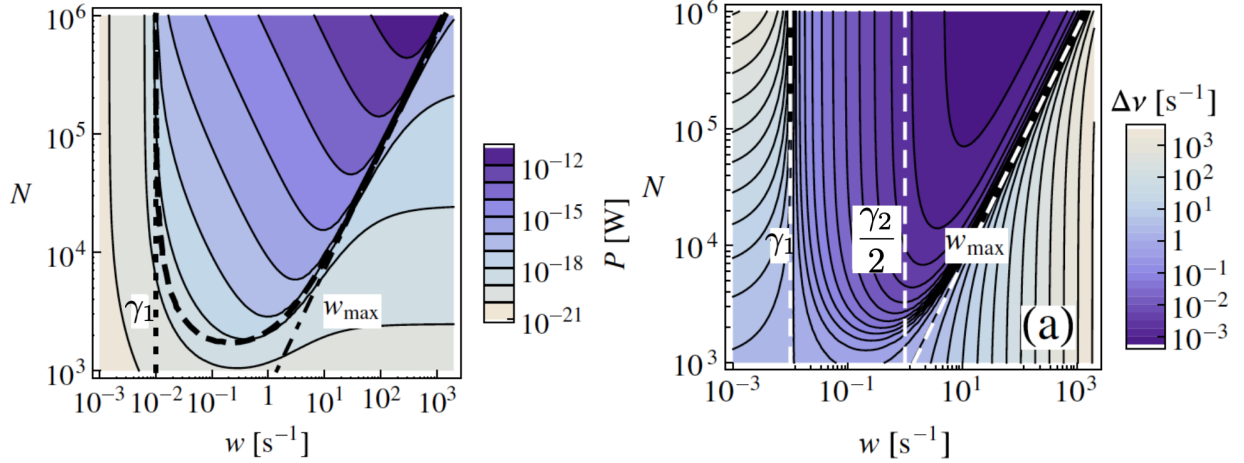


Figure 4.3: Source: Ref. [101] (notations and captions have been adapted). (Left) Power as a function of pump rate w and atom number N . The rapid buildup of power above threshold w can be seen as well as the decrease of emitted power for too strong a pump. The dashed line shows the boundary of the region of collective emission. (Right) Linewidth vs w and N . The white dashed lines indicate (from left to right) the spontaneous decay rate, the inhomogeneous relaxation rate $1/T_2$, and the maximum pump rate w_{\max} .

The above system has been studied extensively [101, 100, 100, 99, 12, 166, 165, 164, 66, 67, 65]. Due to the similarity to the superradiant beam laser system, we leave the detailed derivation of the superradiant master equation and the superradiant Heisenberg-Langevin equations to the next section, and only qualitatively describe the results in the original proposal. The motivation was to generate an ultranarrow linewidth laser with enough output power that can be directly applicable for metrological use. With an ensemble of ^{87}Sr atoms of $N \simeq 10^6$, when the repumping rate w is tuned such that the system is in the superradiant phase, the output light is calculated to simultaneously reach a power of $P \sim 10^{-6}$ W and a linewidth of $\Delta\nu \sim 1$ mHz, as shown in Fig. 4.3 [101].

4.3 Superradiant atomic beam laser

The steady-state superradiant laser has been a promising candidate for the next generation ultracoherent laser since the idea was proposed. However, because of the technical difficulties of trapping a huge number of ultracold atoms and the atom loss due to radiative heating caused by repumping, it has proved challenging to realize a truly CW superradiant laser in the optical domain following the original trapped atom model. For this reason, we were motivated to consider a different model of the steady-state superradiant laser, the superradiant beam laser model [92, 70, 69, 68].

4.3.1 Model

As the name suggests, instead of trapping atoms inside the cavity, the superradiant beam laser model considers an atomic beam transiting the cavity (see Figs. 5.1, 6.1, 7.1, and 8.1 for various schematics of the superradiant beam laser model). Instead of being repumped inside the cavity, the atoms are prepared in the excited state $|e\rangle$ before entering the cavity. Compared to the original proposal, this model has several advantages. First, the atoms do not have to be frozen in the optical trapping fields, which allows for much higher intracavity atom number N . Second, we manually separate the pumping process from the lasing process, thus fundamentally avoiding adverse effects caused by the incoherent repumping, including heating and atom loss. In some sense, the experimental challenge has shifted from trapping a large number of ultracold atoms to maintaining a high atomic beam flux as well as controlling the beam temperature and associated velocity spread, as we will see in the next few chapters.

We now theoretically analyze the superradiant beam laser model. Consider the Tavis-Cummings model similar to Eq. (4.1) but this time with atomic motion ¹.

$$\hat{H} = \sum_j \frac{\hat{\mathbf{P}}_j^2}{2m} + \frac{\hbar\omega_a}{2} \sum_j \hat{\sigma}_j^z + \hbar\omega_c \hat{a}^\dagger \hat{a} + \frac{\hbar g}{2} \sum_j \eta(\hat{\mathbf{x}}_j) \left(\hat{\sigma}_j^+ \hat{a} + \hat{a}^\dagger \hat{\sigma}_j^- \right). \quad (4.3)$$

¹Notice that compared to the Jaynes-Cumming model in Eq. (2.104), we now use the lower case $\{\hat{\mathbf{x}}_j, \hat{\mathbf{p}}_j\}$ to refer to the position and momentum of the center of mass of atom j , whereas in Sec. 2.2.2 and Appx. B this notation refers to those of the j th internal particle of a single atom.

Here, the summation \sum_j goes over all the atoms in the atomic beam. We assume all the atoms are identical with atomic mass m . The operator $\hat{\mathbf{p}}_j$ is the center-of-mass momentum of atom j inside the atomic beam as introduced in Sec. 2.2.2 and Appx. B, and $\eta(\hat{\mathbf{x}}_j)$ is the cavity mode function defined in Eq. (2.98) at the position $\hat{\mathbf{x}}_j$ of atom j . We impose $\eta(\hat{\mathbf{x}}_j) = 0$ if atom j is out of the cavity. In this sense, we can define the mean intracavity atom number N as

$$N = \Phi\tau \tag{4.4}$$

where Φ is the number of atoms passing per unit time (flux times cross section), and τ is the single atom transit time. It thus becomes obvious that by relaxing the Lamb-Dicke regime and moving the repumping process out of the cavity, we are trading off the simplicity in external motion for the simplicity in repumping. In the longitudinal direction (perpendicular to the cavity axis), atoms enter and leave the cavity at a regular rate of $1/\tau$, which can be thought of as an effective rate of pumping from some final states as atoms leave the cavity to the excited state $|e\rangle$. This implies that the parameter $1/\tau$ plays a similar role to w in the control of the superradiant phase transition. In the transverse direction (parallel to the cavity axis), as atoms move across different values of the cavity mode function $\eta(\hat{\mathbf{x}})$, it remains a question as to whether atoms can spontaneously synchronize when they see different phases of the fields from each other. Most importantly, it remains to show that there exists a suitable experimental parameter regime to build this CW superradiant laser.

Before answering the above questions, let us first fill our toolbox by deriving the Heisenberg-Langevin equations and the master equation for the cavity superradiant systems.

4.3.2 Heisenberg-Langevin equations

Using the Hamiltonian (4.3), from Eq. (3.55) and the prescription given in Sec. (3.4), we obtain the Heisenberg-Langevin equations for the the fields \hat{a} , the atomic pseudospins $\hat{\sigma}_j^z$ and $\hat{\sigma}_j^-$,

and the atomic position \hat{x}_j and momentum \hat{p}_j , i.e.,

$$\frac{d\hat{a}}{dt} = -\left(\frac{\kappa}{2} + i\omega_c\right)\hat{a} - \frac{ig}{2}\hat{J}^- - \sqrt{\kappa}\hat{\xi}_\kappa, \quad (4.5)$$

$$\frac{d\hat{\sigma}_j^-}{dt} = -i\omega_a\hat{\sigma}_j^- + \frac{ig}{2}\eta_j\hat{\sigma}_j^z\hat{a} - \frac{1}{2}(\gamma_1 + \gamma_2)\hat{\sigma}_j^- + \sqrt{\gamma_1}\hat{\sigma}_j^z\hat{\xi}_{j,\gamma_1} - \sqrt{\gamma_2}\left(\hat{\sigma}_j^-\hat{\xi}_{j,\gamma_2} - \hat{\xi}_{j,\gamma_2}^\dagger\hat{\sigma}_j^-\right), \quad (4.6)$$

$$\frac{d\hat{\sigma}_j^z}{dt} = ig\eta_j\left(\hat{a}^\dagger\hat{\sigma}_j^- - \hat{\sigma}_j^+\hat{a}\right) - \gamma_1\left(\hat{\sigma}_j^z + 1\right) - 2\sqrt{\gamma_1}\left(\hat{\sigma}_j^+\hat{\xi}_{j,\gamma_1} + \hat{\xi}_{j,\gamma_1}^\dagger\hat{\sigma}_j^-\right), \quad (4.7)$$

$$\frac{d\hat{\mathbf{x}}_j}{dt} = \frac{\hat{\mathbf{p}}_j}{m}, \quad (4.8)$$

$$\frac{d\hat{\mathbf{p}}_j}{dt} = -\frac{\hbar g}{2}\hat{\nabla}\eta_j\left(\hat{\sigma}_j^+\hat{a} + \hat{a}^\dagger\hat{\sigma}_j^-\right). \quad (4.9)$$

Here $\hat{\nabla} = \left(\frac{\partial}{\partial \hat{x}}, \frac{\partial}{\partial \hat{y}}, \frac{\partial}{\partial \hat{z}}\right)^T$ is the gradient operator. Operators $\hat{\xi}_\kappa$, $\hat{\xi}_{j,\gamma_1}$, and $\hat{\xi}_{j,\gamma_2}$ and their Hermitian conjugates are the quantum white noise operators for the corresponding noise sources. We have also used the shorthand notation $\eta_j = \eta(\hat{\mathbf{x}}_j)$, $\hat{\nabla}\eta_j = \hat{\nabla}\eta(\hat{\mathbf{x}})|_{\hat{\mathbf{x}}=\hat{\mathbf{x}}_j}$, and introduced the collective dipole operators that are given by

$$\hat{J}^\pm = \sum_j \eta_j \hat{\sigma}_j^\pm. \quad (4.10)$$

From Eq. (4.10) we immediately see the difference between the superradiant beam laser model and the trapped atom model. The indistinguishability condition of the atoms in the latter case is broken as a result of the spatial (entry position) and temporal (entry time) dependence of the atom-cavity coupling $g\eta_j$. Therefore, although we can still define the collective dipole \hat{J}^\pm , due to the coefficients η_j , the condition for which atoms will synchronize (if they can) is unstudied. Of course in the original Dicke model, the indistinguishability is also an approximation which is valid as long as the atoms are confined within a wavelength λ . Therefore, we would expect the superradiant phase transition to happen for the superradiant beam laser model if the transverse motion of the atoms are confined within a length scale $\sim \lambda$ during the transit time τ . Once the atoms are phase locked and in steady state, the collective dipole formed in the cavity will remain macroscopic although individual atoms are entering and leaving. In this way, the system can have a coherence time much longer than the single-atom transit time τ , resulting in an ultranarrow linewidth. This is the basic principle of the superradiant beam laser.

We can move into the frame rotating with the atomic frequency ω_a to simplify the form of Eqs. (4.5)–(4.9).² Mathematically this corresponds to making the replacements $\hat{a} \rightarrow \hat{a} e^{-i\omega_a t}$, $\hat{\sigma}_j^- \rightarrow \hat{\sigma}_j^- e^{-i\omega_a t}$, $\hat{\xi}_\kappa \rightarrow \hat{\xi}_\kappa e^{-i\omega_a t}$, and $\hat{\xi}_{j,\gamma_1} \rightarrow \hat{\xi}_{j,\gamma_1} e^{-i\omega_a t}$ so that the fast rotating phase factor $e^{i\omega_a t}$ is hidden from our Heisenberg-Langevin equations. In the atomic rotating frame, Eqs. (4.5)–(4.7) become

$$\frac{d\hat{a}}{dt} = -\left(\frac{\kappa}{2} + i\Delta\right)\hat{a} - \frac{ig}{2}\hat{J}^- - \sqrt{\kappa}\hat{\xi}_\kappa, \quad (4.11)$$

$$\frac{d\hat{\sigma}_j^-}{dt} = \frac{ig}{2}\eta_j\hat{\sigma}_j^z\hat{a} - \frac{1}{2}(\gamma_1 + \gamma_2)\hat{\sigma}_j^- + \sqrt{\gamma_1}\hat{\sigma}_j^z\hat{\xi}_{j,\gamma_1} - \sqrt{\gamma_2}\left(\hat{\sigma}_j^-\hat{\xi}_{j,\gamma_2} - \hat{\xi}_{j,\gamma_2}^\dagger\hat{\sigma}_j^-\right), \quad (4.12)$$

$$\frac{d\hat{\sigma}_j^z}{dt} = ig\eta_j\left(\hat{a}^\dagger\hat{\sigma}_j^- - \hat{\sigma}_j^+\hat{a}\right) - \gamma_1\left(\hat{\sigma}_j^z + 1\right) - 2\sqrt{\gamma_1}\left(\hat{\sigma}_j^+\hat{\xi}_{j,\gamma_1} + \hat{\xi}_{j,\gamma_1}^\dagger\hat{\sigma}_j^-\right), \quad (4.13)$$

where $\Delta = \omega_c - \omega_a$ is the cavity detuning from the atomic frequency. The associated diffusion matrix, according to Eq. (3.61), has the form

$$2M_{\text{total}} = \begin{matrix} & a & a^\dagger & \dots & j, - & & j, + & & j, z & & \dots \\ \begin{matrix} a \\ a^\dagger \\ \dots \\ j, - \\ j, + \\ j, z \\ \dots \end{matrix} & \left(\begin{array}{cccccccc} 0 & \kappa & & & & & & & & & \\ 0 & 0 & & & & & & & & & \\ & & \dots & & & & & & & & \\ & & & 0 & & \gamma_1 + \frac{\gamma_2}{2}\left(1 - \langle\hat{\sigma}_j^z\rangle\right) & & & 2\gamma_1\langle\hat{\sigma}_j^-\rangle & & \\ & & & \frac{\gamma_2}{2}\left(1 + \langle\hat{\sigma}_j^z\rangle\right) & & 0 & & & 0 & & \\ & & & 0 & & 2\gamma_1\langle\hat{\sigma}_j^+\rangle & & & 2\gamma_1\left(1 + \langle\hat{\sigma}_j^z\rangle\right) & & \\ & & & & & & & & & \dots & \end{array} \right), \end{matrix} \quad (4.14)$$

where $(2M_{\text{total}})_{\mu\nu}\delta(t-t') = \langle\hat{F}_\mu(t)\hat{F}_\nu(t')\rangle$ with $\mu, \nu \in \{\hat{a}, \hat{a}^\dagger, \dots, \hat{\sigma}_j^-, \hat{\sigma}_j^+, \hat{\sigma}_j^z, \dots\}$ are indices for all the operators in question. From Eq. (4.14) it is obvious that in our description so far all the noise sources are independent, in the sense that the κ noise only affects the fields, that the γ_1 and γ_2 noise terms only affect individual atoms, and that there are no cross diffusion terms (no off-diagonal blocks) between different atoms. This will not be the case after we adiabatically eliminate the cavity fields in the next section.

²See Appx. D for a discussion on rotating frames in the HP for open quantum systems.

For completeness, we follow Chap. 3 and write down the equivalent master equation that corresponds to Eq. (4.5)–(4.9), i.e.,

$$\frac{d\hat{\rho}}{dt} = \frac{1}{i\hbar} [\hat{H}, \hat{\rho}] + \kappa \mathcal{L}[\hat{a}] \hat{\rho} + \sum_j \left(\gamma_1 \mathcal{L}[\hat{\sigma}_j^-] \hat{\rho} + \frac{\gamma_2}{4} \mathcal{L}[\hat{\sigma}_j^z] \hat{\rho} \right), \quad (4.15)$$

where \hat{H} is the Hamiltonian (4.3).

4.3.3 Adiabatic elimination

As introduced in Sec. 4.2, for cavity superradiant systems we work in the “bad cavity” regime where we require $\kappa \gg \sqrt{N}g, \gamma_1, \gamma_2, \frac{1}{\tau}$. Here, compared to the conditions in Sec. 4.2, we have also added the constraint that the cavity decay rate κ is much larger than the single-atom Fourier limit $\frac{1}{\tau}$, which is usually referred to as the single-atom transit time broadening.

Working in the “bad cavity” regime allows us to adiabatically eliminate the fast field variables \hat{a} and \hat{a}^\dagger and derive a coarse-grained model. To see this, we examine Eq. (4.11), which can be solved exactly to obtain

$$\hat{a}(t) = e^{-(\frac{\kappa}{2} + i\Delta)t} \hat{a}(0) - \frac{ig}{2} \int_0^t du e^{-(\frac{\kappa}{2} + i\Delta)u} \hat{J}^-(t-u) - \sqrt{\kappa} \int_0^t du e^{-(\frac{\kappa}{2} + i\Delta)u} \hat{\xi}_\kappa(t-u). \quad (4.16)$$

The “bad cavity” condition assumes that the cavity decay frequency κ is much larger than the dynamical frequency of the collective atomic dipole $\left| \frac{d\hat{J}^\pm}{dt} \right|$. If the timescale of interest is of the same order as that of the collective dipole, then we have the coarse-graining condition $t \gg \kappa^{-1}$. The first term on the right hand side of Equation (4.16) becomes $\sim e^{-\frac{1}{2}\kappa t} \rightarrow 0$. The second term can be Taylor expanded as

$$\begin{aligned} & - \frac{ig}{2} \int_0^t du e^{-(\frac{\kappa}{2} + i\Delta)u} \hat{J}^-(t-u) \\ & \approx - \frac{ig}{2} \int_0^t du e^{-(\frac{\kappa}{2} + i\Delta)u} \left[\hat{J}^-(t) - \frac{d\hat{J}^-(t)}{dt} u + \frac{1}{2!} \frac{d^2\hat{J}^-(t)}{dt^2} u^2 + \dots \right] \\ & \approx - \frac{ig/2}{\kappa/2 + i\Delta} \left[\hat{J}^-(t) - \frac{\frac{d\hat{J}^-(t)}{dt}}{\kappa/2 + i\Delta} + \mathcal{O}[(\kappa t)^{-2}] \right] \\ & \approx - \frac{ig/2}{\kappa/2 + i\Delta} \hat{J}^-(t), \end{aligned} \quad (4.17)$$

which implies that the field variable \hat{a} can be well-approximated by the collective dipole \hat{J}^- (up to some factor). The third term can be dealt with using a similar approach to that in Eq. (4.17), yielding

$$\hat{F}_{\text{eff}}(t) \equiv -\sqrt{\kappa} \int_0^t du e^{-\left(\frac{\kappa}{2} + i\Delta\right)u} \hat{\xi}_{\kappa}(t-u) \approx -\frac{\sqrt{\kappa}}{\kappa/2 + i\Delta} \hat{\xi}_{\kappa}(t). \quad (4.18)$$

Here we have defined the effective coarse-grained quantum noise \hat{F}_{eff} , which can be justified by checking the correlation [164]

$$\begin{aligned} \langle \hat{F}_{\text{eff}}(t) \hat{F}_{\text{eff}}^\dagger(t') \rangle &= \left\langle \left[\sqrt{\kappa} \int_0^t du e^{-\left(\frac{\kappa}{2} + i\Delta\right)u} \hat{\xi}_{\kappa}(t-u) \right] \left[\sqrt{\kappa} \int_0^{t'} du' e^{-\left(\frac{\kappa}{2} - i\Delta\right)u'} \hat{\xi}_{\kappa}^\dagger(t'-u') \right] \right\rangle \\ &= \kappa \int_0^t ds \int_0^{t'} ds' e^{-\left(\frac{\kappa}{2} + i\Delta\right)(t-s)} e^{-\left(\frac{\kappa}{2} - i\Delta\right)(t'-s')} \langle \hat{\xi}_{\kappa}(s) \hat{\xi}_{\kappa}^\dagger(s') \rangle \\ &= e^{-\frac{\kappa}{2}(t+t') - i\Delta(t-t')} \kappa \int_0^t ds \int_0^{t'} ds' e^{\frac{\kappa}{2}(s+s') + i\Delta(s-s')} \delta(s-s') \\ &\approx e^{-\frac{\kappa}{2}|t-t'| - i\Delta(t-t')} \\ &\approx \frac{\kappa}{\kappa^2/4 + \Delta^2} \delta(t-t') \end{aligned} \quad (4.19)$$

where we have used the substitutions $s = t - u$, $s' = t' - u'$, and assumed $\kappa|t - t'| \gg 1$. Physically, this implies that the quantum white noise $\hat{\xi}_{\kappa}$ can be coarse-grained to model another quantum white noise on a much larger timescale. Therefore, in the bad cavity limit, the field \hat{a} that satisfies Eq. (4.11) can be well approximated by the adiabatically eliminated solution

$$\hat{a}(t) \approx -\frac{(\Gamma_{\Delta} + i\Gamma_c)}{g} \hat{J}^- - \frac{(\Gamma_c - i\Gamma_{\Delta})}{g} \frac{2}{\sqrt{\Gamma_0}} \hat{\xi}_{\text{eff}}, \quad (4.20)$$

where we have defined

$$\Gamma_c \equiv \frac{g^2 \kappa/4}{\kappa^2/4 + \Delta^2}, \quad \Gamma_{\Delta} \equiv \frac{g^2 \Delta/2}{\kappa^2/4 + \Delta^2}, \quad \Gamma_0 \equiv \frac{g^2}{\kappa}, \quad (4.21)$$

and the quantum white noise $\hat{\xi}_{\text{eff}}$ that satisfies $\langle \hat{\xi}_{\text{eff}}(t) \hat{\xi}_{\text{eff}}^\dagger(t') \rangle = \delta(t-t')$, $\langle \hat{\xi}_{\text{eff}}(t) \hat{\xi}_{\text{eff}}(t') \rangle = \langle \hat{\xi}_{\text{eff}}^\dagger(t) \hat{\xi}_{\text{eff}}^\dagger(t') \rangle = \langle \hat{\xi}_{\text{eff}}^\dagger(t) \hat{\xi}_{\text{eff}}(t') \rangle = 0$.

Equation (4.20) locks the fast-varying field variable \hat{a} to the collective dipole \hat{J}^- . On the timescale of the atomic dipole, the field does not have memory of its initial value, tracking the

collective dipole but augmented by a Markovian type quantum white noise. In this limit, Γ_c , Γ_Δ , and Γ_0 become useful parameters to describe the system dynamics. When $\Delta = 0$, we have $\Gamma_\Delta = 0$ and $\Gamma_c = \Gamma_0 = \frac{g^2}{\kappa}$, which is consistent with our definition of Γ_c in Sec. 4.2.

4.3.4 Superradiant equations

Equation (4.20) can be used to eliminate the field variable \hat{a} from Eqs. (4.9) and (4.12)–(4.13), resulting in the superradiant Heisenberg-Langevin equations for atom j

$$\begin{aligned} \frac{d\hat{\sigma}_j^-}{dt} = & \frac{1}{2}(\Gamma_c - i\Gamma_\Delta)\eta_j\hat{\sigma}_j^z\hat{J}^- - \frac{1}{2}(\gamma_1 + \gamma_2)\hat{\sigma}_j^- \\ & - (\Gamma_\Delta + i\Gamma_c)\frac{\eta_j}{\sqrt{\Gamma_0}}\hat{\sigma}_j^z\hat{\xi}_{\text{eff}} + \sqrt{\gamma_1}\hat{\sigma}_j^z\hat{\xi}_{j,\gamma_1} - \sqrt{\gamma_2}\left(\hat{\sigma}_j^-\hat{\xi}_{j,\gamma_2} - \hat{\xi}_{j,\gamma_2}^\dagger\hat{\sigma}_j^-\right), \end{aligned} \quad (4.22)$$

$$\begin{aligned} \frac{d\hat{\sigma}_j^z}{dt} = & -(\Gamma_c + i\Gamma_\Delta)\eta_j\hat{J}^+\hat{\sigma}_j^- - (\Gamma_c - i\Gamma_\Delta)\eta_j\hat{\sigma}_j^+\hat{J}^- - \gamma_1(\hat{\sigma}_j^z + 1) \\ & + (\Gamma_\Delta - i\Gamma_c)\frac{2\eta_j}{\sqrt{\Gamma_0}}\hat{\xi}_{\text{eff}}^\dagger\hat{\sigma}_j^- + (\Gamma_\Delta + i\Gamma_c)\frac{2\eta_j}{\sqrt{\Gamma_0}}\hat{\sigma}_j^+\hat{\xi}_{\text{eff}} - 2\sqrt{\gamma_1}\left(\hat{\sigma}_j^+\hat{\xi}_{j,\gamma_1} + \hat{\xi}_{j,\gamma_1}^\dagger\hat{\sigma}_j^-\right), \end{aligned} \quad (4.23)$$

$$\begin{aligned} \frac{d\hat{\mathbf{p}}_j}{dt} = & (\Gamma_\Delta - i\Gamma_c)\frac{\hbar\hat{\nabla}\eta_j}{2}\hat{J}^+\hat{\sigma}_j^- + (\Gamma_\Delta + i\Gamma_c)\frac{\hbar\hat{\nabla}\eta_j}{2}\hat{\sigma}_j^+\hat{J}^- \\ & + (\Gamma_c + i\Gamma_\Delta)\frac{\hbar\hat{\nabla}\eta_j}{\sqrt{\Gamma_0}}\hat{\xi}_{\text{eff}}^\dagger\hat{\sigma}_j^- + (\Gamma_c - i\Gamma_\Delta)\frac{\hbar\hat{\nabla}\eta_j}{\sqrt{\Gamma_0}}\hat{\sigma}_j^+\hat{\xi}_{\text{eff}}. \end{aligned} \quad (4.24)$$

The diffusion matrix for atom j is

$$\begin{aligned} 2M_{jj}^{\mu\nu} = & \\ & \begin{matrix} & j, \nu = - & + & z \\ j, \mu = - & \left(\begin{array}{ccc} 0 & 1 & 2\langle\hat{\sigma}_j^-\rangle \\ 0 & 0 & 0 \\ 0 & 2\langle\hat{\sigma}_j^+\rangle & 2(1 + \langle\hat{\sigma}_j^z\rangle) \end{array} \right) & (\Gamma_1\eta_j^2 + \gamma_1) + & \begin{matrix} & j, \nu = - & + & z \\ j, \mu = - & \left(\begin{array}{ccc} 0 & 1 - \langle\hat{\sigma}_j^z\rangle & 0 \\ 1 + \langle\hat{\sigma}_j^z\rangle & 0 & 0 \\ 0 & 0 & 0 \end{array} \right) & + & \left. \begin{array}{ccc} & & \\ & & \\ & & \end{array} \right) \frac{\gamma_2}{2}, \end{matrix} \end{matrix} \end{aligned} \quad (4.25)$$

and for $j \neq k$ is

$$2M_{jk}^{\mu\nu} = \begin{array}{c} j, \mu = - \\ + \\ z \end{array} \begin{array}{c} k, \nu = - \\ + \\ z \end{array} \begin{pmatrix} 0 & \langle \hat{\sigma}_j^z \hat{\sigma}_k^z \rangle & -2 \langle \hat{\sigma}_j^z \hat{\sigma}_k^- \rangle \\ 0 & 0 & 0 \\ 0 & -2 \langle \hat{\sigma}_j^+ \hat{\sigma}_k^z \rangle & 4 \langle \hat{\sigma}_j^+ \hat{\sigma}_k^- \rangle \end{pmatrix} \Gamma_1 \eta_j \eta_k, \quad (4.26)$$

where we have defined $2M_{jk}^{\mu\nu} \delta(t-t') = \langle \hat{F}_j^\mu(t) \hat{F}_k^\nu(t') \rangle$, with $\mu, \nu \in \{+, -, z\}$ denoting different dipole components, and j, k labeling different atoms. We have also introduced the parameter

$$\Gamma_1 = \frac{\Gamma_c^2 + \Gamma_\Delta^2}{\Gamma_0}. \quad (4.27)$$

We make several comments regarding Eqs. (4.25)–(4.26). First, we have not included the diffusion terms associated with the momentum, since we will always make the ballistic approximation in our later treatment by assuming $\hat{\mathbf{p}}_j$ as a constant during the transit time τ . This approximation is valid as long as the temperature of the atomic beam is high enough that the single-photon recoil is much less than $\langle \hat{\mathbf{p}}_j \rangle$. With the ballistic motion assumption, Eq. (4.24) is approximated by $\frac{d\hat{\mathbf{p}}_j}{dt} = 0$, and the corresponding diffusion elements are zero. Second, it is clear that Eq. (4.25) describes single-atom diffusion, while Eq. (4.26) describes the dipole-dipole interaction, which can be significant for large N . After adiabatic elimination, what used to be the field noise now causes all the dipoles to diffuse through the Γ_1 terms. The cavity-mediated effects manifest as the dipole-dipole diffusion matrices in the “bad cavity” limit. Third, the fact that only Γ_1 appears in the diffusion matrices implies that the relative phase between Γ_c and Γ_Δ does not matter in terms of diffusion. Rather it is their modulus square which is proportional to Γ_1 that gives the second order moments, i.e., the diffusion matrices.

For completeness, we include the equivalent superradiant master equation that is given by [52, 71, 164]

$$\frac{d\hat{\rho}}{dt} = \frac{1}{i\hbar} \left[-\frac{\hbar\Gamma_\Delta}{2} \hat{J}^+ \hat{J}^-, \hat{\rho} \right] + \Gamma_c \mathcal{L}[\hat{J}^-] \hat{\rho} + \sum_j \left(\gamma_1 \mathcal{L}[\hat{\sigma}_j^-] \hat{\rho} + \frac{\gamma_2}{4} \mathcal{L}[\hat{\sigma}_j^z] \hat{\rho} \right), \quad (4.28)$$

where the first term is the collective Lamb shift given a heat bath in vacuum.

4.4 Semiclassical c -number equations

The Heisenberg-Langevin equations (4.22)–(4.23) are stochastic differential equation for operators that are formidable to solve. However, with a semiclassical c -number treatment [141, 155, 133], we can numerically solve the c -number differential equations with consistency up to the second order moments of the operators. In this section we derive these so-called c -number quantum Langevin equations.

4.4.0.1 Hermitian operators

For numerical convenience, it is helpful to first rewrite Eqs. (4.22)–(4.23) in terms of solely Hermitian operators, which allows a pathway to approximate operators by real numbers in the c -number description. Using the transformation matrices

$$R = \begin{pmatrix} 1 & 1 \\ -i & i \end{pmatrix}, \quad R^{-1} = \begin{pmatrix} \frac{1}{2} & \frac{i}{2} \\ \frac{1}{2} & -\frac{i}{2} \end{pmatrix} \quad (4.29)$$

we obtain the relation between $\hat{\sigma}^\pm$ and the Hermitian Pauli operators $\hat{\sigma}^x$ and $\hat{\sigma}^y$, i.e.,

$$\begin{pmatrix} \hat{\sigma}^x \\ \hat{\sigma}^y \end{pmatrix} = R \begin{pmatrix} \hat{\sigma}^+ \\ \hat{\sigma}^- \end{pmatrix}, \quad \begin{pmatrix} \hat{\sigma}^+ \\ \hat{\sigma}^- \end{pmatrix} = R^{-1} \begin{pmatrix} \hat{\sigma}^x \\ \hat{\sigma}^y \end{pmatrix}. \quad (4.30)$$

Then Eqs. (4.22)–(4.23) become ³

$$\begin{aligned} \frac{d\hat{\sigma}_j^x}{dt} &= \frac{\Gamma_c}{2}\eta_j \left(\sum_{k \neq j} \eta_k \hat{\sigma}_k^x \hat{\sigma}_j^z - \eta_j \hat{\sigma}_j^x \right) - \frac{\Gamma_\Delta}{2}\eta_j \left(\sum_{k \neq j} \eta_k \hat{\sigma}_k^y \hat{\sigma}_j^z - \eta_j \hat{\sigma}_j^y \right) - \frac{1}{2}(\gamma_1 + \gamma_2) \hat{\sigma}_j^x \\ &\quad - \frac{\eta_j}{\sqrt{\Gamma_0}} \left[i\Gamma_c \left(\hat{\sigma}_j^z \hat{\xi}_{\text{eff}} - \hat{\xi}_{\text{eff}}^\dagger \hat{\sigma}_j^z \right) + \Gamma_\Delta \left(\hat{\sigma}_j^z \hat{\xi}_{\text{eff}} + \hat{\xi}_{\text{eff}}^\dagger \hat{\sigma}_j^z \right) \right] \\ &\quad + \sqrt{\gamma_1} \left(\hat{\sigma}_j^z \hat{\xi}_{j,\gamma_1} + \hat{\xi}_{j,\gamma_1}^\dagger \hat{\sigma}_j^z \right) + i\sqrt{\gamma_2} \left(\hat{\sigma}_j^y \hat{\xi}_{j,\gamma_2} - \hat{\xi}_{j,\gamma_2}^\dagger \hat{\sigma}_j^y \right), \end{aligned} \quad (4.31)$$

$$\begin{aligned} \frac{d\hat{\sigma}_j^y}{dt} &= \frac{\Gamma_c}{2}\eta_j \left(\sum_{k \neq j} \eta_k \hat{\sigma}_k^y \hat{\sigma}_j^z - \eta_j \hat{\sigma}_j^y \right) + \frac{\Gamma_\Delta}{2}\eta_j \left(\sum_{k \neq j} \eta_k \hat{\sigma}_k^x \hat{\sigma}_j^z - \eta_j \hat{\sigma}_j^x \right) - \frac{1}{2}(\gamma_1 + \gamma_2) \hat{\sigma}_j^y \\ &\quad + \frac{\eta_j}{\sqrt{\Gamma_0}} \left[\Gamma_c \left(\hat{\sigma}_j^z \hat{\xi}_{\text{eff}} + \hat{\xi}_{\text{eff}}^\dagger \hat{\sigma}_j^z \right) - i\Gamma_\Delta \left(\hat{\sigma}_j^z \hat{\xi}_{\text{eff}} - \hat{\xi}_{\text{eff}}^\dagger \hat{\sigma}_j^z \right) \right] \\ &\quad + i\sqrt{\gamma_1} \left(\hat{\sigma}_j^z \hat{\xi}_{j,\gamma_1} - \hat{\xi}_{j,\gamma_1}^\dagger \hat{\sigma}_j^z \right) - i\sqrt{\gamma_2} \left(\hat{\sigma}_j^x \hat{\xi}_{j,\gamma_2} - \hat{\xi}_{j,\gamma_2}^\dagger \hat{\sigma}_j^x \right), \end{aligned} \quad (4.32)$$

$$\begin{aligned} \frac{d\hat{\sigma}_j^z}{dt} &= -(\Gamma_c \eta_j^2 + \gamma_1) (\hat{\sigma}_j^z + 1) - \frac{\Gamma_c}{2}\eta_j \sum_{k \neq j} \eta_k \left(\hat{\sigma}_k^x \hat{\sigma}_j^x + \hat{\sigma}_k^y \hat{\sigma}_j^y \right) + \frac{\Gamma_\Delta}{2}\eta_j \sum_{k \neq j} \eta_k \left(\hat{\sigma}_k^y \hat{\sigma}_j^x - \hat{\sigma}_k^x \hat{\sigma}_j^y \right) \\ &\quad + \frac{\eta_j}{\sqrt{\Gamma_0}} \left\{ i\Gamma_c \left[\left(\hat{\sigma}_j^x + i\hat{\sigma}_j^y \right) \hat{\xi}_{\text{eff}} - \hat{\xi}_{\text{eff}}^\dagger \left(\hat{\sigma}_j^x - i\hat{\sigma}_j^y \right) \right] + \Gamma_\Delta \left[\left(\hat{\sigma}_j^x + i\hat{\sigma}_j^y \right) \hat{\xi}_{\text{eff}} + \hat{\xi}_{\text{eff}}^\dagger \left(\hat{\sigma}_j^x - i\hat{\sigma}_j^y \right) \right] \right\} \\ &\quad - \sqrt{\gamma_1} \left[\left(\hat{\sigma}_j^x + i\hat{\sigma}_j^y \right) \hat{\xi}_{j,\gamma_1} + \hat{\xi}_{j,\gamma_1}^\dagger \left(\hat{\sigma}_j^x - i\hat{\sigma}_j^y \right) \right]. \end{aligned} \quad (4.33)$$

The corresponding diffusion matrices are

$$2M_{jj}^{\mu\nu} = \begin{array}{c} \begin{array}{ccc} & j, \nu=x & y & z \\ \begin{array}{l} j, \mu=x \\ y \\ z \end{array} & \begin{pmatrix} 1 & -i & \langle \hat{\sigma}_j^x \rangle - i \langle \hat{\sigma}_j^y \rangle \\ i & 1 & i \langle \hat{\sigma}_j^x \rangle + \langle \hat{\sigma}_j^y \rangle \\ \langle \hat{\sigma}_j^x \rangle + i \langle \hat{\sigma}_j^y \rangle & -i \langle \hat{\sigma}_j^x \rangle + \langle \hat{\sigma}_j^y \rangle & 2(1 + \langle \hat{\sigma}_j^z \rangle) \end{pmatrix} & + & \begin{array}{ccc} & j, \nu=x & y & z \\ \begin{array}{l} j, \mu=x \\ y \\ z \end{array} & \begin{pmatrix} 1 & i \langle \hat{\sigma}_j^z \rangle & 0 \\ -i \langle \hat{\sigma}_j^z \rangle & 1 & 0 \\ 0 & 0 & 0 \end{pmatrix} & \gamma_2, \end{array} \end{array} \quad (4.34)$$

³A useful set of relations is $(\hat{\sigma}_k^+ \hat{\sigma}_j^- + \hat{\sigma}_j^+ \hat{\sigma}_k^-) = \frac{1}{2}(\hat{\sigma}_k^x \hat{\sigma}_j^x + \hat{\sigma}_k^y \hat{\sigma}_j^y)$ and $(\hat{\sigma}_k^+ \hat{\sigma}_j^- - \hat{\sigma}_j^+ \hat{\sigma}_k^-) = \frac{i}{2}(\hat{\sigma}_j^x \hat{\sigma}_k^y - \hat{\sigma}_k^x \hat{\sigma}_j^y)$.

and for $j \neq k$

$$2M_{jk}^{\mu\nu} = \begin{array}{c} j, \mu=x \\ y \\ z \end{array} \left(\begin{array}{ccc} k, \nu=x & y & z \\ \langle \hat{\sigma}_j^z \hat{\sigma}_k^z \rangle & -i \langle \hat{\sigma}_j^z \hat{\sigma}_k^z \rangle & -\langle \hat{\sigma}_j^z \hat{\sigma}_k^x \rangle + i \langle \hat{\sigma}_j^z \hat{\sigma}_k^y \rangle \\ i \langle \hat{\sigma}_j^z \hat{\sigma}_k^z \rangle & \langle \hat{\sigma}_j^z \hat{\sigma}_k^z \rangle & -\langle \hat{\sigma}_j^z \hat{\sigma}_k^y \rangle - i \langle \hat{\sigma}_j^z \hat{\sigma}_k^x \rangle \\ -\langle \hat{\sigma}_j^x \hat{\sigma}_k^z \rangle - i \langle \hat{\sigma}_j^y \hat{\sigma}_k^z \rangle & -\langle \hat{\sigma}_j^y \hat{\sigma}_k^z \rangle + i \langle \hat{\sigma}_j^x \hat{\sigma}_k^z \rangle & (\langle \hat{\sigma}_j^x \hat{\sigma}_k^x \rangle + \langle \hat{\sigma}_j^y \hat{\sigma}_k^y \rangle) + i (\langle \hat{\sigma}_j^y \hat{\sigma}_k^x \rangle - \langle \hat{\sigma}_j^x \hat{\sigma}_k^y \rangle) \end{array} \right) \Gamma_1 \eta_j \eta_k. \quad (4.35)$$

The diffusion matrices are most useful for the c -number treatment. Here we give the noise terms in Eqs. (4.31)–(4.33) as an reference to Eqs. (4.34)–(4.35).

4.4.1 Rules for c -number equations

So far everything is quantum. In order to numerically simulate the dynamics of the many body pseudospin variables, we make a second-order c -number approximation. Specifically, we introduce the following rules:

- (1) Non-noise terms.

These include the detuning terms and the drift terms in the Heisenberg-Langevin equations.

We establish the mapping

$$\hat{S}_j \mapsto S_j, \quad (4.36)$$

$$(\hat{S}_j \hat{S}_k)_{\text{ordering}} \mapsto S_j S_k, \quad (4.37)$$

where \hat{S}_j is a system operator and S_j is its c -number counterpart. The notation $(\hat{S}_j \hat{S}_k)_{\text{ordering}}$ stands for a chosen ordering of the quantum operators \hat{S}_j and \hat{S}_k , which we will choose as the *symmetric ordering*

$$\left(\hat{S}_j \hat{S}_k \right)_{\text{sym}} = \frac{1}{2} \left(\hat{S}_j \hat{S}_k + \hat{S}_k \hat{S}_j \right). \quad (4.38)$$

Notice that the form of $\hat{S}_j \hat{S}_k$ should not be reducible, as in, $\hat{\sigma}_j^x \hat{\sigma}_j^y$ should be reduced to $i \hat{\sigma}_j^z$ before making the c -number approximation.

(2) Boundary and initial conditions.

We require for initial conditions ($t = 0$) or boundary conditions (when the atomic beam enters the cavity)

$$\langle S_j \rangle_e = \langle \hat{S}_j \rangle, \quad (4.39)$$

$$\langle S_j S_k \rangle_e = \left\langle \left(\hat{S}_j \hat{S}_k \right)_{\text{sym}} \right\rangle, \quad (4.40)$$

where $\langle \cdot \rangle_e$ is the ensemble average (over simulation trajectories) [133]. As an example, for the superradiant beam laser, atomic dipoles enter the cavity in the excited state $|e\rangle$. Thus all the up to second order moments of the pseudospin operators are given by

$$\langle \hat{\sigma}_j^z \rangle = 1, \quad (4.41)$$

$$\langle \hat{\sigma}_j^x \rangle = \langle \hat{\sigma}_j^y \rangle = 0, \quad (4.42)$$

$$\langle (\hat{\sigma}_j^z)^2 \rangle = \langle (\hat{\sigma}_j^x)^2 \rangle = \langle (\hat{\sigma}_j^y)^2 \rangle = 1, \quad (4.43)$$

$$\left\langle \left(\hat{\sigma}_j^\mu \hat{\sigma}_j^\nu \right)_{\text{sym}} \right\rangle = 0, \quad \mu, \nu \in \{x, y, z\}, \quad \mu \neq \nu. \quad (4.44)$$

In order for the c -number moments to match, for each simulation trajectory we let $s_j^z = 1$ and randomly choose s_j^x and s_j^y from ± 1 with equal probability. One can check that this choice will satisfy Eqs. (4.39)–(4.40) with moments given by Eqs. (4.41)–(4.44).

(3) Noise terms.

The first two conditions are sufficient to formulate a c -number theory if the system is closed. In that case, with the initial conditions determined and the differential equations rewritten in c -numbers, each trajectory is deterministic. However, for an open quantum system, it remains for us to choose a rule for the c -number noise terms.

The c -number theory is fundamentally a Gaussian theory, meaning that we cannot match moments of operators higher than second order. However, as mentioned in Chap. 3, the quantum white noise also implicitly assumes a Gaussian noise model. Therefore, it is sufficient to establish a mapping from the operator diffusion matrices to the c -number

diffusion matrices (the mean of the noise is zero). Such a mapping is straightforward. Let F_j be the c -number counterpart of the noise operator \hat{F}_j . Then the c -number diffusion matrices can be defined as

$$2m_{jk}\delta(t-t') = \langle F_j(t)F_k(t') \rangle_e, \quad (4.45)$$

We then establish the mapping

$$(2M_{ij})_{\text{sym}} \mapsto 2m_{ij} \quad (4.46)$$

where we have chosen the symmetric ordering

$$(2M_{ij})_{\text{sym}} = \frac{1}{2}(2M_{ij} + 2M_{ji}). \quad (4.47)$$

In the next section, we use the rules introduced in this section to derive the c -number quantum Langevin equations for the superradiant beam laser model.

4.4.2 c -number Langevin equations

4.4.2.1 Non-noise terms

Following Rule (1) in the previous section, the non-noise parts of the c -number equations for Eqs. (4.31)–(4.33), labeled by D_j^μ , $\mu \in \{x, y, z\}$, are given by

$$D_j^x = \frac{\Gamma_c}{2}\eta_j [\mathcal{J}^x s_j^z - \eta_j s_j^x (s_j^z + 1)] - \frac{\Gamma_\Delta}{2}\eta_j [\mathcal{J}^y s_j^z - \eta_j s_j^y (s_j^z + 1)] - \frac{1}{2}(\gamma_1 + \gamma_2) s_j^x, \quad (4.48)$$

$$D_j^y = \frac{\Gamma_c}{2}\eta_j [\mathcal{J}^y s_j^z - \eta_j s_j^y (s_j^z + 1)] + \frac{\Gamma_\Delta}{2}\eta_j [\mathcal{J}^x s_j^z - \eta_j s_j^x (s_j^z + 1)] - \frac{1}{2}(\gamma_1 + \gamma_2) s_j^y, \quad (4.49)$$

$$D_j^z = -(\Gamma_c \eta_j^2 + \gamma_1)(s_j^z + 1) - \frac{\Gamma_c}{2}\eta_j \left\{ \mathcal{J}^x s_j^x + \mathcal{J}^y s_j^y - \eta_j \left[(s_j^x)^2 + (s_j^y)^2 \right] \right\} + \frac{\Gamma_\Delta}{2}\eta_j (\mathcal{J}^y s_j^x - \mathcal{J}^x s_j^y), \quad (4.50)$$

where we have introduced the c -number collective dipole components

$$\mathcal{J}^x = \sum_j \eta_j s_j^x, \quad \mathcal{J}^y = \sum_j \eta_j s_j^y. \quad (4.51)$$

This c -number replacement is actually trivial because all the non-noise terms in Eqs. (4.31)–(4.33) are already in symmetric ordering. In the large N limit, if the collective dipole is formed, we can ignore single-atom terms and get

$$D_j^x = \frac{\Gamma_c}{2} \eta_j \mathcal{J}^x s_j^z - \frac{\Gamma_\Delta}{2} \eta_j \mathcal{J}^y s_j^z - \frac{1}{2} (\gamma_1 + \gamma_2) s_j^x, \quad (4.52)$$

$$D_j^y = \frac{\Gamma_c}{2} \eta_j \mathcal{J}^y s_j^z + \frac{\Gamma_\Delta}{2} \eta_j \mathcal{J}^x s_j^z - \frac{1}{2} (\gamma_1 + \gamma_2) s_j^y, \quad (4.53)$$

$$D_j^z = -\gamma_1 (s_j^z + 1) - \frac{\Gamma_c}{2} \eta_j (\mathcal{J}^x s_j^x + \mathcal{J}^y s_j^y) + \frac{\Gamma_\Delta}{2} \eta_j (\mathcal{J}^y s_j^x - \mathcal{J}^x s_j^y). \quad (4.54)$$

4.4.2.2 Diffusion matrices

The boundary conditions for the superradiant beam laser have already been discussed as an example following Rule (2) in the last section. The c -number diffusion matrix $2m_{jk}^{\mu\nu}$, by Rule (3), is the c -number mapping of $(2M_{jk}^{\mu\nu})_{\text{sym}}$ from Eqs. (4.34)–(4.35), where

$$\begin{aligned} (2M_{jk}^{\mu\nu})_{\text{sym}} &= \frac{1}{2} (2M_{jk}^{\mu\nu} + 2M_{kj}^{\nu\mu}) \\ &= \begin{array}{c} j, \nu=x \\ y \\ z \end{array} \begin{array}{ccc} & y & z \\ \begin{array}{c} j, \mu=x \\ y \\ z \end{array} & \begin{pmatrix} 1 & 0 & \langle \hat{\sigma}_j^x \rangle \\ 0 & 1 & \langle \hat{\sigma}_j^y \rangle \\ \langle \hat{\sigma}_j^x \rangle & \langle \hat{\sigma}_j^y \rangle & 2(1 + \langle \hat{\sigma}_j^z \rangle) \end{pmatrix} & \end{array} (\Gamma_1 \eta_j^2 + \gamma_1) + \begin{array}{c} j, \nu=x \\ y \\ z \end{array} \begin{array}{ccc} & y & z \\ \begin{array}{c} j, \mu=x \\ y \\ z \end{array} & \begin{pmatrix} 1 & 0 & 0 \\ 0 & 1 & 0 \\ 0 & 0 & 0 \end{pmatrix} & \gamma_2, \end{array} \end{aligned} \quad (4.55)$$

and for $j \neq k$

$$(2\hat{M}_{jk}^{\mu\nu})_{\text{sym}} = \begin{array}{c} j, \mu=x \\ y \\ z \end{array} \begin{array}{ccc} k, \nu=x & y & z \\ \begin{array}{c} j, \mu=x \\ y \\ z \end{array} & \begin{pmatrix} \langle \hat{\sigma}_j^z \hat{\sigma}_k^z \rangle & 0 & -\langle \hat{\sigma}_j^z \hat{\sigma}_k^x \rangle \\ 0 & \langle \hat{\sigma}_j^z \hat{\sigma}_k^z \rangle & -\langle \hat{\sigma}_j^z \hat{\sigma}_k^y \rangle \\ -\langle \hat{\sigma}_j^x \hat{\sigma}_k^z \rangle & -\langle \hat{\sigma}_j^y \hat{\sigma}_k^z \rangle & \langle \hat{\sigma}_j^x \hat{\sigma}_k^x \rangle + \langle \hat{\sigma}_j^y \hat{\sigma}_k^y \rangle \end{pmatrix} & \end{array} \times \Gamma_1 \eta_j \eta_k. \quad (4.56)$$

In other words, taking the symmetric ordering ensures that all the imaginary terms cancel [155].

The c -number diffusion matrices are therefore

$$2m_{jj}^{\mu\nu} = \begin{array}{c} j, \nu=x \\ y \\ z \end{array} \begin{array}{ccc} & y & z \\ \begin{array}{c} j, \mu=x \\ y \\ z \end{array} & \begin{pmatrix} 1 & 0 & \langle s_j^x \rangle_e \\ 0 & 1 & \langle s_j^y \rangle_e \\ \langle s_j^x \rangle_e & \langle s_j^y \rangle_e & 2(1 + \langle s_j^z \rangle_e) \end{pmatrix} & \end{array} (\Gamma_1 \eta_j^2 + \gamma_1) + \begin{array}{c} j, \nu=x \\ y \\ z \end{array} \begin{array}{ccc} & y & z \\ \begin{array}{c} j, \mu=x \\ y \\ z \end{array} & \begin{pmatrix} 1 & 0 & 0 \\ 0 & 1 & 0 \\ 0 & 0 & 0 \end{pmatrix} & \end{array} \gamma_2, \quad (4.57)$$

and for $j \neq k$

$$2m_{jk}^{\mu\nu} = \begin{array}{c} j, \mu=x \\ y \\ z \end{array} \begin{array}{ccc} & k, \nu=x & y & z \\ \begin{array}{c} j, \mu=x \\ y \\ z \end{array} & \begin{pmatrix} \langle s_j^z s_k^z \rangle_e & 0 & -\langle s_j^z s_k^x \rangle_e \\ 0 & \langle s_j^z s_k^z \rangle_e & -\langle s_j^z s_k^y \rangle_e \\ -\langle s_j^z s_k^x \rangle_e & -\langle s_j^z s_k^y \rangle_e & \langle s_j^x s_k^x \rangle_e + \langle s_j^y s_k^y \rangle_e \end{pmatrix} & \end{array} \Gamma_1 \eta_j \eta_k. \quad (4.58)$$

4.4.2.3 Noise terms

Given the c -number diffusion matrices in Eqs. (4.57)–(4.58), we now provide the methods to construct the corresponding c -number noise terms to satisfy the diffusion matrices. Notice that the methods will not be unique because we only require the sufficient conditions.

(1) Γ_1 terms.

For large N , we can ignore the single-atom diffusion matrix for Γ_1 in Eq. (4.57). This corresponds to the superradiant condition when the dipole-dipole terms dominate. The remaining diffusion matrix for the Γ_1 decay without the ensemble average, labeled by $2m'$, has the form

$$2m'_{jk, \Gamma_1} = \begin{pmatrix} s_j^z s_k^z & 0 & -s_j^z s_k^x \\ 0 & s_j^z s_k^z & -s_j^z s_k^y \\ -s_j^z s_k^x & -s_j^z s_k^y & s_j^x s_k^x + s_j^y s_k^y \end{pmatrix} \Gamma_1 \eta_j \eta_k, \quad (4.59)$$

which can be decomposed into

$$2m'_{jk,\Gamma_1} = B_{j,\Gamma_1} (B_{k,\Gamma_1})^\top, \quad (4.60)$$

where

$$B_{a,\Gamma_1} = \begin{pmatrix} s_a^z & 0 \\ 0 & s_a^z \\ -s_a^x & -s_a^y \end{pmatrix} \sqrt{\Gamma_1} \eta_a, \quad a \in \{j, k\}. \quad (4.61)$$

Therefore, we can choose two independent c -number white noise sources ξ_{1,Γ_1} and ξ_{2,Γ_1} , which satisfy

$$\langle \xi_{j,\Gamma_1}(t) \xi_{k,\Gamma_1}(t') \rangle = \delta_{jk} \delta(t - t'), \quad j, k \in \{1, 2\} \quad (4.62)$$

and define the noise vectors

$$\mathbf{F}_{j,\Gamma_1} = \begin{pmatrix} F_{j,\Gamma_1}^x \\ F_{j,\Gamma_1}^y \\ F_{j,\Gamma_1}^z \end{pmatrix} = B_{j,\Gamma_1} \begin{pmatrix} \xi_{1,\Gamma_1} \\ \xi_{2,\Gamma_1} \end{pmatrix} = \begin{pmatrix} s_j^z & 0 \\ 0 & s_j^z \\ -s_j^x & -s_j^y \end{pmatrix} \begin{pmatrix} \xi_{1,\Gamma_1} \\ \xi_{2,\Gamma_1} \end{pmatrix} \sqrt{\Gamma_1} \eta_j. \quad (4.63)$$

Then we have one choice of the c -number noise terms for the Γ_1 decay

$$F_{j,\Gamma_1}^x = \eta_j \sqrt{\Gamma_1} s_j^z \xi_{1,\Gamma_1} = \eta_j \sqrt{\frac{\Gamma_c^2 + \Gamma_\Delta^2}{\Gamma_0}} s_j^z \xi_{1,\Gamma_1}, \quad (4.64)$$

$$F_{j,\Gamma_1}^y = \eta_j \sqrt{\Gamma_1} s_j^z \xi_{2,\Gamma_1} = \eta_j \sqrt{\frac{\Gamma_c^2 + \Gamma_\Delta^2}{\Gamma_0}} s_j^z \xi_{2,\Gamma_1}, \quad (4.65)$$

$$F_{j,\Gamma_1}^z = -\eta_j \sqrt{\Gamma_1} (s_j^x \xi_{1,\Gamma_1} + s_j^y \xi_{2,\Gamma_1}) = -\eta_j \sqrt{\frac{\Gamma_c^2 + \Gamma_\Delta^2}{\Gamma_0}} (s_j^x \xi_{1,\Gamma_1} + s_j^y \xi_{2,\Gamma_1}). \quad (4.66)$$

We can also choose

$$F_{j,\Gamma_1}^x = -\frac{\eta_j}{\sqrt{\Gamma_0}} s_j^z (\Gamma_c \xi^p + \Gamma_\Delta \xi^q), \quad (4.67)$$

$$F_{j,\Gamma_1}^y = \frac{\eta_j}{\sqrt{\Gamma_0}} s_j^z (\Gamma_c \xi^q - \Gamma_\Delta \xi^p), \quad (4.68)$$

$$F_{j,\Gamma_1}^z = \frac{\eta_j}{\sqrt{\Gamma_0}} \left[\Gamma_c (s_j^x \xi^p - s_j^y \xi^q) + \Gamma_\Delta (s_j^x \xi^q + s_j^y \xi^p) \right], \quad (4.69)$$

where ξ^q and ξ^p are only different from ξ_{1,Γ_1} and ξ_{2,Γ_1} by a rotation.

We can check that

$$\langle \mathbf{F}_{j,\Gamma_1} \mathbf{F}_{k,\Gamma_1}^T \rangle = \langle 2m'_{jk,\Gamma_1} \rangle = 2m_{jk,\Gamma_1}. \quad (4.70)$$

Indeed, the noise terms \mathbf{F}_{j,Γ_1} give the correct c -number diffusion matrices.

(2) γ_1 terms.

Similar to our methods for Γ_1 terms, from Eq. (4.57), we get

$$2m'_{j,\gamma_1} = \begin{pmatrix} 1 & 0 & s_j^x \\ 0 & 1 & s_j^y \\ s_j^x & s_j^y & 2(1 + s_j^z) \end{pmatrix} \gamma_1. \quad (4.71)$$

With Cholesky decomposition, we obtain

$$2m'_{j,\gamma_1} = B_{j,\gamma_1} (B_{j,\gamma_1})^T, \quad (4.72)$$

where

$$B_{j,\gamma_1} = \begin{pmatrix} 1 & 0 & 0 \\ 0 & 1 & 0 \\ s_j^x & s_j^y & \sqrt{2(1 + s_j^z) - (s_j^x)^2 - (s_j^y)^2} \end{pmatrix} \sqrt{\gamma_1}. \quad (4.73)$$

Therefore we need to choose for each particle three independent white noise sources

ξ_{j,γ_1}^μ , $\mu \in \{x, y, z\}$, which satisfy ⁴

$$\langle \xi_{j,\gamma_1}^\mu(t) \xi_{k,\gamma_1}^\nu(t') \rangle = \delta_{jk} \delta_{\mu\nu} \delta(t - t'), \quad (4.74)$$

with $\mu, \nu \in \{x, y, z\}$. Then the c -number noises are chosen to be

$$\mathbf{F}_{j,\gamma_1} = B_{j,\gamma_1} \begin{pmatrix} \xi_{j,\gamma_1}^x \\ \xi_{j,\gamma_1}^y \\ \xi_{j,\gamma_1}^z \end{pmatrix}. \quad (4.75)$$

⁴The noises must be independent for different particle to make sure there are no diffusion terms between them.

Notice that there might be numerical issues when $2(1 + s_j^z) - (s_j^x)^2 - (s_j^y)^2 < 0$. In that case, we might need to it to be 0 or its absolute value in simulations.

(3) γ_2 terms.

By Eq. (4.57), the diffusion matrix corresponding to γ_2 decay is

$$2m'_{j,\gamma_2} = \begin{pmatrix} 1 & 0 & 0 \\ 0 & 1 & 0 \\ 0 & 0 & 0 \end{pmatrix} \gamma_2. \quad (4.76)$$

The decomposition is

$$2m'_{j,\gamma_2} = B_{j,\gamma_2} (B_{j,\gamma_2})^T, \quad (4.77)$$

where

$$B_{j,\gamma_2} = \begin{pmatrix} 1 & 0 & 0 \\ 0 & 1 & 0 \\ 0 & 0 & 0 \end{pmatrix} \sqrt{\gamma_2}. \quad (4.78)$$

Therefore we need to choose for each particle two independent white noise sources ξ_{j,γ_2}^μ , $\mu \in \{x, y, z\}$, which satisfy

$$\langle \xi_{j,\gamma_2}^\mu(t) \xi_{k,\gamma_2}^\nu(t') \rangle = \delta_{jk} \delta_{\mu\nu} \delta(t - t'), \quad (4.79)$$

with $\mu, \nu \in \{x, y\}$. Then the c -number noise terms can be chosen as

$$\mathbf{F}_{j,\gamma_2} = B_{j,\gamma_2} \begin{pmatrix} \xi_{j,\gamma_2}^x \\ \xi_{j,\gamma_2}^y \\ 0 \end{pmatrix} = \begin{pmatrix} \xi_{j,\gamma_2}^x \\ \xi_{j,\gamma_2}^y \\ 0 \end{pmatrix} \sqrt{\gamma_2}. \quad (4.80)$$

We see that only two independent noise sources need to be introduced for each atom due to the reduced rank of the matrix B_{j,γ_2} .

As a result, the final c -number quantum Langevin equations for the superradiant beam laser model in the large N limit are

$$\frac{ds_j^x}{dt} = \frac{\Gamma_c}{2}\eta_j\mathcal{J}^x s_j^z - \frac{\Gamma_\Delta}{2}\eta_j\mathcal{J}^y s_j^z - \frac{1}{2}(\gamma_1 + \gamma_2)s_j^x + F_{j,\Gamma_1}^x + F_{j,\gamma_1}^x + F_{j,\gamma_2}^x \quad (4.81)$$

$$\frac{ds_j^y}{dt} = \frac{\Gamma_c}{2}\eta_j\mathcal{J}^y s_j^z + \frac{\Gamma_\Delta}{2}\eta_j\mathcal{J}^x s_j^z - \frac{1}{2}(\gamma_1 + \gamma_2)s_j^y + F_{j,\Gamma_1}^y + F_{j,\gamma_1}^y + F_{j,\gamma_2}^y \quad (4.82)$$

$$\frac{ds_j^z}{dt} = -\gamma_1(s_j^z + 1) - \frac{\Gamma_c}{2}\eta_j(\mathcal{J}^x s_j^x + \mathcal{J}^y s_j^y) + \frac{\Gamma_\Delta}{2}\eta_j(\mathcal{J}^y s_j^x - \mathcal{J}^x s_j^y) + F_{j,\Gamma_1}^z + F_{j,\gamma_1}^z + F_{j,\gamma_2}^z. \quad (4.83)$$

where \mathbf{F}_{j,Γ_1} , \mathbf{F}_{j,γ_1} , and \mathbf{F}_{j,γ_2} are given in Eqs. (4.63), (4.75), and (4.80).

In the remaining of this thesis, we will use the c -number theory developed in this chapter to study various configurations of the superradiant atomic beam laser system. We will also study various superradiant phase transitions resulting from different types of dissipation.

Chapter 5

Rugged mHz-Linewidth Superradiant Laser Driven by a Hot Atomic Beam ¹

5.1 Introduction

Ultracoherent light sources are the foundation of highly accurate atomic clocks [98, 20], measurements of the time variation of fundamental constants [60, 46], novel tests of relativity [132, 78], and dark matter searches [160]. Traditionally, these sources have been generated with cavity stabilization, which involves locking lasers to highly stable optical cavities [55]. Despite their incredible performance [126], these systems are complex, challenging to improve upon, and perform poorly outside of controlled lab environments. However if cavity-stabilized lasers could be made rugged, they could be used for improved global positioning[91], deep space navigation [38], and new geophysical technology [13].

Superradiant lasers [25, 101, 12, 95, 129, 115, 116, 87, 59, 136] are promising candidates for next-generation ultracoherent lasers [117]. However, a continuous wave superradiant laser has not yet been demonstrated because of atomic heating in existing designs, which rely on ultracold atoms [115]. Also, the use of ultracold atoms makes these systems complicated and ill suited to applications in the field.

Here we propose a new kind of superradiant laser built from a hot atomic beam traversing an optical cavity. We show that its theoretical minimum linewidth and maximum output power are competitive with the best ultracoherent lasers. Because of atomic phase synchronization, the phase

¹The bulk of this work has been published in Physical Review Letters [92]. Copyright 2020 American Physical Society.

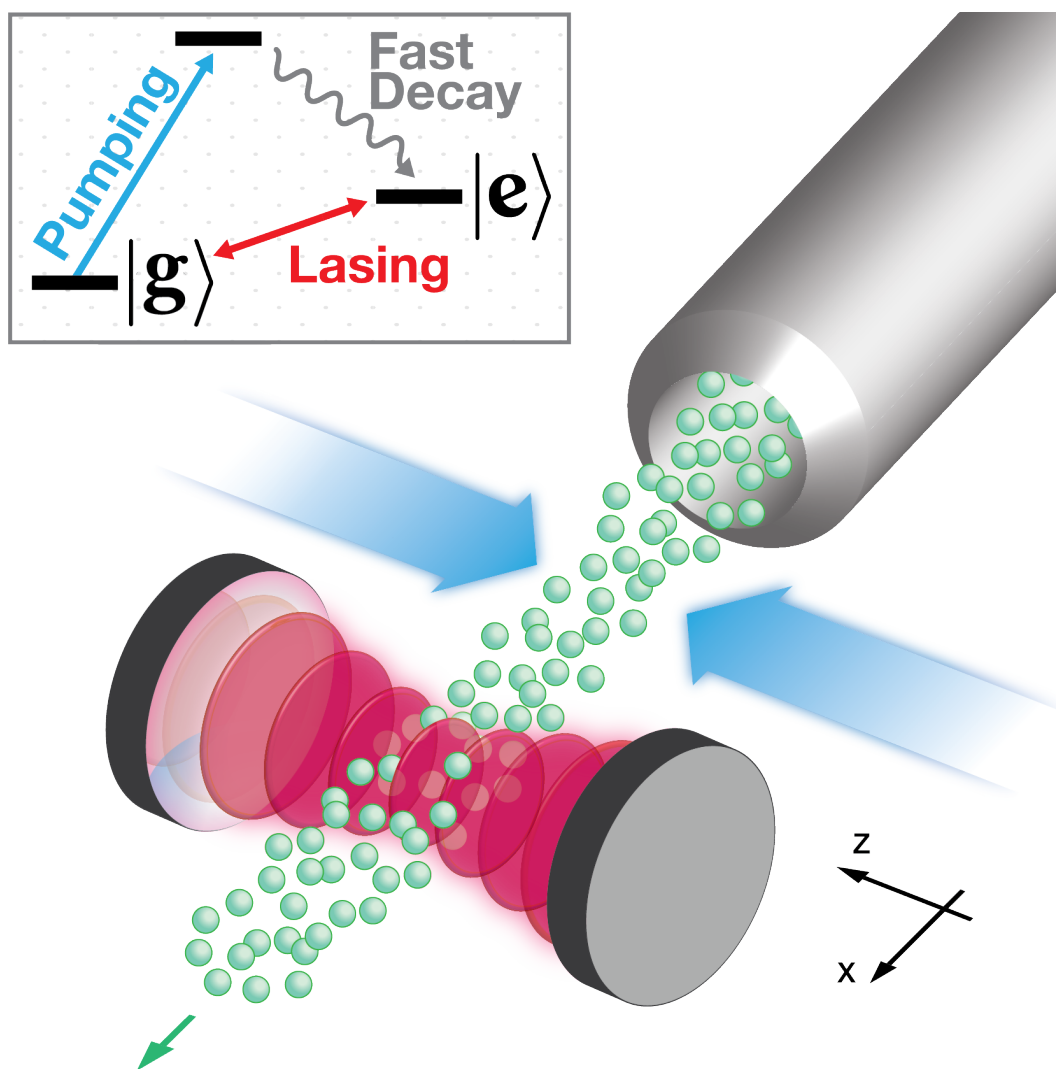


Figure 5.1: The superradiant beam laser. The atomic beam is generated from an effusive source, like a commercial effusion cell. After emerging from the source (upper right), the atoms are prepared by pumping lasers (blue arrows) in a metastable state prior to entering the cavity (lower left). Inset: The minimal atomic structure needed for the superradiant beam laser to operate. In this three-level scheme, atoms are rapidly prepared in a metastable state $|e\rangle$ by pumping (blue) on a broad transition. Lasing (red) occurs on the long-lived $|g\rangle \leftrightarrow |e\rangle$ transition. Real atomic systems may require more complex pumping schemes.

of the output light is robust against decoherence arising from atomic motion, such as Doppler and transit time broadening. Furthermore, our system is naturally continuous wave, and it is inherently insensitive to effects that limit the best cavity-stabilized lasers [55, 126], such as environmental noise and drift. The simplicity and ruggedness of the design make this system promising for applications in challenging real-world environments [149, 78] and for packaging into commercial systems.

5.2 Formalism

Our system consists of a dense atomic beam traveling through an optical cavity. We consider the case of all atoms having a uniform velocity in the x direction (Fig. 5.1). In this chapter, we discuss the examples of ^{40}Ca and ^{88}Sr , but our results apply equally well to many other alkaline-earth-like species. The mean intracavity atom number is $N \equiv \Phi\tau$ in steady state, where Φ is the number of atoms transiting the cavity mode per unit time, and τ is the transit time. The atoms in the beam are described by dipoles that are pumped into a metastable state (Fig. 5.1) before entering the cavity. The dipole transition frequency ω_a is taken to be near resonant with the frequency ω_c of a single cavity mode, where coupling of the dipoles and cavity is described by the Tavis-Cummings Hamiltonian $\hat{H}(t) = (\hbar g/2) \sum_j \eta[\mathbf{x}_j(t)] (\hat{\sigma}_j^+ \hat{a} + \hat{a}^\dagger \hat{\sigma}_j^-)$. Here, the summation runs over all atoms in the beam, $\eta[\mathbf{x}_j(t)]$ is a cavity mode function evaluated at position $\mathbf{x}_j(t)$ of atom j at time t , and g is the vacuum Rabi frequency at a cavity antinode. Furthermore, the atomic dipole raising and lowering operators are $\hat{\sigma}_j^+ = \left(\hat{\sigma}_j^-\right)^\dagger = |e\rangle_j \langle g|_j$, where $|g\rangle$ and $|e\rangle$ are the atomic ground and excited states, respectively, and the photon annihilation and creation operators of the cavity field mode are \hat{a} and \hat{a}^\dagger . Besides this Hamiltonian that couples the atoms and cavity, our model includes photon loss through a cavity mirror with rate κ .

We consider the bad cavity regime, which occurs when κ is much larger than the transit time broadening $1/\tau$, the collective coupling $\sqrt{N}g$, and the Doppler width $\delta_D = k\Delta v_z$. Here $k = 2\pi/\lambda$, λ is the optical wavelength, and Δv_z is the single-atom velocity width along the cavity axis. In this regime, the light field is rigidly anchored to the collective atomic dipole, so that the cavity degrees of freedom can be adiabatically eliminated as $\hat{a} \approx -ig\hat{J}^-/\kappa$. The operator $\hat{J}^- = \sum_j \eta(\mathbf{x}_j)\hat{\sigma}_j^-$ is

the collective dipole, which is the sum of the individual atomic dipoles interacting with the cavity mode. New atomic dipoles entering the cavity synchronize with the existing collective dipole due to the atom-cavity interaction [166]. Since there is a large number of atoms in the cavity mode, the true operator equations are well approximated by stochastic differential equations for their complex amplitude equivalents (as introduced in Chap. 4);

$$\frac{ds_j^x}{dt} = \frac{\Gamma_c}{2}\eta_j [\mathcal{J}^x s_j^z - \eta_j s_j^x (s_j^z + 1)] - \sqrt{\Gamma_c}\eta_j s_j^z \xi^p, \quad (5.1)$$

$$\frac{ds_j^y}{dt} = \frac{\Gamma_c}{2}\eta_j [\mathcal{J}^y s_j^z - \eta_j s_j^y (s_j^z + 1)] + \sqrt{\Gamma_c}\eta_j s_j^z \xi^q, \quad (5.2)$$

$$\begin{aligned} \frac{ds_j^z}{dt} = & -\frac{\Gamma_c}{2}\eta_j \left\{ \mathcal{J}^x s_j^x + \mathcal{J}^y s_j^y - \eta_j \left[(s_j^x)^2 + (s_j^y)^2 \right] \right\} \\ & - \Gamma_c \eta_j^2 (s_j^z + 1) + \sqrt{\Gamma_c}\eta_j \left(s_j^x \xi^p - s_j^y \xi^q \right). \end{aligned} \quad (5.3)$$

Here s_j^x , s_j^y , and s_j^z are the c -number pseudospin variables that correspond to $\hat{\sigma}_j^x = \hat{\sigma}_j^- + \hat{\sigma}_j^+$, $\hat{\sigma}_j^y = i(\hat{\sigma}_j^- - \hat{\sigma}_j^+)$, and $\hat{\sigma}_j^z = \hat{\sigma}_j^+ \hat{\sigma}_j^- - \hat{\sigma}_j^- \hat{\sigma}_j^+$. Similarly, \mathcal{J}^x and \mathcal{J}^y represent the operators $\hat{J}^x = \hat{J}^- + \hat{J}^+$ and $\hat{J}^y = i(\hat{J}^- - \hat{J}^+)$. We have defined $\Gamma_c = \mathcal{C}\gamma$, where $\mathcal{C} = g^2/(\kappa\gamma)$ is the cavity cooperativity and γ is the free-space spontaneous emission rate. We use the shorthand $\eta_j = \eta[\mathbf{x}_j(t)]$ and model the cavity mode by $\eta(\mathbf{x}) = [\Theta(x+w) - \Theta(x-w)] \cos(kz)$, where $\Theta(x)$ is the Heaviside step function and w is the cavity beam waist. Spontaneous emission into free space is neglected in Eqs. (5.1)–(5.3) because the collective lifetime is much shorter than the spontaneous lifetime [101, 100, 166].² Along the cavity axis, the atoms are randomly assigned a velocity drawn from a Maxwell-Boltzmann distribution at a given temperature. Cavity shot noise is denoted by the stochastic noise variables ξ^q and ξ^p , which have zero mean and are delta correlated as $\langle \xi^a(t) \xi^b(t') \rangle = \delta_{ab} \delta(t-t')$, $a, b \in \{q, p\}$. Each atom enters the cavity with $s_j^z = 1$, and projection noise is included by choosing random (and independent) values $+1$ or -1 for s_j^x and s_j^y [133].

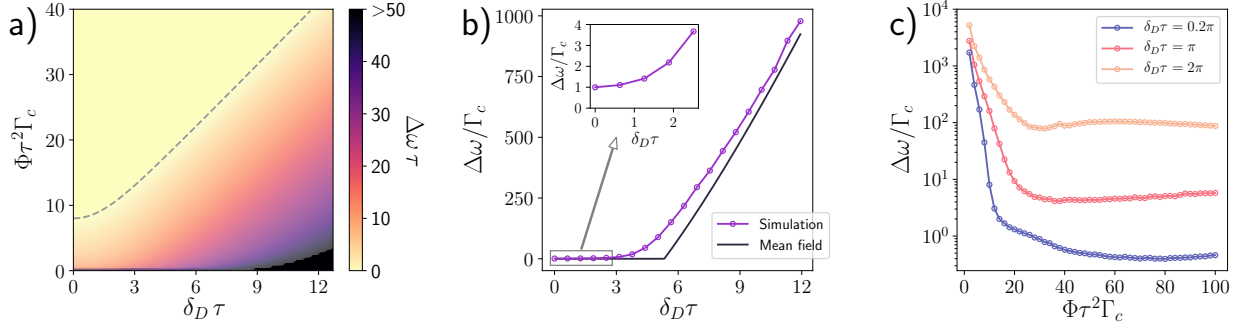


Figure 5.2: (a) Mean-field calculations of the linewidth in units of the transit time broadening $1/\tau$, as a function of the Doppler width $\delta_D\tau$ and $\Phi\tau^2\Gamma_c$. Here $\Phi\tau^2\Gamma_c$ is the number of collective lifetimes that elapse during the transit time τ . The black dashed line is the phase transition threshold for steady-state superradiance, above which mean-field calculations predict a zero linewidth. (b) The linewidth in units of Γ_c as a function of the Doppler width for $\Phi\tau^2\Gamma_c = 20$. The markers are simulation results using Eqs. (5.1)–(5.3) with $\Phi = 1000/\tau$ and $\Gamma_c = 0.02/\tau$. For every data point, we calculated 100 trajectories each with a simulation time of $T = 2000\tau$. This numerical simulation is compared with the mean-field theory, which is analytic. Inset: Below the phase transition, simulations show an ultranarrow linewidth of order Γ_c , which is 50 times smaller than transit time broadening for these simulation parameters. (c) Simulation results of the linewidth in units of Γ_c as a function of $\Phi\tau^2\Gamma_c$. For every data point, we calculated 100 trajectories each with a simulation time of $T = 200\tau$ and $\Phi = 500/\tau$.

5.3 Results

Typically, resonance widths in hot gases of atoms are dominated by Doppler and transit time broadening. Although our system is based on a hot gas, these broadening mechanisms vanish when the collective linewidth $N\Gamma_c$ is much greater than δ_D and $1/\tau$. The collective linewidth $N\Gamma_c$ is the rate for an atom to spontaneously emit into the cavity in the presence of other atoms. The principal features of this model can be obtained by dropping the noise terms in Eqs. (5.1)–(5.3), corresponding to a mean-field solution that is simple enough to be solved analytically and allows us to classify different phases of emission. The form of the solution for the laser linewidth $\Delta\omega$ is determined by two independent parameters, the first being δ_D and the second being $\Phi\tau^2\Gamma_c = \tau/(N\Gamma_c)^{-1}$, which is the number of collective lifetimes that elapse during τ . In general, we observe a phase transition from broad linewidth emission to superradiant emission with an ultranarrow linewidth [Fig. 5.2(a)]. Specifically, for large $\delta_D\tau$, the transition threshold is governed by the Doppler width, whereas for small $\delta_D\tau$, transit time broadening determines the regime of superradiant emission. The latter is evident because there is no superradiant emission for $\Phi\tau^2\Gamma_c < 8$ even in the absence of Doppler broadening ($\delta_D\tau \ll 1$). This is because unsynchronized atoms are introduced to the cavity so rapidly that the collective dipole does not establish.

The mean-field analysis predicts an unphysical zero linewidth in the superradiant regime because it neglects quantum noise. In reality, vacuum fluctuations entering the cavity and quantum fluctuations in the atomic dipole components cause phase diffusion, resulting in a nonvanishing linewidth. To determine this linewidth we simulate Eqs. (5.1)–(5.3) with noise terms included for $\Phi\tau^2\Gamma_c = 20$. The mean-field theory and c -number simulations agree outside the superradiant regime, whereas inside the superradiant regime only the c -number simulations predict a nonvanishing linewidth. Here the minimum achievable linewidth is Γ_c [Fig. 5.2(b) inset], which is much smaller than $1/\tau$, implying that our system is robust against single-atom transit time broadening.

²The conditions for neglecting free space spontaneous emission are that $N\Gamma_c \gg \gamma$ and $\gamma\tau \ll 1$. We simulated this system with free space spontaneous emission and confirmed that our model (which neglects this effect) reproduces the correct minimum $\Delta\omega$, maximum P , and minimum \wp .

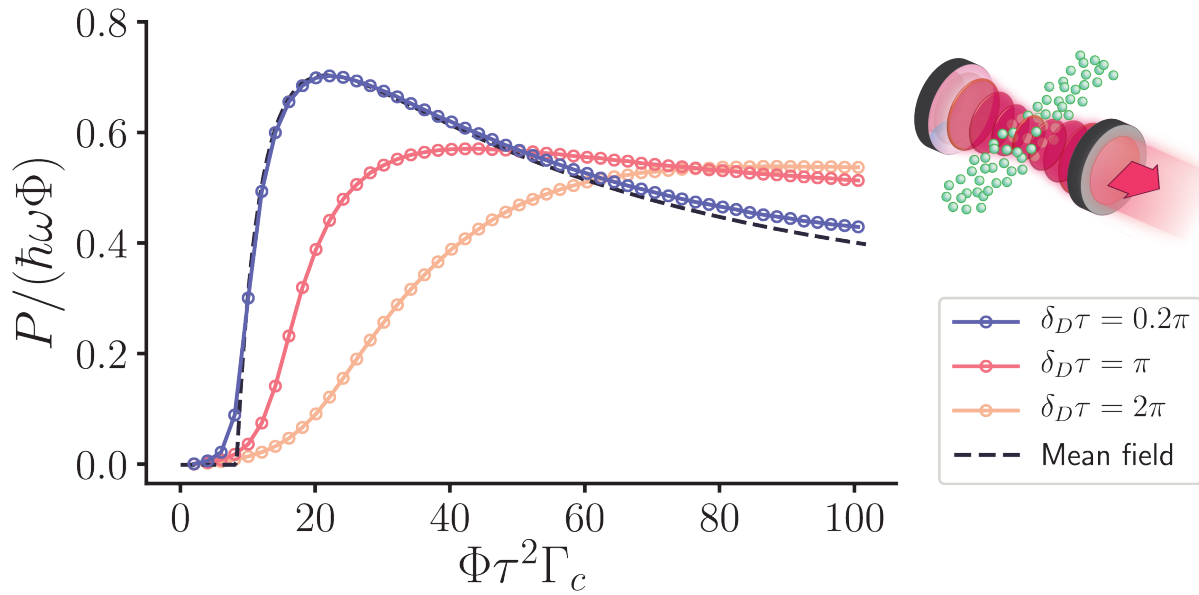


Figure 5.3: The output power of the superradiant beam laser. The markers are c -number simulation results. For every data point, we calculated 100 trajectories each with a simulation time of $T = 200\tau$ and $\Phi = 500/\tau$. For $\delta_D\tau = 0.2\pi$, both the mean-field and simulation results peak at $\Phi\tau^2\Gamma_c \approx 20$ with $P = 0.7\hbar\omega\Phi$.

In other words, the collective atomic dipole stores the optical phase for much longer than the time any individual atom spends in the cavity.

To see how the minimum linewidth in the superradiant phase varies with δ_D , we run simulations with three Doppler widths [Fig. 5.2(c)]. For $\delta_D\tau = \pi$, the linewidth can be brought down to several Γ_c , and for $\delta_D\tau = 0.2\pi$, the linewidth is Γ_c . These numbers elucidate that narrow-linewidth superradiant emission occurs when the atoms are flying through the cavity so quickly that they move less than $\lambda/2$ along the cavity axis during τ .

To understand the scale of these quantities, we evaluate numerical values for the $^3P_1 \rightarrow ^1S_0$, $\gamma = 2\pi \times 400$ Hz transition in ^{40}Ca . We take the velocity in the x direction to be that of Ca atoms from an effusion cell operating at $\sim 800^\circ\text{C}$. We also consider the case where $\Phi \sim 10^{14}$ atoms/s and the atomic beam is laser cooled in the transverse direction to $\Delta v_z \simeq 0.41$ m/s, corresponding to the $\delta_D\tau = \pi$ curve in Fig. 5.2(c). Considering a simple cavity with straightforward dimensions (a finesse of 20, a cavity length of 3 cm, and beam waist $w = 300 \mu\text{m}$), we calculated a minimum linewidth of order 10 mHz, competitive with the best stable lasers to date [105]. A similar analysis based on the ^{88}Sr intercombination transition yields a minimum linewidth of order 100 mHz. The detailed design parameters can be found in Sec. 5.4. Therefore, ultracoherent light can be extracted from a hot atomic beam with a significant Doppler width, which implies that ultracold atoms may not be required to achieve narrow linewidth superradiant laser emission.

We now turn our attention to the laser output power P . While individual atoms would rarely emit into the cavity mode during their passage, the emission rate is greatly enhanced by collective effects. This enhanced rate leads to a N^2 power scaling [101, 100],³ which is a principal feature of superradiant emission. Determining P from both the mean-field and c -number simulation approaches, we find good agreement between the two when $\delta_D\tau$ is comparable to (or below) 0.2π (Fig. 5.3). For Doppler widths in this regime and for $\Phi\tau^2\Gamma_c = 2\pi^2 \approx 20$, P achieves its maximum value of $0.7\hbar\omega\Phi$, where ω is the center frequency of the output field. Physically this corresponds to each atom emitting an average of 0.7 photons into the cavity mode. Furthermore, we find that the

³This N^2 enhancement is analyzed in detail in Chap. 6.

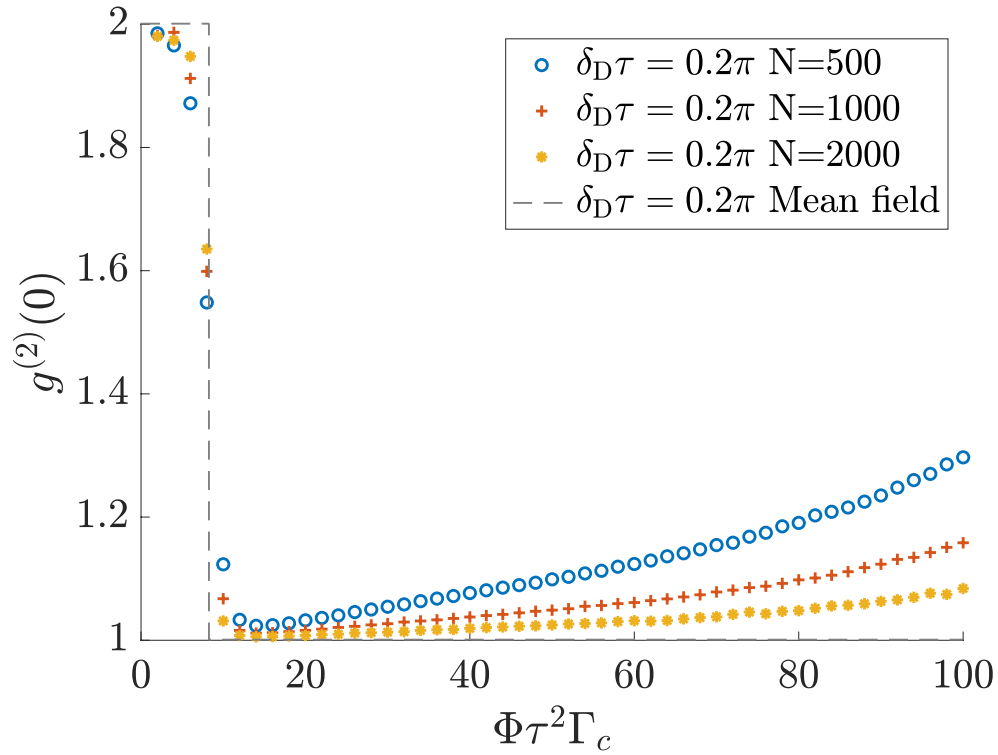


Figure 5.4: Simulation results of the second-order time correlation function $g^{(2)}(0)$ compared to the mean-field prediction. For each data point, we calculated 100 trajectories each with a simulation time of $T = 200$ with $\Phi = 500$, $\tau = 1$, and $\delta_D\tau = 0.2\pi$.

emitted light is second-order coherent by calculating $g^{(2)}(0) \approx 1$ (see Fig. 5.4). Together, Fig. 5.2(c) and Fig. 5.3 show that the maximum power and a linewidth of order Γ_c can be simultaneously achieved when $\Phi\tau^2\Gamma_c \approx 20$ and $\delta_D\tau \lesssim 0.2\pi$.

For the ^{40}Ca example mentioned above, we find that $P \approx 0.1$ mW at a linewidth of 40 mHz. For ^{88}Sr , $P = 2.5$ μW at a linewidth of 150 mHz. Significantly, these powers should be sufficient for use with standard laser technology. In contrast the previously considered cold atom version of the superradiant laser has orders of magnitude weaker power, restricting its use to specialized equipment [101]. The power P is greater in the superradiant beam laser because it has the potential for a much larger intracavity atom number than cold atom systems, where particle numbers have been limited by intrinsic inefficiencies in ultracold gas preparation techniques.

In addition to its relatively large output power and insensitivity to Doppler and transit time broadening, this design is robust against environmental noise. This noise causes cavity length fluctuations, which manifest as cavity resonance frequency noise that dominates the linewidths of cavity-stabilized narrow-linewidth lasers [97]. For these lasers, the frequency noise on the laser output field is equal to the environmental noise in the cavity resonance frequency. However, in a superradiant laser, phase information is stored primarily in the atomic medium, which makes the phase rigid against cavity resonance fluctuations; therefore, these fluctuations are written onto the laser output frequency with a strong suppression factor. This factor is the cavity pulling coefficient [12], defined as $\wp = (\omega - \omega_a)/(\omega_c - \omega_a)$, which is the fractional change in the laser frequency when the cavity resonance fluctuates with respect to the atomic transition. Using mean-field theory, we analytically find that $\wp \propto 1/(\kappa\tau)$, which is the ratio of the cavity photon lifetime to the atom transit time. A value of $\kappa\tau = 1000$ can be achieved with standard optics, resulting in $\wp \approx 0.004$ for $\Phi\tau^2\Gamma_c = 20$ (see Fig. 5.5).

This small \wp makes our design robust against environmental noise sources that limit linewidths of cavity-stabilized lasers. The most common examples are vibration noise [40], thermal Brownian noise [97], and slow drift in the cavity length. The response of cavity resonance frequency to vibration noise is characterized by the acceleration sensitivity K . For the superradiant beam

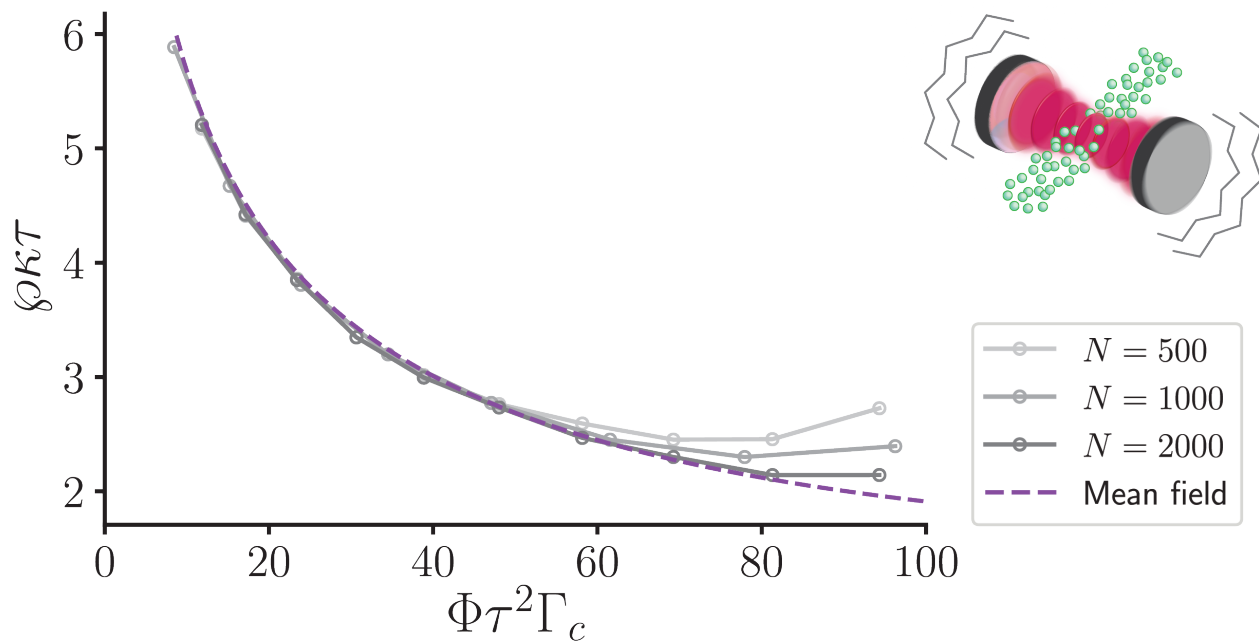


Figure 5.5: The cavity pulling coefficient φ at $\delta_D \tau = 0.2\pi$. A small cavity pulling makes the laser frequency insensitive to environmental noise, such as vibrations. The markers are c -number simulation results with $\kappa = 1000/\tau$ and $\omega_c - \omega_a = 100/\tau$. For every data point, we calculated 100 trajectories each with a simulation time of $T = 100\tau$. As N increases, the simulation results approach the mean-field calculation.

laser, the laser output frequency has an effective acceleration sensitivity φK . If our design uses a simple V-block cavity with no regard for the vibration isolation found in cutting-edge stable lasers, it would have an acceleration sensitivity of $\varphi K \sim 10^{-13}/(\text{m/s}^2)$. Meanwhile, the acceleration sensitivity of the best cavity-stabilized laser to date is of the same order, i.e., $K \sim 10^{-13}/(\text{m/s}^2)$ [126].

Thermal Brownian noise causes cavity resonance fluctuations that scale as $1/L$, where L is the cavity length. To suppress this effect, stabilization cavities have been made as long as half a meter [61]. For the superradiant beam laser, the amplitude of thermal noise behaves according to the effective cavity length L/φ . This means that the output frequency of a beam laser based on a compact $L = 3$ cm cavity has the thermal noise of a 7.5 m cavity. Furthermore, slow thermal drift is a practical challenge for cavity-stabilized lasers. The superradiant beam laser has an effective coefficient of thermal expansion (CTE) of $\varphi\alpha$, where α is the CTE of the bare cavity. This means that a beam laser based on Invar (an inexpensive and easy-to-machine material) with modest temperature control would have a drift rate similar to that of an ultrastable cavity based on highly temperature-stabilized ultralow expansion glass.

5.4 Sample design constraints

In this section, we give two examples of sample experimental parameters that are consistent with the production of ultranarrow linewidth laser light within our presented theoretical framework. We have chosen as our examples the $2\pi \times 400$ Hz transition line of ^{40}Ca and the $2\pi \times 7.5$ kHz transition line of ^{88}Sr , respectively. In order to emphasize the potential simplicity, we consider here the most direct implementation, i.e., a hot atomic beam, a single mode cavity, and a simplified model of the atom delivery system where transverse collimation or transverse laser cooling is implemented but no longitudinal cooling is assumed. On the other hand, we recognize that in a real device, transverse cooling, velocity selective techniques, or alternative beam delivery approaches, might be employed in order to more easily satisfy the Doppler constraint and enhance the effective atomic beam flux through cavity mode. In the case of a more sophisticated design choice, the parameters may be considerably more favorable than the numbers we give here for a simple configuration.

However, the constraints $\Phi\tau^2\Gamma_c > 8$ and $\delta_D\tau = k\Delta v_z\tau < \pi$ must always be satisfied in order to realize CW superradiant emission with linewidth in the ultranarrow regime, which is a principal point of our proposal.

5.4.1 First example: $2\pi \times 400$ Hz line of ^{40}Ca

Transition Rate	γ	$2\pi \times (400 \text{ Hz})$
Effective Beam Rate	Φ	$6.1 \times 10^{14}/\text{s}$
Transit Time	$\tau = \frac{2w}{v_L}$	$0.81 \mu\text{s}$
Intracavity Atom Number	$N = \Phi\tau$	4.9×10^8
Transverse Velocity Threshold	$\Delta v = \frac{\lambda}{2\tau}$	41 cm/s
Minimum Linewidth	$\Gamma_c = \gamma\mathcal{C}$	$2\pi \times (8 \text{ mHz})$
Peak Power	$P_{max} \approx 0.7\Phi\hbar\omega$	0.1 mW
Cavity Pulling	\wp	0.004

Table 5.1: Sample model parameters for the superradiant beam laser utilizing the $2\pi \times 400$ Hz transition line of ^{40}Ca .

For the Ca case (see Table 5.1), we consider a hot oven operating at temperature $842 \text{ }^\circ\text{C}$, which gives an out-of-oven beam rate $\Phi_0 \sim 10^{19}/\text{s}$. As the atomic beam propagates from the oven to the cavity, we assume that no longitudinal cooling is used, so the mean longitudinal velocity is well approximated by the mean Maxwellian velocity as $v_L = 765.9 \text{ m/s}$. In the transverse direction, laser cooling or velocity selection is needed to restrict the transverse Doppler width to below $\delta_D = 2\pi \times 0.6 \text{ MHz}$ ($\Delta v_z = 0.41 \text{ m/s}$), in order to operate below the critical Doppler threshold discussed in the main text. Prior to the atomic beam entering the cavity, the atoms must be optically pumped into the excited electronic state. We estimate that for this situation, the effective beam rate entering the cavity should be of order $\Phi = 6.1 \times 10^{14}/\text{s}$. We choose cavity parameters by considering a lossy cavity of length $L = 3.3 \text{ cm}$, beam waist $w = 0.31 \text{ mm}$, and finesse $F = 22.8$, which corresponds to a cavity decay $\kappa = 2\pi \times (197 \text{ MHz})$ and cavity cooperativity $\mathcal{C} = 2 \times 10^{-5}$. Given these parameters, our calculation predicts an output field of power 0.1 mW and linewidth of the order 10 mHz . Meanwhile, $\kappa\tau \approx 1000$ gives a cavity pulling \wp as small as 0.004 as shown in Fig. 4 of the main text.

5.4.2 Second example: $2\pi \times 7.5$ kHz line of ^{88}Sr

Transition Rate	γ	$2\pi \times (7.5 \text{ kHz})$
Effective Beam Rate	Φ	$1.2 \times 10^{13}/\text{s}$
Transit Time	τ	$1.3 \mu\text{s}$
Intracavity Atom Number	N	1.6×10^7
Transverse Velocity Threshold	Δv	26 cm/s
Minimum Linewidth	Γ_c	$2\pi \times (150 \text{ mHz})$
Peak Power	P_{max}	$2.5 \mu\text{W}$
Cavity Pulling	\wp	0.004

Table 5.2: Sample model parameters for the superradiant beam laser utilizing the $2\pi \times 7.5$ kHz transition line of ^{88}Sr .

For the Sr case (see Table 5.2), we consider a similar experimental design to the case for Ca. The oven operating at 650°C gives a $\Phi_0 \sim 10^{18}/\text{s}$ and $v_L = 469.8 \text{ m/s}$. The required Doppler threshold is $\delta_D = 2\pi \times 0.4 \text{ MHz}$ ($\Delta v_z = 0.26 \text{ m/s}$), and the required effective beam rate is $\Phi = 1.2 \times 10^{13}/\text{s}$. Considering a cavity of length $L = 6.0 \text{ cm}$, beam waist $w = 0.31 \text{ mm}$, and finesse $F = 20.8$, which corresponds to $\kappa = 2\pi \times (121 \text{ MHz})$ and cavity cooperativity $\mathcal{C} = 2 \times 10^{-5}$, we calculate an output field of power $2.5 \mu\text{W}$ and linewidth of the order 150 mHz . Since $\kappa\tau \approx 1000$, we predict a cavity pulling coefficient of $\wp \approx 0.004$.

5.5 Conclusion

Superradiant lasers based on cold atoms have achieved impressive results, but parasitic heating from atomic repumping has so far limited these systems to pulsed operation [115]. The beam laser design avoids the heating problem since pumping is performed outside the cavity (Fig. 5.1). Therefore, the beam laser configuration may be a more promising approach for realizing a CW superradiant laser. Furthermore, our design could conceivably be made simpler and less fragile than cold-atom or cavity-stabilized systems. For this reason, the superradiant beam laser may be well suited to operate in accelerating frames, making this design potentially useful for space technology, inertial sensors, geodesy, field-based magnetometry, and astrophysical measurements. We hope that our design will make ultracoherent lasers, which are currently limited to a handful

of specialized labs, ubiquitous in quantum science.

Chapter 6

Superradiant Emission of a Thermal Atomic Beam into an Optical Cavity ¹

6.1 Introduction

In this chapter we study in detail the effect of Doppler broadening on collective emission when atoms traverse the optical resonator. We consider this to be the dominant broadening mechanism for metastable atomic dipoles and thermal atomic beams. We derive a general theoretical framework to study the collective emission of the atomic beam that includes a description of the atomic state when the atoms move through the cavity. This is then used to analyze the stability of the non-superradiant (NSR) and superradiant atomic configurations. For the latter, we predict a stable phase of the emitted light whereby phase diffusion is suppressed because of the formation of a large and robust collective dipole. Analyzing a realistic physical example, we show that superradiant emission is possible when the collective linewidth exceeds both the transit-time and Doppler broadening. In this regime we show that superradiant emission can appear in two forms; (i) steady-state superradiance (SSR), where the collective dipole is stable and phase diffusion dominates the dynamics of the collective dipole, and (ii) multi-component superradiance (MCSR), where the amplitude of the collective dipole oscillates in time. In the MCSR phase, we observe long-lived coherent oscillations in which the Doppler broadening itself is responsible for establishing the dynamical phase.

This chapter is organized as follows. In Sec. 6.2 we introduce the model and derive the theoretical description that we will use throughout the chapter. This description is analyzed in Sec. 6.3 using a mean-field treatment. We derive the stability of the mean-field results and use

¹The bulk of this work has been published in Physical Review A [69]. Copyright 2021 American Physical Society.

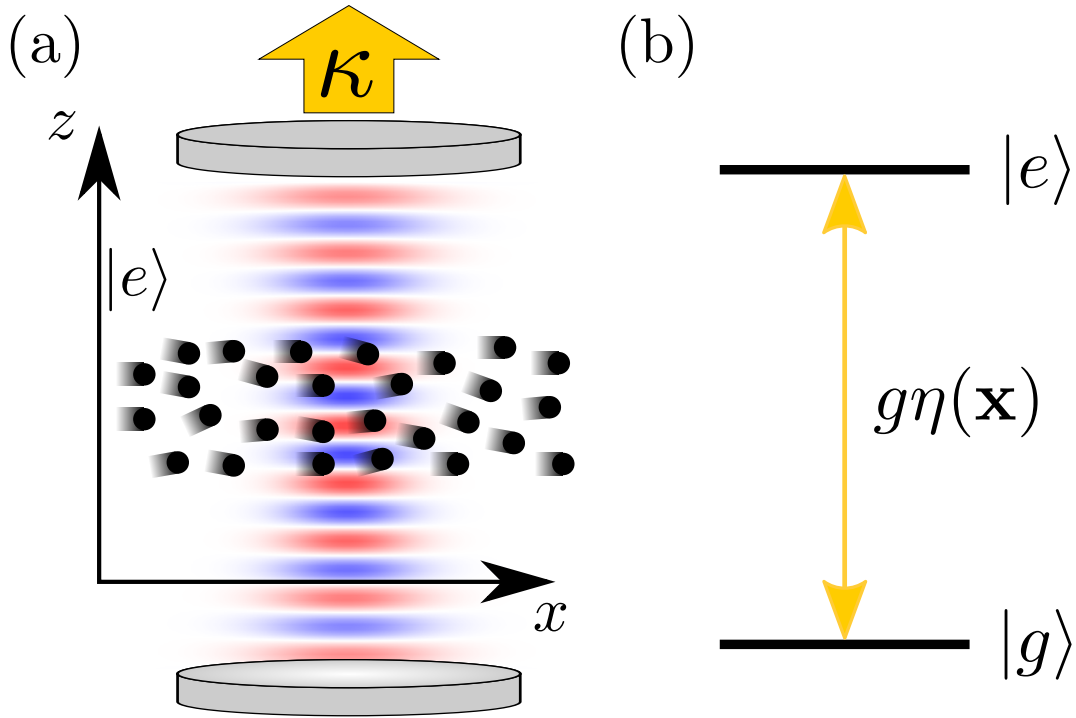


Figure 6.1: Schematic of the system (a) and the atom-cavity coupling (b). We consider a beam of two-level atoms in the excited state $|e\rangle$ traversing an optical cavity of loss rate κ with a given velocity distribution. The x and z axes are chosen perpendicular and parallel to the cavity axis. The atomic beam is much broader than the optical wavelength λ so that the atoms experience different phases of the cavity mode (blue and red denote different signs of the cavity mode function). The excited state $|e\rangle$ of the atomic dipoles (b) couples to the ground state $|g\rangle$ via photon emission into the cavity with coupling $g\eta(\mathbf{x})$. The function $\eta(\mathbf{x})$ is the mode function of the cavity.

them in Sec. 6.4 to give analytical expressions for the linewidth of the emitted light. In Sec. 6.5 we present the analysis of the dipole dynamics of a thermal beam traversing the cavity and compare simulation and analytical results. We conclude our discussion in Sec. 6.6.

6.2 Derivation of the model

In this section we introduce the physical setup of the system and derive a theoretical description for it.

6.2.1 System and master equation

We consider a beam of metastable atomic dipoles with mass m that travel through an optical cavity. Within the cavity the atoms couple to a single resonator mode. We choose x and z axes perpendicular and parallel to the cavity axis respectively [see Fig. 6.1(a)]. We describe the evolution of the atomic dipoles and the cavity field using a master equation for the density matrix $\hat{\rho}$, including internal and external degrees of freedom of the atoms and the cavity variables. The time evolution of $\hat{\rho}$ is given by

$$\frac{d\hat{\rho}}{dt} = \frac{1}{i\hbar} [\hat{H}, \hat{\rho}] + \kappa \mathcal{L}[\hat{a}]\hat{\rho}, \quad (6.1)$$

where $\mathcal{L}[\hat{O}]\hat{\rho} = (2\hat{O}\hat{\rho}\hat{O}^\dagger - \hat{O}^\dagger\hat{O}\hat{\rho} - \hat{\rho}\hat{O}^\dagger\hat{O})/2$ is the Lindblad superoperator.

The first term in Eq. (6.1) describes the coherent evolution and is governed by the Hamiltonian

$$\hat{H} = \sum_j \left[\frac{\hat{\mathbf{p}}_j^2}{2m} + \frac{\hbar g}{2} \eta(\hat{\mathbf{x}}_j) \left(\hat{a}^\dagger \hat{\sigma}_j^- + \hat{\sigma}_j^+ \hat{a} \right) \right], \quad (6.2)$$

which is presented in the frame rotating with the atomic transition frequency ω_a . We have assumed the resonance condition of zero detuning between the cavity frequency ω_c and ω_a , i.e., $\Delta \equiv \omega_c - \omega_a = 0$. The summation runs over all atoms in the beam. Inside the summation, the first term describes the atomic kinetic energy, and the second term describes the coherent coupling of atom j to the single resonator mode. Here, $\hat{\mathbf{x}}_j = (\hat{x}_j, \hat{y}_j, \hat{z}_j)^\text{T}$ and $\hat{\mathbf{p}}_j = (\hat{p}_{x,j}, \hat{p}_{y,j}, \hat{p}_{z,j})^\text{T}$ are the position and momentum operators that satisfy the commutation relations $[\hat{\alpha}_j, \hat{p}_{\beta,k}] = i\hbar\delta_{jk}\delta_{\alpha\beta}$, with $\alpha, \beta \in$

$\{x, y, z\}$. The function $g\eta(\hat{\mathbf{x}})$ describes the coupling between the cavity and atoms [Fig. 6.1(b)], where g is the vacuum Rabi frequency at the field antinodes and $\eta(\mathbf{x})$ is the spatial mode profile. The operators \hat{a} and \hat{a}^\dagger are the photonic annihilation and creation operators that fulfill the usual bosonic commutation relation $[\hat{a}, \hat{a}^\dagger] = 1$, while $\hat{\sigma}_j^+ = |e\rangle_j \langle g|_j$ and $\hat{\sigma}_j^- = |g\rangle_j \langle e|_j$ are the atomic pseudospin raising and lowering operators, where $|e\rangle_j, |g\rangle_j$ are the electronic excited and ground state of atom j , respectively.

The second term in Eq. (6.1) describes the leakage of cavity photons into the electromagnetic field modes external to the cavity. The rate κ is the cavity decay rate and determines the linewidth of the cavity field mode when the atoms are not present. In the main part of this chapter we will consider the cavity decay channel as the only source of decoherence, while we discuss additional noise sources in Sec. 6.5.5.

6.2.2 Elimination of the cavity field

We describe our system in the superradiant regime where κ exceeds all other atomic relaxation frequencies [17, 100, 92]. In this regime we can adiabatically eliminate the fast cavity variables, which leads to an effective master equation for the atomic degrees of freedom described by the reduced density matrix

$$\hat{\rho}_{\text{atom}} = \text{Tr}_{\text{cav}}(\hat{\rho}), \quad (6.3)$$

where $\text{Tr}_{\text{cav}}(\dots)$ denotes the partial trace over the cavity degrees of freedom. The resulting master equation for $\hat{\rho}_{\text{atom}}$ reads

$$\frac{d\hat{\rho}_{\text{atom}}}{dt} = \frac{1}{i\hbar} \left[\sum_j \frac{\hat{\mathbf{p}}_j^2}{2m}, \hat{\rho}_{\text{atom}} \right] + \Gamma_c \mathcal{L}[\hat{J}^-] \hat{\rho}_{\text{atom}}, \quad (6.4)$$

where the incoherent part is governed by the single-atom linewidth

$$\Gamma_c \equiv \frac{g^2}{\kappa}. \quad (6.5)$$

We have also introduced the generalized collective dipoles

$$\hat{J}^\pm = \sum_j \eta(\hat{\mathbf{x}}_j) \hat{\sigma}_j^\pm. \quad (6.6)$$

For the remainder of the chapter we focus on the dynamics of the atomic degrees of freedom. A useful description is given by the Heisenberg-Langevin equations that are equivalent to the master equation formalism, i.e.,²

$$\frac{d\hat{\sigma}_j^-}{dt} = \frac{\Gamma_c}{2} \eta(\hat{\mathbf{x}}_j) \hat{\sigma}_j^z \hat{J}^- + \hat{S}_j^-, \quad (6.7)$$

$$\frac{d\hat{\sigma}_j^z}{dt} = -\Gamma_c \eta(\hat{\mathbf{x}}_j) \left(\hat{J}^+ \hat{\sigma}_j^- + \hat{\sigma}_j^+ \hat{J}^- \right) + \hat{S}_j^z, \quad (6.8)$$

$$\frac{d\hat{\mathbf{x}}_j}{dt} = \frac{\hat{\mathbf{p}}_j}{m}, \quad (6.9)$$

$$\frac{d\hat{\mathbf{p}}_j}{dt} = \frac{i\hbar\Gamma_c}{2} (\hat{\sigma}_j^+ \hat{J}^- - \hat{J}^+ \hat{\sigma}_j^-) \nabla_{\mathbf{x}} \eta(\mathbf{x})|_{\mathbf{x}=\hat{\mathbf{x}}_j} + \hat{N}_j, \quad (6.10)$$

where the noise terms are given by $\hat{S}_j^- = \eta(\hat{\mathbf{x}}_j) \hat{\sigma}_j^z \hat{F}^-$, $\hat{S}_j^z = -2\eta(\hat{\mathbf{x}}_j) (\hat{F}^+ \hat{\sigma}_j^- + \hat{\sigma}_j^+ \hat{F}^-)$ for internal degrees of freedom and by $\hat{N}_j = i\hbar \nabla_{\mathbf{x}} \eta(\mathbf{x})|_{\mathbf{x}=\hat{\mathbf{x}}_j} (\hat{\sigma}_j^+ \hat{F}^- - \hat{F}^+ \hat{\sigma}_j^-)$ for the external force acting on atom j . The terms \hat{F}^\pm are effective noise terms on the coarse-grained timescale on which this system of equations evolve and satisfy the correlations $\langle \hat{F}^-(t) \hat{F}^-(t') \rangle_q = 0 = \langle \hat{F}^+(t) \hat{F}^-(t') \rangle_q$ and $\langle \hat{F}^-(t) \hat{F}^+(t') \rangle_q = \Gamma_c \delta(t - t')$, $\hat{F}^+ = (\hat{F}^-)^\dagger$. The expectation value $\langle \cdot \rangle_q$ is over the cavity degrees of freedom and the free-space photonic modes external to the cavity.

6.2.3 Parameter regime and c -number approximations

Our theoretical description is used to analyze the dynamics of the atoms that travel ballistically through the cavity. This requires neglecting optomechanical forces in Eq. (6.10) by assuming

$$\frac{d\hat{\mathbf{p}}_j}{dt} = 0 \quad (6.11)$$

for all atoms. We now discuss the validity of this approximation. Optomechanical forces are described in Eq. (6.10). In order to justify the approximation of a ballistic motion, we estimate the mean force $\mathbf{F}_{\text{mean}} \sim \hbar N \Gamma_c \nabla_{\mathbf{x}} \eta(\mathbf{x})$ from Eq. (6.10) and the mean momentum change $\mathbf{F}_{\text{mean}} \tau$, where

²See Chap. 4 for a detailed derivation.

$\tau \equiv 2w/\langle v_x \rangle$ is the transit time. Here w is the cavity waist and $\langle v_x \rangle = \langle p_x \rangle/m$ is the mean atomic velocity in the x direction. The mean momentum change has to be compared with the momentum widths of the initial atomic momentum distribution in the corresponding Cartesian coordinates. Along the z axis, assuming a standing wave potential with wavenumber $k = 2\pi/\lambda$, optomechanical forces are negligible if $\hbar k N \Gamma_c \tau \ll \Delta p_z$, where Δp_z is the momentum width in z direction. For $N \Gamma_c \tau \gtrsim 1$ this requires a momentum width that is much larger than the a single photon recoil $\hbar k$. Vertical to the cavity axis, the mean force can be roughly approximated by $\hbar w^{-1} N \Gamma_c$. The condition reads as then $\hbar w^{-1} N \Gamma_c \tau \ll \Delta p_y$ and $\hbar w^{-1} N \Gamma_c \tau \ll \langle p_x \rangle$. Therefore, we conclude that optomechanical forces are negligible as long as the temperature of the incoming atoms is sufficiently high. Moreover, we will mostly work in the regime where atoms collectively emit into the cavity mode. This is possible if the transit time τ of an individual atom is of the same order of magnitude as the characteristic timescale of superradiant emission $1/(N \Gamma_c)$, where N is the mean intracavity atom number.

In order to simulate the Heisenberg-Langevin equations in Eqs. (6.7)–(6.10), we make a semiclassical approximation where we exchange the quantum operators by c -numbers and use noise terms that simulate quantum noise as introduced in Chap. 4 [133, 92, 70]. This semiclassical description can be derived by first writing down the Heisenberg-Langevin equations for the dipole components $\hat{\sigma}_j^x = \hat{\sigma}_j^- + \hat{\sigma}_j^+$, $\hat{\sigma}_j^y = i(\hat{\sigma}_j^- - \hat{\sigma}_j^+)$, $\hat{\sigma}_j^z$ and then exchanging them with their corresponding c -number equivalents s_j^x , s_j^y , and s_j^z . The same approach is repeated with the external operators $\hat{\mathbf{x}}_j$ and $\hat{\mathbf{p}}_j$ that are replaced by their corresponding classical counterparts \mathbf{x}_j and \mathbf{p}_j . With this procedure we obtain the following c -number stochastic differential equations

$$\frac{ds_j^x}{dt} = \frac{\Gamma_c}{2} \eta(\mathbf{x}_j) s_j^z J^x + \mathcal{S}_j^x, \quad (6.12)$$

$$\frac{ds_j^y}{dt} = \frac{\Gamma_c}{2} \eta(\mathbf{x}_j) s_j^z J^y + \mathcal{S}_j^y, \quad (6.13)$$

$$\frac{ds_j^z}{dt} = -\frac{\Gamma_c}{2} \eta(\mathbf{x}_j) \left(J^x s_j^x + J^y s_j^y \right) + \mathcal{S}_j^z, \quad (6.14)$$

$$\frac{d\mathbf{x}_j}{dt} = \frac{\mathbf{p}_j}{m}, \quad (6.15)$$

where

$$J^\alpha = \sum_j \eta(\mathbf{x}_j) s_j^\alpha, \quad \alpha \in \{x, y\}. \quad (6.16)$$

are the c -number collective dipole components. We have neglected single-atom terms in Eqs. (6.12)–(6.15) that scale with Γ_c compared to the collective terms that scale with $N\Gamma_c$. The noise terms are defined by $\mathcal{S}_j^\alpha = \eta(\mathbf{x}_j) s_j^\alpha \mathcal{F}^\alpha$, $\alpha \in \{x, y\}$ and $\mathcal{S}_j^z = -\eta(\mathbf{x}_j)(s_j^x \mathcal{F}^x + s_j^y \mathcal{F}^y)$. The independent random noise terms \mathcal{F}^x and \mathcal{F}^y fulfill $\langle \mathcal{F}^x(t) \mathcal{F}^x(t') \rangle = \Gamma_c \delta(t - t') = \langle \mathcal{F}^y(t) \mathcal{F}^y(t') \rangle$. These equations have been derived using the symmetric orderings of the operators and replacing these by their classical c -number counterparts [92].

Beside the noise that is induced by \mathcal{F}^x and \mathcal{F}^y we also need to include another noise source that arises from introducing new atoms into the cavity. We assume throughout this chapter that the atoms enter in the excited state $|e\rangle$. In that case an atom indexed by j enters the cavity with $s_j^z = 1$. Since the atom is in $|e\rangle$, the quantum uncertainty in s_j^x and s_j^y is maximal. This is modeled by randomly and independently initializing $s_j^x = \pm 1$ and $s_j^y = \pm 1$ [133]. With this methodology we fulfill up to second order the correct initial spin-moments for the entering atoms, i.e., $\langle s_j^\alpha \rangle = \langle \hat{\sigma}_j^\alpha \rangle$, $\langle s_j^\alpha s_k^\alpha \rangle = \langle \hat{\sigma}_j^\alpha \hat{\sigma}_k^\alpha \rangle = \delta_{jk}$, $\alpha \in \{x, y\}$, and $\langle s_j^x s_k^y \rangle = \langle \{\hat{\sigma}_j^x \hat{\sigma}_k^y\}_{\text{sym}} \rangle = 0$, where δ_{jk} is Kronecker-delta and $\{\hat{\sigma}_j^x \hat{\sigma}_k^y\}_{\text{sym}} \equiv (\hat{\sigma}_j^x \hat{\sigma}_k^y + \hat{\sigma}_k^y \hat{\sigma}_j^x) / 2$ is the symmetric ordering of operators $\hat{\sigma}_j^x$ and $\hat{\sigma}_k^y$.

In the next subsection we will apply Eqs. (6.12)–(6.15) with the noise terms introduced above to derive a phase-space density description of the atomic dipoles.

6.2.4 Phase-space density description

The phase-space density description of our model is derived by defining the classical phase-space density and the spin densities of the atomic beam as

$$f(\mathbf{x}, \mathbf{p}, t) = \sum_j \delta(\mathbf{x} - \mathbf{x}_j) \delta(\mathbf{p} - \mathbf{p}_j), \quad (6.17)$$

$$s^\alpha(\mathbf{x}, \mathbf{p}, t) = \sum_j s_j^\alpha \delta(\mathbf{x} - \mathbf{x}_j) \delta(\mathbf{p} - \mathbf{p}_j), \quad (6.18)$$

where s_j^α is the single-atom spin component with $\alpha \in \{x, y, z\}$. The collective dipole components defined in Eq. (6.16) are given by

$$J^\alpha = \int d\mathbf{x} \int d\mathbf{p} \eta(\mathbf{x}) s^\alpha(\mathbf{x}, \mathbf{p}, t), \quad \alpha \in \{x, y\}, \quad (6.19)$$

and Eqs. (6.12)–(6.15) can be rewritten with density variables as

$$\frac{\partial f}{\partial t} + \frac{\mathbf{p}}{m} \cdot \nabla_{\mathbf{x}} f = 0, \quad (6.20)$$

$$\frac{\partial s^x}{\partial t} + \frac{\mathbf{p}}{m} \cdot \nabla_{\mathbf{x}} s^x = \frac{\Gamma_c}{2} \eta(\mathbf{x}) s^z J^x + \mathcal{S}^x, \quad (6.21)$$

$$\frac{\partial s^y}{\partial t} + \frac{\mathbf{p}}{m} \cdot \nabla_{\mathbf{x}} s^y = \frac{\Gamma_c}{2} \eta(\mathbf{x}) s^z J^y + \mathcal{S}^y, \quad (6.22)$$

$$\frac{\partial s^z}{\partial t} + \frac{\mathbf{p}}{m} \cdot \nabla_{\mathbf{x}} s^z = -\frac{\Gamma_c}{2} \eta(\mathbf{x}) (J^x s^x + J^y s^y) + \mathcal{S}^z. \quad (6.23)$$

Here, Eq. (6.20) describes the free flight of the atomic beam. The noise terms are given by $\mathcal{S}^\alpha = \eta(\mathbf{x}) \mathcal{F}^\alpha s^z$, with $\alpha \in \{x, y, z\}$, and $\mathcal{S}^z = -\eta(\mathbf{x}) (\mathcal{F}^x s^x + \mathcal{F}^y s^y)$. We emphasize that these noise terms are still local in time but long range in space.

The initial conditions for the atoms entering the cavity can be formulated as noisy spatial boundary conditions for the stochastic partial differential equations (6.20)–(6.23). In order to formulate these boundary conditions, we define $x = -x_0$ as the position on the x axis where the atoms enter the cavity. Notice that the exact choice of x_0 depends on the choice of the mode function $\eta(\mathbf{x})$ and can in principle be $x_0 = \infty$. We assign

$$f(-x_0, y, z, \mathbf{p}, t) = f_0(y, z, \mathbf{p}, t), \quad (6.24)$$

$$s^x(-x_0, y, z, \mathbf{p}, t) = W^x(y, z, \mathbf{p}, t), \quad (6.25)$$

$$s^y(-x_0, y, z, \mathbf{p}, t) = W^y(y, z, \mathbf{p}, t), \quad (6.26)$$

$$s^z(-x_0, y, z, \mathbf{p}, t) = f_0(y, z, \mathbf{p}, t) \quad (6.27)$$

as the initial conditions for the system at every instant of time t . Here, we have used

$$f_0(y, z, \mathbf{p}, t) = \sum_j \delta(\mathbf{x}_0 - \mathbf{x}_j) \delta(\mathbf{p} - \mathbf{p}_j), \quad (6.28)$$

and ascribed $\mathbf{x}_0 = (-x_0, y, z)^T$ to be the entrance surface. Since the atoms enter the cavity in $|e\rangle$, the boundary conditions for f and s^z are the same. The initial noise terms in the s^x and s^y components can be described by

$$W^\alpha(y, z, \mathbf{p}, t) = \sum_j s_j^\alpha \delta(\mathbf{x}_0 - \mathbf{x}_j) \delta(\mathbf{p} - \mathbf{p}_j), \quad \alpha \in \{x, y\}. \quad (6.29)$$

These noise terms have the second moments

$$\langle W^\alpha (W^\beta)' \rangle = \frac{m}{p_x} \delta_{\alpha\beta} \delta(t - t') \delta(y - y') \delta(z - z') \times \delta(\mathbf{p} - \mathbf{p}') f_0(y, z, \mathbf{p}, t), \quad (6.30)$$

where we have simplified notation as $W^\alpha = W^\alpha(y, z, \mathbf{p}, t)$ and $(W^\beta)' = W^\beta(y', z', \mathbf{p}', t')$. Notice that such noise processes are both spatially and temporally local.

Throughout this chapter we will assume that the distribution of the atoms is spatially homogeneous. This requires that the diameter of the atomic beam is much larger than λ [see Fig. 6.1(a)] and the cavity waist w . This assumption allows for the formulation of an averaged atomic density $\rho(\mathbf{p})$ using the ensemble average $\langle \cdot \rangle_{\text{ens}}$ of the boundary condition $f_0(y, z, \mathbf{p}, t)$, i.e.,

$$\rho(\mathbf{p}) \equiv \langle f_0(y, z, \mathbf{p}, t) \rangle_{\text{ens}}, \quad (6.31)$$

which is independent of space and time. As a result, after a time t that is much larger than τ , we achieve a stationary state for f that satisfies $\langle f \rangle_{\text{ens}} = \rho(\mathbf{p})$ and describes a spatially homogeneous atomic density in the cavity mode volume. However, this does not imply that the spin densities s^a are spatially homogeneous, which can already be seen in a mean-field description.

6.3 Mean-field analysis

In order to describe the mean-field dynamics of the spin densities, we discard for the moment any noise terms introduced by W^α and \mathcal{F}^α , $\alpha \in \{x, y\}$. The resulting partial differential equations from Eqs. (6.21)–(6.23) read as

$$\frac{\partial s^x}{\partial t} + \frac{\mathbf{p}}{m} \cdot \nabla_{\mathbf{x}} s^x = \frac{\Gamma_c}{2} \eta(\mathbf{x}) J^x s^z, \quad (6.32)$$

$$\frac{\partial s^y}{\partial t} + \frac{\mathbf{p}}{m} \cdot \nabla_{\mathbf{x}} s^y = \frac{\Gamma_c}{2} \eta(\mathbf{x}) J^y s^z, \quad (6.33)$$

$$\frac{\partial s^z}{\partial t} + \frac{\mathbf{p}}{m} \cdot \nabla_{\mathbf{x}} s^z = -\frac{\Gamma_c}{2} \eta(\mathbf{x}) (J^x s^x + J^y s^y). \quad (6.34)$$

In the following two subsections we will distinguish between the case when there is no superradiance $J^x = J^y = 0$ and when there is superradiance $(J^x, J^y) \neq (0, 0)$.

6.3.1 Non-superradiant phase (NSR)

The system is in the non-superradiant phase (NSR) when there is no collective dipole, i.e., $J^x = J^y = 0$. In this phase, the mean-field stationary state is given by

$$s^x = 0, \quad (6.35)$$

$$s^y = 0, \quad (6.36)$$

$$s^z = \rho(\mathbf{p}). \quad (6.37)$$

Here, we only report the density inside of the cavity for $t \gg \tau$.

Although Eqs. (6.35)–(6.37) always represent a stationary solution of the mean-field equations, they are not necessarily stable. Any noise, for instance introduced by W^α and \mathcal{F}^α , could potentially destabilize the stationary state.

In order to determine the stability of the NSR phase, we calculate the evolution of small fluctuations in spin densities by letting $s^x = \delta s^x$ and $s^y = \delta s^y$ and $s^z = \rho(\mathbf{p}) + \delta s^z$. We do not need to specify the source of these small terms explicitly, but note that such fluctuations will be introduced by the noise processes when extending the theory to the full description of the dipole densities.

The equations for δs^x , δs^y , and δs^z are given by

$$\frac{\partial \delta s^x}{\partial t} + \frac{\mathbf{p}}{m} \cdot \nabla_{\mathbf{x}} \delta s^x \approx \frac{\Gamma_c}{2} \eta(\mathbf{x}) \delta J^x \rho(\mathbf{p}), \quad (6.38)$$

$$\frac{\partial \delta s^y}{\partial t} + \frac{\mathbf{p}}{m} \cdot \nabla_{\mathbf{x}} \delta s^y \approx \frac{\Gamma_c}{2} \eta(\mathbf{x}) \delta J^y \rho(\mathbf{p}), \quad (6.39)$$

$$\frac{\partial \delta s^z}{\partial t} + \frac{\mathbf{p}}{m} \cdot \nabla_{\mathbf{x}} \delta s^z \approx 0, \quad (6.40)$$

where we have neglected terms that are second order in the fluctuations. Since Eqs. (6.38) and (6.39) are equivalent, we solve without loss of generality only the equation for δs^x .

Applying the Laplace transform

$$L[g](\nu) = \int_0^\infty dt e^{-\nu t} g(t), \quad (6.41)$$

on Eq. (6.38), we obtain

$$[\nu - \mathcal{L}_0] L[\delta s^x] = \delta s^x(\mathbf{x}, \mathbf{p}, 0) + \frac{\Gamma_c}{2} \eta(\mathbf{x}) \rho(\mathbf{p}) L[\delta J^x], \quad (6.42)$$

where we have used the definition

$$\mathcal{L}_0 g(\mathbf{x}) = -\frac{\mathbf{p}}{m} \cdot \nabla_{\mathbf{x}} g(\mathbf{x}). \quad (6.43)$$

Next we multiply Eq. (6.42) first by the inverse of $[\nu - \mathcal{L}_0]$ and then by $\eta(\mathbf{x})$. After an integration over space and momentum, we obtain a linear equation for $L[\delta J^x]$. This linear equation can be solved to find the result

$$L[\delta J^x] = \frac{\int d\mathbf{x} \int d\mathbf{p} \eta(\mathbf{x}) [\nu - \mathcal{L}_0]^{-1} \delta s^x(\mathbf{x}, \mathbf{p}, 0)}{1 - \frac{\Gamma_c}{2} \int d\mathbf{x} \int d\mathbf{p} \eta(\mathbf{x}) [\nu - \mathcal{L}_0]^{-1} \eta(\mathbf{x}) \rho(\mathbf{p})}. \quad (6.44)$$

The denominator is the dispersion function $D(\nu)$ and takes the form

$$D(\nu) = 1 - \frac{\Gamma_c}{2} \int_0^\infty dt e^{-\nu t} \int d\mathbf{x} \int d\mathbf{p} \eta(\mathbf{x}) e^{\mathcal{L}_0 t} \eta(\mathbf{x}) \rho(\mathbf{p}).$$

Now using the action of the propagator

$$e^{\mathcal{L}_0 t} f(\mathbf{x}) = f\left(\mathbf{x} - \frac{\mathbf{p}}{m} t\right), \quad (6.45)$$

and after performing a change of variables $\mathbf{x} \mapsto \mathbf{x} + \mathbf{p}t/m$, we obtain

$$D(\nu) = 1 - \frac{\Gamma_c}{2} \int_0^\infty dt e^{-\nu t} \int d\mathbf{x} \int d\mathbf{p} \eta\left(\mathbf{x} + \frac{\mathbf{p}}{m} t\right) \eta \rho, \quad (6.46)$$

which is dispersion relation for the NSR phase.

The zeros of the dispersion relation $D(\nu)$ determine the exponents in the time evolution of δJ^x . Assuming that these exponents are negative, the largest exponent (with smallest absolute value) determines the characteristic timescale for a perturbation to relax the spin states again to zero. On the other hand if there exists a zero of the dispersion relation with positive real part, then the NSR phase is unstable. In this case the real part can be seen as the superradiant emission rate.

6.3.2 Steady-state superradiant phase (SSR)

We will now investigate the mean-field properties of the superradiant phase with a stationary collective dipole. We will refer to the phase as steady-state superradiant (SSR) providing the system reaches a stationary state that fulfills $(J^x, J^y) \neq (0, 0)$. Strictly speaking, this is only true in the absence of noise. In the presence of noise, $(J^x, J^y) \neq (0, 0)$ is almost always true. In that case steady-state superradiance can be well-characterized by the length of the vector (J^x, J^y) increasing in proportion to the intracavity atom number N , i.e., $\|(J^x, J^y)\| \propto N$.

6.3.2.1 Analytical solution to the SSR phase

Equations. (6.21)–(6.23) and their mean-field versions Eqs. (6.32)–(6.34) have a U(1) symmetry. This symmetry is given by a rotation with an arbitrary $\varphi \in \mathbb{R}$,

$$\begin{pmatrix} s^x \\ s^y \end{pmatrix} = \begin{pmatrix} \cos \varphi & -\sin \varphi \\ \sin \varphi & \cos \varphi \end{pmatrix} \begin{pmatrix} \tilde{s}^x \\ \tilde{s}^y \end{pmatrix} \quad (6.47)$$

that transforms Eqs. (6.21) and (6.22) to

$$\frac{\partial \tilde{s}^x}{\partial t} + \frac{\mathbf{p}}{m} \cdot \nabla_{\mathbf{x}} \tilde{s}^x = \frac{\Gamma_c}{2} \eta(\mathbf{x}) \tilde{J}^x s^z + \tilde{\mathcal{S}}^x \quad (6.48)$$

$$\frac{\partial \tilde{s}^y}{\partial t} + \frac{\mathbf{p}}{m} \cdot \nabla_{\mathbf{x}} \tilde{s}^y = \frac{\Gamma_c}{2} \eta(\mathbf{x}) \tilde{J}^y s^z + \tilde{\mathcal{S}}^y \quad (6.49)$$

with corresponding noisy initial conditions \tilde{W}^x and \tilde{W}^y . Here, all objects labeled by $(\tilde{\cdot})$ are transformed according to the linear operation in Eq. (6.47). Therefore this SSR phase can be seen as a symmetry-broken phase [30]. We can always rotate the system to a frame where the stationary collective dipole (J^x, J^y) points in x direction (see Fig. 6.2). We denote the new x axis by \parallel and the perpendicular direction by \perp . The resulting equations in the new frame are

$$\frac{\partial s^{\parallel}}{\partial t} + \frac{\mathbf{p}}{m} \cdot \nabla_{\mathbf{x}} s^{\parallel} = \frac{\Gamma_c}{2} \eta(\mathbf{x}) J^{\parallel} s^z + \mathcal{S}^{\parallel}, \quad (6.50)$$

$$\frac{\partial s^{\perp}}{\partial t} + \frac{\mathbf{p}}{m} \cdot \nabla_{\mathbf{x}} s^{\perp} = \frac{\Gamma_c}{2} \eta(\mathbf{x}) J^{\perp} s^z + \mathcal{S}^{\perp}, \quad (6.51)$$

$$\frac{\partial s^z}{\partial t} + \frac{\mathbf{p}}{m} \cdot \nabla_{\mathbf{x}} s^z = -\frac{\Gamma_c}{2} \eta(\mathbf{x}) \left(J^{\parallel} s^{\parallel} + J^{\perp} s^{\perp} \right) + \mathcal{S}^z, \quad (6.52)$$

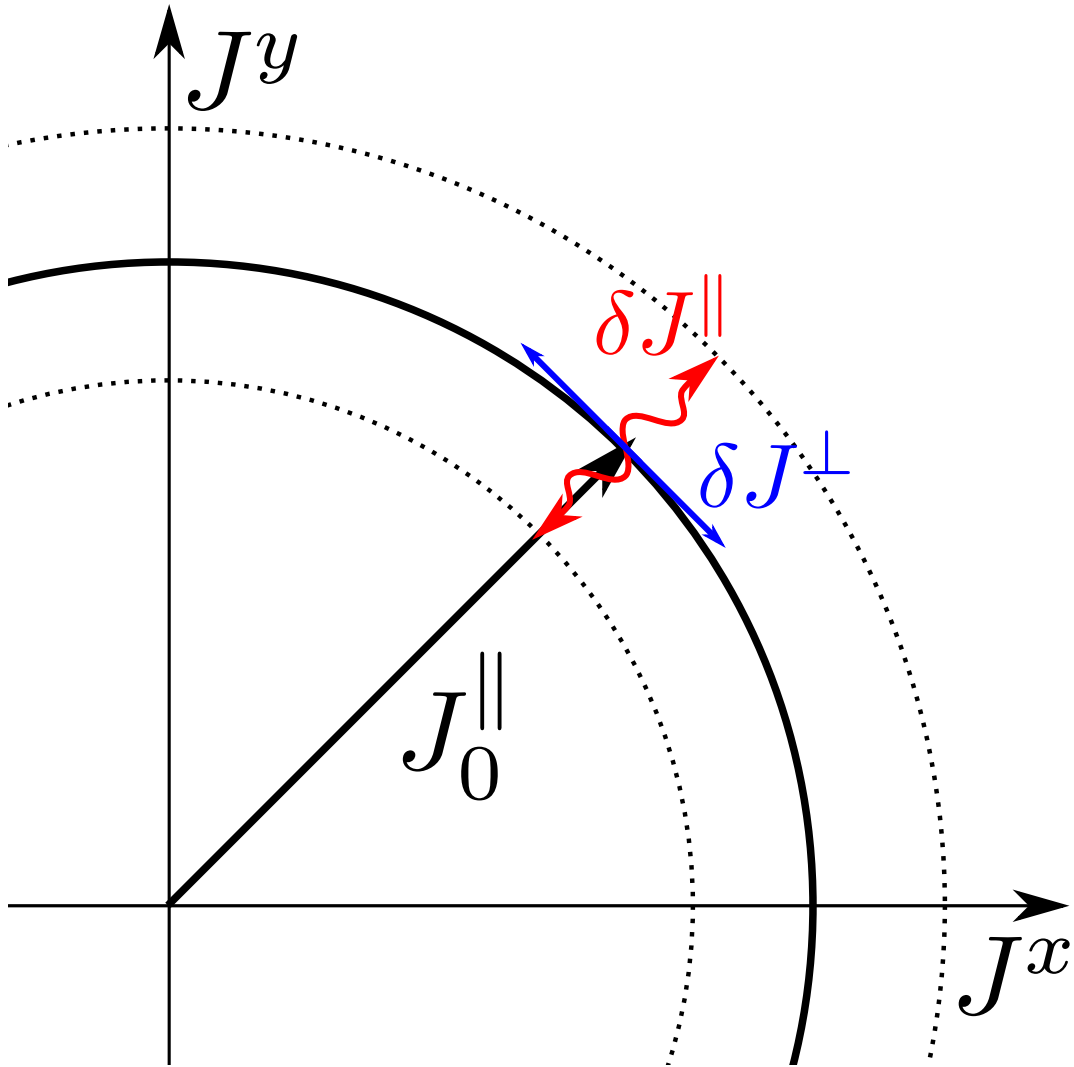


Figure 6.2: Schematic of the stationary collective dipole in the J^x - J^y plane. Its mean length is given by J_0^{\parallel} as defined in Eq. (6.55). The dynamics of its length fluctuations, δJ^{\parallel} , we interpret as a Higgs mode, and the dynamics of its phase fluctuations, δJ^{\perp} , as a Goldstone mode (see Sec. 6.3.2.2).

with corresponding input noise W^{\parallel} and W^{\perp} . Since the collective dipole points in the \parallel direction, the perpendicular direction \perp is solely noisy with zero mean, implying that $J^{\perp} \approx 0$. This leads to the stationary solution for the dipole density $s^{\perp} \approx 0$.

Neglecting all noise sources, we can derive the stationary mean-field densities. The mean-field dipole in the perpendicular direction is just $s_0^{\perp} = 0$. The mean-field densities s_0^{\parallel} and s_0^z are determined by

$$\frac{\mathbf{p}}{m} \cdot \nabla_{\mathbf{x}} s_0^{\parallel} = \frac{\Gamma_c}{2} \eta(\mathbf{x}) J_0^{\parallel} s_0^z, \quad (6.53)$$

$$\frac{\mathbf{p}}{m} \cdot \nabla_{\mathbf{x}} s_0^z = -\frac{\Gamma_c}{2} \eta(\mathbf{x}) J_0^{\parallel} s_0^{\parallel}, \quad (6.54)$$

where

$$J_0^{\parallel} = \int d\mathbf{x} \int d\mathbf{p} \eta(\mathbf{x}) s_0^{\parallel} \quad (6.55)$$

is the stationary length of the collective dipole. Equations (6.53)–(6.54) can be collected into a single equation

$$\frac{\mathbf{p}}{m} \cdot \nabla_{\mathbf{x}} \left[(s_0^{\parallel})^2 + (s_0^z)^2 \right] = 0$$

and therefore solved as

$$s_0^z = \rho(\mathbf{p}) \cos[K(\mathbf{x}, \mathbf{p})], \quad (6.56)$$

$$s_0^{\parallel} = \rho(\mathbf{p}) \sin[K(\mathbf{x}, \mathbf{p})], \quad (6.57)$$

where the argument $K(\mathbf{x}, \mathbf{p})$ is determined by

$$\frac{\mathbf{p}}{m} \cdot \nabla_{\mathbf{x}} K(\mathbf{x}, \mathbf{p}) = \frac{\Gamma_c}{2} \eta(\mathbf{x}) J_0^{\parallel}. \quad (6.58)$$

We will now derive the stability of the SSR phase.

6.3.2.2 Stability of the SSR phase

Similar to our methods in Sec. 6.3.1, we derive the dynamics of small perturbations around the stationary mean-field results by writing the spin densities as $s^{\parallel} = s_0^{\parallel} + \delta s^{\parallel}$, $s^z = s_0^z + \delta s^z$, and

$s^\perp = \delta s^\perp$. The dynamics of the small fluctuations is governed by the following set of linearized equations

$$\frac{\partial \delta s^\parallel}{\partial t} + \frac{\mathbf{p}}{m} \cdot \nabla_{\mathbf{x}} \delta s^\parallel = \frac{\Gamma_c}{2} \eta(\mathbf{x}) \delta J^\parallel s_0^z + \frac{\Gamma_c}{2} \eta(\mathbf{x}) J_0^\parallel \delta s^z, \quad (6.59)$$

$$\frac{\partial \delta s^\perp}{\partial t} + \frac{\mathbf{p}}{m} \cdot \nabla_{\mathbf{x}} \delta s^\perp = \frac{\Gamma_c}{2} \eta(\mathbf{x}) \delta J^\perp s_0^z, \quad (6.60)$$

$$\frac{\partial \delta s^z}{\partial t} + \frac{\mathbf{p}}{m} \cdot \nabla_{\mathbf{x}} \delta s^z = -\frac{\Gamma_c}{2} \eta(\mathbf{x}) \left(\delta J^\parallel s_0^\parallel + J_0^\parallel \delta s^\parallel \right). \quad (6.61)$$

Notice that using Eq. (6.60) the dynamics of δs^\perp is completely decoupled from the dynamics of δs^\parallel and δs^z . We will rely on this fact to treat the dynamics of these equations separately. Specifically, we interpret the dynamics of δJ^\parallel and δJ^\perp as the Higgs and the Goldstone mode respectively (see Fig. 6.2), as we will now elaborate on by examining key aspects of the form of the solutions.

(1) **Higgs mode.**

The time evolution of δs^\parallel together with the coupling to δs^z describes the relaxation dynamics of the amplitude of the collective dipole. This can be interpreted as a Higgs mode [58, 39].

In order to derive the dispersion relation for the Higgs mode, we first define $\delta s^+ = \delta s^\parallel + i \delta s^z$ and $\delta s^- = \delta s^\parallel - i \delta s^z$. We can then use Eqs. (6.59) and (6.61) to derive two decoupled equations

$$\begin{aligned} \frac{\partial \delta s^+}{\partial t} + \frac{\mathbf{p}}{m} \cdot \nabla_{\mathbf{x}} \delta s^+ &= -i \frac{\Gamma_c}{2} \eta J_0^\parallel \delta s^+ + \frac{\Gamma_c}{2} \rho(\mathbf{p}) \eta \delta J^\parallel e^{-iK}, \\ \frac{\partial \delta s^-}{\partial t} + \frac{\mathbf{p}}{m} \cdot \nabla_{\mathbf{x}} \delta s^- &= i \frac{\Gamma_c}{2} \eta J_0^\parallel \delta s^- + \frac{\Gamma_c}{2} \rho(\mathbf{p}) \eta \delta J^\parallel e^{iK}, \end{aligned}$$

where we have used the notations $K = K(\mathbf{x}, \mathbf{p})$, $\rho = \rho(\mathbf{p})$, and $\eta = \eta(\mathbf{x})$. These equations can be solved using the Laplace transform given by Eq. (6.41) and we find

$$[\nu - \mathcal{L}_1] L[\delta s^+] = \delta s^+(\mathbf{x}, \mathbf{p}, 0) + \frac{\Gamma_c}{2} \rho L[\delta J^\parallel] \eta e^{-iK}, \quad (6.62)$$

$$[\nu - \mathcal{L}_2] L[\delta s^-] = \delta s^-(\mathbf{x}, \mathbf{p}, 0) + \frac{\Gamma_c}{2} \rho L[\delta J^\parallel] \eta e^{iK}, \quad (6.63)$$

where we have defined $\delta J^\parallel = \int d\mathbf{x} \int d\mathbf{p} \delta s^\parallel$ and used

$$\mathcal{L}_1 g(\mathbf{x}) = -\frac{\mathbf{p}}{m} \cdot \nabla_{\mathbf{x}} g(\mathbf{x}) - i\frac{\Gamma_c}{2} \eta(\mathbf{x}) J_0^\parallel g(\mathbf{x}), \quad (6.64)$$

$$\mathcal{L}_2 g(\mathbf{x}) = -\frac{\mathbf{p}}{m} \cdot \nabla_{\mathbf{x}} g(\mathbf{x}) + i\frac{\Gamma_c}{2} \eta(\mathbf{x}) J_0^\parallel g(\mathbf{x}). \quad (6.65)$$

We can now solve Eqs. (6.62) and (6.63) formally for $L[\delta s^+]$ and $L[\delta s^-]$. Using $L[\delta s^\parallel] = (L[\delta s^+] + L[\delta s^-])/2$, multiplying this expression by $\eta(\mathbf{x})$, and integrating over the whole phase space, we end up with an expression for $L[\delta J_\parallel]$. Solving that equation for $L[\delta J_\parallel]$ leads to the final expression given by

$$L[\delta J^\parallel] = \frac{A^\parallel(\nu)}{D_\parallel(\nu)}, \quad (6.66)$$

with

$$A^\parallel(\nu) = \frac{1}{2} \int d\mathbf{x} \int d\mathbf{p} \eta(\mathbf{x}) [\nu - \mathcal{L}_1]^{-1} \delta s^+(\mathbf{x}, \mathbf{p}, 0) + \frac{1}{2} \int d\mathbf{x} \int d\mathbf{p} \eta(\mathbf{x}) [\nu - \mathcal{L}_2]^{-1} \delta s^-(\mathbf{x}, \mathbf{p}, 0), \quad (6.67)$$

$$D_\parallel(\nu) = 1 - \frac{\Gamma_c}{4} \int d\mathbf{x} \int d\mathbf{p} \eta(\mathbf{x}) [\nu - \mathcal{L}_1]^{-1} \eta e^{-iK} \rho - \frac{\Gamma_c}{4} \int d\mathbf{x} \int d\mathbf{p} \eta(\mathbf{x}) [\nu - \mathcal{L}_2]^{-1} \eta e^{iK} \rho. \quad (6.68)$$

Using the actual form of the propagators

$$e^{\mathcal{L}_1 t} g(\mathbf{x}) = e^{-i\frac{\Gamma_c}{2} \int_0^t \eta(\mathbf{x} - \frac{\mathbf{p}}{m} \tau) J_0^\parallel d\tau} g\left(\mathbf{x} - \frac{\mathbf{p}}{m} t\right) = e^{i[K(\mathbf{x} - \frac{\mathbf{p}}{m} t, \mathbf{p}) - K(\mathbf{x}, \mathbf{p})]} g\left(\mathbf{x} - \frac{\mathbf{p}}{m} t\right),$$

$$e^{\mathcal{L}_2 t} g(\mathbf{x}) = e^{i\frac{\Gamma_c}{2} \int_0^t \eta(\mathbf{x} - \frac{\mathbf{p}}{m} \tau) J_0^\parallel d\tau} g\left(\mathbf{x} - \frac{\mathbf{p}}{m} t\right) = e^{i[K(\mathbf{x}, \mathbf{p}) - K(\mathbf{x} - \frac{\mathbf{p}}{m} t, \mathbf{p})]} g\left(\mathbf{x} - \frac{\mathbf{p}}{m} t\right),$$

and Eq. (6.56), we obtain the Higgs mode dispersion relation

$$D_\parallel(\nu) = 1 - \frac{\Gamma_c}{2} \int_0^\infty dt e^{-\nu t} \int d\mathbf{x} \int d\mathbf{p} \eta\left(\mathbf{x} - \frac{\mathbf{p}}{m} t\right) \eta s_0^z. \quad (6.69)$$

We emphasize that in the limit of no superradiance, i.e., $s_0^z = \rho$, we obtain the same dispersion relation as we have derived in Eq. (6.46).

If the SSR phase is stable, we need all the zeros of the dispersion relation $D_\parallel(\nu)$ to have negative real parts. These zeros describe the relaxation dynamics of perturbations in the collective dipole's longitudinal direction.

(2) **Goldstone mode.**

The dynamics of δs_\perp is decoupled from the Higgs mode and describes the evolution of fluctuations perpendicular to it. This is related to the dynamics of the phase of the collective dipole (see Fig. 6.2). Because of this observation we refer to this mode as the Goldstone mode [47, 48].

The stability of the Goldstone mode can be calculated by solving Eq. (6.60). Laplace transformation leads to

$$[\nu - \mathcal{L}_0] L[\delta s^\perp] = \delta s^\perp(\mathbf{x}, \mathbf{p}, 0) + \frac{\Gamma_c}{2} L[\delta J^\perp] \eta(\mathbf{x}) s_0^z(\mathbf{x}, \mathbf{p}), \quad (6.70)$$

where we have used the definition of Eq. (6.43). Using the same steps as in Sec. 6.3.1, we find

$$L[\delta J^\perp] = \frac{A^\perp(\nu)}{D_\perp(\nu)}, \quad (6.71)$$

with

$$A^\perp(\nu) = \int d\mathbf{x} \int d\mathbf{p} \eta(\mathbf{x}) [\nu - \mathcal{L}_0]^{-1} \delta s^\perp(\mathbf{x}, \mathbf{p}, 0), \quad (6.72)$$

$$D_\perp(\nu) = 1 - \frac{\Gamma_c}{2} \int d\mathbf{x} \int d\mathbf{p} \eta(\mathbf{x}) [\nu - \mathcal{L}_0]^{-1} \eta s_0^z. \quad (6.73)$$

Using Eq. (6.45) we find the result

$$D_\perp(\nu) = 1 - \frac{\Gamma_c}{2} \int_0^\infty dt e^{-\nu t} \int d\mathbf{x} \int d\mathbf{p} \eta\left(\mathbf{x} + \frac{\mathbf{p}}{m} t\right) \eta s_0^z. \quad (6.74)$$

This dispersion relation, just like the dispersion relation for the Higgs mode, simplifies to Eq. (6.46) in the limit $J_0^\parallel \rightarrow 0$. Let us emphasize that the dispersion relations for the Higgs and the Goldstone look very similar but are only equivalent in the NSR phase. In fact in the superradiant phase one main difference between the Higgs and Goldstone modes is that the latter is always undamped. This can be seen using Eq. (6.53) such that we can transform the dispersion relation (6.74) to

$$D_\perp(\nu) = 1 - \frac{\int_0^\infty dt e^{-\nu t} \int d\mathbf{x} \int d\mathbf{p} \eta\left(\mathbf{x} + \frac{\mathbf{p}}{m} t\right) \frac{\mathbf{p}}{m} \cdot \nabla_{\mathbf{x}} s_0^\parallel}{J_0^\parallel}.$$

For this and the following equations we use the notation $s_0^\parallel = s_0^\parallel(\mathbf{x}, \mathbf{p})$. Applying the Gauß theorem and explicitly using the fact that the atoms enter in $|e\rangle$ and that the mode function vanishes at infinity, we get

$$D_\perp(\nu) = 1 + \frac{\int_0^\infty dt e^{-\nu t} \int d\mathbf{x} \int d\mathbf{p} \frac{d}{dt} \eta \left(\mathbf{x} + \frac{\mathbf{p}}{m} t \right) s_0^\parallel}{J_0^\parallel}.$$

After another partial integration we obtain the Goldstone mode dispersion relation

$$D_\perp(\nu) = \nu \frac{\int_0^\infty e^{-\nu t} dt \int d\mathbf{x} \int d\mathbf{p} \eta \left(\mathbf{x} + \frac{\mathbf{p}}{m} t \right) s_0^\parallel}{J_0^\parallel}. \quad (6.75)$$

where we have used Eq. (6.55).

In order for the SSR phase to be stable we require that every zero of Eq. (6.75) cannot have a positive real part. However, we find that the Goldstone dispersion relation always has a zero $\nu = 0$ in the SSR phase. This shows that there is no damping of the phase as a consequence of the underlying U(1) symmetry. Every noise will lead to a slight and slow change in J_\perp . This dynamics is slow compared to the exponents given by the Higgs dispersion relation that determine the relaxation time to the stable length of the collective dipole. However, the slow change in J_\perp leads to phase diffusion and this determines the linewidth of the emitted light in the SSR phase [82] as we will explain in the next section.

6.4 Analytical estimates for the linewidth

In the ‘bad cavity’ regime, where the cavity linewidth exceeds all other frequencies in the system, the coherence is stored in the collective dipole rather than in the cavity field. Therefore the first-order coherence function, $g_1(t)$, for the cavity field is determined by the dipole-dipole correlations

$$\lim_{t_0 \rightarrow \infty} \langle \hat{a}^\dagger(t+t_0) \hat{a}(t_0) \rangle \propto \lim_{t_0 \rightarrow \infty} \langle \hat{J}^+(t+t_0) \hat{J}^-(t_0) \rangle. \quad (6.76)$$

In our semiclassical description we exchange the quantum operators for their classical noisy counterparts and correspondingly define the g_1 function as

$$g_1(t) = \lim_{t_0 \rightarrow \infty} \langle J^*(t+t_0)J(t_0) \rangle, \quad (6.77)$$

where we have used $J^* = (J^x + iJ^y)/2$ and $J = (J^x - iJ^y)/2$.

6.4.1 Linewidth in the NSR phase

We first study the behavior of the g_1 function in the NSR phase. Here, both dipole components J^x and J^y can be analyzed independently since they are dominated by noise. In this regime we can calculate the g_1 function as

$$g_1(t) \approx \lim_{t_0 \rightarrow \infty} \frac{\langle J^x(t+t_0)J^x(t_0) \rangle + \langle J^y(t+t_0)J^y(t_0) \rangle}{4}. \quad (6.78)$$

Since the noise terms are isotropic, the correlation function for J^x and J^y are the same. Without loss of generality we will focus on the J^x correlation function. For this we define the g_1^x function as

$$g_1^x(t) = \lim_{t_0 \rightarrow \infty} \langle J^x(t+t_0)J^x(t_0) \rangle. \quad (6.79)$$

We now calculate the time dependence of the $g_1^x(t)$ function.

In order to do this we integrate Eq. (6.21) where we assume $s^z = \rho(\mathbf{p})$ and drop second order terms in the noise contribution. This integration is done using the characteristics method. Defining $s^x(t) = s^x[\mathbf{x}_i + \mathbf{p}(t-t_i)/m, t]$, with $\mathbf{x}_i = (-x_i, y_i, z_i)$ the position where the atom enters the cavity and t_i the initial time, we obtain

$$s^x(t) = s^x(t_i) + \int_{t_i}^t dt' \eta[\mathbf{x}(t')] \left[\frac{\Gamma_c}{2} J^x(t') + \mathcal{F}^x(t') \right] \rho,$$

where $\mathbf{x}(t') = \mathbf{x}_i + \mathbf{p}(t' - t_i)/m$. We can now use $t - t_i = m(x + x_i)/p_x$ to express $s^x(t_i) = W^x(y_i, z_i, \mathbf{p}, t_i)$ where $y_i = y - p_y(x + x_i)/p_x$, $z_i = z - p_z(x + x_i)/p_x$, and $t_i = t - m(x + x_i)/p_x$. After a change of variables $t' \mapsto t - t'$ we get

$$s^x(t) = s^x(t_i) + \int_0^\infty dt' \eta[\mathbf{x}(t-t')] \left[\frac{\Gamma_c}{2} J^x(t-t') + \mathcal{F}^x(t-t') \right] \rho,$$

where we extend the integral to infinity because we assume that $\eta(\mathbf{x}) = 0$ for $x < -x_i$. Furthermore $\mathbf{x}(t - t') = \mathbf{x} - \mathbf{p}t'/m$ is independent of t . Multiplying $s^x(t)$ by $\eta(\mathbf{x})$ and integrating over the phase space leads to a linear equation for J^x . This can be solved using the Laplace transformation and we get

$$L[J^x] = \frac{L[J_{W^x}] + 2\frac{1-D(\nu)}{\Gamma_c}L[\mathcal{F}^x]}{D(\nu)}, \quad (6.80)$$

where $D(\nu)$ is the dispersion relation in Eq. (6.46), and

$$J_{W^x}(t) = \int d\mathbf{x} \int d\mathbf{p} \eta(\mathbf{x}) W^x(y_i, z_i, \mathbf{p}, t_i). \quad (6.81)$$

Notice that y_i and z_i depend on \mathbf{x} and \mathbf{p} . The time t_i depends on \mathbf{x} , \mathbf{p} , and t . Since we are in the NSR regime we expect all zeros of $D(\nu)$ to be negative. We denote now by ν_0 the zero with the largest real part. We assume in the following that this is a zero of first order. In the long time limit we can conclude that, defining the inverse of the residue of $1/D(\nu)$ as

$$C_0 = \lim_{\nu \rightarrow \nu_0} \frac{D(\nu)}{\nu - \nu_0}, \quad (6.82)$$

the dipole is given by

$$J^x(t) \approx J_{\text{in}}^x(t) + J_{\text{c}}^x(t), \quad (6.83)$$

where

$$J_{\text{in}}^x(t) = \frac{\int_0^t dt' e^{\nu_0(t-t')} \int d\mathbf{x} \int d\mathbf{p} \eta(\mathbf{x}) W^x(y_i, z_i, \mathbf{p}, t'_i)}{C_0}, \quad (6.84)$$

$$J_{\text{c}}^x(t) = \frac{\int_0^t dt' e^{\nu_0(t-t')} \frac{2}{\Gamma_c} \mathcal{F}^x(t')}{C_0}, \quad (6.85)$$

originate from the noise introduced by the incoming atoms and by the cavity noise, respectively.

Here, $t'_i = t' - m(x + x_i)/p_x$.

Since the cavity noise and the input noise are independent, the g_1^x function is now completely determined by

$$g_1^x(t) = \langle J^x(t + t_0) J^x(t_0) \rangle \approx g_{1,\text{in}}^x(t) + g_{1,\text{c}}^x(t), \quad (6.86)$$

where

$$g_{1,\text{in}}^x(t) = \langle J_{\text{in}}^x(t+t_0) J_{\text{in}}^x(t_0) \rangle, \quad (6.87)$$

$$g_{1,c}^x(t) = \langle J_c^x(t+t_0) J_c^x(t_0) \rangle. \quad (6.88)$$

It is straightforward to calculate the cavity noise that takes the form

$$g_{1,c}^x(t) = \frac{2e^{\nu_0 t}}{\nu_0 \Gamma_c C_0^2}. \quad (6.89)$$

For the calculations of the contribution of the incoming atoms we use the noise correlations that are defined in Eq. (7.28). The input noise term takes the form

$$g_{1,\text{in}}^x(t) = \frac{\int_0^{t+t_0} dt' \int_0^{t_0} dt'' e^{\nu_0(t+2t_0-t'-t'')} \chi(t'-t'')}{C_0^2}, \quad (6.90)$$

where

$$\chi(t'-t'') = \int d\mathbf{x} \int d\mathbf{p} \rho(\mathbf{p}) \eta \left[\mathbf{x} + \frac{\mathbf{p}}{m}(t'-t'') \right] \eta(\mathbf{x}). \quad (6.91)$$

While the actual form of this integral is dependent on the distribution and the mode function η , we can still analyze it in the limit where the time is much larger than the transit time τ . For a time $t' \gg \tau$ we obtain $\eta(\mathbf{x} + \frac{\mathbf{p}}{m}t') \eta(\mathbf{x}) \approx 0$. Therefore it is reasonable to define

$$t_{\text{char}} = \int_{-\infty}^{\infty} dt' \chi(t'), \quad (6.92)$$

and approximate

$$\chi(t'-t'') \approx t_{\text{char}} \delta(t'-t''). \quad (6.93)$$

Here t_{char} is the characteristic timescale for the decay of χ . Using Eq. (6.93) we can calculate

$$g_{1,\text{in}}^x(t) \approx \frac{t_{\text{char}} e^{\nu_0 t}}{2\nu_0 C_0^2}. \quad (6.94)$$

We emphasize that the actual form of $g_{1,\text{in}}^x(t)$ for small $t \lesssim \tau$ depends on the density $\rho(\mathbf{p})$ and the mode function $\eta(\mathbf{x})$. However, the results in Eqs. (6.89) and (6.94) show that the long time behavior ($t \gg \tau$) of the g_1 function can be described by an exponential with decay ν_0 . In the

NSR phase, we require that all zeros of Eq. (6.46) are negative. Therefore the g_1 function shows an exponential decay on a typical timescale $-1/\text{Re}(\nu_0)$. On the other hand if we approach the transition to the SSR phase we expect that $\text{Re}(\nu_0)$ becomes vanishingly small. This results in an increasing coherence time when approaching the threshold to SSR.

However, also in the SSR phase, we do not find an actual diverging coherence time. In this phase we have to use a different method to find an estimate for the linewidth as we will now show.

6.4.2 Linewidth in the SSR phase

The dynamics of g_1 and its analysis are very different in the SSR phase. The main difference is that the collective dipole is macroscopic and not dominated by noise. As we have shown in the previous section, we can still decouple two different modes of this dipole, one along the direction of the collective dipole (Higgs mode) and another perpendicular to this direction (Goldstone mode). It is reasonable to write the g_1 function in Eq. (6.77) as

$$g_1(t) = \lim_{t_0 \rightarrow \infty} \frac{\langle J^\parallel(t+t_0)J^\parallel(t_0)e^{i[\varphi(t+t_0)-\varphi(t_0)]} \rangle}{4}, \quad (6.95)$$

where we define the collective dipole to be $J(t) = J^\parallel(t)e^{-i\varphi(t)}/2$.

Since the length of the dipole is assumed to be stable, we can always write $J^\parallel(t) = J_0^\parallel + \delta J^\parallel(t)$, where the first term is the stationary length of the collective dipole and $\delta J^\parallel(t)$ describes noisy fluctuations around this length (see Fig. 6.2). Assuming now that all zeros of the Higgs dispersion relation in Eq. (6.69) have negative real part, we can conclude that these fluctuations decay rapidly. Therefore, we can simplify the g_1 function as

$$g_1(t) \approx \lim_{t_0 \rightarrow \infty} \frac{(J_0^\parallel)^2}{4} \langle e^{i[\varphi(t+t_0)-\varphi(t_0)]} \rangle. \quad (6.96)$$

In this picture the dynamics of the g_1 function is determined by the dynamics of its phase. The dynamics of the phase can be approximated by

$$\frac{d\varphi(t)}{dt} \approx \frac{dJ^\perp}{J_0^\parallel}. \quad (6.97)$$

With this result it is sufficient to determine the time evolution of J^\perp . To do this, we use Eq. (6.51) to calculate $s^\perp(t)$. Multiplying it by $\eta(\mathbf{x})$ and integrating over the whole phase space, we obtain J^\perp . The resulting equation can be solved using a Laplace transformation where we eventually get

$$L[J^\perp] \approx \frac{L[J_{W^\perp}] + 2 \frac{1-D_\perp(\nu)}{\Gamma_c} L[\mathcal{F}^\perp]}{D_\perp(\nu)}. \quad (6.98)$$

This result is completely equivalent to Eq. (6.80) except we use now the dispersion relation of the Goldstone mode in Eq. (6.75). The noise equivalent to Eq. (6.81) is given by

$$J_{W^\perp}(t) = \int d\mathbf{x} \int d\mathbf{p} \eta(\mathbf{x}) W^\perp(y_i, z_i, \mathbf{p}, t_i). \quad (6.99)$$

The main difference between Eqs. (6.80) and (6.98) is the different zeros of the dispersion relations in Eqs. (6.46) and (6.74). While the zero of Eq. (6.46) always results in an exponential behavior, the dominant zero of Eq. (6.74) is $\nu_0 = 0$. This implies that the dynamics of J^\perp and the resulting phase $\varphi = J^\perp/J_0^\parallel$ are diffusive.

For simplicity let us again assume that $\nu_0 = 0$ is a first order zero of Eq. (6.74). In that case we can define a non-vanishing

$$C_\perp = \lim_{\nu \rightarrow 0} \frac{D_\perp(\nu)}{\nu} = \frac{\int_0^\infty dt \int d\mathbf{x} \int d\mathbf{p} \eta\left(\mathbf{x} + \frac{\mathbf{p}}{m}t\right) s_0^\parallel}{J_0^\parallel}, \quad (6.100)$$

and use it to obtain

$$J^\perp(t) \approx J_{\text{in}}^\perp(t) + J_c^\perp(t), \quad (6.101)$$

where

$$J_{\text{in}}^\perp(t) = \frac{\int_0^t dt' \int d\mathbf{x} \int d\mathbf{p} \eta(\mathbf{x}) W^\perp(y_i, z_i, \mathbf{p}, t'_i)}{C_\perp}, \quad (6.102)$$

$$J_c^\perp(t) = \frac{\int_0^t dt' \frac{2}{\Gamma_c} \mathcal{F}^\perp(t')}{C_\perp}, \quad (6.103)$$

are the input and cavity noise terms, respectively.

We can now give a simple expression for the g_1 function

$$g_1(t) \approx \lim_{t_0 \rightarrow \infty} \frac{(J_0^\parallel)^2}{4} e^{-\frac{\langle \Delta\varphi(t, t_0)^2 \rangle}{2}}, \quad (6.104)$$

where $\Delta\varphi(t, t_0) = \varphi(t + t_0) - \varphi(t_0)$. Let us without loss of generality choose $t_0 = 0$ and write $\Delta\varphi(t, 0) = \Delta\varphi(t)$. Since input noise and cavity noise are independent, we obtain

$$\langle \Delta\varphi(t)^2 \rangle = \langle \Delta\varphi_{\text{in}}(t)^2 \rangle + \langle \Delta\varphi_{\text{c}}(t)^2 \rangle, \quad (6.105)$$

with $\Delta\varphi_{\text{in}}(t) = J_{\text{in}}^{\perp}/J_0^{\parallel}$ and $\Delta\varphi_{\text{c}}(t) = J_{\text{c}}^{\perp}/J_0^{\parallel}$.

The term corresponding to the cavity noise is given by

$$\langle \Delta\varphi_{\text{c}}(t)^2 \rangle = \frac{4}{\Gamma_{\text{c}} C_{\perp}^2 (J_0^{\parallel})^2} t, \quad (6.106)$$

showing the usual increase of the variance with t of a diffusion process.

For the noise term that arises from incoming atoms, we use Eq. (7.28) to obtain

$$\langle \Delta\varphi_{\text{in}}(t)^2 \rangle = \frac{\int_0^t dt' \int_0^t dt'' \chi(t' - t'')}{C_{\perp}^2 (J_0^{\parallel})^2}, \quad (6.107)$$

where we have used the definition in Eq. (6.91). While this process has a non-trivial time dependence for $t \lesssim \tau$ we can write in the large time limit $t \gg \tau$ the following expression

$$\langle \Delta\varphi_{\text{in}}(t)^2 \rangle \approx \frac{t_{\text{char}}}{C_{\perp}^2 (J_0^{\parallel})^2} t, \quad (6.108)$$

with the characteristic timescale t_{char} defined in Eq. (6.92). In the $t \gg \tau$ limit we obtain

$$g_1(t) \propto e^{-\frac{\Gamma}{2}t}, \quad (6.109)$$

with a linewidth

$$\Gamma = \frac{4}{\Gamma_{\text{c}} C_{\perp}^2 (J_0^{\parallel})^2} + \frac{t_{\text{char}}}{C_{\perp}^2 (J_0^{\parallel})^2}. \quad (6.110)$$

Here, t_{char} is the characteristic time that has the form

$$t_{\text{char}} = \int_{-\infty}^{\infty} dt \int d\mathbf{x} \int d\mathbf{p} \rho(\mathbf{p}) \eta\left(\mathbf{x} + \frac{\mathbf{p}}{m}t\right) \eta(\mathbf{x}) \quad (6.111)$$

and the quantity C_{\perp} is defined as

$$C_{\perp} = \frac{\int_0^{\infty} dt \int d\mathbf{x} \int d\mathbf{p} \eta\left(\mathbf{x} + \frac{\mathbf{p}}{m}t\right) s_0^{\parallel}}{J_0^{\parallel}}. \quad (6.112)$$

6.4.3 Discussion and limitations

Here we give an example of the order of magnitude, in particular, regarding the number N of dipoles that effectively interact with the cavity mode. We discuss the behavior of the presented quantities when we increase N . Notice that we scale $\Gamma_c \propto N^{-1}$ so that $N\Gamma_c$ is considered to be of order 1. This implies a linear scaling of the maximum output power of the field

$$\kappa \langle \hat{a}^\dagger \hat{a} \rangle \approx \Gamma_c \langle \hat{J}^+ \hat{J}^- \rangle \propto N. \quad (6.113)$$

This choice of scaling allows the dispersion relations given in Eqs. (6.46), (6.69), and (6.75) to be independent of N . Therefore the linewidth in the NSR phase, given by $2\nu_0$, is of order 1 which is the scaling of the collective linewidth. In the SSR phase, however, we have $J_0^\parallel \propto N$ and therefore $(J_0^\parallel)^2 \propto N^2$ implying a coherent collective dipole. In this regime the linewidth, given in Eq. (6.110), is of order $\Gamma \propto 1/N$ where we have used that $t_{\text{char}} \propto N$ and $C_\perp \propto 1$. This highlights the fact that a macroscopic, coherent collective dipole $\propto N$ is needed for a narrow linewidth that is a factor N smaller than that in the NSR phase.

We remark that the calculation of the g_1 function in the NSR phase needs the zero ν_0 of $D(\nu)$ to be sufficiently isolated such that the contribution of exponents with faster decay rate only plays a minor role. In general it is possible that ν_0 is complex in that case. Since the dispersion relation is real, there is always a second root ν_0^* that would need to be included in our calculation. However, this will not affect the decay of the g_1 function for very large values of t that is only determined by the real part of ν_0 .

In the SSR phase, our calculation is only valid if every zero of the dispersion relation of the Higgs mode in Eq. (6.69) is negative. In this case the decay of the Higgs mode is a factor N faster than the dephasing process determined by Γ . However, if a zero of Eq. (6.69) has zero real part, our calculation becomes invalid and predicts an instability of the system. In this situation, the system will be either not superradiant or in a dynamical multi-component superradiant (MCSR) phase, as we will see later in Sec. 6.5. Such an instability will also occur if there is a solution ν_0 with positive real part to $D_\perp(\nu_0) = 0$, where $D_\perp(\nu_0)$ is the Goldstone dispersion relation in Eq. (6.75)

(see Ref. [70]).

6.5 A thermal beam traversing the cavity

We will now analyze an explicit model in detail. To be specific, we use a cavity mode function that is given by

$$\eta(\mathbf{x}) = [\Theta(x+w) - \Theta(x-w)] \cos(kz), \quad (6.114)$$

where $\Theta(x)$ is the Heaviside step function, w is the cavity mode waist, and k is the wavenumber. We consider an atomic beam traversing this cavity mode with a constant single velocity $v_x = p_x/m$ and a homogeneous spatial atomic density. The transit time is then $\tau = 2w/v_x$. In the z direction, we assume a Maxwell distribution of velocities. We can thus express $\rho(\mathbf{p})$ as

$$\rho = \rho(p_z) = \frac{N}{2w\lambda} \sqrt{\frac{\beta_z}{2m\pi}} e^{-\beta_z \frac{p_z^2}{2m}}, \quad (6.115)$$

where N is the intracavity atom number and β_z characterizes the momentum width in the z direction.

6.5.1 NSR phase

In the NSR phase all atoms remain in the excited state while they traverse the cavity. The stability of this phase is determined by the dispersion relation in Eq. (6.46). For the specific case of Eqs. (6.114) and (6.115), we can solve the integrals in Eq. (6.46) analytically and obtain

$$D(\nu) = 1 + \frac{N\Gamma_c\tau}{4} F(\nu), \quad (6.116)$$

with

$$F(\nu) = \frac{1 - e^{-\frac{\delta_D^2 \tau^2 + 2\nu\tau}{2}}}{\delta_D^2 \tau^2} - \sqrt{\frac{\pi}{2\delta_D^2 \tau^2}} e^{\frac{\nu^2}{2\delta_D^2}} \left(1 + \frac{\nu\tau}{\delta_D^2 \tau^2} \right) \left[\operatorname{erf} \left(\frac{\nu + \delta_D^2 \tau}{\sqrt{2\delta_D^2}} \right) - \operatorname{erf} \left(\frac{\nu}{\sqrt{2\delta_D^2}} \right) \right].$$

Here, we have defined the Doppler width as

$$\delta_D = \frac{k\Delta p_z}{m} = \frac{k}{\sqrt{m\beta_z}}, \quad (6.117)$$

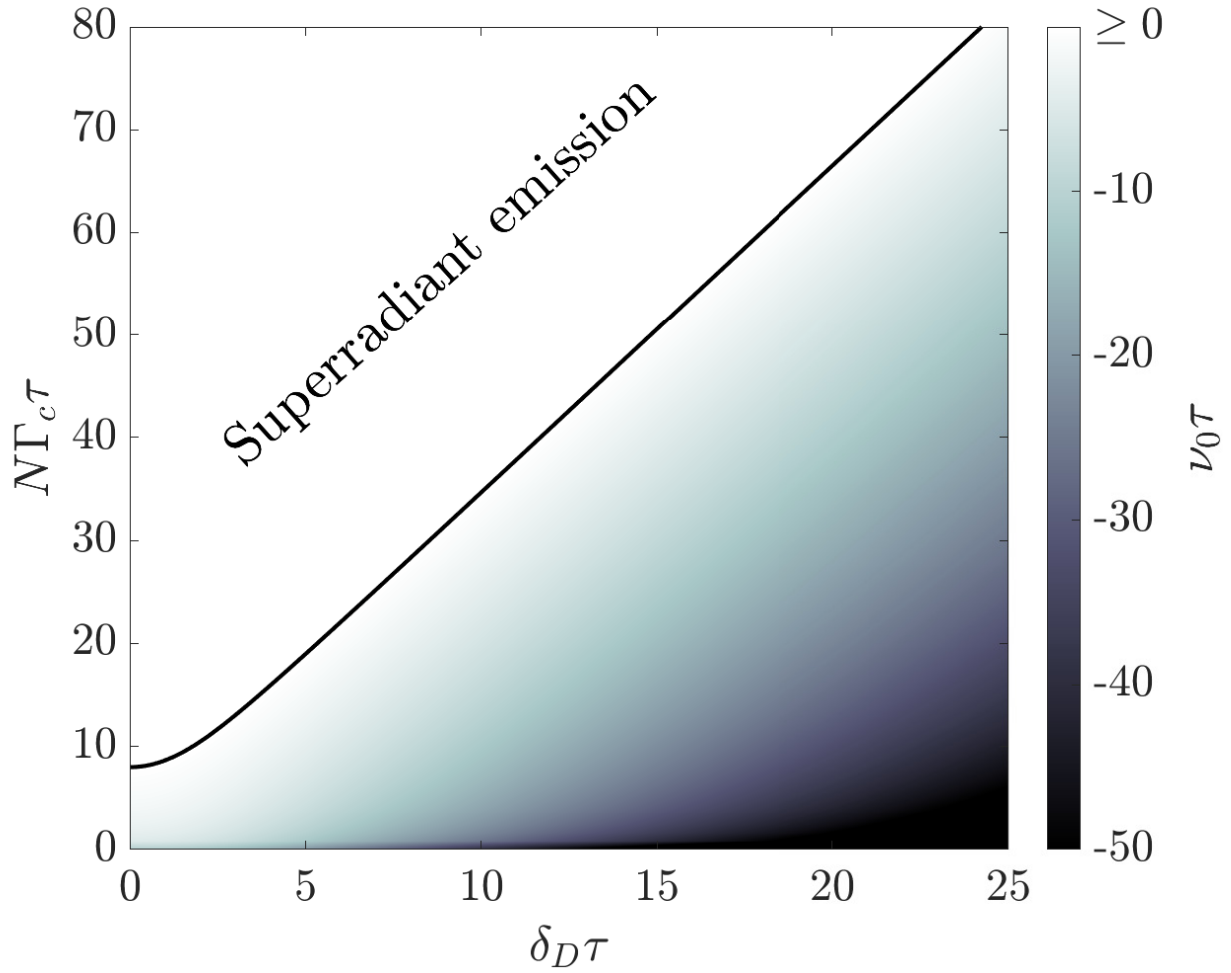


Figure 6.3: The zero ν_0 of $D(\nu)$ from Eq. (6.116) with the largest real part as a function of the Doppler width δ_D and of the collective linewidth $N\Gamma_c$, all in units of $1/\tau$. In the region where $\nu_0 > 0$ (shown as white region) the state of the atomic beam is unstable and the beam of excited dipoles will undergo superradiant emission. The solid black line indicates the transition where $\nu_0 = 0$ [Eq. (6.118)].

and $\text{erf}(\dots)$ denotes the error function. The zero ν_0 of Eq. (6.116) with the maximum real part is shown in Fig. 6.3 as a function of $N\Gamma_c\tau$ and $\delta_D\tau$. For our parameter range solutions are restricted to the domain $\nu_0 \in \mathbb{R}$. The shaded area where $\nu_0 < 0$ describes the region where the NSR phase is stable. Here, fluctuations decay with the exponent ν_0 . In the white region where $\nu_0 \geq 0$ we expect that fluctuations will be amplified and therefore the atoms will undergo superradiant emission. The condition $\nu_0 = 0$ describes the phase boundary between the superradiant emission and the NSR phase. This phase boundary can be calculated by solving $D(0) = 0$ which results in the equation

$$\frac{N\Gamma_c\tau}{8} = \frac{\delta_D^2\tau^2}{\sqrt{2\pi}\delta_D\tau \text{erf}\left[\frac{\delta_D\tau}{\sqrt{2}}\right] + 2e^{-\frac{\delta_D^2\tau^2}{2}} - 2}. \quad (6.118)$$

We first consider the limit where Doppler broadening is very small, i.e., $\delta_D\tau \ll 1$. In this case the atoms remain almost in the same position in the standing wave while traversing the cavity. For this choice the right-hand side of Eq. (6.118) simplifies and we obtain

$$\frac{N\Gamma_c\tau}{8} = 1. \quad (6.119)$$

This shows that even in the absence of Doppler broadening, the collective linewidth $N\Gamma_c$ has to overcome transit-time broadening $1/\tau$, i.e., $N\Gamma_c > 8/\tau$, so that the atomic beam can induce superradiant emission above threshold.

In the large Doppler broadening limit $\delta_D\tau \gg 1$, the atoms move many wavelengths during the transit time τ . In that case, the right-hand side of Eq. (6.118) can again be simplified, giving

$$\frac{N\Gamma_c}{8} = \frac{\delta_D}{\sqrt{2\pi}}. \quad (6.120)$$

This result is a second condition for superradiance; the collective linewidth has to overcome Doppler broadening, i.e., $N\Gamma_c > 8\delta_D/\sqrt{2\pi}$. Remarkably, this condition is completely independent of τ .

Both conditions $N\Gamma_c > 8/\tau$ and $N\Gamma_c > 8\delta_D/\sqrt{2\pi}$ are visible in Fig. 6.3 in the small ($\delta_D\tau \ll 1$) and large ($\delta_D\tau \gg 1$) Doppler broadening limits, respectively.

We will now present results for the g_1 function in the NSR phase as defined in Eq. (6.77) for $t_0 \gg \tau$. The analytical estimates of $g_1(t)$ have already been discussed in Sec. 6.4.1. Numerically,

we find that the g_1 function has a non-vanishing imaginary part. However, this imaginary part becomes vanishingly small after averaging over many trajectories. In Fig. 6.4, we plot the absolute value of the g_1 function in (a) for $\delta_D\tau = 0.1$, $N\Gamma_c\tau = 4$ and in (b) for $\delta_D\tau = 10$, $N\Gamma_c\tau = 20$. Well inside the NSR phase, these parameters are chosen to represent the case (a) where transit-time broadening dominates Doppler broadening with $\delta_D\tau = 0.1$, and (b) where Doppler broadening dominates transit-time broadening with $\delta_D\tau = 10$. For both cases we observe a long-time behavior that is essentially exponential. To show this we have performed a numerical fit to the tail of the g_1 function assuming an exponential $\propto \exp(ct)$ and have calculated for (a) $c\tau \approx -1.9$, and for (b) $c\tau \approx -6.5$. Those two values are in very good agreement with the calculated values of ν_0 that are for (a) $\nu_0\tau = -1.8$, and for (b) $\nu_0\tau = -6.2$ (see Sec. 6.4.1). However, the short time behavior for both parameter choices is not exponential. In Fig. 6.4(a) we observe initially an almost linear decay of the g_1 function that abruptly ends at the transit time $t = \tau$. The g_1 function in Fig. 6.4(b) shows a Gaussian behavior for short times. The timescale where this Gaussian behavior is visible is in much shorter $t < 0.1\tau$ in agreement with the timescale expected from the larger Doppler width $t \sim 1/(\delta_D) = 0.1\tau$. The two-stage behavior of the g_1 function has the signature of being dominated by single-particle effects for short times and by collective effects, as determined by ν_0 , for long times.

In the next subsection we will discuss the superradiant regime.

6.5.2 SSR phase

For the analysis of the SSR phase we solve the partial differential equation Eq. (6.58). The solution is given by

$$K(x - w, z, p_z) = \frac{\Gamma_c J_0^{\parallel} m}{2kp_z} \left[\sin(kz) - \sin\left(kz - \frac{kp_z}{mv_x} x\right) \right]. \quad (6.121)$$

This solution has the correct boundary condition $K(-w, z, p_z) = 0$ implying that all atomic dipoles are in the excited state when entering the cavity. Substituting Eq. (6.121) in Eq. (6.57) and then

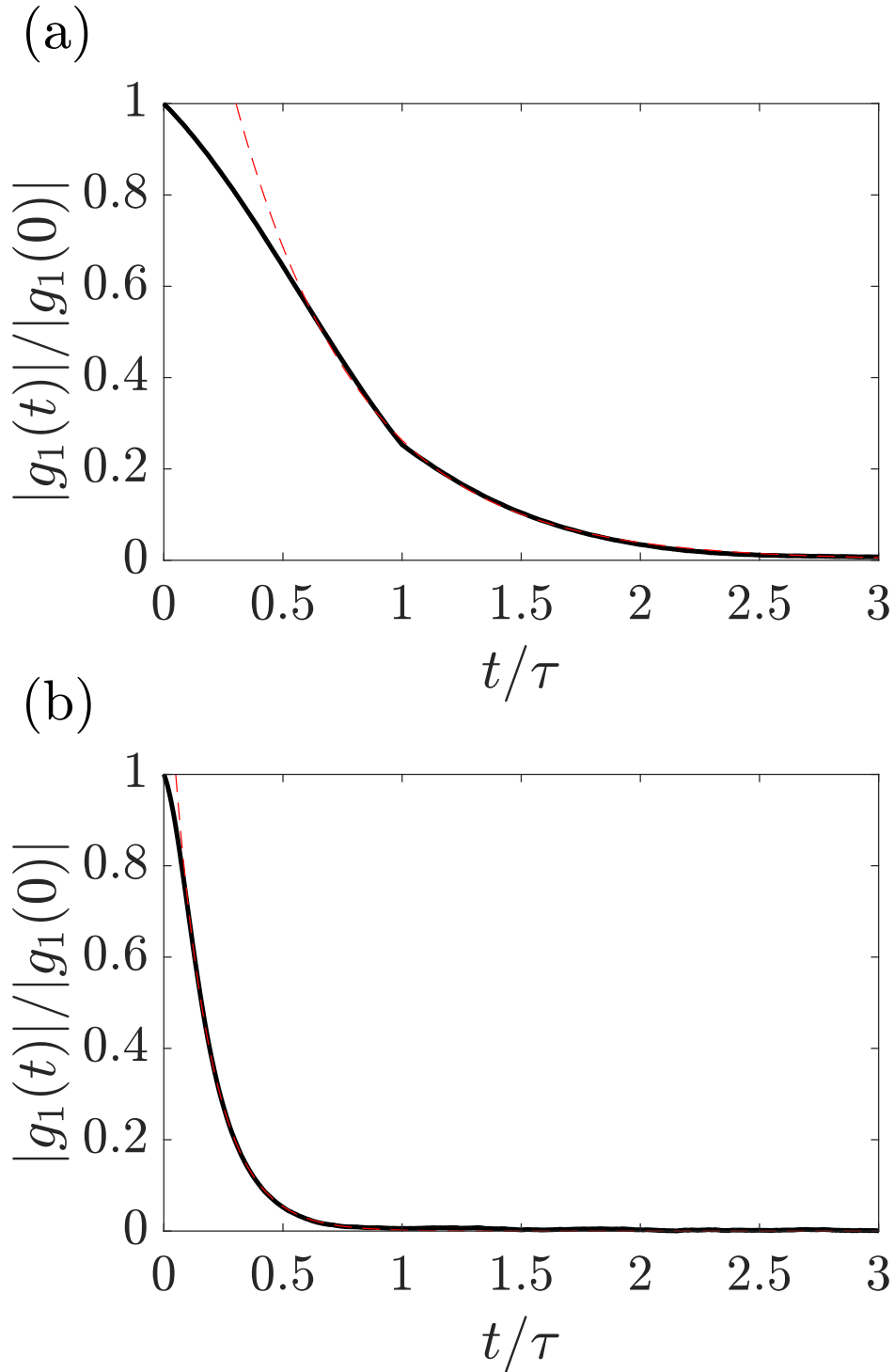


Figure 6.4: The absolute value of the g_1 function [Eq. (6.77)] normalized by $|g_1(0)|$ as a function of time t in units of τ for (a) $\delta_D\tau = 0.1$, $N\Gamma_c\tau = 4$ and (b) $\delta_D\tau = 10$, $N\Gamma_c\tau = 20$. The g_1 function is calculated by numerically integrating Eqs. (6.20)–(6.23) using Eqs. (6.114)–(6.115) over a total time $t_{\text{sim}} = 200\tau$ with $N = 2000$ atoms, and averaging over 100 trajectories. For the calculation of g_1 we have chosen $t_0 = 10\tau$. The red dashed line is an exponential fit $\propto \exp(ct)$ of the tail with an exponent $c\tau \approx -1.9$ (a) and $c\tau \approx -6.5$ (b), respectively. The values of ν_0 (see Fig. 6.3) for the same parameters are $\nu_0\tau = -1.8$ (a), and $\nu_0\tau = -6.2$ (b).

calculating J_0^{\parallel} defined in Eq. (6.55), we obtain

$$J_0^{\parallel} = N \int_{-\infty}^{\infty} du \frac{e^{-\frac{u^2}{2\delta_D^2}}}{\sqrt{2\pi\delta_D^2}} \frac{1 - \mathcal{J}_0 \left[\frac{\Gamma_c J_0^{\parallel} \tau \sin(\frac{u\tau}{2})}{2} \right]}{\frac{\Gamma_c J_0^{\parallel} \tau}{2}}, \quad (6.122)$$

where \mathcal{J}_n is the Bessel function of the first kind of order n . This is a non-linear equation for J_0^{\parallel} that can be simplified by defining the average dipole $j_0^{\parallel} = J_0^{\parallel}/N$ that can be calculated by

$$j_0^{\parallel} = \int_{-\infty}^{\infty} du \frac{e^{-\frac{u^2}{2\delta_D^2}}}{\sqrt{2\pi\delta_D^2}} \frac{1 - \mathcal{J}_0 \left[\frac{N\Gamma_c \tau j_0^{\parallel} \sin(\frac{u\tau}{2})}{2} \right]}{\frac{N\Gamma_c \tau j_0^{\parallel}}{2}}. \quad (6.123)$$

This shows the value of j_0^{\parallel} is completely determined by the value of $N\Gamma_c\tau$ and $\delta_D\tau$. For $j_0^{\parallel} \neq 0$ we obtain a superradiant scaling [100]

$$\left(J_0^{\parallel}\right)^2 = N^2 \left(j_0^{\parallel}\right)^2 \propto N^2. \quad (6.124)$$

The stability of this collective dipole is determined by the zero ν_0 with the largest real part of the Higgs and Goldstone mode dispersion relations [Eqs. (6.69) and (6.75)]. However, for the considered parameter regime we only find an instability in the Higgs mode and not in the Goldstone mode. Because of this, we focus on the Higgs mode dispersion relation in Fig. 6.5. In order to calculate the zeros of the Higgs dispersion, we substitute Eq. (6.123) in Eq. (6.121) to solve for $K(\mathbf{x}, \mathbf{p})$, and then use Eq. (6.56) to calculate the zeros of the dispersion function Eq. (6.69). We numerically solve the equation and report the real and imaginary parts of the solution in Figs. 6.5(a) and 6.5(b), respectively. We find a parameter regime where $\text{Re}(\nu_0) < 0$ and this marks the regime where the SSR phase is stable. However, we observe also an unstable area that is defined by $\text{Re}(\nu_0) > 0$. This area is indicated by a gray color in Fig. 6.5 and is bounded by a dashed line that has been determined numerically. In this parameter range we expect neither the NSR nor the SSR phase to be stable. Therefore, we find a dynamical and superradiant behavior of the system that is most clearly visible in the spectrum that has several peaks. Because of this we refer to this phase as multi-component superradiant (MCSR).

In the SSR phase, where $\text{Re}(\nu_0) < 0$, we always find a non-vanishing imaginary part $\text{Im}(\nu_0)$ indicating that any fluctuation in the collective dipole length will decay as a damped oscillation.

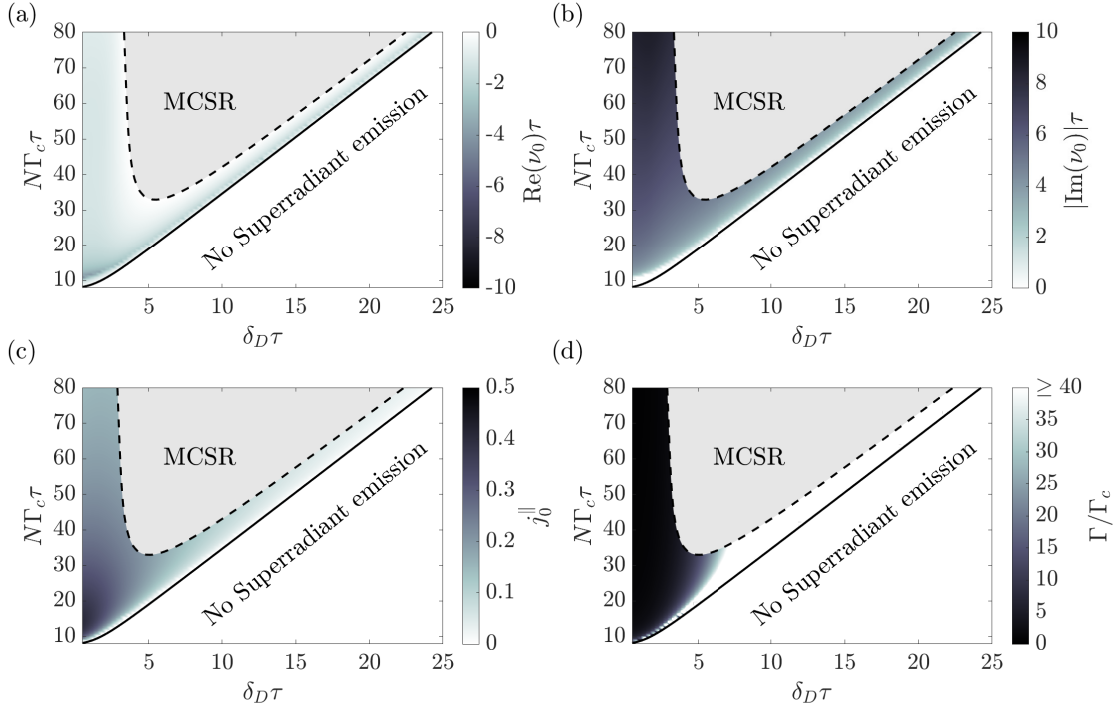


Figure 6.5: The real part $\text{Re}(\nu_0)$ (a) and the absolute value of the imaginary part $|\text{Im}(\nu_0)|$ (b) in units of $1/\tau$ of the zero ν_0 with the largest real part of the Higgs dispersion relation [Eq. (6.69)] as a function of the Doppler width δ_D and the collective linewidth NT_c in units of $1/\tau$. The parameter region where the Higgs mode is unstable, $\text{Re}(\nu_0) > 0$, is marked as gray area and bounded by a dashed black line. We call this phase multi-component superradiant (MCSR). The solid black line, given by Eq. (6.118), marks the transition from SSR to the NSR phase (see also Fig. 6.3). Subplots (c) and (d) show the value of the collective dipole j_0^{\parallel} [Eq. (6.123)] and the linewidth Γ [Eq. (6.110)] in units of Γ_c , respectively. They are shown as a function of the same parameters as subplots (a) and (b) for the parameter regime where the Higgs mode is stable. For all calculations we have used Eq. (6.114) and Eq. (6.115).

For the whole parameter region of the SSR phase we have also calculated the Goldstone dispersion relation and have not found any additional instabilities.

Figure 6.5(c) shows the normalized collective dipole j_0^{\parallel} calculated using Eq. (6.123). We see that the maximum dipole in the SSR regime is close to $N\Gamma_c\tau = 20$ and for $\delta_D\tau \ll 1$. Using the previous results we can also calculate the linewidth Γ using Eq. (6.110). We expect that this analytical result is valid as long as the collective dipole is stable. The results are apparent in Fig. 6.5(d). Here, we report a narrow linewidth, $\Gamma < 40\Gamma_c$, only for sufficiently small values of $\delta_D\tau \lesssim 5$.

To analyze and compare our analytical results we have simulated Eqs. (6.20)–(6.23) across the different transitions between the SSR, MCSR, and NSR phases.

6.5.3 Transition from SSR to NSR

We first analyze our simulations for the transition from SSR to the NSR phase for various values of $\delta_D\tau$ and fixed $N\Gamma_c\tau = 20$. In Fig. 6.6 we show the results of our numerical integration where different markers indicate different intracavity atom numbers [see inset of Fig. 6.6(a)].

In Fig. 6.6(a) we show the collective dipole correlation $\langle J^*J \rangle = \langle (J^x)^2 + (J^y)^2 \rangle / 4$ (proportional to the intensity of the output field) where the red dashed vertical line marks the threshold between the SSR and NSR phases. The analytical prediction is visible as a black solid line and agrees very well with the simulated results. In general we observe that the analytical result is in better agreement for larger intracavity atom number N .

In Figs. 6.6(b) and 6.6(c) we show the linewidth Γ that is extracted by fitting the g_1 function in Eq. (6.77) with $\exp(-\Gamma t/2)$. In subplot (b) the linewidth Γ is shown in units of the collective linewidth $N\Gamma_c$ while in subplot (c) we show the linewidth in units of the single-atom linewidth Γ_c . We observe convergence of the simulation data for different N in the NSR phase in subplot (b). On the other hand we observe convergence of the simulation data in the SSR phase in subplot (c). This finding suggests that the linewidth Γ scales with $N\Gamma_c$ in the NSR phase while it scales with Γ_c in the SSR phase.

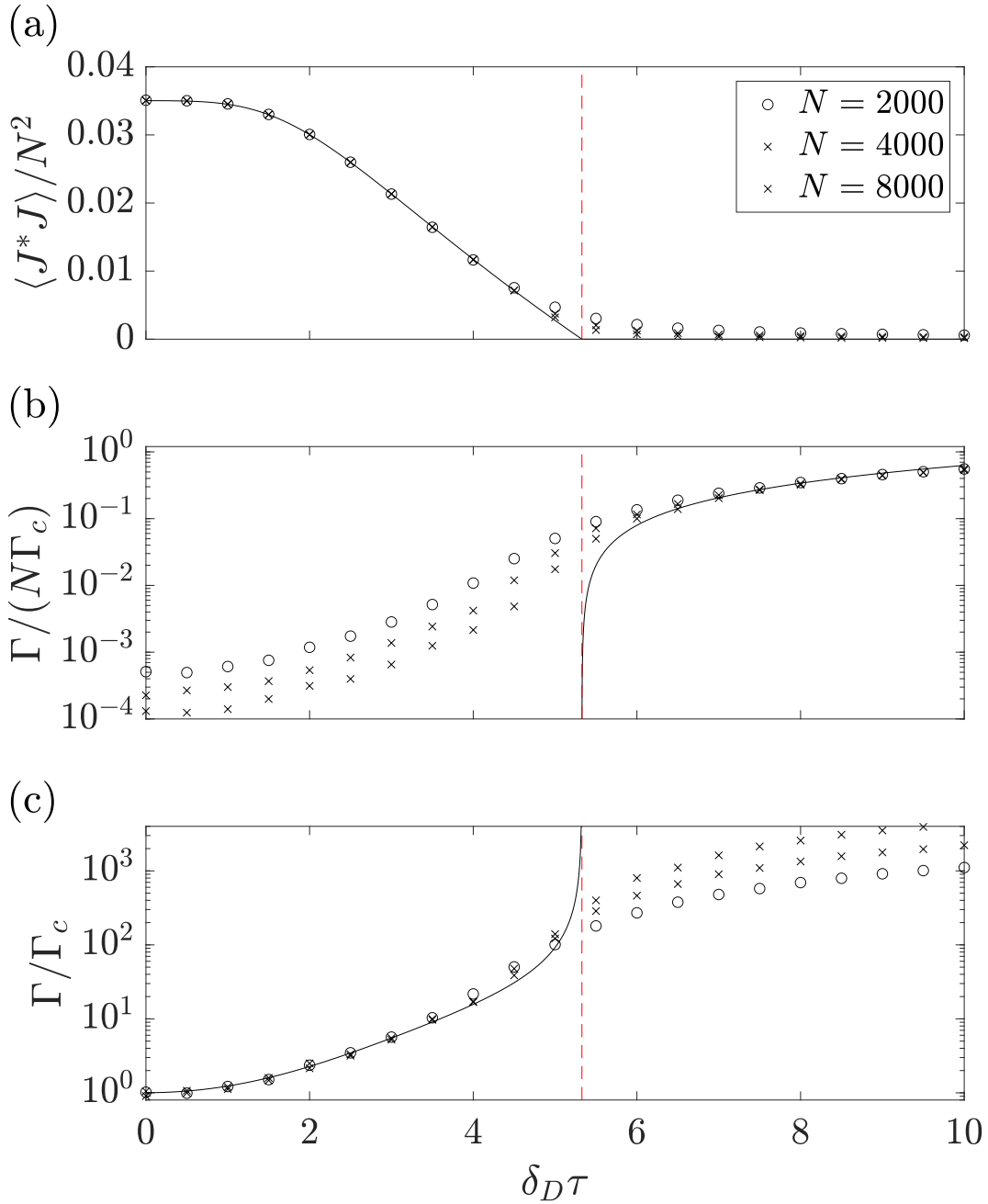


Figure 6.6: (a) The normalized collective dipole correlation $\langle J^* J \rangle / N^2$, (b) the linewidth Γ in units of the collective linewidth $N\Gamma_c$, and (c) the linewidth in units of the single-atom linewidth Γ_c as a function of the Doppler width δ_D in units of $1/\tau$. The different markers correspond to different intracavity atom number N as described in the inset of subplot (a). The linewidth is calculated by fitting the g_1 function using $t_0 = 10\tau$ to an exponential $\propto \exp(-\Gamma t/2)$ over a time interval of length $t_f = 20\tau$. The solid line in subplot (a) is the value of $(j_0^{\parallel})^2/4$ calculated from Eq. (6.123). The linewidths in (b) visible as solid line are $-2\nu_0$, where ν_0 is the zero with the largest real part of the dispersion relation in Eq. (6.116). In (c) the solid line gives the solution of Eq. (6.110) calculated using Eq. (6.121) for given values of j_0^{\parallel} . The red dashed vertical lines mark the transition from SSR to the NSR phase. We have chosen $N\Gamma_c\tau = 20$ with a simulation time of $t_{\text{sim}} = 200\tau$ and a total number of trajectories $200000/N$ for corresponding N .

To further compare our numerical results with analytical predictions we have also calculated the exponent ν_0 that is the zero of the dispersion relation in Eq. (6.116) and plotted it as the black solid line in subplot (b). Numerical and analytical results are in very good agreement in the NSR phase. This description breaks down at the transition where the exponent ν_0 vanishes. After that in the SSR phase we expect that the linewidth of the collectively emitted light is dominated by phase diffusion. In order to show this we have calculated the linewidth in Eq. (6.110) using Eqs. (6.121) and (6.123). This linewidth is plotted as the black line in subplot (c). We find good agreement of the theoretical prediction and the numerical result.

For the derivation of the linewidth in the SSR phase we have assumed a stable length of the collective dipole. This is guaranteed by choosing $N\Gamma_c\tau = 20$, where there is no instability in the superradiant regime [see Fig. 6.5(a)]. In the next subsection we will explicitly study the crossover from the SSR to the MCSR phase, where the Higgs mode becomes unstable.

6.5.4 Transition from SSR to MCSR

We choose $N\Gamma_c\tau = 50$ and perform simulations for different values of $\delta_D\tau$ across the transition between the SSR and MCSR phases [see Fig. 6.5(a)]. In Fig. 6.7(a) we show $\langle J^*J \rangle = \langle (J^x)^2 + (J^y)^2 \rangle / 4$ for different values of N [see inset of Fig. 6.7(a)]. The red dashed vertical lines mark the thresholds from SSR to the MCSR phase, and from the MCSR to the SSR phase. The first threshold is close to $\delta_D\tau \approx 3$ while the second threshold appears at $\delta_D\tau \approx 12$. For comparison we have also calculated the predicted mean-field value using Eq. (6.123) that is visible as the black solid line. We find very good agreement in the superradiant phase for small values of $\delta_D\tau$. At the threshold we see an increase of $\langle J^*J \rangle$ in the numerical results that shows a clear deviation from the black line.

The instability at the transition from SSR to the MCSR phase has been derived from the Higgs dispersion relation that describes the relaxation dynamics of the amplitude of the collective dipole. Therefore we expect to see this instability also in the fluctuations of the collective dipole

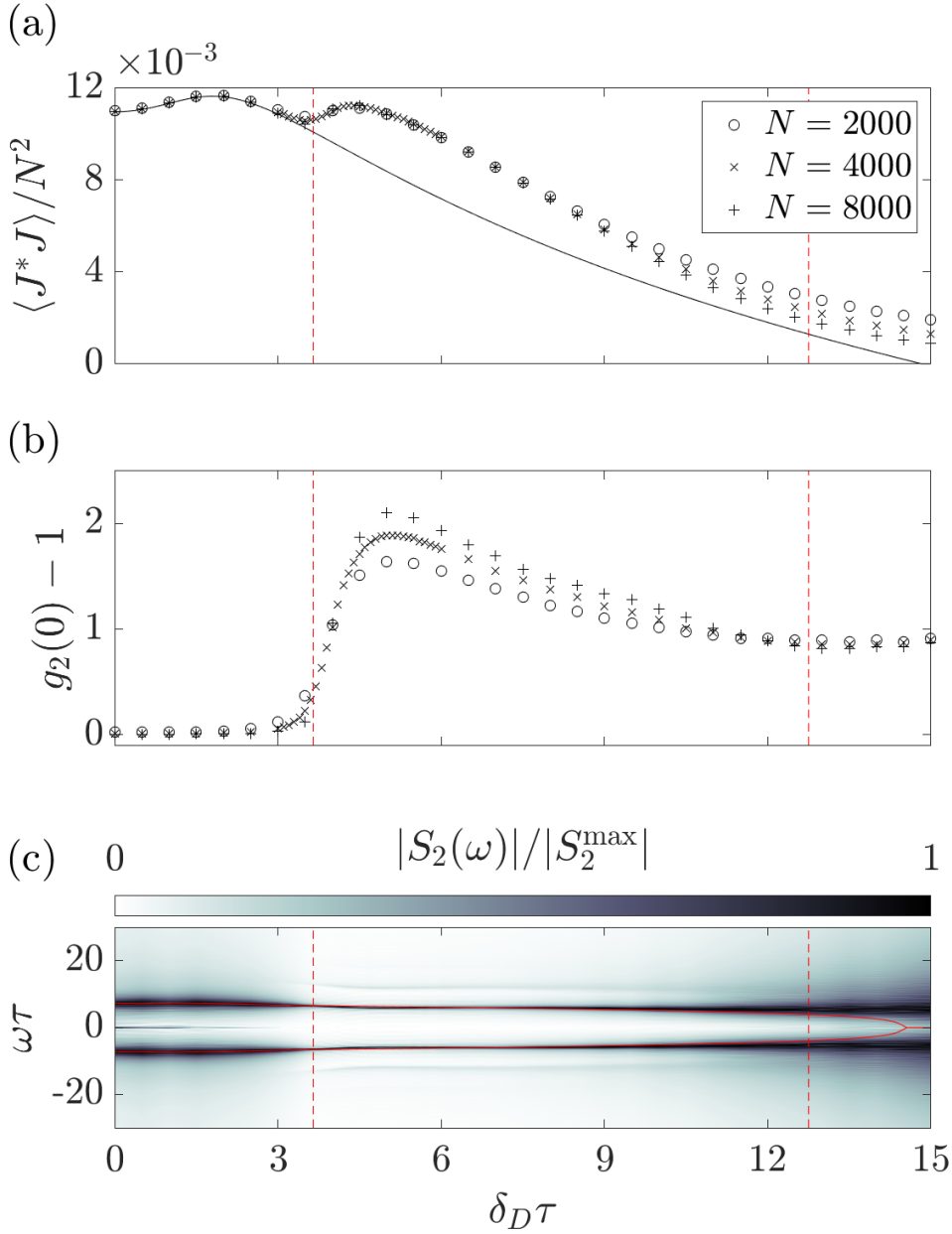


Figure 6.7: The collective dipole correlation $\langle J^* J \rangle / N^2$ (a) and the value of $g_2(0) - 1$ [Eq. (6.125)] (b) as a function of δ_D in units of $1/\tau$. The different symbols indicate different intracavity atom numbers N [see inset of subplot (a)]. The solid line in subplot (a) is the value of $(j_0^{\parallel})^2/4$ calculated from Eq. (6.123). Subplot (c) shows the intensity spectrum $|S_2(\omega)|$ defined in Eq. (6.126) as a function of ω and δ_D in units of $1/\tau$. The value of $|S_2(\omega)|$ is normalized for every δ_D by the maximum $|S_2^{\max}| \equiv \max_{\omega} |S_2(\omega)|$ and calculated for $N = 4000$. The red vertical dashed lines indicate the threshold from SSR to MCSR and from the MCSR to the SSR phases [see Fig.6.5(a)]. The red horizontal solid lines in subplot (c) are the values of $\pm \text{Im}(\nu_0)$ corresponding to the zero ν_0 of Eq. (6.69) with the largest real part. For the calculation of g_2 we have used $t_0 = 10\tau$ and for the calculation of $S_2(\omega)$ and integration time of $t_f = 20\tau$. All simulations were performed with $N\Gamma_c\tau = 50$ and with a simulation time of $t_{\text{sim}} = 200\tau$. For every N we have averaged over $200000/N$ trajectories.

length. For this we calculate the g_2 function which is defined as

$$g_2(t) = \frac{\langle J^*(t+t_0)J(t+t_0)J^*(t_0)J(t_0) \rangle}{\langle J^*J \rangle^2}, \quad (6.125)$$

where $t_0 \gg \tau$ is a sufficiently long time. We plot $g_2(0) - 1$ in Fig. 6.7(b) for the same values of $\delta_D\tau$. We find $g_2(0) = 1$ well inside the SSR regime ($\delta_D\tau < 3$); therefore we expect second-order coherent light. Beyond the transition ($\delta_D\tau \gtrsim 3$) we find a sudden increase of $g_2(0)$ highlighting the transition point. This increase cannot be explained by chaotic light because it even exceeds the value of $g_2(0) = 2$. Remarkably, the second threshold $\delta_D\tau \approx 12$ is not visible in subplot (b) while we would expect a transition to the SSR phase there with $g_2(0) \approx 1$. We understand that this finding is due to finite size effects that are pronounced in this regime because of a small value of $\langle J^*J \rangle/N^2 \lesssim 2 \times 10^{-3}$. This is comparable with finite size effects that we consider to scale like $1/N$.

Because the exponent ν_0 also has an imaginary part [Fig. 6.5(b)], we also expect an oscillatory behavior in the unstable phase. In order to analyze this we have calculated the intensity spectrum

$$S_2(\omega) = \int_0^{t_f} dt e^{i\omega t} [g_2(t) - 1], \quad (6.126)$$

where t_f is the integration time. We plot $|S_2(\omega)|$ in Fig. 6.7(c) as a function of ω in units of $1/\tau$. The vertical red dashed lines mark the thresholds and the red horizontal solid lines are the values of $\pm \text{Im}(\nu_0)$ visible in Fig. 6.5(b). We find very good agreement of the values of $\pm \text{Im}(\nu_0)$ with the peaks of $|S_2(\omega)|$ until $\delta_D\tau \lesssim 12$.

The transition between the SSR and the MCSR phase is also visible in Fig. 6.7(c). The function $|S_2(\omega)|$ shows very broad peaks in the SSR phase suggesting that the amplitude oscillations are strongly damped. This is not true in the MCSR phase where the peaks are narrower suggesting long-lived amplitude oscillations.

We will study this dynamical feature using the spectrum

$$S_1(\omega) = \int_0^{t_f} dt e^{i\omega t} g_1(t), \quad (6.127)$$

which we have calculated for the same parameters (see Fig. 6.8). Figure 6.8(d) shows the absolute value of the spectrum $|S_1(\omega)|$ as a function of ω and δ_D in units of $1/\tau$. The horizontal dashed red line marks the threshold from SSR to MCSR around $\delta_D\tau \approx 3$. The red circles indicate the value of $\pm \text{Im}(\nu_0)$ at the threshold. In general we find three different appearances in the spectrum:

- (i) For sufficiently small values of $\delta_D\tau$ we find one narrow peak at $\omega = 0$ indicating coherent and steady-state superradiant emission with the atomic transition frequency. As an example we present a cut of the spectrum in this SSR phase in Fig. 6.8(a) where we also compare the spectrum for different values of N . We remark that in Fig. 6.8(a) the central peak is Fourier limited because of the finite integration time t_f .
- (ii) Beyond the transition we find beside the central peak at $\omega = 0$ also sidebands. These sidebands appear at the predicted value of $\pm \text{Im}(\nu_0)$. This is also visible in Fig. 6.8(b) where we have also plotted $\pm \text{Im}(\nu_0)$ as red vertical solid lines for the given parameters. The sidebands become better resolved with increasing N .
- (iii) Well inside the unstable regime, we find a third behavior where the central peak at $\omega = 0$ vanishes and we observe sidepeaks at odd multiples of $\pm \text{Im}(\nu_0)/2$. This is best visible in Fig. 6.8(c) where we also show $\pm \text{Im}(\nu_0)/2$ as vertical red solid lines corresponding to the given parameters. Here we also find that the peaks become better resolved for increasing N . The fact that we find a decreasing width of the sidebands for increasing N , as visible in Fig. 6.8(b–c), suggests that they are due to collective emission.

Remarkably, while the transition from (i)–(ii) is already visible in the length of the collective dipole and the intensity spectrum, the transition (ii)–(iii) is only visible in the coherences that are described by g_1 . In g_1 the peaks occur at $\pm \text{Im}(\nu_0)/2$ while the peaks in g_2 are still at $\pm \text{Im}(\nu_0)$. The reason for this is that during an intensity oscillation period $T = 2\pi/\text{Im}(\nu_0)$ the collective dipole gains the opposite sign ($J \rightarrow -J$). This phase-shift in the collective dipole results in the same intensity ($J^*J \rightarrow J^*J$) but doubles the period in J to $2T$. This highlights that the collective dipole is switching between two \mathbb{Z}_2 symmetric states in (iii).

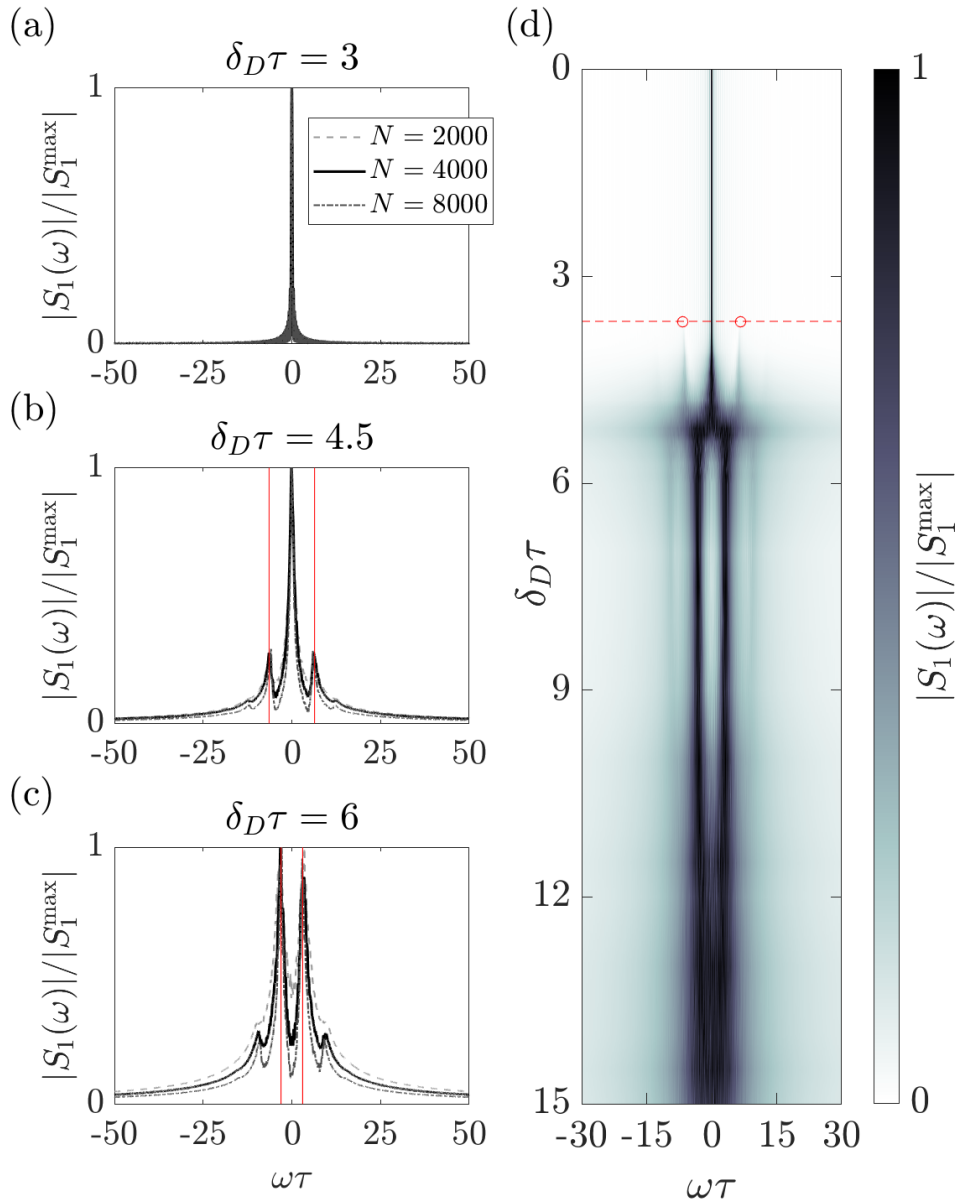


Figure 6.8: The spectrum $|S_1(\omega)|$ [Eq. (6.127)] plotted for $\delta_D\tau = 3$ (a), $\delta_D\tau = 4.5$ (b), $\delta_D\tau = 6$ (c) as a function of ω in units of $1/\tau$. The different lines correspond to different intracavity atom numbers N as shown in the inset of subplot (a). The spectrum is normalized for every δ_D by the maximum $|S_1^{\max}| \equiv \max_{\omega} |S_1(\omega)|$. The red vertical lines in (b) correspond to $\pm \text{Im}(\nu_0)$ where ν_0 is the zero of Eq. (6.69) with the largest real part. The red vertical lines in (c) correspond to $\pm \text{Im}(\nu_0)/2$. Subplot (d) shows the spectrum $|S_1(\omega)|$ as a function of δ_D and ω in units of τ for $N = 4000$. The red dashed horizontal line marks the threshold from the SSR to MCSR regime. The circles on this line are the values of $\pm \text{Im}(\nu_0)$ for the given parameters. All simulations were performed with $N\Gamma_c\tau = 50$, with a simulation time of $t_{\text{sim}} = 200\tau$ and averaged over $200000/N$ trajectories. The spectra are calculated using $t_0 = 10\tau$ and $t_f = 20\tau$.

To provide further details on this transition we use now a fixed value for the Doppler width $\delta_D\tau = 6$ and change the collective linewidth $N\Gamma_c\tau = 30\text{--}60$. For these parameters Fig. 6.5(a) predicts a transition from SSR to the MCSR phase. The corresponding results for $|S_1(\omega)|$ and $|S_2(\omega)|$ are visible in Figs. 6.9(a) and 6.9(b), respectively. The values of $\pm \text{Im}(\nu_0)$ are visible as red lines in Fig. 6.9(b) and are in good agreement with the sidebands of $|S_2(\omega)|$. We find that the sidebands become narrower when entering the MCSR phase, indicating long-lived intensity oscillations. In the spectrum $|S_1(\omega)|$ in Fig. 6.9(a) we have marked the theoretically predicted threshold from SSR to MCSR as red dashed horizontal line. The circles on this line show the values of $\pm \text{Im}(\nu_0)$ that agree with the emerging sidebands in $|S_1(\omega)|$. These sidebands become more and more pronounced, emerging from a broad distribution at approximately $N\Gamma_c\tau \approx 42$. Beyond this point we find no central peak but a period doubling that we compare to $\pm \text{Im}(\nu_0)/2$ visible as the red lines in Fig. 6.9(a). We find very good agreement between the sidebands of $|S_1(\omega)|$ and $\pm \text{Im}(\nu_0)/2$ for $N\Gamma_c\tau \gtrsim 42$.

In Fig. 6.9(c) we show

$$\Omega^2 \equiv (N\Gamma_c)^2 \langle J^* J \rangle, \quad (6.128)$$

which can be seen as the square of an effective Rabi frequency driving the individual dipoles. The quantity is reported in units of $1/\tau^2$ for different intracavity atom numbers [see legend of Fig. 6.9(c)]. The black solid line is the theoretical prediction obtained from Eq. (6.123) and is only in good agreement in the SSR phase. The transition between the SSR and the MCSR phases are shown as the vertical red dashed line. We find that the effective Rabi frequency is always larger than the theoretically predicted value.

6.5.5 Spontaneous emission and T_2 dephasing

In this section, we discuss the effect of additional noise terms on the observed superradiant phases. So far in our description we have neglected free-space spontaneous emission with rate γ_1 as well as T_2 dephasing. This can be justified if $\gamma_1\tau \ll 1$ and $\tau/T_2 \ll 1$. In this limit, both effects

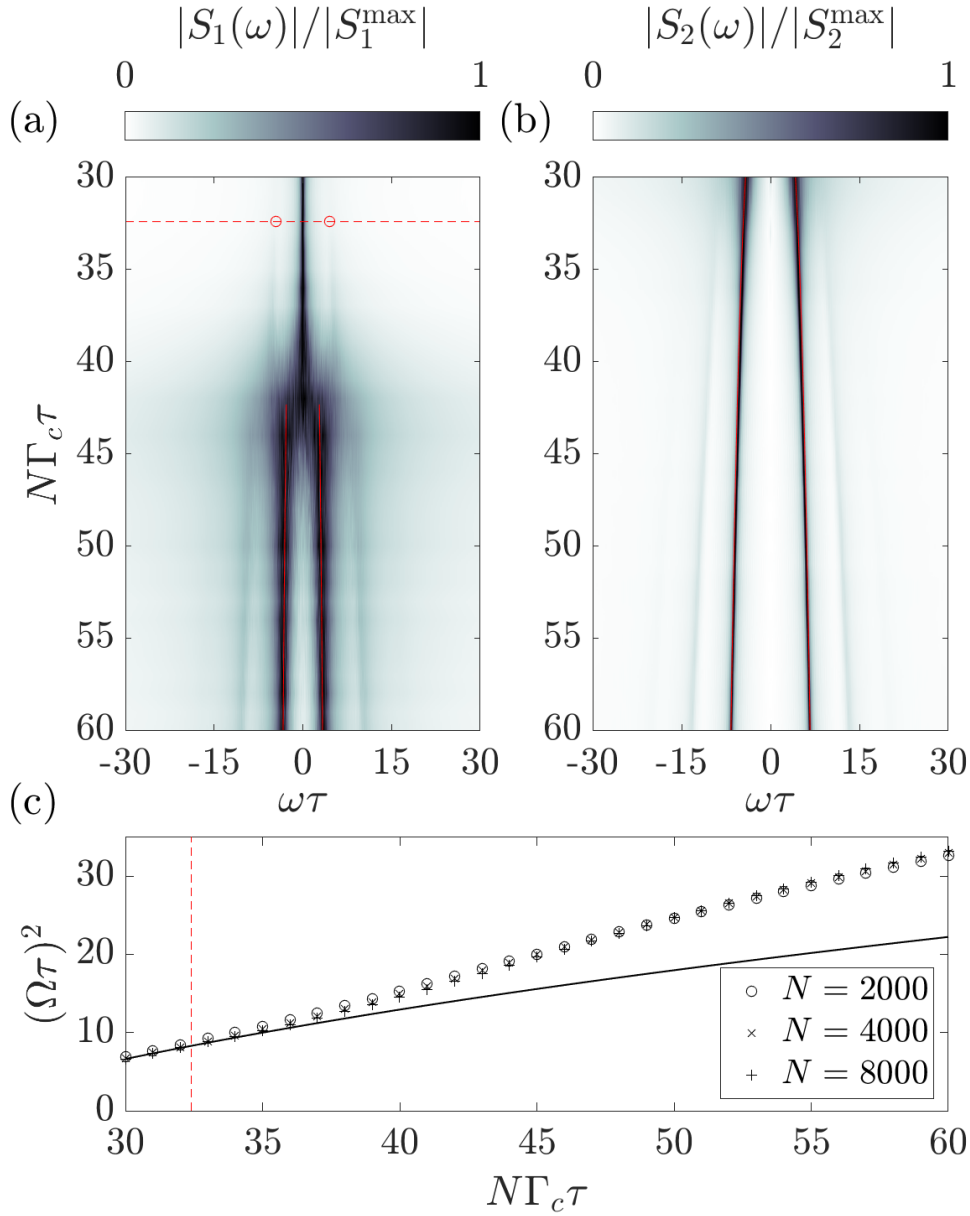


Figure 6.9: The spectrum $|S_1(\omega)|$ [Eq. (6.127)] (a) and the intensity spectrum $|S_2(\omega)|$ [Eq. (6.126)] (b) as a function of $N\Gamma_c$ and ω in units of $1/\tau$. Both spectra are normalized for every δ_D by the maximum $|S_n^{\max}| \equiv \max_{\omega} |S_n(\omega)|$ with $n \in \{1, 2\}$. The red dashed horizontal line in (a) marks the threshold between the SSR and the MCSR phase and the circles are the values of $\pm \text{Im}(\nu_0)$. Here, ν_0 is the zero of Eq. (6.69) with the largest real part. The red solid vertical lines are given by $\pm \text{Im}(\nu_0)/2$. In subplot (b) the red lines show the values of $\pm \text{Im}(\nu_0)$. For all results in subplots (a) and (b) we have used $N = 4000$, $t_0 = 10\tau$, $t_f = 20\tau$, and averaged over 50 trajectories. Subplot (c) shows the squared effective Rabi frequency [Eq. (6.128)] in units of $1/\tau^2$ as a function of the collective linewidth $N\Gamma_c$ in units of $1/\tau$. The data are shown for various values of N (see inset). The black solid line shows the result obtained from Eq. (6.123) and the red vertical dashed line shows the transition from SSR to MCSR. All simulations are performed for $\delta_D\tau = 6$.

are negligible during the transit time of an atom, and the corresponding noise is dominated by input noise and cavity shot noise. In order to observe superradiance we require $N\Gamma_c\tau > 1$, which results in $N\Gamma_c \gg \gamma_1$ given $\gamma_1\tau \ll 1$. This means that we assume a large collective cooperativity $NC = Ng^2/(\kappa\gamma_1) \gg 1$.

We will now show how we can add the effects of spontaneous emission and dephasing to our model.³ For this we now generalize the master equation in Eq. (6.1) to

$$\frac{d\hat{\rho}}{dt} = \frac{1}{i\hbar} [\hat{H}, \hat{\rho}] + \kappa\mathcal{L}[\hat{a}]\hat{\rho} + \sum_j \left\{ \gamma_1\mathcal{L}[\hat{\sigma}_j^-] + \frac{\gamma_2}{4}\mathcal{L}[\hat{\sigma}_j^z] \right\} \hat{\rho}, \quad (6.129)$$

where $\gamma_2 = 2/T_2$ is the rescaled T_2 dephasing rate [101]. Using this master equation, we can eliminate the cavity field and derive the full c -number Heisenberg-Langevin equations. These c -number stochastic differential equations for the dipole components are given by

$$\frac{ds_j^x}{dt} = \frac{\Gamma_c}{2}\eta(\mathbf{x}_j)s_j^z J^x - \frac{\gamma_1 + \gamma_2}{2}s_j^x + \mathcal{F}_j^x, \quad (6.130)$$

$$\frac{ds_j^y}{dt} = \frac{\Gamma_c}{2}\eta(\mathbf{x}_j)s_j^z J^y - \frac{\gamma_1 + \gamma_2}{2}s_j^y + \mathcal{F}_j^y, \quad (6.131)$$

$$\frac{ds_j^z}{dt} = -\frac{\Gamma_c}{2}\eta(\mathbf{x}_j) \left(J^x s_j^x + J^y s_j^y \right) - \gamma_1(s_j^z + 1) + \mathcal{F}_j^z, \quad (6.132)$$

where we have used noise terms $\mathcal{F}_j^\alpha = \mathcal{S}_j^\alpha + \mathcal{F}_{j,\gamma_1}^\alpha + \mathcal{F}_{j,\gamma_2}^\alpha$ for $\alpha \in \{x, y, z\}$. While the noise terms \mathcal{S}_j^α have been given in Eqs. (6.12)–(6.15), we now introduce two additional independent noise sources $\mathcal{F}_{j,\gamma_1}^\alpha$ and $\mathcal{F}_{j,\gamma_2}^\alpha$, which originate from spontaneous emission and T_2 dephasing, respectively. These noise terms fulfill $\langle \mathcal{F}_{j,\gamma_1}^\alpha(t) \mathcal{F}_{k,\gamma_1}^\beta(t') \rangle = 2(m_{j,\gamma_1})_{\alpha\beta} \delta_{jk} \delta(t-t')$ and $\langle \mathcal{F}_{j,\gamma_2}^\alpha(t) \mathcal{F}_{k,\gamma_2}^\beta(t') \rangle = 2(m_{j,\gamma_2})_{\alpha\beta} \delta_{jk} \delta(t-t')$, with the diffusion matrices given by

$$m_{j,\gamma_1} = \begin{array}{c} \beta=x \quad y \quad z \\ \alpha=x \quad \left(\begin{array}{ccc} 1 & 0 & s_j^x \\ 0 & 1 & s_j^y \\ s_j^x & s_j^y & 2(1+s_j^z) \end{array} \right) \\ y \\ z \end{array} \frac{\gamma_1}{2} \quad (6.133)$$

³See Chap. 4 for a detailed discussion on how to include these effects.

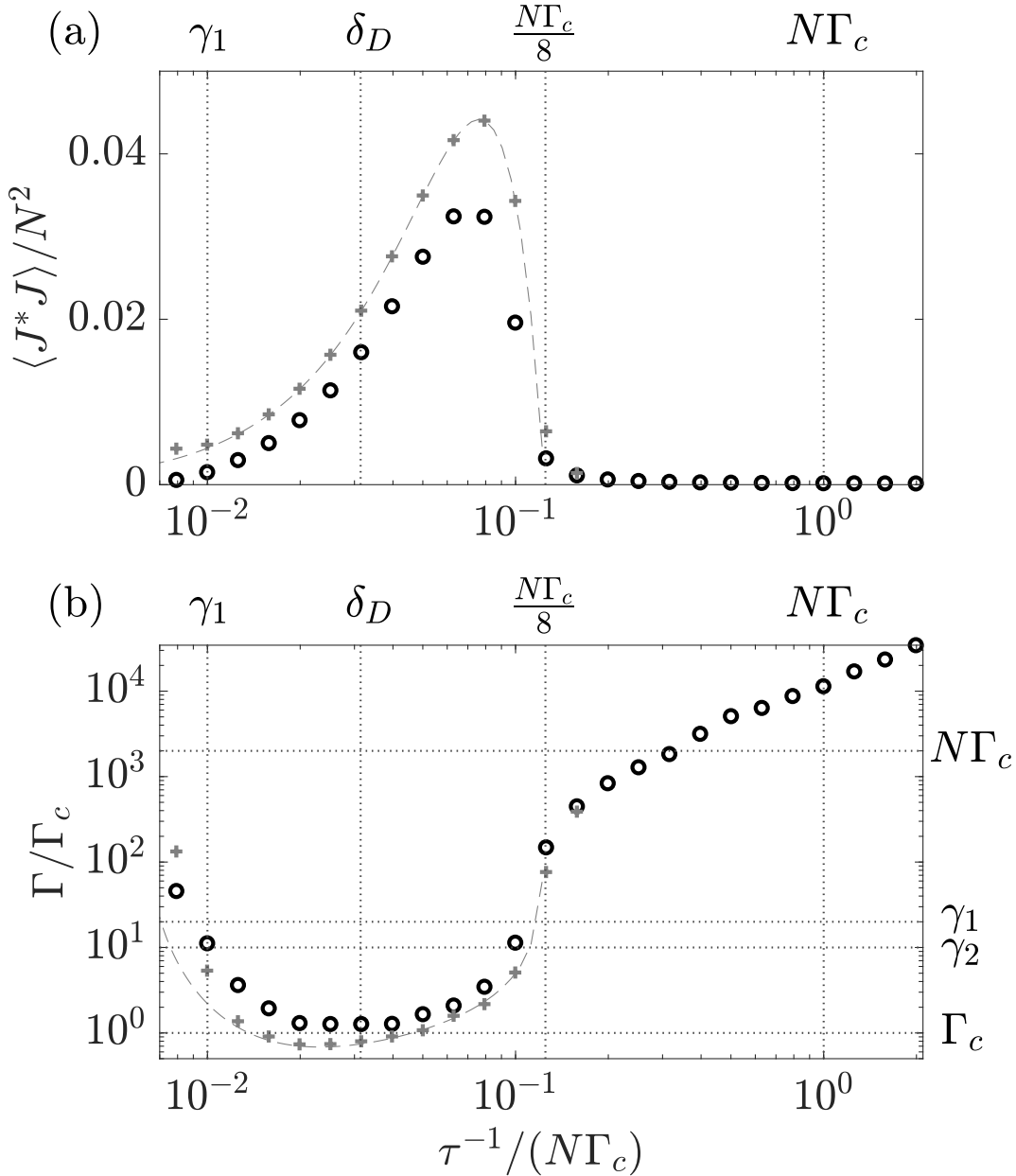


Figure 6.10: The normalized collective dipole correlation $\langle J^* J \rangle / N^2$ (a) and the linewidth Γ in units of the single-atom linewidth Γ_c (b) as a function of transit-time broadening τ^{-1} in units of $N\Gamma_c$. The black circles are simulation results using Eqs. (6.130)–(6.132). We have fixed $\delta_D / (N\Gamma_c) = \pi \times 10^{-2}$, $\gamma_1 / (N\Gamma_c) = 10^{-2}$, $\gamma_2 / (N\Gamma_c) = 5 \times 10^{-3}$, and the intracavity atom number $N = 2000$. The linewidth is calculated by fitting the g_1 function using $t_0 = 10\tau$ to an exponential $\propto \exp(-\Gamma t/2)$ over a varying t_f . All the simulations were performed with $t_{\text{sim}} = 100\tau$ and averaged over 100 trajectories. The gray plus symbols are simulation results using the same parameters except for $\gamma_1 = 0 = \gamma_2$. The gray dashed lines are analytical solutions, giving in (a) the value of $(j_0^{\parallel})^2/4$ using Eq. (6.123), and in (b) the linewidth Eq. (6.110) calculated using Eq. (6.121) with corresponding values of j_0^{\parallel} , respectively.

and

$$m_{j,\gamma_2} = \begin{matrix} & \beta=x & y & z \\ \alpha=x & \left(\begin{array}{ccc} 1 & 0 & 0 \\ 0 & 1 & 0 \\ 0 & 0 & 0 \end{array} \right) & & \\ y & & & \\ z & & & \end{matrix} \frac{\gamma_2}{2}. \quad (6.134)$$

We simulate Eqs. (6.130)–(6.132) for the numerical results we present below.

We first investigate how these noise sources affect the SSR phase and in particular the intensity and the linewidth of the produced light. In particular we focus on the regime where the collective linewidth is much larger than the Doppler width $\delta_D/(N\Gamma_c) = \pi \times 10^{-2}$, the spontaneous emission rate $\gamma_1/(N\Gamma_c) = 10^{-2}$, and the dephasing $\gamma_2/(N\Gamma_c) = 5 \times 10^{-3}$. We fix the intracavity atom number $N = 2000$ and vary the ratio between τ^{-1} and $N\Gamma_c$. In Fig. 6.10(a) we show the results of $\langle J^* J \rangle / N^2$ for these parameters as black circles. For comparison we have performed simulations with $\gamma_1 = 0 = \gamma_2$ visible as gray pluses and also plotted the analytical result corresponding to the solution of Eq. (6.123) as gray dashed line. While we find almost perfect agreement between the analytical result and the simulation with $\gamma_1 = 0 = \gamma_2$, the numerical results including spontaneous emission are always smaller. This can be expected because spontaneous emission and dephasing will both result in a decrease of coherence in the atomic dipoles and therefore result in a reduced light intensity. In addition, free-space spontaneous emission also leads to a loss of excitations into electromagnetic modes external to the cavity mode. Nevertheless, we find very good agreement for the threshold of superradiance that for the considered parameter regime is close to $\tau^{-1}/(N\Gamma_c) = 1/8$. We also find a similar functional behavior of $\langle J^* J \rangle / N^2$ for the simulations with and without spontaneous emission and dephasing.

Figure 6.10(b) shows the linewidth Γ calculated by fitting the g_1 function given by Eq. (6.77) with $\exp(-\Gamma t/2)$ obtained from simulations including (black circles) and without spontaneous emission and dephasing (gray pluses). We also compare our results to the analytical estimate from Eq. (6.110) visible as gray dashed line. We find very good agreement between the simulations without spontaneous emission and dephasing and the analytical result as long as $\tau^{-1}/(N\Gamma_c) > 10^{-2}$.

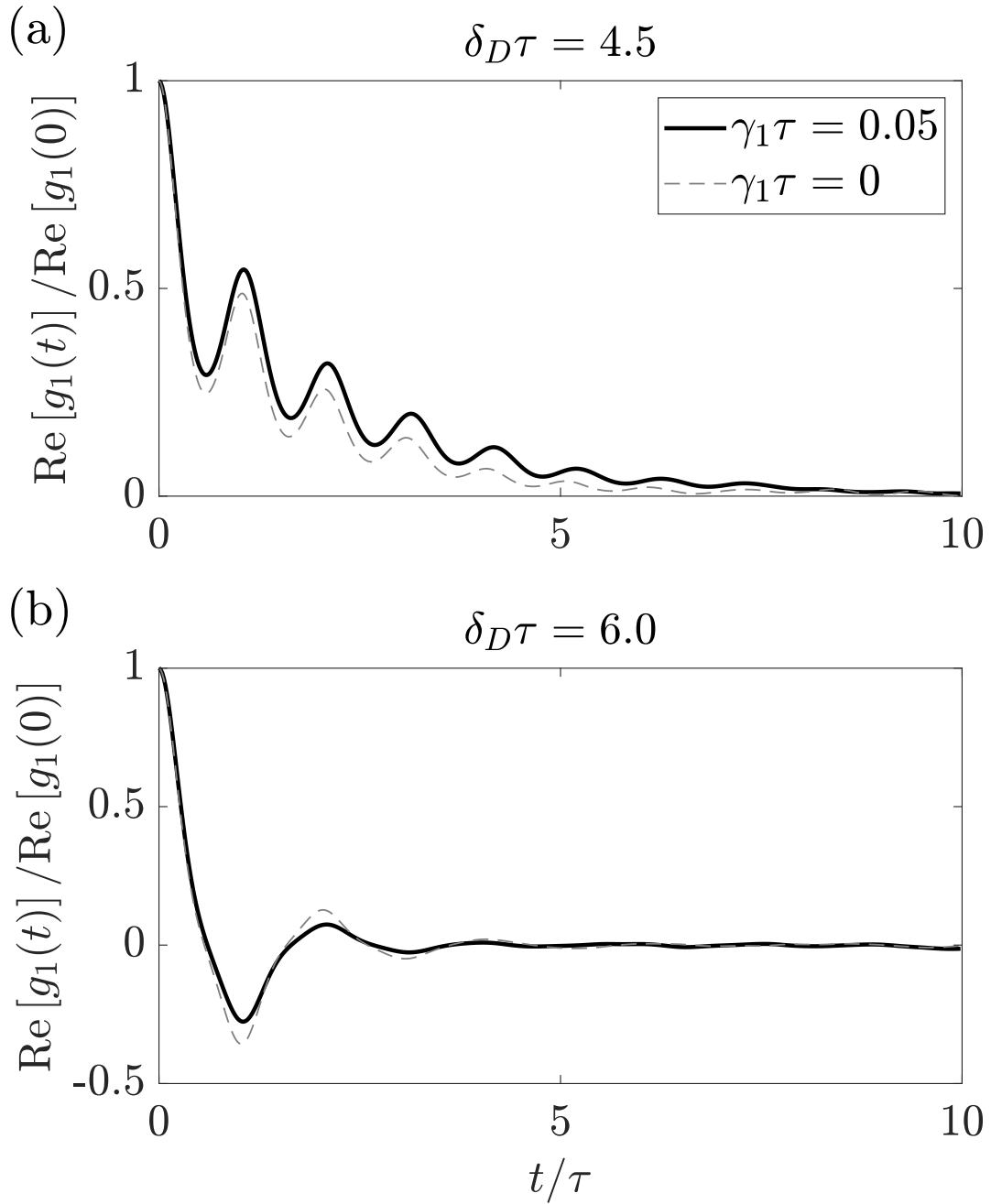


Figure 6.11: Simulation results of the real part of $g_1(t)$ normalized by $\text{Re}[g_1(0)]$ for $\delta_D \tau = 4.5$ (a) and $\delta_D \tau = 6.0$ (b). For the black solid lines we have used $N\Gamma_c \tau = 50$, $\gamma_1 = 0.05\tau^{-1}$ with $N = 4000$ and $t_{\text{sim}} = 200$. The g_1 function is calculated using $t_0 = 10\tau$ and averaged over 50 trajectories. For the gray dashed lines we have used the same parameters except for $\gamma_1 = 0$. These dashed lines are the real parts of the g_1 functions that are used to calculate the spectra shown in Figs. 6.8(b) and 6.8(c).

Below this point we find a rather small coherent collective dipole component and cannot expect that the phase diffusion argument that has been used to derive the analytical result will still be valid. The simulations including spontaneous emission show a very similar functional dependence but are almost always slightly above the simulation results without spontaneous emission. Still, we find a minimum linewidth of the order of Γ_c that is orders of magnitude smaller than γ_1 and γ_2 . This highlights the fact that the linewidth of the generated light is typically not limited by any single-particle dephasing mechanism.

We will now study the stability of the MCSR phase. For this we choose the same parameters where we have observed the two different emission regimes in Figs. 6.8(b) and 6.8(c), i.e., $N\Gamma_c\tau = 50$, $\delta_D\tau = 4.5$ and $\delta_D\tau = 6.0$, respectively. We now add a small spontaneous emission rate $\gamma_1\tau = 0.05$ to our previous simulations. We plot the real part of the g_1 function $\text{Re}(g_1)$ in Fig. 6.11 for $\delta_D\tau = 4.5$ (a) and $\delta_D\tau = 6.0$ (b). The simulations without spontaneous emission are visible as gray dashed lines and the simulations with spontaneous emission as black solid lines.

In Fig. 6.11(a) we find a positive $\text{Re}(g_1)$ with oscillations for both simulation types that are in good agreement. As a consequence, we also find a similar spectrum as shown in Fig. 6.8(b). Remarkably, our simulation results suggest that the oscillations have a slightly longer lifetime for non-vanishing γ_1 .

Figure 6.11(b) shows very good agreement between the two simulations with and without spontaneous emission. We find $\text{Re}(g_1)$ oscillating around zero, therefore giving rise to a similar spectrum as in Fig. 6.8(c). Our findings show that the change of the sign in $\text{Re}(g_1)$ that occurs with half the frequency of the intensity oscillations is robust against small additional noise sources.

6.6 Conclusions

In this chapter we have studied the onset and stability of collective emission of an atomic beam that traverses an optical cavity. We have developed a semiclassical theoretical framework to study the dynamics of the atomic dipoles in the presence of Doppler broadening. We have analyzed this model using a mean-field description and determined the stability of the non-superradiant (NSR)

and steady-state superradiant (SSR) phases. These results were used to analyze the stationary light emission of the corresponding phases and predict a linewidth of the emitted light. After that we investigated a model using numerical simulations and presented analytical techniques that provide supporting analysis. We explored a SSR phase and a dynamical superradiant phase with a multi-component superradiant (MCSR) light output. With our derived theory we were able to quantitatively predict the threshold of the MCSR phase and the occurrence of sidebands in the spectra. In addition, we found that these results are robust against free-space spontaneous emission and T_2 dephasing processes if they are small compared to transit-time broadening and Doppler broadening.

We highlight that the MCSR phase is observed in presence of relatively large Doppler broadening. This is potentially easier to realize in actual experimental setups working with thermal atomic beams. Nevertheless, for the observation of the MCSR phase one still requires a collective linewidth that overcomes all broadening mechanism including Doppler broadening.

We have focused on the interplay between collective emission and thermal broadening in the parameter regime where thermal effects dominate dephasing processes such as free-space spontaneous emission. However, we expect that these effects become important for cold or even ultracold atomic beams when the Doppler broadening becomes comparable to the linewidth of the atomic dipoles. In this parameter regime one could potentially study subradiance in the regime where the transit time becomes comparable to the atomic lifetime [153, 143]. Additionally, one could explore the regime where the collective linewidth becomes comparable to the recoil frequency [16, 15, 14, 145, 66, 67] and the semiclassical theory used in this chapter becomes invalid. Such parameter regimes could be achievable regarding the recent progress on producing high phase-space density atomic beams [24].

Chapter 7

Collective Emission of an Atomic Beam into an Off-Resonant Cavity Mode ¹

7.1 Introduction

Atomic ensembles in optical cavities provide a versatile platform to study collective effects that arise from strong light-matter interactions. These systems have been employed to study spatial pattern formation including self-organization [37, 8, 125], synchronization [3, 56, 166, 172, 161], and also spin ordering or texturing [106, 79, 84]. They are intrinsically open quantum systems because photons can enter and leave through the cavity mirrors while external driving usually balances cavity losses and allows the stabilization of coherent out-of-equilibrium states.

The success of these systems also relies on the good controllability of cavity-mediated interactions in atomic systems. These can be tuned by adjusting the parameters of the driving lasers but also by varying the detunings between the atomic transitions and cavity mode frequencies. For instance, if an ensemble of metastable dipoles couple to a resonant cavity the dynamics will mostly be dominated by dissipation in form of spontaneous as well as superradiant or subradiant emission [32, 52, 154, 116]. In contrast, for the case of large detuning, the dynamics remains coherent on long timescales, and these setups can be used for quantum simulations of collective physics [108] and even for spin squeezing [89, 90, 118].

However, fluctuations in the cavity detuning are also a major source of noise. One of the main obstacles that limit the precision of the state-of-the-art cavity-assisted atomic clocks is the quantum noise caused by cavity detuning from mirror fluctuations. Recently, it has been found that

¹The bulk of this work has been published in Physical Review A [68]. Copyright 2021 American Physical Society.

the noise caused by such fluctuations can be minimized by having systems working in a so-called “bad cavity” parameter regime [101, 12, 115, 59]. In this regime, the phase information of the output field is stored in the atomic ensemble rather than the cavity. Such systems, including active atomic clocks [25] and superradiant lasers [12, 115, 87, 136, 150, 29], are becoming candidates for future standards of quantum metrology.

Despite the fundamental interest in these kind of systems, only a few works investigate the effect of continuously introducing and removing atoms. Recently, the use of an atomic beam to study superradiant lasing and dynamical phases have been discussed [153, 92, 70, 69]. These atomic-beam cavity configurations represent interesting situations where neither photons nor individual atoms remain in the cavity on long timescales, but nevertheless cooperative effects can beat single-atom constraints.

In this chapter we investigate the collective emission of an atomic beam into an off-resonant cavity. The finite detuning between the cavity and atomic transitions results in a collective Lamb shift [52]. We investigate the special case where the atoms enter in their electronic excited state and discuss how the collectively emitted light depends on the detuning. We study cavity pulling effects in this setup, which describes the shift of the emission frequency in the direction of the cavity resonance, and investigate the dynamical superradiant phases that emerge.

This chapter is structured as follows. In Sec. 7.2 we introduce the theoretical framework to describe the coupled dynamics between the atomic beam and the cavity mode. We derive stationary solutions of this description in Sec. 7.3 where we also derive an analytical expression for the cavity pulling coefficient. Section 7.4 treats the stability of the stationary atomic configuration and studies the onset of superradiance and the destabilization of the superradiant phase. In Sec. 7.5 we investigate a specific model and derive expressions for the stationary phases, and we compare our results to numerical simulations of this system. After that we conclude our results in Sec. 7.6 while the Appendix provides further details to some calculations contained in Sec. 7.4.

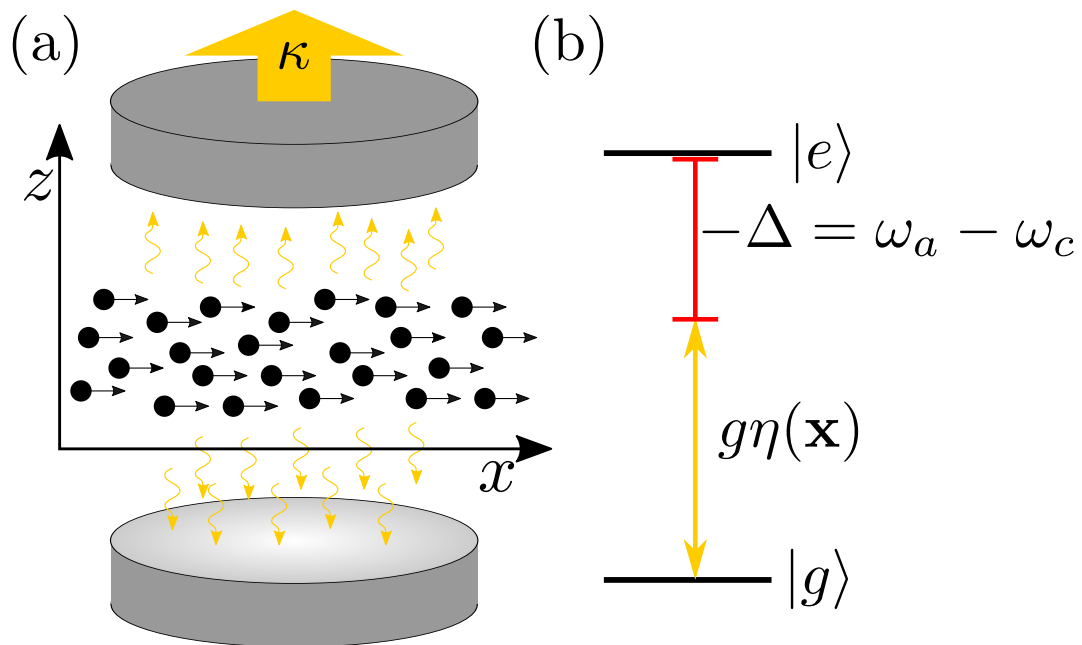


Figure 7.1: (a) Atoms enter the cavity in the excited state $|e\rangle$ and can emit photons into a single cavity mode. Photons leak out through the cavity output mirror with rate κ . (b) Each atom is represented as an optical dipole of transition frequency ω_a coupled to the cavity mode of frequency ω_c . The coupling $g\eta(\mathbf{x})$ depends on the position \mathbf{x} of the atom, where g is the vacuum Rabi frequency or Jaynes-Cummings coupling coefficient and $\eta(\mathbf{x})$ is the mode function. The cavity-atom detuning frequency is given by $\Delta = \omega_c - \omega_a$.

7.2 Theoretical model

In this section we introduce the theoretical description of the dynamics of the atomic beam coupled to an off-resonant cavity.

7.2.1 Master equation formalism

We consider a beam of two-level atomic dipoles in their excited state $|e\rangle$ with transition frequency ω_a and mass m traversing an optical cavity. These atoms can emit photons into a single cavity mode of frequency ω_c (see Fig. 7.1).

The density matrix $\hat{\rho}$ describing the atomic and cavity degrees of freedom is governed by a Born-Markov master equation

$$\frac{d\hat{\rho}}{dt} = \frac{1}{i\hbar} [\hat{H}, \hat{\rho}] - \frac{\kappa}{2} (\hat{a}^\dagger \hat{a} \hat{\rho} + \hat{\rho} \hat{a}^\dagger \hat{a} - 2\hat{a} \hat{\rho} \hat{a}^\dagger). \quad (7.1)$$

Here, the Hamiltonian

$$\hat{H} = \hbar\Delta \hat{a}^\dagger \hat{a} + \sum_j \left[\frac{\hat{\mathbf{p}}_j^2}{2m} + \frac{\hbar g}{2} \eta(\hat{\mathbf{x}}_j) (\hat{a}^\dagger \hat{\sigma}_j^- + \hat{\sigma}_j^+ \hat{a}) \right] \quad (7.2)$$

describes the coherent dynamics of the coupled atom-cavity system in a frame rotating with ω_a . The first term determines the energy of cavity photons where $\Delta = \omega_c - \omega_a$ is the detuning between the cavity and the atomic frequency. Operators \hat{a} and \hat{a}^\dagger are the photonic annihilation and creation operators that fulfill the commutation relation $[\hat{a}, \hat{a}^\dagger] = 1$. The second term in Eq. (7.2) is the kinetic energy of atom j where j runs over all atoms in the atomic beam. The last term in Eq. (7.2) describes the Jaynes-Cummings coupling between an atom and the cavity, where g is the vacuum Rabi frequency at a field maximum and $\eta(\hat{\mathbf{x}})$ is the cavity mode function evaluated at position $\hat{\mathbf{x}}$.

The atomic position operator $\hat{\mathbf{x}}_j = (\hat{x}_j, \hat{y}_j, \hat{z}_j)^\text{T}$ is conjugate to the momentum operator $\hat{\mathbf{p}}_j = (\hat{p}_{x,j}, \hat{p}_{y,j}, \hat{p}_{z,j})^\text{T}$ with the usual canonical commutation relations $[\hat{\mu}_j, \hat{p}_{\nu,k}] = i\hbar \delta_{jk} \delta_{\mu\nu}$, $\mu, \nu \in \{x, y, z\}$. The operators $\hat{\sigma}_j^+ = |e\rangle_j \langle g|_j$ and $\hat{\sigma}_j^- = |g\rangle_j \langle e|_j$ are the atomic raising and lowering operators, where $|e\rangle_j, |g\rangle_j$ denote electronic excited and ground states.

Dissipation in this system is described by the Lindblad term in the master equation Eq. (7.1). This describes the leakage of cavity photons into the free-space electromagnetic field with rate κ , typically referred to as the cavity linewidth.

7.2.2 Heisenberg-Langevin equations

The master equation formalism introduced in Sec. 7.2.1 is equivalent to the Heisenberg-Langevin equations that are given by

$$\frac{d\hat{a}}{dt} = - \left(i\Delta + \frac{\kappa}{2} \right) \hat{a} - i\frac{g}{2} \hat{J}^- + \hat{\mathcal{F}}^-, \quad (7.3)$$

$$\frac{d\hat{\sigma}_j^-}{dt} = \frac{ig}{2} \eta(\hat{\mathbf{x}}_j) \hat{\sigma}_j^z \hat{a}, \quad (7.4)$$

$$\frac{d\hat{\sigma}_j^z}{dt} = ig\eta(\hat{\mathbf{x}}_j) \left(\hat{a}^\dagger \hat{\sigma}_j^- - \hat{\sigma}_j^+ \hat{a} \right), \quad (7.5)$$

$$\frac{d\hat{\mathbf{x}}_j}{dt} = \frac{\hat{\mathbf{p}}_j}{m}, \quad (7.6)$$

$$\frac{d\hat{\mathbf{p}}_j}{dt} = - \frac{g\hbar}{2} (\hat{a}^\dagger \hat{\sigma}_j^- + \hat{\sigma}_j^+ \hat{a}) \nabla_{\mathbf{x}} \eta(\mathbf{x})|_{\mathbf{x}=\hat{\mathbf{x}}_j}. \quad (7.7)$$

Here we have represented the gradient as $\nabla_{\mathbf{x}} \equiv (\partial/\partial x, \partial/\partial y, \partial/\partial z)^T$, and included the cavity shot noise $\hat{\mathcal{F}}^-$ that fulfills expectation values $\langle \hat{\mathcal{F}}^-(t) \rangle = 0$, $\langle \hat{\mathcal{F}}^-(t') \hat{\mathcal{F}}^-(t) \rangle = 0 = \langle \hat{\mathcal{F}}^+(t') \hat{\mathcal{F}}^-(t) \rangle$, and $\langle \hat{\mathcal{F}}^-(t') \hat{\mathcal{F}}^+(t) \rangle = \kappa \delta(t - t')$, with $\hat{\mathcal{F}}^+ = (\hat{\mathcal{F}}^-)^\dagger$. The operators $\hat{\sigma}_j^z = \hat{\sigma}_j^+ \hat{\sigma}_j^- - \hat{\sigma}_j^- \hat{\sigma}_j^+$ describe the population inversion. The operator \hat{J}^- is the collective dipole and is defined as

$$\hat{J}^- = \sum_j \eta(\hat{\mathbf{x}}_j) \hat{\sigma}_j^-. \quad (7.8)$$

We are interested in the situation where dipoles in the atomic beam transverse the cavity mode with a large velocity. Assuming a mean velocity v_x perpendicular to the cavity axis [see Fig.7.1(a)], we can estimate the transit time as $\tau = 2w/v_x$ where w is the beam waist of the cavity mode. Throughout this chapter we will neglect optomechanical forces that are described by Eq. (7.7) and consider only ballistic motion. This is valid in the parameter regime where the atomic momentum distribution has a width $\Delta p_\mu = \sqrt{\langle \hat{p}_\mu^2 \rangle - \langle \hat{p}_\mu \rangle^2}$ that exceeds the mean force F_a times the transit time τ in every spatial direction $\mu \in \{x, y, z\}$. In this regime we may assume that the momentum of each atom is constant.

7.2.3 Semiclassical description

We will now make a semiclassical approximation where we substitute the operators by c -number variables and add noise terms that give the correct second moments. Similar approaches have been used in Refs. [92, 70, 69, 133]. Specifically, we replace the position operators $\hat{\mathbf{x}}_j$ by the classical variables \mathbf{x}_j . We derive the time evolution of the Hermitian cavity operators $\hat{a}^x = \hat{a} + \hat{a}^\dagger$, $\hat{a}^y = i(\hat{a} - \hat{a}^\dagger)$ and atomic dipole operators $\hat{\sigma}_j^x = \hat{\sigma}_j^- + \hat{\sigma}_j^+$, $\hat{\sigma}_j^y = i(\hat{\sigma}_j^- - \hat{\sigma}_j^+)$, $\hat{\sigma}_j^z$, and then substitute them by their classical counterparts; α^x , α^y for the cavity and s_j^x , s_j^y , and s_j^z for the dipoles. The c -number noise terms are chosen such that the second moments of two classical variables A , B relate in the form $\langle AB \rangle = \langle \hat{A}\hat{B} + \hat{B}\hat{A} \rangle / 2$ to the second moment of their corresponding operators \hat{A} and \hat{B} ; i.e., we choose symmetric ordering of the operators. The resulting c -number stochastic differential equations read

$$\frac{d\alpha^x}{dt} = -\frac{\kappa}{2}\alpha^x - \Delta\alpha^y - \frac{g}{2}J^y + \mathcal{F}^x, \quad (7.9)$$

$$\frac{d\alpha^y}{dt} = \Delta\alpha^x - \frac{\kappa}{2}\alpha^y + \frac{g}{2}J^x + \mathcal{F}^y, \quad (7.10)$$

$$\frac{ds_j^x}{dt} = \frac{g}{2}\eta(\mathbf{x}_j)s_j^z\alpha^y, \quad (7.11)$$

$$\frac{ds_j^y}{dt} = -\frac{g}{2}\eta(\mathbf{x}_j)s_j^z\alpha^x, \quad (7.12)$$

$$\frac{ds_j^z}{dt} = \frac{g}{2}\eta(\mathbf{x}_j)(\alpha^x s_j^y - \alpha^y s_j^x). \quad (7.13)$$

$$\frac{d\mathbf{x}_j}{dt} = \frac{\mathbf{p}_j}{m}, \quad (7.14)$$

Here, \mathcal{F}^x and \mathcal{F}^y are independent noise terms defined by $\langle \mathcal{F}^x \rangle = \langle \mathcal{F}^y \rangle = \langle \mathcal{F}^x(t)\mathcal{F}^y(t') \rangle = 0$ and $\langle \mathcal{F}^x(t)\mathcal{F}^x(t') \rangle = \langle \mathcal{F}^y(t)\mathcal{F}^y(t') \rangle = \kappa\delta(t-t')$. In Eqs. (7.9)–(7.10), J_x and J_y are the classical x and y components of the collective dipole given by $J^x = \sum_j \eta(\mathbf{x}_j)s_j^x$ and $J^y = \sum_j \eta(\mathbf{x}_j)s_j^y$. Eq. (7.14) describes the ballistic trajectory.

Noise is not only introduced by the cavity degrees of freedom, but also by the boundary conditions. We will investigate the dynamics of atoms that enter the cavity in the excited state $|e\rangle$. Therefore if an atom indexed by j enters the cavity, we initialize $s_j^z = 1$ and choose the x and y components of the dipoles randomly and independently from $s_j^x = \pm 1$ and $s_j^y = \pm 1$. This

accounts for the correct second moments of all dipole components (see Refs. [92, 70, 69]). With these boundary constraints, Eqs. (7.9)–(7.14) can be directly implemented in numerical simulations. In the next section, we will introduce a density method to analytically solve these equations.

7.2.4 Density description

We will now use Eqs. (7.11)–(7.14) to derive a collective description of the atomic beam. For this we define the densities

$$f(\mathbf{x}, \mathbf{p}, t) = \sum_j \delta(\mathbf{x} - \mathbf{x}_j) \delta(\mathbf{p} - \mathbf{p}_j), \quad (7.15)$$

$$s^\mu(\mathbf{x}, \mathbf{p}, t) = \sum_j s_j^\mu \delta(\mathbf{x} - \mathbf{x}_j) \delta(\mathbf{p} - \mathbf{p}_j), \quad (7.16)$$

where the s_j^μ are pseudospin components with $\mu \in \{x, y, z\}$. Using these definitions together with Eqs. (7.11)–(7.14) we obtain

$$\frac{\partial f}{\partial t} + \frac{\mathbf{p}}{m} \cdot \nabla_{\mathbf{x}} f = 0, \quad (7.17)$$

$$\frac{\partial s^x}{\partial t} + \frac{\mathbf{p}}{m} \cdot \nabla_{\mathbf{x}} s^x = \frac{g}{2} \eta(\mathbf{x}) s^z \alpha^y, \quad (7.18)$$

$$\frac{\partial s^y}{\partial t} + \frac{\mathbf{p}}{m} \cdot \nabla_{\mathbf{x}} s^y = -\frac{g}{2} \eta(\mathbf{x}) s^z \alpha^x, \quad (7.19)$$

$$\frac{\partial s^z}{\partial t} + \frac{\mathbf{p}}{m} \cdot \nabla_{\mathbf{x}} s^z = \frac{g}{2} \eta(\mathbf{x}) (\alpha^x s^y - \alpha^y s^x). \quad (7.20)$$

The collective dipole in Eqs. (7.9)–(7.10) can be also expressed as an integral over dipole densities

$$J^\mu = \int d\mathbf{x} \int d\mathbf{p} \eta(\mathbf{x}) s^\mu(\mathbf{x}, \mathbf{p}, t), \quad (7.21)$$

with $\mu \in \{x, y\}$.

Equations (7.17)–(7.20) are closed with the time evolution of the field variables in Eq. (7.9)–(7.10). It remains to include the atomic noise terms in this density formalism. To do this, we formulate the initial conditions for the atoms entering the cavity as boundary conditions for the partial differential equations (7.17)–(7.20). Assuming that the atoms enter the cavity in the plane

$x = -x_0$ [see Fig. 7.1(a)], we can ascribe as initial conditions;

$$f(-x_0, y, z, \mathbf{p}, t) = f_0(y, z, \mathbf{p}, t), \quad (7.22)$$

$$s^x(-x_0, y, z, \mathbf{p}, t) = W^x(y, z, \mathbf{p}, t), \quad (7.23)$$

$$s^y(-x_0, y, z, \mathbf{p}, t) = W^y(y, z, \mathbf{p}, t), \quad (7.24)$$

$$s^z(-x_0, y, z, \mathbf{p}, t) = f_0(y, z, \mathbf{p}, t). \quad (7.25)$$

The boundary condition for the density is given by

$$f_0(y, z, \mathbf{p}, t) = \sum_j \delta(\mathbf{x}_0 - \mathbf{x}_j) \delta(\mathbf{p} - \mathbf{p}_j), \quad (7.26)$$

where $\mathbf{x}_0 = (-x_0, y, z)^T$ is the position where the atoms enter. We can therefore express the initial condition for the dipoles as

$$W^\mu(y, z, \mathbf{p}, t) = \sum_j s_j^\mu \delta(\mathbf{x}_0 - \mathbf{x}_j) \delta(\mathbf{p} - \mathbf{p}_j), \quad (7.27)$$

with $\mu \in \{x, y\}$, and for the second moment as

$$\langle W^\mu (W^\nu)' \rangle = \frac{m}{p_x} \delta_{\mu\nu} \delta(t - t') \delta(y - y') \delta(z - z') \delta(\mathbf{p} - \mathbf{p}') f_0(y, z, \mathbf{p}, t), \quad (7.28)$$

where we have used the notation $W^\mu = W^\mu(y, z, \mathbf{p}, t)$ and $(W^\nu)' = W^\nu(y', z', \mathbf{p}', t')$.

Throughout this chapter we will assume that the atomic density after one transit time τ is spatially homogeneous in the cavity. This results in the property

$$\langle f(\mathbf{x}, \mathbf{p}, t \gg \tau) \rangle = \rho(\mathbf{p}), \quad (7.29)$$

where $\rho(\mathbf{p})$ is a continuous spatially homogeneous density of the atoms that is time independent. This, however, does not imply that the dipole densities s^μ , $\mu \in \{x, y, z\}$, are spatially independent, as we will expand on in the next section.

7.3 Stationary states of the system

We will now investigate the asymptotic stationary solution reached after a sufficiently long time, $t \gg \tau$, of the coupled equations for the field, Eqs. (7.9)–(7.10), and dipole densities,

Eqs. (7.18)–(7.20). To obtain these results we will use the previously mentioned assumption of a spatially homogeneous atomic density. In addition, we will discard all noise terms, which implies a mean-field approximation.

7.3.1 The non-superradiant solution

We begin with the simplest solution that describes the situation when the atoms cross the cavity without generating a coherent light field. This is a trivial stationary state of the system given by

$$\alpha_0^x = 0, \quad (7.30)$$

$$\alpha_0^y = 0, \quad (7.31)$$

$$s_0^x = 0, \quad (7.32)$$

$$s_0^y = 0, \quad (7.33)$$

$$s_0^z = \rho(\mathbf{p}). \quad (7.34)$$

In this case, the atoms simply remain in the excited state $|e\rangle$ while traveling through the cavity region.

7.3.2 The superradiant solution

We now derive the more interesting superradiant solution. In order to reduce the equations, we rotate to a complex field $\alpha = (\alpha^x - i\alpha^y)/2$ and complex dipole density $s = (s^x - is^y)/2$. Using these definitions in Eqs. (7.9)–(7.10) and Eqs. (7.18)–(7.19), we derive the following mean-field equations

$$\frac{d\alpha}{dt} = - \left(i\Delta + \frac{\kappa}{2} \right) \alpha - i\frac{g}{2} \int d\mathbf{x} \int d\mathbf{p} \eta(\mathbf{x}) s, \quad (7.35)$$

$$\frac{\partial s}{\partial t} = - \frac{\mathbf{p}}{m} \cdot \nabla_{\mathbf{x}} s + \frac{ig}{2} \eta(\mathbf{x}) s^z \alpha, \quad (7.36)$$

$$\frac{\partial s^z}{\partial t} = - \frac{\mathbf{p}}{m} \cdot \nabla_{\mathbf{x}} s^z + ig\eta(\mathbf{x}) (\alpha^* s - s^* \alpha), \quad (7.37)$$

where we have used the collective dipole defined in Eq. (7.21).

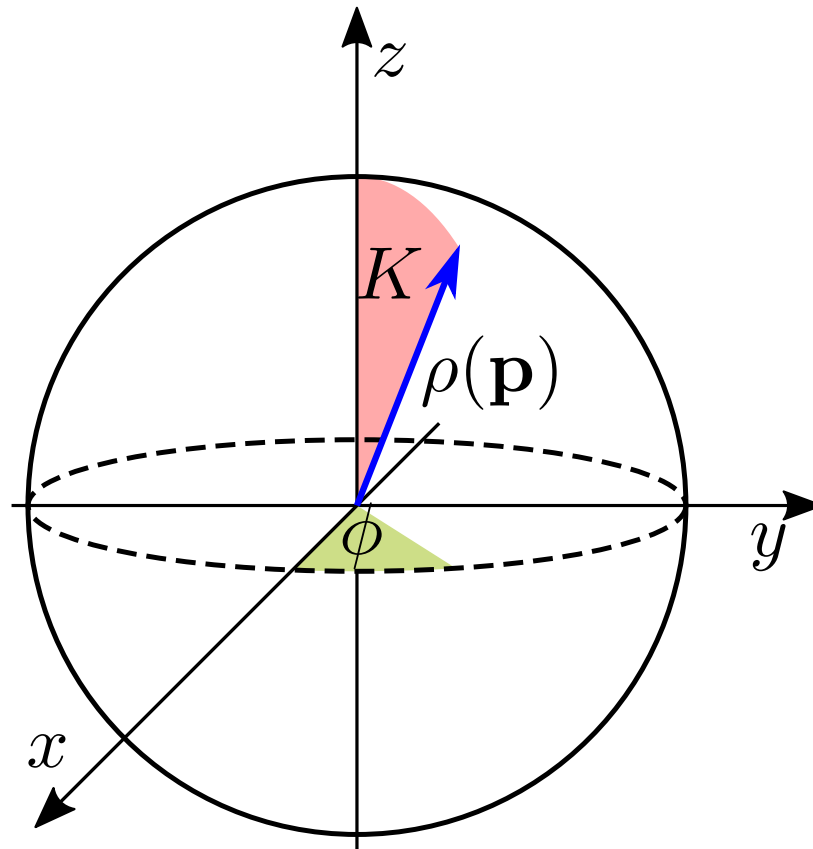


Figure 7.2: Sketch of the Bloch sphere where the dipole density can be mapped on a point of the sphere (here visible as the blue arrow) with radius $\rho(\mathbf{p})$ depending solely on the momentum \mathbf{p} . The angles K and ϕ depend on position \mathbf{x} , momentum \mathbf{p} , and time t .

Equations (7.36)–(7.37) imply a conserved length of the dipole density

$$\left(\frac{\partial}{\partial t} + \frac{\mathbf{p}}{m} \cdot \nabla_{\mathbf{x}} \right) [4|s|^2 + (s^z)^2] = 0, \quad (7.38)$$

which can be seen by realizing $4|s|^2 + (s^z)^2 = (s^x)^2 + (s^y)^2 + (s^z)^2$. Therefore it is useful to represent the stationary dipole components in spherical coordinates

$$\begin{aligned} s_0 &= \frac{\rho(\mathbf{p})}{2} e^{-i\phi} \sin(K), \\ s_0^z &= \rho(\mathbf{p}) \cos(K), \end{aligned} \quad (7.39)$$

where the dipole length is determined by the boundary conditions of the atomic beam density $\rho(\mathbf{p})$ as in Eq. (7.17), and ϕ , K are spherical angles dependent on position, momentum, and time. In that case, for every fixed value of \mathbf{x} , \mathbf{p} , t , we can assign a Bloch vector to the density of the atomic dipoles (see Fig. 7.2). The boundary condition for K is determined by the fact that the atoms enter in the excited state and thus $K(\mathbf{x}_0, \mathbf{p}, t) = 0$.

To find the superradiant solution, we assume that the atomic beam undergoes collective emission with a single frequency ω . In that case we can express the phase ϕ as

$$\phi(\mathbf{x}, \mathbf{p}, t) = \omega t + \psi(\mathbf{x}, \mathbf{p}), \quad (7.40)$$

where the first term on the right hand side describes the monochromatic oscillation of the density with frequency ω , and the second term ψ is a time-independent phase in phase space. The angle $K(\mathbf{x}, \mathbf{p})$ is not explicitly time dependent in this case.

This assumption allows us to solve the cavity field analytically from Eq. (7.35) and obtain

$$\alpha_0 \approx -i \frac{\Gamma_c}{g} \cos(\chi) e^{-i\chi} J_0, \quad (7.41)$$

where we have defined

$$\Gamma_c = \frac{g^2}{\kappa}, \quad (7.42)$$

$$\tan(\chi) = \frac{\Delta - \omega}{\kappa/2}, \quad (7.43)$$

and

$$J_0 = \int d\mathbf{x} \int d\mathbf{p} \eta(\mathbf{x}) s_0. \quad (7.44)$$

We mention that α_0 , s_0 , and J_0 are all proportional to $\exp(-i\omega t)$, which constitutes their only time dependence. Our result for the field goes beyond the typical adiabatic elimination of the cavity fields since it includes retardation effects that are apparent in χ and that explicitly depend on the frequency ω . Using Eqs. (7.39) and Eq. (7.41) in Eq. (7.36), we can derive the following equations for the angles

$$\frac{\mathbf{p}}{m} \cdot \nabla_{\mathbf{x}} \psi = -\omega - \frac{\Gamma(\mathbf{x})}{2} \cot(K) C(\psi), \quad (7.45)$$

$$\frac{\mathbf{p}}{m} \cdot \nabla_{\mathbf{x}} K = \frac{\Gamma(\mathbf{x})}{2} \int d\mathbf{x}' S(\psi), \quad (7.46)$$

with

$$C(\psi) = \int d\mathbf{x}' \int d\mathbf{p}' \eta' \rho' \sin(\psi - \psi' - \chi) \sin(K'),$$

$$S(\psi) = \int d\mathbf{p}' \eta' \rho' \cos(\psi - \psi' - \chi) \sin(K'),$$

and where we have used

$$\Gamma(\mathbf{x}) = \Gamma_c \eta(\mathbf{x}) \cos(\chi). \quad (7.47)$$

As a simplification, we have employed the notation $\mathcal{A}' = \mathcal{A}(\mathbf{x}', \mathbf{p}')$ where \mathcal{A} can be η , ρ , ψ , and K . Equations (7.45)–(7.46) have a U(1) symmetry since they are invariant under a rotation $\psi \mapsto \psi + \varphi$, where φ is an arbitrary phase that is independent on position, momentum, and time. We will now explicitly break this U(1) symmetry by choosing the phase offset such that

$$J_0^{\parallel} = \int d\mathbf{x}' \int d\mathbf{p}' \eta' \rho' \cos(\psi') \sin(K'), \quad (7.48)$$

$$0 = \int d\mathbf{x}' \int d\mathbf{p}' \eta' \rho' \sin(\psi') \sin(K'). \quad (7.49)$$

Notice that J_0^{\parallel} is not time dependent; the value of J_0^{\parallel} is the stationary length of the collective dipole and has the relation $J_0^{\parallel} = 2|J_0|$.

With this choice of J_0^\parallel , we can simplify Eq. (7.45) and Eq. (7.46) to

$$\frac{\mathbf{p}}{m} \cdot \nabla_{\mathbf{x}} \psi = -\omega - \frac{\Gamma(\mathbf{x})J_0^\parallel}{2} \cot(K) \sin(\psi - \chi), \quad (7.50)$$

$$\frac{\mathbf{p}}{m} \cdot \nabla_{\mathbf{x}} K = \frac{\Gamma(\mathbf{x})J_0^\parallel}{2} \cos(\psi - \chi). \quad (7.51)$$

Since all atoms enter the cavity in the excited state we have the boundary condition $K(\mathbf{x}_0, \mathbf{p}) = 0$. If we now impose that the gradient of the angle $\nabla_{\mathbf{x}} \psi$ cannot diverge at $\mathbf{x} = \mathbf{x}_0$, we obtain the boundary condition for the angle $\psi(\mathbf{x}_0, \mathbf{p}) = \chi$.

Although we will give a simple example in Sec. 7.5 where we can explicitly solve Eqs. (7.50)–(7.51), we are not aware of a general solution. However, in the limit where $\chi \ll 1$, we can apply perturbation theory as we will show now.

7.3.3 Perturbative solution for $\chi \ll 1$: Cavity pulling

We consider now the case where $\chi \ll 1$ and also $\psi \ll 1$. The latter is a consequence of the boundary condition $\psi(\mathbf{x}_0, \mathbf{p}) = \chi$ together with the approximation $\sin(\psi - \chi) \approx \psi - \chi$ that implies that ψ according to Eq. (7.50) is only slowly varying. In this parameter regime we can approximate χ by

$$\chi \approx \frac{\Delta - \omega}{\kappa/2} \quad (7.52)$$

from Eq. (7.43) and simplify Eq. (7.50) and Eq. (7.51) to get

$$\frac{\mathbf{p}}{m} \cdot \nabla_{\mathbf{x}} \psi = -\omega - \frac{\Gamma_c J_0^\parallel}{2} \eta \cot(K) (\psi - \chi), \quad (7.53)$$

$$\frac{\mathbf{p}}{m} \cdot \nabla_{\mathbf{x}} K = \frac{\Gamma_c J_0^\parallel}{2} \eta. \quad (7.54)$$

The second equation is now completely decoupled and independent of ω . Using the substitution

$$\psi = \frac{\Psi}{\sin(K)} + \chi, \quad (7.55)$$

we can derive

$$\frac{\mathbf{p}}{m} \cdot \nabla_{\mathbf{x}} \Psi = -\omega \sin(K) \quad (7.56)$$

with the boundary condition $\Psi(\mathbf{x}_0, \mathbf{p}) = 0$. This can be integrated to obtain

$$\Psi(\mathbf{x}, \mathbf{p}) = -\omega \int_0^\infty dt \sin \left[K \left(\mathbf{x} - \frac{\mathbf{p}}{m}t, \mathbf{p} \right) \right], \quad (7.57)$$

where we have extended the upper limit of the integral to infinity assuming that $K(x, y, z, \mathbf{p}) = 0$ for $x < -x_0$.

Using Eqs. (7.55) and (7.57) in Eqs. (7.48) and (7.49), we obtain

$$0 = \int d\mathbf{x}' \int d\mathbf{p}' \eta' \rho' \Psi' + \chi J_0^\parallel. \quad (7.58)$$

Combining Eqs. (7.52), (7.57), and (7.58), we can now solve for the frequency

$$\omega = \frac{\Delta}{\frac{\kappa C_\perp}{2} + 1} \quad (7.59)$$

where we have defined

$$C_\perp = \frac{\int_0^\infty dt \int d\mathbf{x} \int d\mathbf{p} \eta \left(\mathbf{x} + \frac{\mathbf{p}}{m}t \right) \rho \sin(K)}{J_0^\parallel} \quad (7.60)$$

as a timescale.

The result given in Eq. (7.59) can be rewritten to calculate the cavity pulling coefficient

$$\wp = \frac{\omega}{\Delta} = \frac{1}{\frac{\kappa C_\perp}{2} + 1} \quad (7.61)$$

that describes the emission frequency of the atomic beam relative to the detuning between the cavity resonance and the atomic resonance. While the exact form of C_\perp depends on the actual model, there is still a very general physical observation that we can make. If the timescale C_\perp is small enough such that $\kappa C_\perp \ll 1$, we get a pulling coefficient $\wp \lesssim 1$. In this case, light will essentially be emitted with the cavity frequency and not with the atomic frequency for $\Delta \ll \kappa$. On the other hand, if $\kappa C_\perp \gg 1$, we have a cavity pulling coefficient $\wp \ll 1$ and therefore the emitted light is almost resonant with the atomic transition frequency. This has been shown to be the case for superradiant lasers [12, 92] that work in the regime where κ is much larger than any atomic linewidth, in particular $\kappa \gg N\Gamma_c$. For situations where a stable emission frequency is desired that

is independent of cavity length noise, we would like \wp to be as small as possible. For the remainder of this article we will now focus exactly on this regime and first determine the stability of the atomic beam configuration.

7.4 Stability in the bad cavity regime

In the limit where κ determines the shortest timescale, we can eliminate α from Eqs. (7.18)–(7.20) according to Eq. (7.41) and also neglect the the explicit ω dependence of χ , i.e.,

$$\tan(\chi) = \frac{\Delta}{\kappa/2}. \quad (7.62)$$

We then obtain the following stochastic differential equations for the dipole densities

$$\frac{\partial s^x}{\partial t} + \frac{\mathbf{p}}{m} \cdot \nabla_{\mathbf{x}} s^x = \frac{\Gamma(\mathbf{x})}{2} [\cos(\chi)J^x - \sin(\chi)J^y] s^z + \mathcal{S}^x, \quad (7.63)$$

$$\frac{\partial s^y}{\partial t} + \frac{\mathbf{p}}{m} \cdot \nabla_{\mathbf{x}} s^y = \frac{\Gamma(\mathbf{x})}{2} [\sin(\chi)J^x + \cos(\chi)J^y] s^z + \mathcal{S}^y, \quad (7.64)$$

$$\frac{\partial s^z}{\partial t} + \frac{\mathbf{p}}{m} \cdot \nabla_{\mathbf{x}} s^z = -\frac{\Gamma(\mathbf{x})}{2} \cos(\chi) (s^x J^x + s^y J^y) - \frac{\Gamma(\mathbf{x})}{2} \sin(\chi) (s^y J^x - s^x J^y) + \mathcal{S}^z, \quad (7.65)$$

where we have used the definition given in Eq. (7.47).

Equations (7.63)–(7.65) also include stochastic noise terms $\mathcal{S}^x = \eta(\mathbf{x})\mathcal{N}^x s^z$, $\mathcal{S}^y = \eta(\mathbf{x})\mathcal{N}^y s^z$, and $\mathcal{S}^z = -\eta(\mathbf{x})(\mathcal{N}^x s^x + \mathcal{N}^y s^y)$, where the noise terms \mathcal{N}^x and \mathcal{N}^y can be assumed to be δ -correlated on the typical evolution timescale of the atomic degrees of freedom. This implies $\langle \mathcal{N}^x(t)\mathcal{N}^y(t') \rangle = 0$ and $\langle \mathcal{N}^x(t)\mathcal{N}^x(t') \rangle = \langle \mathcal{N}^y(t)\mathcal{N}^y(t') \rangle = \Gamma_c \cos^2(\chi)\delta(t-t')$.

These noise terms are important for the dynamics since they introduce small fluctuations into the dipole components that can destabilize the state. In order to predict this destabilization, we investigate the stability of the stationary phases that we have introduced in Sec. 7.3.

7.4.1 Stability of the non-superradiant configuration

For the non-superradiant configuration, we study small fluctuations δs^x and δs^y around the solution given in Eqs. (7.30)–(7.34). For this kind of analysis we can drop the noise terms. We find

the linearized equations

$$\frac{\partial \delta s^x}{\partial t} + \frac{\mathbf{p}}{m} \cdot \nabla_{\mathbf{x}} \delta s^x = \frac{\Gamma(\mathbf{x})}{2} [\cos(\chi) \delta J^x - \sin(\chi) \delta J^y] \rho, \quad (7.66)$$

$$\frac{\partial \delta s^y}{\partial t} + \frac{\mathbf{p}}{m} \cdot \nabla_{\mathbf{x}} \delta s^y = \frac{\Gamma(\mathbf{x})}{2} [\sin(\chi) \delta J^x + \cos(\chi) \delta J^y] \rho. \quad (7.67)$$

Since we neglect terms that are second-order in the fluctuations, these equations become decoupled from fluctuations δs^z around $s^z = \rho$. We have also introduced $\delta J^\mu = \int d\mathbf{x} \int d\mathbf{p} \eta \delta s^\mu$ with $\mu = x, y$.

Equations (7.66) and (7.67) can be reduced to uncoupled equations for $\delta s = (\delta s^x - i\delta s^y)/2$ and its complex conjugate. Without loss of generality, we focus on the solution of δs and derive

$$\frac{\partial \delta s}{\partial t} + \frac{\mathbf{p}}{m} \cdot \nabla_{\mathbf{x}} \delta s = \frac{\Gamma(\mathbf{x})}{2} e^{-i\chi} \delta J \rho, \quad (7.68)$$

where $\delta J = (\delta J^x - i\delta J^y)/2$. Applying the Laplace transformation

$$L[g](\nu) = \int_0^\infty dt e^{-\nu t} g(t) \quad (7.69)$$

to Eq. (7.68), we obtain

$$[\nu - \mathcal{L}_0] L[\delta s] = \delta s(\mathbf{x}, \mathbf{p}, 0) + \frac{\Gamma(\mathbf{x})}{2} e^{-i\chi} \rho(\mathbf{p}) L[\delta J], \quad (7.70)$$

where we have defined the operator

$$\mathcal{L}_0 g(\mathbf{x}) = -\frac{\mathbf{p}}{m} \cdot \nabla_{\mathbf{x}} g(\mathbf{x}). \quad (7.71)$$

Multiplying Eq. (7.70) by the inverse of operator $[\nu - \mathcal{L}_0]$ and $\eta(\mathbf{x})$, and then integrating over space and momentum, we obtain

$$L[\delta J] = \frac{\int d\mathbf{x} \int d\mathbf{p} \eta(\mathbf{x}) [\nu - \mathcal{L}_0]^{-1} \delta s^x(\mathbf{x}, \mathbf{p}, 0)}{D(\nu)}, \quad (7.72)$$

where the denominator is given by the dispersion relation

$$D(\nu) = 1 - \int_0^\infty dt e^{-\nu t - i\chi} \int d\mathbf{x} \int d\mathbf{p} \eta\left(\mathbf{x} + \frac{\mathbf{p}}{m} t\right) \frac{\Gamma(\mathbf{x})}{2} \rho. \quad (7.73)$$

The asymptotic time evolution of δJ is determined by the zeros of the dispersion relation $D(\nu)$. In fact the zero, ν_0 , that has the largest real component is the principal one that controls the dynamics. As long as we satisfy $\text{Re}(\nu_0) < 0$, the non-superradiant configuration is stable. The imaginary part $\text{Im}(\nu_0)$ then determines the frequency of the light emission.

In the case where $\text{Re}(\nu_0) > 0$, a qualitatively distinct solution is anticipated in which we expect an exponential build-up of fluctuations that results in superradiant emission, implying the formation of a macroscopic collective dipole. In the remainder of this section, we will determine the stability of this stationary superradiant phase.

7.4.2 Stability of the superradiant configuration

We analyze the dynamics of small fluctuations around the configuration that is determined by Eqs. (7.39), (7.53), and (7.54). To do so it is convenient to move into a frame rotating with frequency ω , and define

$$\tilde{s} = e^{i\omega t} s \quad (7.74)$$

and $\tilde{s}^x = \tilde{s} + \tilde{s}^*$, $\tilde{s}^y = i(\tilde{s} - \tilde{s}^*)$, as well as $\tilde{J}^\mu = \int d\mathbf{x} \int d\mathbf{p} \eta(\mathbf{x}) \tilde{s}^\mu$ for $\mu \in \{x, y\}$, accordingly. This frame is chosen such that the steady state $\tilde{s}_0 = e^{i\omega t} s_0$ is time-independent, i.e.,

$$\frac{d\tilde{s}_0}{dt} = \left(i\omega s_0 + \frac{ds_0}{dt} \right) e^{i\omega t} = 0. \quad (7.75)$$

We now consider small fluctuations $\delta\tilde{\mathbf{s}} = (\delta\tilde{s}^x, \delta\tilde{s}^y, \delta\tilde{s}^z)^\text{T}$ around the stationary solutions that we can parametrize by

$$\tilde{s}_0^x = \rho \cos(\psi) \sin(K), \quad (7.76)$$

$$\tilde{s}_0^y = \rho \sin(\psi) \sin(K), \quad (7.77)$$

$$\tilde{s}_0^z = \rho \cos(K). \quad (7.78)$$

In this rotating frame, we also keep the convention introduced in Eqs. (7.48) and (7.49)

$$J_0^{\parallel} = \int d\mathbf{x} \int d\mathbf{p} \eta \tilde{s}_0^x, \quad (7.79)$$

$$0 = \int d\mathbf{x} \int d\mathbf{p} \eta \tilde{s}_0^y, \quad (7.80)$$

meaning that the collective dipole is chosen to be always pointing in the x direction. Using Eqs. (7.63)–(7.64) in the frame rotating with ω , the dynamics of $\delta\tilde{\mathbf{s}}$ is then governed by

$$\frac{\partial \delta\tilde{\mathbf{s}}}{dt} = \mathcal{L} \delta\tilde{\mathbf{s}} + \mathbf{S}_0 \delta\tilde{\mathbf{J}}, \quad (7.81)$$

where

$$\mathcal{L} = \mathcal{L}_0 \hat{\mathbf{1}}_3 + \mathcal{L}_1. \quad (7.82)$$

Here, we have defined

$$\mathcal{L}_1 = \begin{pmatrix} 0 & \omega & \frac{\Gamma(\mathbf{x})}{2} \cos(\chi) J_0^{\parallel} \\ -\omega & 0 & \frac{\Gamma(\mathbf{x})}{2} \sin(\chi) J_0^{\parallel} \\ -\frac{\Gamma(\mathbf{x})}{2} \cos(\chi) J_0^{\parallel} & -\frac{\Gamma(\mathbf{x})}{2} \sin(\chi) J_0^{\parallel} & 0 \end{pmatrix} \quad (7.83)$$

and

$$\mathbf{S}_0 = \frac{\Gamma(\mathbf{x})}{2} \begin{pmatrix} \cos(\chi) \tilde{s}_0^z & -\sin(\chi) \tilde{s}_0^z \\ \sin(\chi) \tilde{s}_0^z & \cos(\chi) \tilde{s}_0^z \\ -\cos(\chi) \tilde{s}_0^x - \sin(\chi) \tilde{s}_0^y & \sin(\chi) \tilde{s}_0^x - \cos(\chi) \tilde{s}_0^y \end{pmatrix} \quad (7.84)$$

with $\delta\tilde{\mathbf{J}} = (\delta\tilde{J}^x, \delta\tilde{J}^y)^T$. The operator \mathcal{L}_0 has been given in Eq. (7.71), and $\hat{\mathbf{1}}_3$ is the 3×3 identity matrix.

The Laplace transformation of Eq. (7.81) leads to

$$\nu L[\delta\tilde{\mathbf{s}}] = \delta\tilde{\mathbf{s}}(\mathbf{x}, \mathbf{p}, 0) + \mathcal{L} L[\delta\tilde{\mathbf{s}}] + \mathbf{S}_0 L[\delta\tilde{\mathbf{J}}]. \quad (7.85)$$

Now, we first solve for $L[\delta\tilde{\mathbf{s}}]$. Then we project on the first two components by multiplying with the matrix $\hat{\mathbf{1}}_{2,3} \in \mathbb{C}^{2 \times 3}$ with ones on the diagonal and zeros elsewhere. This results in two coupled equations for $L[\delta\tilde{s}^x]$ and $L[\delta\tilde{s}^y]$.

After multiplying with $\eta(\mathbf{x})$ and integrating over the whole phase space, we arrive at

$$\begin{aligned} L[\delta\tilde{\mathbf{J}}] &= \int d\mathbf{x} \int d\mathbf{p} \eta(\mathbf{x}) \hat{\mathbb{1}}_{2,3} (\nu \hat{\mathbb{1}}_3 - \mathcal{L})^{-1} \delta\tilde{\mathbf{s}}(\mathbf{x}, \mathbf{p}, 0) \\ &\quad + \int d\mathbf{x} \int d\mathbf{p} \eta(\mathbf{x}) \hat{\mathbb{1}}_{2,3} (\nu \hat{\mathbb{1}}_3 - \mathcal{L})^{-1} \mathbf{S}_0 L[\delta\tilde{\mathbf{J}}], \end{aligned} \quad (7.86)$$

which can be used to solve for $L[\delta\tilde{\mathbf{J}}]$, resulting in

$$L[\delta\tilde{\mathbf{J}}] = \mathbf{D}(\nu)^{-1} \int d\mathbf{x} \int d\mathbf{p} \eta(\mathbf{x}) \hat{\mathbb{1}}_{2,3} (\nu \hat{\mathbb{1}}_3 - \mathcal{L})^{-1} \delta\tilde{\mathbf{s}}(\mathbf{x}, \mathbf{p}, 0). \quad (7.87)$$

where we have defined

$$\begin{aligned} \mathbf{D}(\nu) &= \mathbf{1}_2 - \int d\mathbf{x} \int d\mathbf{p} \eta(\mathbf{x}) \hat{\mathbb{1}}_{2,3} (\nu \hat{\mathbb{1}}_3 - \mathcal{L})^{-1} \mathbf{S}_0 \\ &= \mathbf{1}_2 - \int_0^\infty e^{-\nu t} \int d\mathbf{x} \int d\mathbf{p} \eta(\mathbf{x}) \hat{\mathbb{1}}_{2,3} e^{\mathcal{L}t} \mathbf{S}_0. \end{aligned} \quad (7.88)$$

The dynamics of $\delta\tilde{\mathbf{J}}$ are now determined by the value of ν for which $\mathbf{D}(\nu)$ is not invertible. We find then that the time evolution is described by

$$\delta\tilde{\mathbf{J}} \propto e^{\nu_0 t},$$

where ν_0 is the zero of the dispersion relation

$$D_{\text{SR}}(\nu) = \det[\mathbf{D}(\nu)] \quad (7.89)$$

with the largest real component.

This dispersion relation can be used to determine the nature of the instability of the super-radiant configuration. Specifically, for a particular example that we study later in Sec. 7.6, we will show that the amplification of fluctuations occurring for $\text{Re}(\nu_0) > 0$ can lead to a transition to a multicomponent superradiant emission regime.

After providing all the theory that is required to analyze the beam-cavity system, we will analyze in the next section a specific model where we apply all the results of Sec. 7.3 and 7.4.

7.5 An atomic beam with a single velocity traversing an off-resonant optical cavity

We will now investigate a system consisting of an atomic beam composed of atoms with an identical velocity $\mathbf{v} = (v_x, 0, 0)^T$ travelling across one antinode of the cavity mode (see Fig. 7.1). We assume that the cavity mode can be modeled by

$$\eta(\mathbf{x}) = \Theta(x + w) - \Theta(x - w), \quad (7.90)$$

which simplifies the cavity profile to a box with length $2w$, where w is the waist of the cavity mode. The transit time τ is thus fixed to be $\tau = 2w/v_x$. For $t > \tau$, the corresponding homogeneous density of atoms is given by

$$\rho = \frac{N}{2w}. \quad (7.91)$$

7.5.1 Non-superradiant phase

We will first determine the stability of the non-superradiant configuration given by Eqs. (7.30)–(7.34). Using Eq. (7.90) and Eq. (7.91), we can explicitly calculate the dispersion relation $D(\nu)$ given in Eq. (7.73) that takes the form

$$D(\nu) = 1 - \frac{N\Gamma_c\tau}{2} \cos(\chi) e^{-i\chi} \frac{1}{\nu\tau} \left(1 - \frac{1 - e^{-\nu\tau}}{\nu\tau} \right). \quad (7.92)$$

We then numerically find the solution ν_0 of $D(\nu_0) = 0$ with the largest real component. In Fig. 7.3, we show the real component $\text{Re}(\nu_0)$ in subplot (a) and the imaginary component $\text{Im}(\nu_0)$ in subplot (b) as a function of $N\Gamma_c\tau$ and of $\Delta/(\kappa/2)$, respectively. In Fig. 7.3(a), we observe $\text{Re}(\nu_0) < 0$ for sufficiently small $N\Gamma_c\tau$ or large enough $\Delta/(\kappa/2)$. The solid black line marks the phase transition threshold below which the non-superradiant configuration is stable, and above which we expect superradiant emission. Specifically, for $\Delta/(\kappa/2) = 0$ this threshold is given by $N\Gamma_c\tau = 4$, which means that superradiant emission is only possible if the collective linewidth $N\Gamma_c$ is essentially

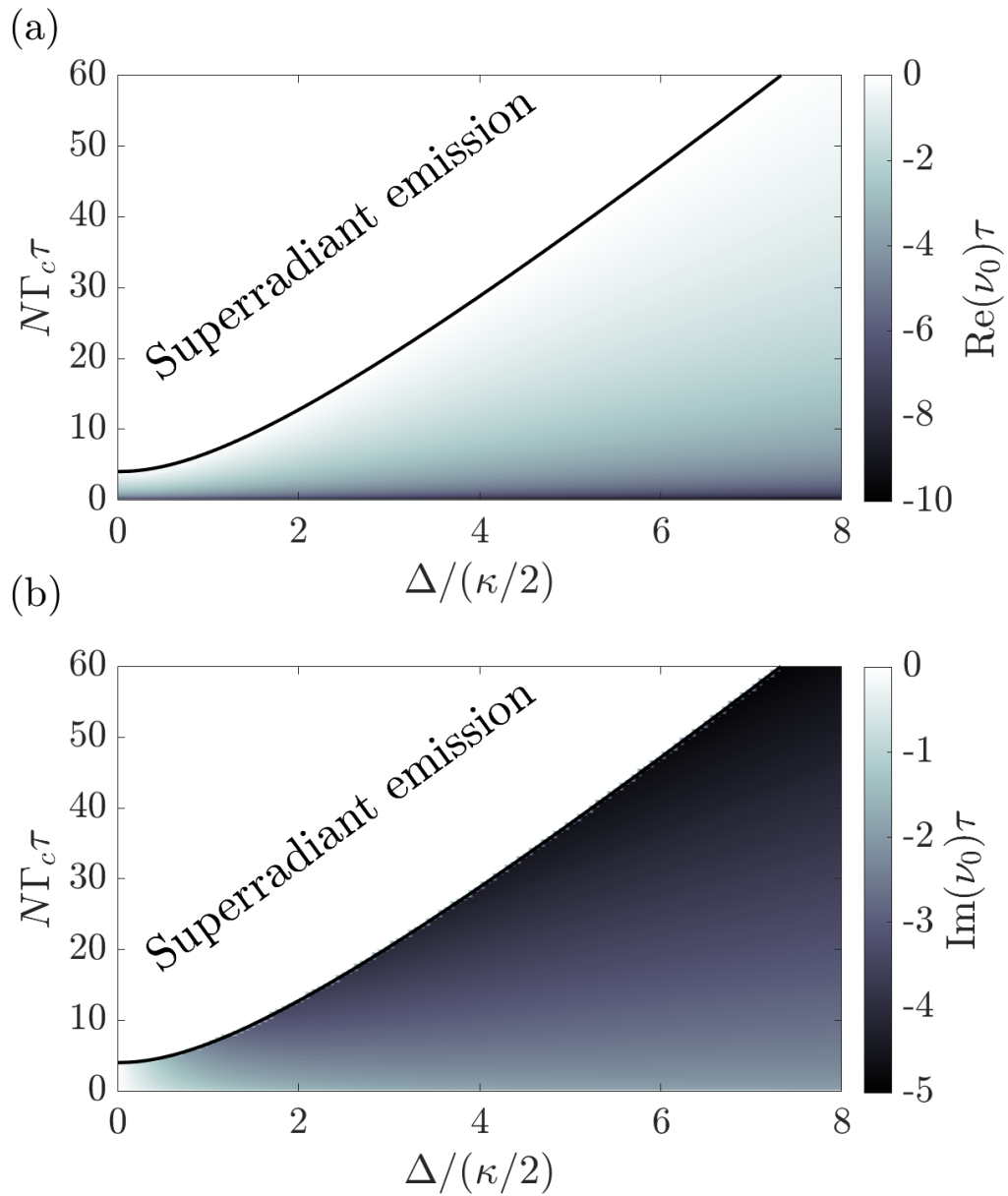


Figure 7.3: (a) The real component $\text{Re}(\nu_0)$ and (b) the imaginary component $\text{Im}(\nu_0)$ of the zero ν_0 with the largest real component of $D(\nu)$ in Eq. (7.92). They are plotted as a function of the detuning Δ in units of $\kappa/2$ and the collective linewidth $N\Gamma_c$ in units of $1/\tau$. The black solid line is determined by $\text{Re}(\nu_0) = 0$ above which we expect superradiant emission.

larger than the transit time broadening $1/\tau$. In Fig. 7.3(b), we plot the imaginary component $\text{Im}(\nu_0)$ which is the frequency of the atomic emission relative to the atomic resonance frequency ω_a . Therefore it is clear that $\text{Im}(\nu_0) = 0$ for $\Delta = 0$, implying that the atomic frequency, the cavity frequency, and the emission frequency are all equal. When $\Delta \neq 0$, the emission frequency depends not only on $\Delta/(\kappa/2)$ but also on $N\Gamma_c\tau$.

7.5.2 Superradiant phase

We will now study the superradiant configuration as shown in Fig. 7.3 above the phase transition threshold. For this we need to solve Eqs. (7.50) and (7.51) given Eqs. (7.90) and (7.91). Using the substitution

$$\sin(\psi - \chi) = \frac{\Psi}{\sin(K)} \quad (7.93)$$

we derive the differential equation

$$-\omega \sin(K)v_x \frac{\partial K}{\partial x} = \frac{\Gamma_c \cos(\chi) J_0^{\parallel}}{2} \eta v_x \frac{\partial \Psi}{\partial x}. \quad (7.94)$$

This equation implies

$$\Psi = [1 - \cos(K)]f \quad (7.95)$$

with

$$f = -\frac{2\omega}{\Gamma_c \cos(\chi) J_0^{\parallel}}, \quad (7.96)$$

where we have used the fact that η is unity for $-w \leq x \leq w$ by Eq. (7.90). Combining this result with Eq. (7.93) and then solving Eq. (7.51) we obtain

$$\sin \left[\frac{K(x)}{2} \right] = \frac{\sin \left[\frac{\sqrt{1+f^2} \Gamma_c \cos(\chi) J_0^{\parallel}(x+w)}{4v_x} \right]}{\sqrt{1+f^2}}. \quad (7.97)$$

We have now found the solutions for K and ψ and will use them to determine the frequency ω and the collective dipole J_0^{\parallel} . Using the results for ψ and K in Eqs. (7.48) and (7.49), after some

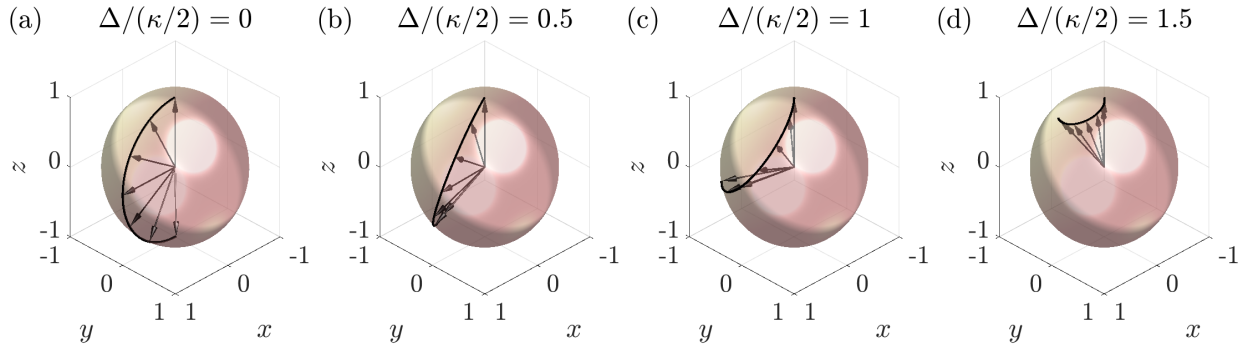


Figure 7.4: Bloch vectors parametrized according to Eqs. (7.76)–(7.78) where we have combined Eqs. (7.98) and (7.99) to calculate ω and J_0^{\parallel} and then Eqs. (7.93), (7.95), and (7.97) to calculate $K(x)$ and $\psi(x)$. The black solid lines are the traces of the Bloch vectors for $-w \leq x \leq w$. We have used $N\Gamma_c\tau = 10$ and four different values of $\Delta/(\kappa/2)$ [see titles of subplots (a)–(d)] for the numerical values used.

algebra we find

$$\xi = N\Gamma_c\tau \frac{\sin^2\left(\frac{\xi}{2}\right)}{\xi}, \quad (7.98)$$

$$-\xi \tan(\chi) = \frac{N\Gamma_c\tau}{2} \frac{f}{\sqrt{1+f^2}} \left[1 - \frac{\sin(\xi)}{\xi} \right], \quad (7.99)$$

with

$$\xi = \frac{\sqrt{1+f^2}\Gamma_c \cos(\chi) J_0^{\parallel}\tau}{2}. \quad (7.100)$$

Given a value of $\Delta/(\kappa/2)$ and $N\Gamma_c\tau$, we can now numerically determine ξ and f and then calculate J_0^{\parallel} and ω . These values can then be used to derive $K(x)$ and $\psi(x)$.

In Fig. 7.4 we show the result for four different values of $\Delta/(\kappa/2)$ with a fixed $N\Gamma_c\tau = 10$ where we derive $K(x)$ and $\psi(x)$ and then use Eqs. (7.76)–(7.78) to illustrate the dynamics of the dipoles on the Bloch sphere (see Fig. 7.2 with $\phi = \psi$) for $-w \leq x \leq w$. We have normalized the Bloch vector to length unity.

Since the atoms enter in the excited state $|e\rangle$, the Bloch vector is pointing along the z direction initially for $x = -w$. For all cases the collective dipole J_0^{\parallel} , which is here determined by the integral of all the Bloch vectors along the trajectory for $-w \leq x \leq w$, points in the x direction by choice

[see Eqs. (7.49) and (7.79)]. In Fig. 7.4(a) where $\Delta = 0$, the Bloch vector remains in a plane that is spanned by the z axis and the collective dipole. This is different for nonvanishing Δ values [see Figs. 7.4(b)–7.4(d)] where the Bloch vectors leave this plane. We observe that the total curve becomes shorter for increasing Δ values and the length of the collective dipole also decreases for these parameters.

In order to study this effect, in Fig. 7.5(a) we show the normalized collective dipole $j_0^{\parallel} = J_0^{\parallel}/N$ for different values of $N\Gamma_c\tau$ and $\Delta/(\kappa/2)$. We observe the same transition threshold between the superradiant and non-superradiant phases as shown by the black solid line in Fig. 7.3. This transition is continuous but not differentiable. Above the threshold, we find a non-vanishing value for the collective dipole. In Fig. 7.5(b) we show the value of the frequency ω that has been calculated for the same parameter regime as j_0^{\parallel} in Fig. 7.5(a). We see that ω vanishes for $\Delta = 0$ which implies that the atomic frequency ω_a , the cavity frequency ω_c , and ω are equal. For a given value of $N\Gamma_c\tau$ the frequency ω increases linearly with $\Delta/(\kappa/2)$. This shows that the cavity pulling coefficient $\wp = \omega/\Delta$ in the superradiant regime is independent of Δ even for large values of $\Delta/(\kappa/2)$.

We have also derived the stability of the superradiant configuration using the dispersion relation in Eq. (7.89). We have found zeros ν_0 with positive real part for the parameter region that is shown as a gray area in Fig. 7.5 bounded by a black dashed line. This is the parameter space where we expect a different dynamical phase because the stationary superradiant and the non-superradiant solutions are unstable.

We will now compare our analytical finding with numerical simulations.

7.5.3 Numerical study

We numerically integrate Eqs. (7.63)–(7.65) using the mode function in Eq. (7.90) and the homogeneous density in Eq. (7.91).

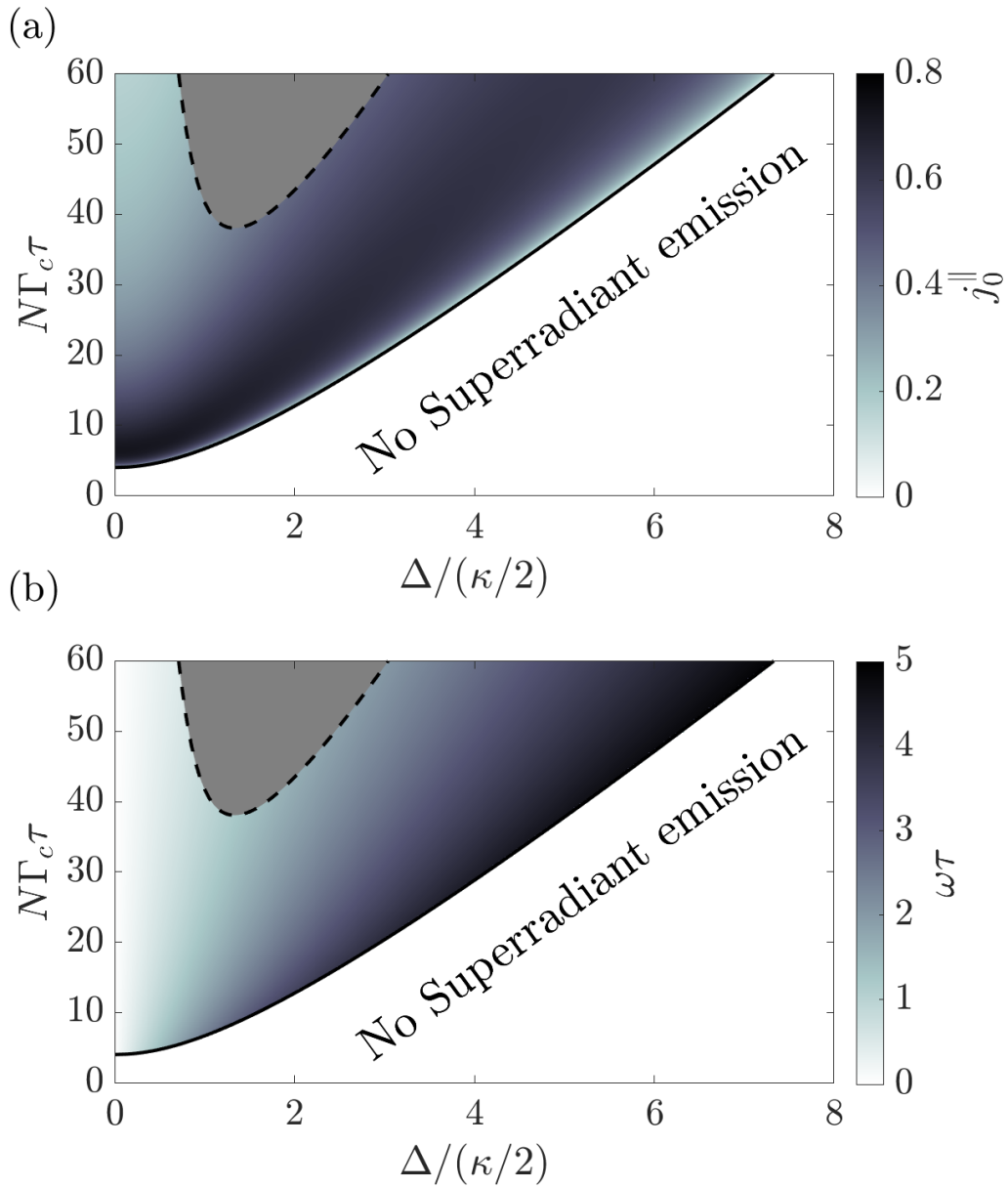


Figure 7.5: The normalized collective dipole $j_0^{\parallel} = J_0^{\parallel}/N$ (a) and the frequency ω in units of $1/\tau$ (a) as a function of $\Delta/(\kappa/2)$ and the collective linewidth $N\Gamma_c$ in units of $1/\tau$. The results are calculated using Eq. (7.98) and Eq. (7.99). The black dashed line is the boundary of the gray area where the superradiant configuration transitions to a multicomponent superradiant regime. This has been determined using the solution of j_0^{\parallel} and ω to find zeros of the dispersion relation in Eq. (7.89).

7.5.3.1 Superradiant to non-superradiant regime

We first investigate the crossover regime from the superradiant to the non-superradiant phase for a fixed $N\Gamma_c\tau = 20$ and various values of $\Delta/(\kappa/2)$ and N . Figure 7.6(a) shows the cavity output power in units of N/τ . This quantity can be interpreted as the number of photons that are emitted per atom during the transit time τ . It is calculated from

$$\frac{\kappa\langle\hat{a}^\dagger\hat{a}\rangle}{N/\tau} = \Gamma_c \cos^2(\chi)\tau \frac{\langle J^*J \rangle}{N}, \quad (7.101)$$

where we have used Eq. (7.41) and $J = (J^x - iJ^y)/2$ is taken from the numerical integration. On the other hand we can take our analytical results where we expect $\langle J^*J \rangle = N^2 j_0^\parallel/4$ to predict the cavity output power. In Fig. 7.6(a), we show the numerical results of the output power as dotted lines with different markers which indicate different atom numbers (see inset). The analytical results calculated from j_0^\parallel is shown as the solid black line. We find very good agreement of the numerical and analytical results for all parameters. In general we observe that at the transition from the superradiant to the non-superradiant phase (dashed vertical red line), finite size effects smooth out the non-analyticity, which is expected from the analytical results.

To study the coherence properties we also investigate the second-order Glauber g_2 function defined as

$$g_2(0) = \frac{\langle J^*J J^*J \rangle}{\langle J^*J \rangle^2}, \quad (7.102)$$

which is shown in Fig. 7.6(b). Well inside the superradiant phase we observe $g_2(0) \approx 1$, which indicates second-order coherent light. This result is as expected because in this regime and for large intracavity atom number N , the collective dipole is coherent and therefore noise only plays a minor role. As a consequence we can use $\langle J^*J \rangle \approx (Nj_0^\parallel/2)^2$ and $\langle J^*J J^*J \rangle \approx \langle J^*J \rangle^2$. The value of $g_2(0)$ increases at the threshold and reaches $g_2(0) \approx 2$ well inside the non-superradiant regime. This result indicates thermal light.

In order to have access to the emission frequency of the cavity field we have also calculated

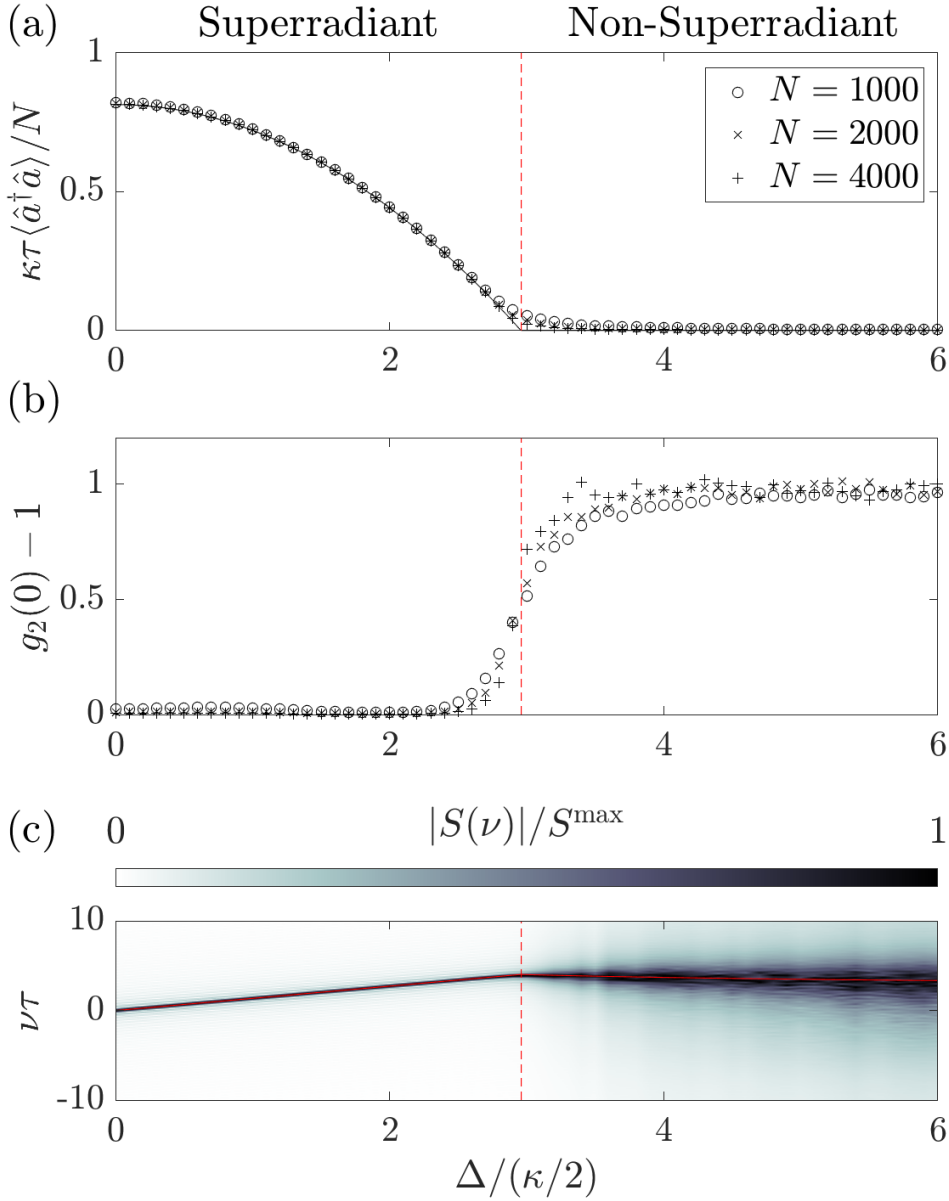


Figure 7.6: (a) The cavity output power $\kappa\langle\hat{a}^\dagger\hat{a}\rangle$ in units of N/τ [see Eq. (7.101)] and (b) the value of $g_2(0) - 1$ [see Eq. (7.102)] as functions of $\Delta/(\kappa/2)$ for various values of N [see inset of subplot (a)]. (c) The spectrum $|S(\nu)|$ [see Eq. (7.103)] normalized for every value of $\Delta/(\kappa/2)$ by the maximum $S^{\max} = \max_\nu |S(\nu)|$ as a function of ν in units of $1/\tau$ and of $\Delta/(\kappa/2)$ obtained by numerically integrating Eqs. (7.63)–(7.65) for $N = 4000$. For all simulations we have used $N\Gamma_c\tau = 20$. The black solid line in subplot (a) is calculated from the solution j_0^\parallel obtained from Eqs. (7.98) and (7.99). The vertical red dashed lines mark the analytical threshold between the superradiant and non-superradiant emission regimes. For (c) we have used $t_0 = 10\tau$ and $t_{\text{cut}} = 20\tau$. The red solid line in (c) in the superradiant regime is the frequency ω calculated using Eqs. (7.98) and (7.99). The red solid line in (c) in the non-superradiant regime is $\text{Im}(\nu_0)$ where ν_0 is the zero of Eq. (7.73) with the largest real part. All simulations have been performed for a total time $T = 200\tau$ and averaged over $100000/N$ different initializations.

the spectrum

$$S(\nu) = \int_0^{t_{\text{cut}}} dt e^{-i\nu t} \langle J^*(t + t_0) J(t_0) \rangle, \quad (7.103)$$

where $t_0 \gg \tau$ is a time after which we expect the system to reach a stationary state and t_{cut} is a numerical integration time. This spectrum is shown in Fig. 7.6(c) as a function of the frequency ν in units of $1/\tau$ and for different values of $\Delta/(\kappa/2)$. We have normalized this spectrum for every value of $\Delta/(\kappa/2)$ such that $|S(\nu)| \leq 1$. In the superradiant phase we observe a narrow peak of the spectrum. Specifically, the peak is centered at $\omega = 0$ for $\Delta = 0$. For increasing values of $\Delta/(\kappa/2)$ from zero, we find a linear increase of the emission frequency described by this peak. The red solid line in the superradiant regime indicates the analytical solution of ω that has been presented in Fig. 7.5(b) and is in very good agreement with the numerical results. The linear behavior of the emission frequency is determined by the pulling coefficient, $\omega = \wp \Delta$, where we find $\wp \kappa \tau \approx 2.8$.

In the non-superradiant regime we observe a much broader spectrum and also a different behavior of the emission frequency. The red solid line in the non-superradiant regime describes the solution $\text{Im}(\nu_0)$ shown in Fig. 7.3(b). We find good agreement between this solution and the peak of the spectrum in the non-superradiant phase.

7.5.3.2 Stationary to multicomponent superradiant regime

We will now investigate the transition from the stationary superradiant phase to a multicomponent superradiant phase (gray region in Fig. 7.5), first along $N\Gamma_c\tau = 50$ for different values of $\Delta/(\kappa/2)$. As we will show below, in this multicomponent superradiant phase we observe polychromatic superradiant emission where the spectrum shows several frequency components. We first study the output power $\kappa\tau\langle\hat{a}^\dagger\hat{a}\rangle/N$ in Fig. 7.7(a), where different markers indicate different values of N (see inset). The analytical results derived from j_0^\parallel in Eqs. (7.98) and (7.99) are shown as the black solid line. The vertical dashed red lines indicate the transition from the stationary to the multicomponent superradiant region ($\Delta \lesssim 1$) and from the multicomponent to the stationary region ($\Delta \lesssim 2.5$). Inside the stationary superradiant phase, we find good agreement between the

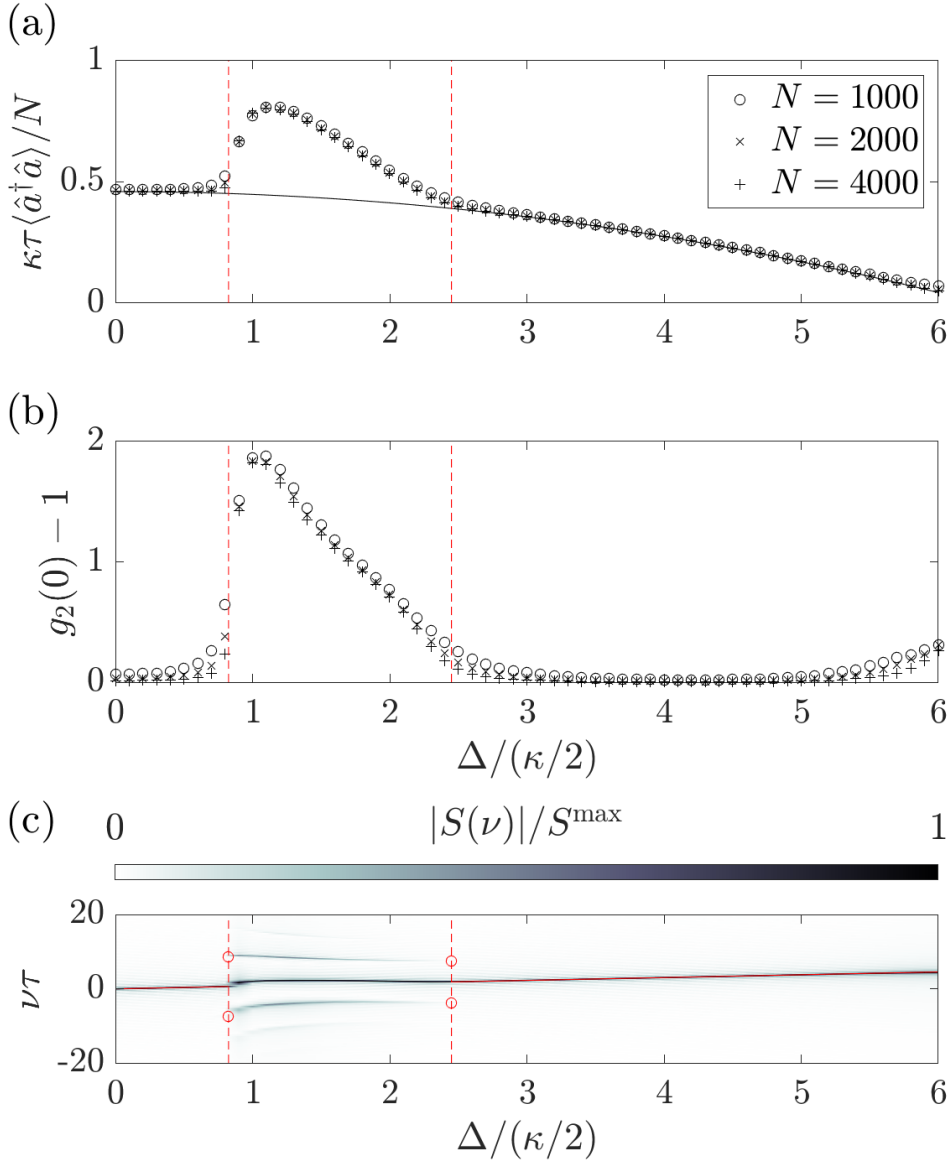


Figure 7.7: (a) The cavity output power $\kappa\langle\hat{a}^\dagger\hat{a}\rangle$ in units of N/τ [see Eq. (7.101)] and (b) the value of $g_2(0) - 1$ [see Eq. (7.102)] as functions of $\Delta/(\kappa/2)$ for various values of N [see inset of subplot (a)]. (c) The spectrum $|S(\nu)|$ [see Eq. (7.103)] normalized for every value of $\Delta/(\kappa/2)$ by the maximum $S^{\max} = \max_\nu |S(\nu)|$ as a function of ν in units of $1/\tau$ and of $\Delta/(\kappa/2)$ obtained by numerically integrating Eqs. (7.63)–(7.65) for $N = 4000$. For all simulations we have used $N\Gamma_c\tau = 50$. The black solid line in subplot (a) is calculated from the solution j_0^\parallel obtained from Eq. (7.98) and Eq. (7.99). The vertical red dashed lines border the multicomponent regime. For subplot (c) we have taken the values $t_0 = 10\tau$ and $t_{\text{cut}} = 20\tau$. The red solid line in (c) in the superradiant regime is the frequency ω calculated using Eq. (7.98) and Eq. (7.99). The red circles in (c) at the phase thresholds are the values of $\omega \pm \text{Im}(\nu_1)$, where ν_1 is the zero of Eq. (7.89) with the largest real part. All simulations have been performed for a total time $T = 200\tau$ and averaged over $100000/N$ different initializations.

numerical and the analytical results. In the multicomponent regime, however, we observe that the output power spikes, indicating that every atom emits more photons than expected from the analytical theory (black solid line).

We also show the $g_2(0)$ for the same parameters in Fig. 7.7(b). We find that $g_2(0) \approx 1$ in the stationary superradiant regime. The slight increase for $\Delta/(\kappa/2) > 5$ is due to the fact that we approach the transition to the non-superradiant regime. This can also be seen because the output power in that parameter regime approaches zero in Fig. 7.7(a).

In the multicomponent regime that is bordered by the two red vertical dashed lines, the $g_2(0)$ function spikes. The fact that we find values $g_2(0) > 2$ indicates photon bunching in this parameter regime that cannot be explained by thermal light.

The features of the emitted light are best illustrated in Fig. 7.7(c) where we plot the spectrum $|S(\nu)|$ as a function of ν in units of $1/\tau$. In the stationary superradiant regime we find a narrow single peak. The position of this peak agrees very well with the frequency ω that has been calculated in Fig. 7.5(b). The emission frequency follows the description $\omega = \wp\Delta$ and we find $\wp\kappa\tau \approx 1.6$.

For parameters within the region that is bordered by the two vertical red dashed lines, however, we find several narrow peaks which means that the light emission is polychromatic. The origin of the sidebands can be explained by the zero ν_1 of the dispersion relation Eq. (7.89) with $\text{Re}(\nu_1) > 0$, signaling an unstable superradiant configuration. The imaginary component $\text{Im}(\nu_1)$ is expected to be the frequency of the sidebands relative to the central frequency ω . We show $\omega \pm \text{Im}(\nu_1)$ at the phase thresholds as red circles. They are in good agreement with the emerging sidebands. We emphasize that our linearized description used to calculate ν_1 does not work beyond the phase thresholds to the multicomponent regime, where we need to include the full dynamical description of the atomic dipoles.

We have also studied the same transition for a fixed value of $\Delta/(\kappa/2) = 1.5$ when we vary $N\Gamma_c\tau > 20$. For these parameters, we expect the phase threshold to be around $N\Gamma_c\tau \approx 40$, shown as the vertical red dashed line in Fig. 7.8. In Fig. 7.8(a) we show the output power for different values of N using different markers (see inset). The black solid line is the analytical result calculated

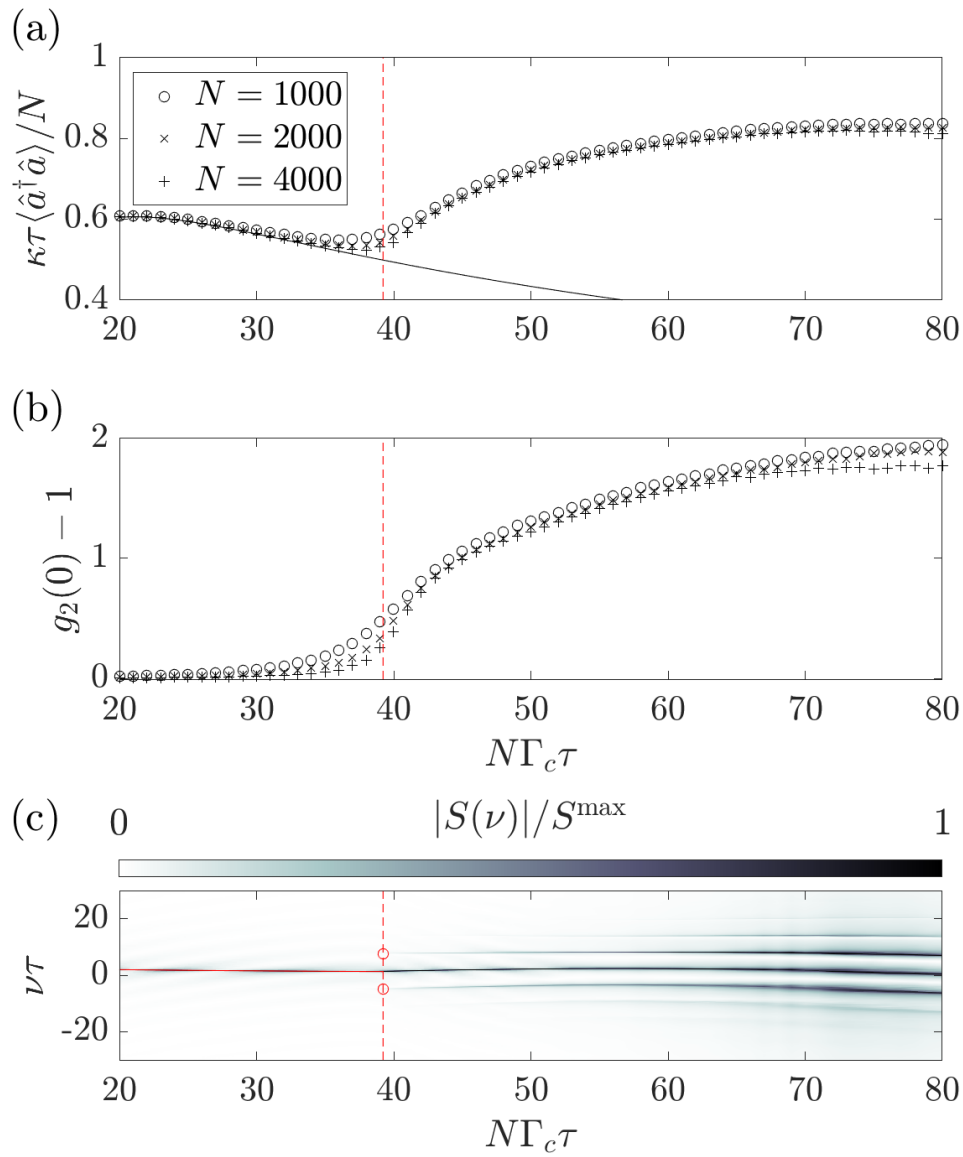


Figure 7.8: The same quantities as shown in Fig. 7.7 but for a fixed value of $\Delta/(\kappa/2) = 1.5$ and as a function of $N\Gamma_c\tau$. The vertical red dashed line marks the transition from the stationary to the polychromatic superradiant regime and the red circles in (c) at the phase threshold are the values of $\omega \pm \text{Im}(\nu_1)$. The remaining parameters are the same as in Fig. 7.7.

from j_0^{\parallel} . In the stationary superradiant regime the analytical and the numerical results are in good agreement. Beyond the threshold we observe an increasing value of the numerically calculated output power while the analytical result keeps decreasing.

In Fig. 7.8(b) we find that the light field is second order coherent [i.e., $g_2(0) \approx 1$] inside the stationary superradiant phase. When we enter the multicomponent regime we observe an increasing value of $g_2(0)$. The maximum value of $g_2(0)$ for the given parameters is close to $g_2(0) \approx 3$.

The spectrum $|S(\nu)|$ is visible in Fig. 7.8(c) as a function of ν in units of $1/\tau$. We find one narrow peak of the spectrum in the stationary superradiant regime. The corresponding emission frequency is in good agreement with the analytical value (red solid line) of ω calculated in Fig. 7.5(b). At the transition we find two emerging sidebands. These sidebands have been compared with $\omega \pm \text{Im}(\nu_1)$ (red circles), where ν_1 is the zero of Eq. (7.89) with the largest real component. They are in good agreement with the numerical results. Beyond the transition point we observe an increasing number of sidebands.

7.5.4 Cavity pulling

At the end of this section we derive the cavity pulling coefficient \wp that describes the change of the emission frequency ω when the atomic transition and the cavity mode are not resonant. For this we use Eq. (7.61) and solve the integral in Eq. (7.60) using the mode function in Eq. (7.90) and the atomic density in Eq. (7.91). Since the cavity pulling coefficient is the result for small detuning $\Delta/(\kappa/2) \ll 1$, we can use Eq. (7.99) and find $f \propto \Delta/(\kappa/2)$ and neglect the second order in $f^2 \approx 0$. Consequently, we find $\xi = \Gamma_c J_0^{\parallel} \tau / 2$ and can use Eq. (7.98) to calculate J_0^{\parallel} . The value of ξ can then be used to calculate the timescale

$$C_{\perp} = \frac{N\Gamma_c \tau^2}{2} \frac{1 - \frac{\sin(\xi)}{\xi}}{\xi^2}. \quad (7.104)$$

The value of \wp is shown in Fig. 7.9(a) as a function of $N\Gamma_c$ and κ both in units of $1/\tau$. The latter is given in a logarithmic scale to show different orders of magnitude for $\kappa\tau$. For $\kappa\tau \ll 1$, the lifetime of photons is much shorter than the transit time of the atoms. In this case we expect

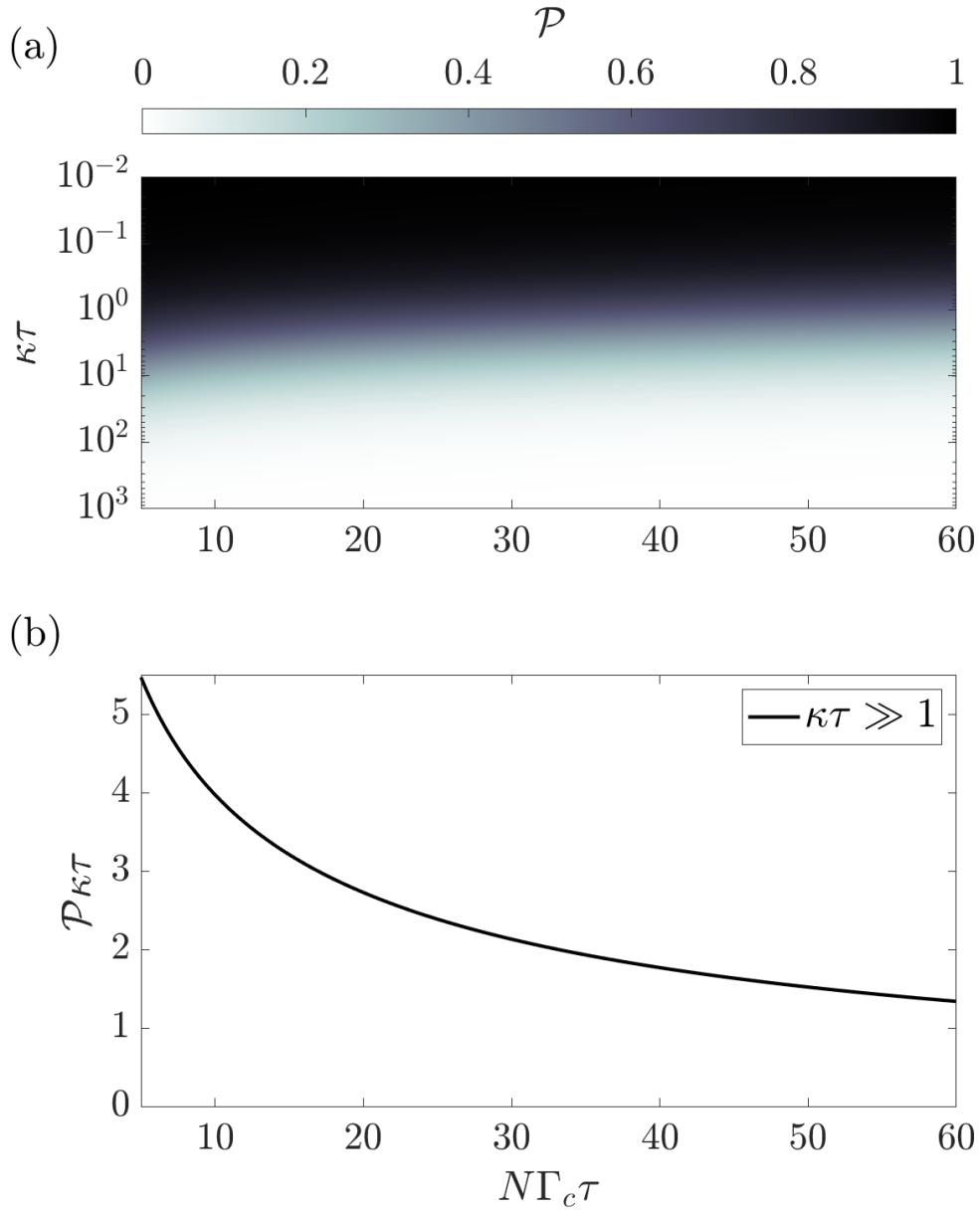


Figure 7.9: (a) The cavity pulling coefficient \wp defined in Eq. (7.61) as a function of the cavity linewidth κ and the collective decay $N\Gamma_c$, both in units $1/\tau$. For the calculation of \wp we have solved Eq. (7.60) using the solution of Eq. (7.98) for $f = 0$. (b) The cavity pulling coefficient \wp normalized by $1/(\kappa\tau)$ as a function of $N\Gamma_c$ in units $1/\tau$. For the derivation we have calculated $\wp = \omega/\Delta$ that is independent of Δ in the limit $\kappa\tau \gg 1$ where the cavity field can be eliminated.

many photons in the cavity and the resulting pulling coefficient is $\wp \lesssim 1$, showing that emission appear almost in resonance with the cavity degrees of freedom. For $\kappa\tau \gg 1$, photons leave the cavity earlier than the atoms traverse the cavity. In this regime the atoms store the coherence and the frequency of the collectively emitted light is almost in resonance with the atomic transition, $\wp \approx 0$.

The results obtained in the regime $\kappa\tau \gg 1$ can be directly compared with our simulations. In Figs. 7.6(c) and 7.7(c), we have seen that the frequency ω is linear in Δ even if $\Delta/(\kappa/2) \approx 1$. This is equivalent to the fact that \wp is independent on Δ in the limit $\kappa\tau \gg 1$. In Fig. 7.9(b), we show \wp normalized by $1/(\kappa\tau)$. This pulling coefficient is slightly different from the one that has been reported in Ref. [92]. The reason for this discrepancy is the absence of Doppler-broadening and the cosine term in the cavity mode function in the model studied here. In fact the results in Ref. [92] seem to be displaced by approximately a factor of 1/2 that is due to an average over cosine-squared, and this results in a weaker effective coupling. In addition, we remark that this pulling coefficient is only valid in the stationary superradiant regime, and cannot be used for the multicomponent regime where we observe several peaks in the emission spectrum.

7.6 Conclusion

In this chapter we have introduced a theoretical description for the dynamics of an atomic beam that traverses a single mode optical cavity. The atoms are described by optical dipoles with transition frequency that is detuned from the cavity frequency. We have derived the stationary phases of the atomic beam including the non-superradiant and superradiant configurations. The latter was used to calculate the cavity pulling coefficient in both the “bad” (large κ) and “good” (small κ) cavity regimes. After deriving an analytical theory for the stationary phases, we have determined the stability of the atomic dipole densities. By applying our theory to a specific model we have predicted three phases of the atomic beam. Our findings are in good agreement with numerical results where we highlight the phase transitions by examining the output power, the g_2 function, and also the emission spectrum. In the end we discuss cavity pulling for this specific

model.

The model analyzed in Sec. 7.5 represents an idealized model since it does not capture additional relevant effects of an actual experiment such as the Doppler broadening, inhomogeneous coupling, and homogeneous broadening. However, we have shown that even such a minimal model has non-trivial solutions with monochromatic light emission and even highly dynamical phases with polychromatic light emission. Therefore we rather see this work as a stepping stone towards understanding the physics of more specific setups. Our idealized model highlights that multicomponent superradiant emission can originate from collective homogeneous frequency shifts. This work extends previous scenarios that have been studied where the dynamical phase emerges because of optomechanical effects [66, 67] and inhomogeneous frequency shifts [136, 150, 69]. Although extensions may be necessary, the general theoretical methodology developed here will provide a good foundation for understanding any potential experimental systems.

In the future, it would be interesting to understand the interplay and relation to dynamical phases that have been studied in similar atomic beam setups [70, 69]. Moreover, while our analysis has been focusing on the light that is produced by the collective emission of the atomic beam, we have not yet investigated the atomic state in great detail. This might be especially interesting in the multicomponent superradiant regime because the dynamical character of the light field must result in a dynamical spin density. We expect that this is interesting for the study of dynamical phases and dissipative time crystals [49, 62, 156, 75].

Chapter 8

Regular and Bistable Steady-State Superradiant Phases of an Atomic Beam Traversing an Optical Cavity ¹

8.1 Introduction

Coupling quantum particles to bosonic modes enables the building of versatile platforms to study driven-dissipative dynamics in various physical setups. Prominent examples include trapped ions [21], color centers in diamonds [5], semiconductor systems [127], and atoms in optical cavities [108]. The bosonic modes typically serve as common and intrinsically lossy channels that enable strong interactions. In particular atomic ensembles in optical cavities have been used to investigate many-body effects that are of elementary and fundamental interest, such as exotic quantum phases [110, 85, 86, 8, 53, 83, 94, 93, 79, 84, 36] and collective dissipative dynamics [37, 10, 125, 138, 137, 165, 72], but are often accompanied by potential technological applications [101, 134, 12, 119, 90, 142, 144].

An example of such technology is the steady-state superradiant laser [101, 12]. This laser works in the regime where the lifetime of cavity photons is orders of magnitude shorter than the lifetime of the coherent dipoles. In this regime, coherences are stored in the atoms and are robust against environmental noise [101, 12, 100, 99, 11, 115, 116]. Besides this technological feature, this setup has also been connected to time crystals [156, 62, 49, 74, 171], synchronization [107, 3, 166, 172, 161], and dynamical phase transitions [7, 114, 66, 108, 67]. The rich dynamics of this system is based on effective interactions between the atoms and requires that the atoms remain in the cavity

¹The bulk of this work has been published in Physical Review A [70]. Copyright 2021 American Physical Society.

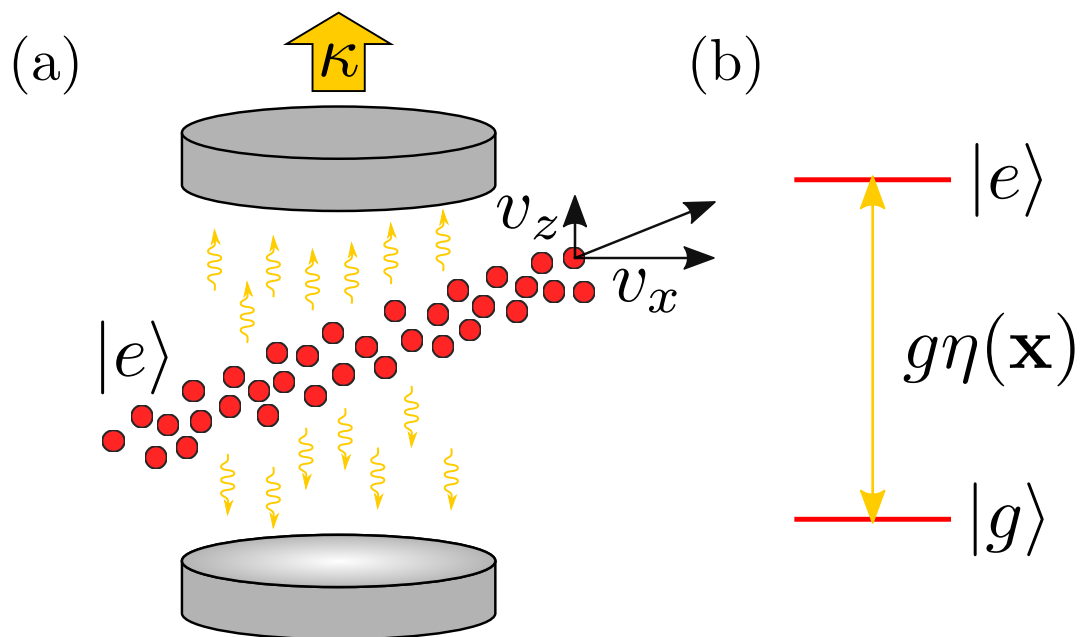


Figure 8.1: (a) Atoms are preexcited and pass through a lossy optical cavity. (b) Two-level atoms resonantly exchange photons with the cavity mode with a spatially dependent coupling $g\eta(\mathbf{x})$.

over long time scales.

In this chapter, we will investigate superradiant phases that establish and persist on timescales that are much longer than the lifetime of any individual photon or atom in the cavity. In order to show this, we consider an atomic beam that traverses an optical cavity (see Fig. 8.1a). A similar system has been studied in [92] for purposes of realistic quantum metrology applications such as active optical clocks [25] and ultra-narrow linewidth lasing in the field [78, 149]. The superradiant phases that arise from such systems highlight the ability of many-body states to store coherence on timescales exceeding the lifetime of their constituents.

The chapter is structured as follows. In Sec. 8.2 we introduce a semiclassical treatment to describe the dynamics of the atomic beam. In Sec. 8.3 we determine the parameter regime where the atomic beam will undergo superradiant emission. In Sec. 8.4 we analyze the two occurring superradiant phases and study in detail the crossover between the two phases. We conclude with a discussion of the results and their implications in Sec. 8.5. The Appendix provides additional details of the calculations presented in the main text.

8.2 Model

We study the dynamics of a collimated atomic beam that passes through an optical cavity. In our model, the atomic beam is composed of atoms that have the same identical velocity $\mathbf{v} = (v_x, v_z)$, where v_x (v_z) is the longitudinal (transverse) component perpendicular (parallel) to the cavity axis (see Fig. 8.1a). Each atom possesses internal degrees of freedom that are described as a two-level system representing an optical dipole with transition frequency ω_a between its excited $|e\rangle$ and ground state $|g\rangle$. We assume throughout this chapter that the atoms are preexcited in $|e\rangle$ before they enter the cavity. Once in the cavity, every atom interacts during its transit time τ with a single cavity mode with linewidth κ and frequency ω_c that is on resonance, i.e., $\omega_c = \omega_a$. The atom-cavity coupling is characterized by a vacuum Rabi frequency g at the maximum of the cavity mode function $\eta(\mathbf{x})$ (see Fig. 8.1b).

8.2.1 Parameter regime and quantum mechanical description

We investigate the regime where the lifetime of cavity photons is much shorter than the atom transit time, i.e., $\kappa^{-1} \ll \tau$, and the Rabi splitting due to the coherent atom-cavity exchange is unresolvable, i.e., $\sqrt{N}g \ll \kappa$, where N is the mean intracavity atom number. In this regime, the field mode mediates an all-to-all interaction between the atoms, and exposes the dipoles to quantum noise that physically arises from the vacuum leaking through the cavity output. Consequently, we can adiabatically eliminate the field variables and describe the dynamics of the atomic degrees of freedom using the following Heisenberg-Langevin equations

$$\frac{d\hat{\sigma}_j^-}{dt} = \frac{\Gamma_c}{2}\eta(\mathbf{x}_j)\hat{\sigma}_j^z\hat{J}^- + \hat{S}_j^-, \quad (8.1)$$

$$\frac{d\hat{\sigma}_j^z}{dt} = -\Gamma_c\eta(\mathbf{x}_j)\left(\hat{J}^+\hat{\sigma}_j^- + \hat{\sigma}_j^+\hat{J}^-\right) + \hat{S}_j^z, \quad (8.2)$$

$$\frac{d\mathbf{x}_j}{dt} = \mathbf{v}_j. \quad (8.3)$$

These equations are presented in the reference frame rotating with frequency ω_a . Here j labels the individual atoms and $\hat{\sigma}_j^- = |g\rangle_j\langle e|_j$, $\hat{\sigma}_j^+ = \left(\hat{\sigma}_j^-\right)^\dagger$ are the annihilation and creation operators of an electronic excitation and $\hat{\sigma}_j^z = |e\rangle_j\langle e|_j - |g\rangle_j\langle g|_j$ for atom j . The internal degrees together with the position $\mathbf{x}_j = (x_j, z_j)$ describe the instantaneous state of each atom. Furthermore we have introduced the single-atom emission rate $\Gamma_c = g^2/\kappa$ into the cavity mode and collective operators for the atomic dipoles

$$\hat{J}^\pm = \sum_j \eta(\mathbf{x}_j)\hat{\sigma}_j^\pm. \quad (8.4)$$

The summation runs over all atoms in the beam. The effect of the shot noise that is present in this system is apparent in the terms given by $\hat{S}_j^- = \eta(\hat{\mathbf{x}}_j)\hat{\sigma}_j^z\hat{\mathcal{F}}^-$ and $\hat{S}_j^z = -2\eta(\hat{\mathbf{x}}_j)(\hat{\mathcal{F}}^+\hat{\sigma}_j^- + \hat{\sigma}_j^+\hat{\mathcal{F}}^-)$. The term $\hat{\mathcal{F}}^-$ is effectively delta-correlated on the slow timescale associated with the dynamics of the atomic degrees of freedom. This property is represented by the set of correlations that can be written as $\langle \hat{\mathcal{F}}^-(t)\hat{\mathcal{F}}^-(t') \rangle_c = 0 = \langle \hat{\mathcal{F}}^+(t)\hat{\mathcal{F}}^-(t') \rangle_c$ and $\langle \hat{\mathcal{F}}^-(t)\hat{\mathcal{F}}^+(t') \rangle_c = \Gamma_c\delta(t-t')$, $\hat{\mathcal{F}}^+ = (\hat{\mathcal{F}}^-)^\dagger$. The expectation value $\langle \dots \rangle_c$ is taken over the cavity degrees of freedom and the vacuum electromagnetic modes external to the cavity. In our treatment we have neglected spontaneous emission and other

dephasing mechanisms, since we assume that τ is much shorter than any single-atom decoherence time. Furthermore we assume that the atomic motion is ballistic, which is an approximation that is valid when optomechanical forces can be ignored. This requires that $\mathbf{F}\tau/m \ll \mathbf{v}$, where we can estimate the optomechanical force $\mathbf{F} \approx \hbar N \Gamma_c \nabla_{\mathbf{x}} \eta(\mathbf{x})$ that is acting on an individual atom during its transit. Here, m is the mass of the atom and $\nabla_{\mathbf{x}} = (\partial_x, \partial_z)$ is the gradient operator.

8.2.2 Semiclassical description of the atomic degrees of freedom

We are interested in the $N \gg 1$ limit where many atoms couple to the cavity mode at the same time. Because of the exponentially large Hilbert space dimension an exact solution of the quantum mechanical Heisenberg-Langevin equations is intractable. Therefore we make a semiclassical approximation where we replace the quantum operators by c -numbers and add fluctuating noise terms that account for the true quantum noise. This can be done by writing down the Heisenberg-Langevin equations for the Hermitian dipole components $\hat{\sigma}_j^x = \hat{\sigma}_j^- + \hat{\sigma}_j^+$, $\hat{\sigma}_j^y = i(\hat{\sigma}_j^- - \hat{\sigma}_j^+)$, and $\hat{\sigma}_j^z$, and replacing them by their corresponding c -number variables s_j^x , s_j^y , and s_j^z . This results in the following stochastic differential equations that completely characterize our model ²

$$\frac{ds_j^x}{dt} = \frac{\Gamma_c}{2} \eta(\mathbf{x}_j) s_j^z J_x + \mathcal{S}_j^x, \quad (8.5)$$

$$\frac{ds_j^y}{dt} = \frac{\Gamma_c}{2} \eta(\mathbf{x}_j) s_j^z J_y + \mathcal{S}_j^y, \quad (8.6)$$

$$\frac{ds_j^z}{dt} = -\frac{\Gamma_c}{2} \eta(\mathbf{x}_j) (J_x s_j^x + J_y s_j^y) + \mathcal{S}_j^z, \quad (8.7)$$

$$\frac{d\mathbf{x}_j}{dt} = \mathbf{v}_j. \quad (8.8)$$

The expressions

$$J_a = \sum_j \eta(\mathbf{x}_j) s_j^a, \quad (8.9)$$

with $a \in \{x, y\}$ define the x and y components of the collective dipole. In this semiclassical description, the cavity vacuum noise is represented by the terms $\mathcal{S}_j^a = \eta(\mathbf{x}_j) s_j^z \mathcal{F}_a$ and

²We have neglected single-particle terms that scale with Γ_c under the assumption that $\Gamma_c \tau \ll 1$. Furthermore, our approach requires that $N \gg 1$. In this regime the emission is mostly collective.

$\mathcal{S}_j^z = -\eta(\mathbf{x}_j)(s_j^x \mathcal{F}_x + s_j^y \mathcal{F}_y)$, where \mathcal{F}_x and \mathcal{F}_y have zero mean and are defined by the correlation matrix elements $\langle \mathcal{F}_a(t) \mathcal{F}_b(t') \rangle = \Gamma_c \delta_{ab} \delta(t - t')$ with $a, b \in \{x, y\}$ and δ_{ij} the Kronecker delta. In our approach, these noise terms have been derived using the symmetric ordering of the operators, where we identify the symmetric ordered moment $\langle \hat{\sigma}_i^a \hat{\sigma}_j^b + \hat{\sigma}_j^b \hat{\sigma}_i^a \rangle / 2$ as the second moment $\langle s_i^a s_j^b \rangle$ of the classical c -number variables. Besides the fluctuations arising from the cavity vacuum noise (i.e., \mathcal{F}_x and \mathcal{F}_y), there are additional noise source terms that arise from the effective pumping that is introduced by atoms sporadically entering and leaving the cavity mode. For atom j that enters in $|e\rangle$ with $s_j^z = 1$, the uncertainty in s_j^x and s_j^y needs to be maximal (see Ref. [133]). This is modeled by randomly and independently initializing $s_j^x = \pm 1$ and $s_j^y = \pm 1$. With this we fulfill the boundary conditions for the preexcited dipoles as they enter the cavity, i.e., $\langle \hat{\sigma}_j^x \hat{\sigma}_i^x \rangle = \langle s_j^x s_i^x \rangle = \delta_{ij}$, $\langle \hat{\sigma}_j^y \hat{\sigma}_i^y \rangle = \langle s_j^y s_i^y \rangle = \delta_{ij}$, and $\langle \hat{\sigma}_j^x \hat{\sigma}_i^y + \hat{\sigma}_i^y \hat{\sigma}_j^x \rangle / 2 = \langle s_j^x s_i^y \rangle = 0$.

While the microscopic description of Eqs. (8.5)–(8.8) is used for the numerical analysis of the setup, we can also derive a macroscopic description that allows for (semi)analytical results. To obtain this macroscopic description of the atomic beam we examine the dynamics of the densities $s_a(\mathbf{x}, t) = \sum_j s_j^a \delta(\mathbf{x} - \mathbf{x}_j)$ with $a \in \{x, y, z\}$. Using Eqs. (8.5)–(8.8) we obtain Klimontovich-like stochastic equations [22] for the densities

$$\frac{\partial s_x}{\partial t} + \mathbf{v} \cdot \nabla_{\mathbf{x}} s_x = \frac{\Gamma_c}{2} \eta(\mathbf{x}) J_x s_z + \mathcal{S}_x, \quad (8.10)$$

$$\frac{\partial s_y}{\partial t} + \mathbf{v} \cdot \nabla_{\mathbf{x}} s_y = \frac{\Gamma_c}{2} \eta(\mathbf{x}) J_y s_z + \mathcal{S}_y, \quad (8.11)$$

$$\frac{\partial s_z}{\partial t} + \mathbf{v} \cdot \nabla_{\mathbf{x}} s_z = -\frac{\Gamma_c}{2} \eta(\mathbf{x}) (J_x s_x + J_y s_y) + \mathcal{S}_z. \quad (8.12)$$

The left-hand sides of Eqs. (8.10)–(8.12) describe the free flight of the atoms. The first term on the right-hand side of each equation characterizes the collective decay mediated by the cavity field. In this density notation the x and y components for the collective dipole defined in Eq. (8.9) can be expressed as

$$J_a = \int d\mathbf{x} \eta(\mathbf{x}) s_a(\mathbf{x}, t), \quad (8.13)$$

where we have used $\int d\mathbf{x} f(\mathbf{x}) = \int_{-\infty}^{\infty} dx \int_{-\infty}^{\infty} dz f(x, z)$ and $a \in \{x, y\}$. The \mathcal{S}_a terms in

Eqs. (8.10)–(8.12) are stochastic variables that are described by $\mathcal{S}_a(\mathbf{x}, t) = \eta(\mathbf{x})\mathcal{F}_a s_z$ and $\mathcal{S}_z(\mathbf{x}, t) = -\eta(\mathbf{x})(\mathcal{F}_x s_x + \mathcal{F}_y s_y)$.

While the derivation so far is quite general, our analytical and numerical analyses focus on a simplified cavity mode function with a rectangular profile that is given explicitly by the form

$$\eta(\mathbf{x}) = \cos(k_c z) [\Theta(x + w) - \Theta(x - w)]. \quad (8.14)$$

Here, $\Theta(x)$ is the Heaviside step function, w is a width parameter that effectively corresponds to the cavity beam waist, and $k_c = 2\pi/\lambda$ is the wavenumber with λ the optical wavelength. The transit time is directly related to the cavity beam waist and the velocity vertical to the cavity axis, i.e., $\tau = 2w/v_x$. The prescribed condition that new atoms are introduced in state $|e\rangle$ leads to a boundary condition $s_z(x = -w, z, t) = N/(2w\lambda)$. This is derived assuming that the diameter of the atomic beam is much larger than the wavelength λ . In this case we can use λ -periodic boundary conditions in the z direction and restrict the z values to the interval $[0, \lambda)$. In order to describe the quantum fluctuations of the introduced dipoles it is necessary to establish the correct magnitudes of the second moments [133]. This results in initializing the s_x and s_y components with the aid of a simulated noise process that is defined by the following properties: $s_a(x = -w, z, t) = W_a(z, t)$, with $\langle W_a(z, t) \rangle = 0$ and $\langle W_a(z, t) W_b(z', t') \rangle = N/(2w\lambda) \delta_{ab} \delta(z - z') \delta(t - t')/v_x$, $a, b \in \{x, y\}$.

In the following section we will use this density description to study the onset of superradiance.

8.3 Onset of superradiance

We first solve Eqs. (8.10)–(8.12) within the scope of a mean-field approximation. That is, we assume $s_a \approx \langle s_a \rangle$, $a \in \{x, y, z\}$, and calculate the expectation values of the individual dipole components. For clarity, here the expectation value $\langle \dots \rangle$ denotes an average over different initializations and noises. By replacing the fluctuating variables s_a and J_a by their expectation values,

we obtain the mean-field description

$$\frac{\partial \langle s_x \rangle}{\partial t} + \mathbf{v} \cdot \nabla_{\mathbf{x}} \langle s_x \rangle = \frac{\Gamma_c}{2} \eta(\mathbf{x}) \langle J_x \rangle \langle s_z \rangle, \quad (8.15)$$

$$\frac{\partial \langle s_y \rangle}{\partial t} + \mathbf{v} \cdot \nabla_{\mathbf{x}} \langle s_y \rangle = \frac{\Gamma_c}{2} \eta(\mathbf{x}) \langle J_y \rangle \langle s_z \rangle, \quad (8.16)$$

$$\frac{\partial \langle s_z \rangle}{\partial t} + \mathbf{v} \cdot \nabla_{\mathbf{x}} \langle s_z \rangle = -\frac{\Gamma_c}{2} \eta(\mathbf{x}) [\langle J_x \rangle \langle s_x \rangle + \langle J_y \rangle \langle s_y \rangle]. \quad (8.17)$$

Without any noise, the system will always remain in a non-superradiant configuration $\langle s_x \rangle = 0 = \langle s_y \rangle$, and consequently $\langle J_x \rangle = 0 = \langle J_y \rangle$. In this case the atoms essentially do not interact with the cavity and there is no emission of photons. Therefore, during the transit the atoms remain in their electronic excited state, i.e.,

$$\langle s_z \rangle = \frac{N}{2w\lambda}. \quad (8.18)$$

However, this mean-field solution is in general not stable with respect to perturbations by the physical noise sources. Fluctuations of the dipoles and cavity shot noise would initiate a transient avalanche emission process and lead to collective emission by the dipoles into the cavity mode. In order to find the threshold for this effect we calculate the stability of the non-superradiant solution with respect to a small fluctuation $\delta s_a = s_a - \langle s_a \rangle$, $a \in \{x, y\}$. The equations for δs_a read

$$\frac{\partial \delta s_a}{\partial t} + \mathbf{v} \cdot \nabla_{\mathbf{x}} \delta s_a = \frac{N\Gamma_c}{4w\lambda} \eta(\mathbf{x}) \delta J_a. \quad (8.19)$$

Here, we have defined $\delta J_a = \int d\mathbf{x} \eta(\mathbf{x}) \delta s_a$ and neglected second order terms in the fluctuations.

Define the operator

$$\mathcal{L}_0 f(\mathbf{x}) = -\mathbf{v} \cdot \nabla_{\mathbf{x}} f(\mathbf{x}), \quad (8.20)$$

with a function $f(\mathbf{x}) = f(x, z)$. With this definition, we use the Laplace transformation $L[f](\nu) =$

$\int_0^\infty e^{-\nu t} f(t) dt$ on Eq. (8.19) and obtain

$$[\nu - \mathcal{L}_0] L[\delta s_a] - \delta s_a(\mathbf{x}, 0) = \frac{N\Gamma_c}{4w\lambda} \eta(\mathbf{x}) L[\delta J_a]. \quad (8.21)$$

We solve this for $L[\delta s_a]$ where we obtain

$$L[\delta s_a] = [\nu - \mathcal{L}_0]^{-1} \delta s_a(\mathbf{x}, 0) + \frac{N\Gamma_c}{4w\lambda} L[\delta J_a] [\nu - \mathcal{L}_0]^{-1} \eta, \quad (8.22)$$

where we have relied on the fact that $L[\delta J_a]$ does not depend on \mathbf{x} . We can now multiply this equation by η and integrate over \mathbf{x} to obtain

$$L[\delta J_a] = J_1 + J_2, \quad (8.23)$$

with

$$J_1 = \int d\mathbf{x} \eta(\mathbf{x}) [\nu - \mathcal{L}_0]^{-1} \delta s_a(\mathbf{x}, 0), \quad (8.24)$$

$$J_2 = \int d\mathbf{x} \eta(\mathbf{x}) \frac{N\Gamma_c}{4w\lambda} L[\delta J_a] [\nu - \mathcal{L}_0]^{-1} \eta. \quad (8.25)$$

We solve the equation for $L[\delta J_a]$ and the final result reads

$$L[\delta J_a] = \frac{J_1}{1 - \frac{N\Gamma_c}{4w\lambda} \int d\mathbf{x} \eta(\mathbf{x}) [\nu - \mathcal{L}_0]^{-1} \eta(\mathbf{x})}. \quad (8.26)$$

Using now the relations

$$[\nu - \mathcal{L}_0]^{-1} = \int_0^\infty dt e^{-\nu t} e^{\mathcal{L}_0 t}, \quad (8.27)$$

$$e^{\mathcal{L}_0 t} f(\mathbf{x}) = f(\mathbf{x} - \mathbf{v}t), \quad (8.28)$$

and after a substitution $\mathbf{x} \mapsto \mathbf{x} + \mathbf{v}t$ we obtain

$$L[\delta J_a] = \frac{\int d\mathbf{x} \int_0^\infty dt e^{-\nu t} \eta(\mathbf{x} + \mathbf{v}t) \delta s_a(\mathbf{x}, 0)}{1 - \frac{N\Gamma_c}{4w\lambda} \int d\mathbf{x} \int_0^\infty dt e^{-\nu t} \eta(\mathbf{x} + \mathbf{v}t) \eta(\mathbf{x})}, \quad (8.29)$$

where $\delta s_a(\mathbf{x}, 0)$ is the fluctuating initial condition and we have used the notation $\int d\mathbf{x} f(\mathbf{x}) = \int_{-w}^w dx \int_0^\lambda dz f(x, z)$ for any function $f(\mathbf{x}) = f(x, z)$. The inverse transform back into the time domain would provide the solution for δJ_a . However, what we are interested in here is the stability of this solution, that is, whether δJ_a is exponentially damped or exponentially grows. This behavior can be studied directly using the dispersion relation, i.e., the denominator of Eq. (8.29), whose roots determine the exponents in the time domain. The dispersion relation reads

$$D(\nu) = 1 - \frac{N\Gamma_c}{4w\lambda} \int d\mathbf{x} \int_0^\infty dt e^{-\nu t} \eta(\mathbf{x} + \mathbf{v}t) \eta(\mathbf{x}). \quad (8.30)$$

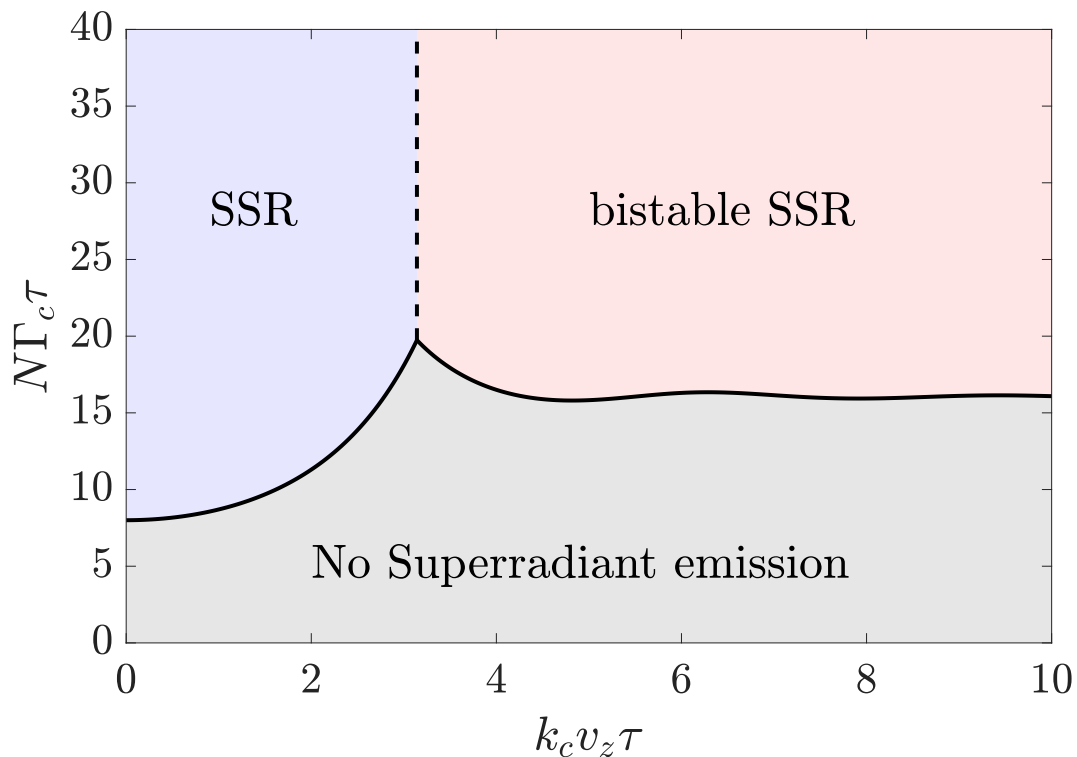


Figure 8.2: The resulting phase diagram describing the light emission for different values of the Doppler shift, $k_c v_z$, and the collective linewidth, $N\Gamma_c$, both in units of the inverse transit time, $1/\tau$. For small values of $N\Gamma_c\tau$ we find no superradiant emission. For sufficiently large values of $N\Gamma_c\tau$, regimes of either regular steady-state superradiance (SSR) or bistable SSR are observed depending on the magnitude of $k_c v_z \tau$.

The long-time behavior of $\delta J_a \propto e^{\nu_0 t}$ is determined by the root ν_0 of $D(\nu)$ with the largest real part. If ν_0 has a negative real part the non-superradiant state is stable and ν_0 determines the decay rate of fluctuations. On the other hand, if ν_0 has a positive real part the fluctuations will exponentially grow and thereby seed a superradiant emission from the ensemble.

The boundary between the regime of no superradiant emission and that of superradiant emission is visible in Fig. 8.2 as a solid black line. This black line has been calculated by finding the roots ν_0 of Eq. (8.30) with $\text{Re}(\nu_0) = 0$. As visible in Fig. 8.2, superradiant emission emerges when the transit time broadening $1/\tau$ is small compared to the collective linewidth $N\Gamma_c$. The exact threshold between no superradiant emission and superradiant emission depends on how many wavelengths an atom traverses during its transit. This quantity is shown as the x axis in Fig. 8.2 that represents $k_c v_z \tau = 2\pi \times (v_z \tau)/\lambda$. However, superradiance can be observed for every v_z as long as $N\Gamma_c \tau > 20$.

While in this section, we have been primarily concerned with the difference between superradiant and no superradiant emission, we also show in Fig. 8.2 two different superradiant phases. In the next section we will explain how we distinguish between these two superradiant phases and provide a detailed analysis for parameters that cross the transition boundary that separates them.

8.4 Superradiant phases

We now focus entirely on the superradiant emission regime. In particular, we are interested in understanding the effect of v_z along the cavity axis that leads to a transverse Doppler shift in the frequency of emitted photons. For a single atom, the emission of photons into the direction of motion shifts the frequency to the blue of the atomic resonance frequency ω_a , while emission in the opposite direction shifts the frequency to the red. In the following subsection we will demonstrate that this simple single-atom picture is inadequate to describe the collective system.

8.4.1 Regular SSR and bistable SSR

In order to study the regimes of coherent emission, we integrate the stochastic differential equations (8.5)–(8.8) numerically for various parameters. In general, we observe that for small velocities v_z the atomic beam undergoes superradiant emission that is still resonant with the bare atomic resonance frequency. This finding highlights the many-body character of the superradiant atomic beam since one might expect a Doppler-shifted frequency for the single-atom case. In order to demonstrate this behavior, we show the spectrum (see Fig. 8.3a)

$$S(\omega) \propto \left| \int_0^T dt e^{i\omega t} \langle J^*(t+t_0)J(t_0) \rangle \right|, \quad (8.31)$$

where $t_0 \gg \tau$ is a sufficiently large time after which the system has evolved to a stationary state, and $J(t) = [J_x(t) - iJ_y(t)]/2$. The time T is the integration time after t_0 (see caption of Fig. 8.3). For $k_c v_z \tau = 2\pi \times 0.3$, i.e., when each atom traverses 0.3 wavelengths along the cavity axis during the transit time, the spectrum shows a narrow Lorentzian peak at $\omega = 0$ corresponding to continuous superradiant emission with central frequency ω_a . We label this phase as SSR, due to the similarities with regular steady-state superradiance (Fig. 8.2).

While this behavior remains stable at first as v_z is increased, once a critical velocity is reached we observe a threshold beyond which a qualitatively different behavior emerges. As an example, we show $S(\omega)$ for $k_c v_z \tau = 2\pi \times 0.8$ in Fig. 8.3b, corresponding to each atom traversing 0.8 wavelengths along the cavity axis. In this case, the spectrum exhibits two narrow Lorentzian peaks that are symmetrically shifted from the resonance frequency of the atoms. While the form of the spectrum suggests simultaneous emission with both frequencies, we find that the atomic beam will randomly undergo superradiant emission with either the red or the blue detuned frequency. The random choice is seeded by the first emission with probability of 0.5 for each of the two possibilities. Subsequently collective spontaneous emission events will amplify the light field with that frequency.

To further demonstrate this behavior, we illustrate in the left (right) inset of Fig. 8.3b the emission spectrum corresponding to trajectories that emit with red (blue) detuned frequencies. Since we have a finite number of initializations we may observe a slight imbalance of red-detuned

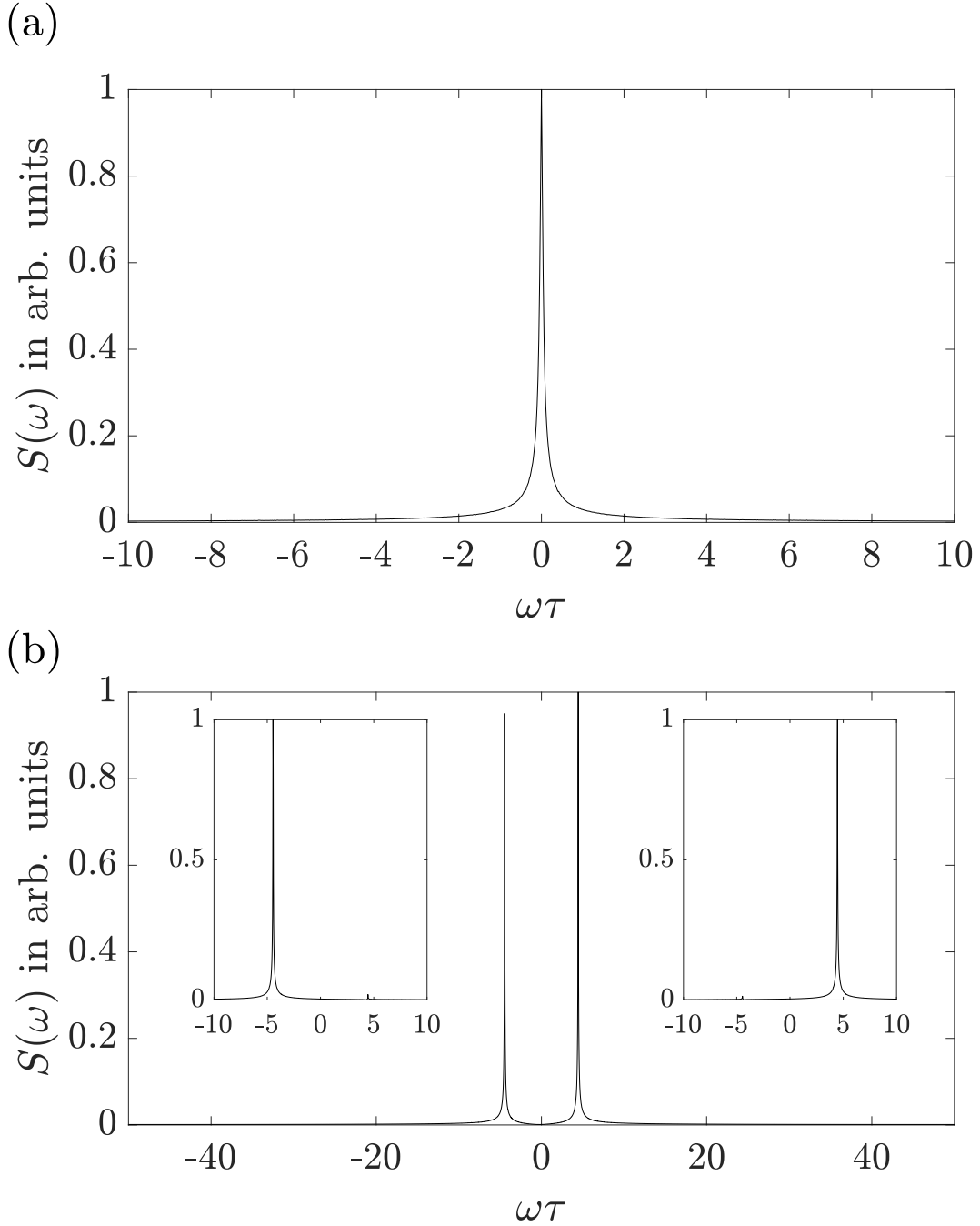


Figure 8.3: The spectrum $S(\omega)$, defined in Eq. (8.31), as a function of the frequency ω in units of $1/\tau$ in the SSR phase for $k_c v_z \tau = 2\pi \times 0.3$ (a) and in the bistable SSR phase $k_c v_z \tau = 2\pi \times 0.8$ (b). For the simulation we used $N\Gamma_c \tau = 30$, $N = 800$, and a total integration time of $t_0 + T = t_{\text{sim}} = 2000\tau$. The spectra are calculated using 500 independent initializations and after a time $t_0 = 10\tau$ (after which the system is well described as being in steady state). The two insets in subplot (b) show the averaged spectrum of the trajectories that correspond to a negative frequency $\omega\tau \approx -4.46$ (238 trajectories) and positive frequency $\omega\tau \approx 4.46$ (262 trajectories).

frequencies with respect to blue-detuned frequencies in each trial batch. This imbalance can be seen as different heights in the spectrum shown in Fig. 8.3b. In the insets we see only one peak supporting our claim that superradiant emission appears for the shown parameters only on one sideband. Because of the bistable nature of the superradiant peaks, this is reminiscent of optical bistability of intensity solutions [1], and consequently we refer to this phase as bistable SSR (Fig. 8.2).

This bistable behavior is best visible in the dynamics of the phase

$$\Delta\varphi(t) = \arg \left(\int_{t_0}^{t_1} dt' \frac{\langle J^*(t+t')J(t') \rangle}{t_1 - t_0} \right), \quad (8.32)$$

where $\arg(\dots)$ denotes the argument and t_0 and t_1 are the initial and final times of an averaging window. We show the dynamics of the phase $\Delta\varphi$ in Fig. 8.4 with 500 initializations and for the same parameters as in Fig. 8.3b, $N\Gamma_c\tau = 30$ and $k_c v_z \tau = 2\pi \times 0.8$. Most of the 500 trajectories remain on straight lines with a constant slope. This slope corresponds to the two frequencies that are visible in Fig. 8.3b. However, some of the trajectories jump between the two slopes, signifying clearly the bistable nature of the frequency solutions.

In order to understand further properties of the two superradiant phases and to provide insight that is evident from an analytic treatment, we now develop a mean-field theoretic description.

8.4.2 Intensity and emission frequency

Both superradiant phases can be classified by a non-vanishing collective dipole with a constant length. However, in one phase the collective dipole oscillates with a non-vanishing frequency ω (bistable SSR) while in the other regime the phase of the collective dipole remains almost constant (regular SSR).

In order to analyze this behavior we solve the mean-field equations

$$\frac{\partial \langle s \rangle}{\partial t} + \mathbf{v} \cdot \nabla_{\mathbf{x}} \langle s \rangle = \frac{\Gamma_c}{2} \eta(\mathbf{x}) \langle s_z \rangle \langle J \rangle, \quad (8.33)$$

$$\frac{\partial \langle s_z \rangle}{\partial t} + \mathbf{v} \cdot \nabla_{\mathbf{x}} \langle s_z \rangle = -\Gamma_c \eta(\mathbf{x}) [\langle J^* \rangle \langle s \rangle + \langle s^* \rangle \langle J \rangle], \quad (8.34)$$

that are presented in the form above for the complex dipole $s = (s_x - i s_y)/2$ with $J = \int d\mathbf{x} s$.

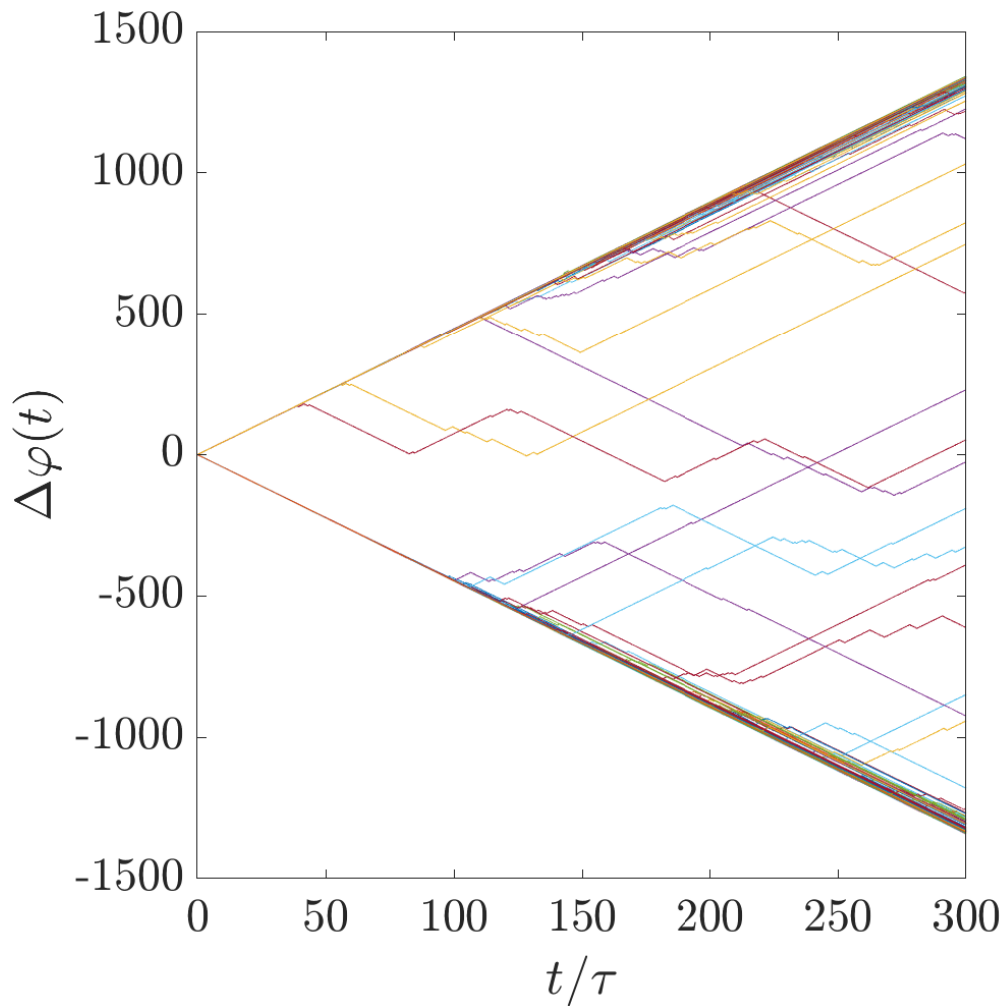


Figure 8.4: The phase difference $\Delta\varphi(t)$, defined in Eq. (8.32), as a function of time in units of τ for $N = 800$. The time window is defined by $t_0 = 10\tau$ and $t_1 = 1700\tau$, and the total simulation time is $t_{\text{sim}} = 2000\tau$. For the simulations we used 500 trajectories and the parameters $k_c v_z \tau = 2\pi \times 0.8$ and $N\Gamma_c \tau = 30$.

From Eqs. (8.33)–(8.34) one can verify that

$$\left(\frac{\partial}{\partial t} + \mathbf{v} \cdot \nabla_{\mathbf{x}} \right) [\langle s_z \rangle^2 + 4|\langle s \rangle|^2] = 0. \quad (8.35)$$

This equation highlights that in our model the length of the Bloch vector is conserved. This is a consequence of the form of Eqs. (8.33)–(8.34) that describe collective emission as Rabi oscillations with a self-consistent Rabi frequency $\propto \langle J \rangle$. As a result we can use spherical coordinates to describe the dipole densities. Together with the boundary conditions, we therefore parametrize the pseudospin variables by the following geometrical quantities

$$\langle s \rangle = \frac{N}{4w\lambda} e^{-i\phi(\mathbf{x}, t)} \sin [K(\mathbf{x}, t)], \quad (8.36)$$

$$\langle s_z \rangle = \frac{N}{2w\lambda} \cos [K(\mathbf{x}, t)], \quad (8.37)$$

with space and time dependent angles $\phi(\mathbf{x}, t)$ and $K(\mathbf{x}, t)$.

While this description is always valid we will now focus on the stationary properties of the atomic beam that are realized after a sufficiently long time t . In both regular SSR and bistable SSR, we anticipate a behavior for $\phi(\mathbf{x}, t)$ according to

$$\phi(\mathbf{x}, t) = \omega t + \psi(\mathbf{x}), \quad (8.38)$$

where ω is the frequency of the emitted light and ψ is a position dependent but time independent phase. Assuming K is not explicitly time dependent, we obtain the following coupled differential equations for ψ and K

$$\omega + \mathbf{v} \cdot \nabla_{\mathbf{x}} \psi = -\Gamma_c \eta(\mathbf{x}) |\langle J \rangle| \sin(\psi) \cot(K), \quad (8.39)$$

$$\mathbf{v} \cdot \nabla_{\mathbf{x}} K = \Gamma_c \eta(\mathbf{x}) |\langle J \rangle| \cos(\psi). \quad (8.40)$$

These equations can be solved together with the two equations emerging from the real and imaginary parts of $\int d\mathbf{x} \langle s \rangle e^{i\omega t} = |\langle J \rangle|$. The solution of all four equations result in a value for the length of the collective dipole $|\langle J \rangle|$, the emission frequency ω , and the functions $K(\mathbf{x})$ and $\psi(\mathbf{x})$. We have derived these equations, without loss of generality, under the assumption that $\langle J(t=0) \rangle = \langle J_x(t=0) \rangle / 2$ points in the x direction at $t=0$. This is equivalent to the assumption $\langle J \rangle = |\langle J \rangle| e^{-i\omega t}$.

The complexity in solving Eqs. (8.39)–(8.40) is tremendously simplified in the case where $\omega = 0$ (regular SSR phase) because we directly obtain the result $\psi = 0$. In this case Eq. (8.39) can be directly solved using $\psi = 0$ and this results in the partial differential equation

$$\mathbf{v} \cdot \nabla_{\mathbf{x}} K = \Gamma_c \eta(\mathbf{x}) |\langle J \rangle|. \quad (8.41)$$

The solution of this equation is straight forward and reads

$$K(x - w, z) = \frac{\Gamma_c J_{\parallel, \text{st}} \sin\left(\frac{v_z}{2v_x} k_c x\right) \cos\left(k_c \left[z - \frac{v_z}{2v_x} x\right]\right)}{k_c v_z}, \quad (8.42)$$

where we have used

$$\begin{aligned} J_{\parallel, \text{st}} &= 2|\langle J \rangle| \\ &= \int d\mathbf{x} \eta(\mathbf{x}) \frac{N}{2w\lambda} \sin(K(\mathbf{x})) \\ &= N \frac{1 - \mathcal{J}_0\left(\frac{\Gamma_c J_{\parallel, \text{st}} \tau}{2} \frac{\sin\left(\frac{k_c v_z \tau}{2}\right)}{\frac{k_c v_z \tau}{2}}\right)}{\frac{\Gamma_c J_{\parallel, \text{st}} \tau}{2}}. \end{aligned} \quad (8.43)$$

Solving this implicit equation for $J_{\parallel, \text{st}}$ and using the result in Eq. (8.42) allows us to describe the dipole density in the regular SSR phase. However, for the general case we have to solve the coupled partial differential equations.

We show the mean-field results for ω and $|\langle J \rangle|$ across the regular SSR to bistable SSR transition and compare them with the results of a numerical integration of Eqs. (8.5)–(8.8). The results are calculated for $N\Gamma_c\tau = 20$ visible in Fig. 8.5a–b, close to the non-superradiant regime, and for $N\Gamma_c\tau = 30$ shown in Fig. 8.5c–d, well inside of the superradiant regime. In Fig. 8.5, we illustrate $\langle J^* J \rangle / N^2$ and the emission frequency ω as a function of $k_c v_z \tau$. The mean-field theory predicts a non-analytical behavior of both $\langle J^* J \rangle / N^2$ and ω at a threshold value of $k_c v_z \tau = \pi$. It shows a kink-like local minimum for $\langle J^* J \rangle / N^2$ and a bifurcation of ω at the threshold that is in agreement with the simulations. In general we find that the non-analyticities are smoothed out by noise and finite size effects. The rather large discrepancies between the mean-field results and the simulations in Fig. 8.5a are likely due to these effects that are more pronounced close to a tri-critical

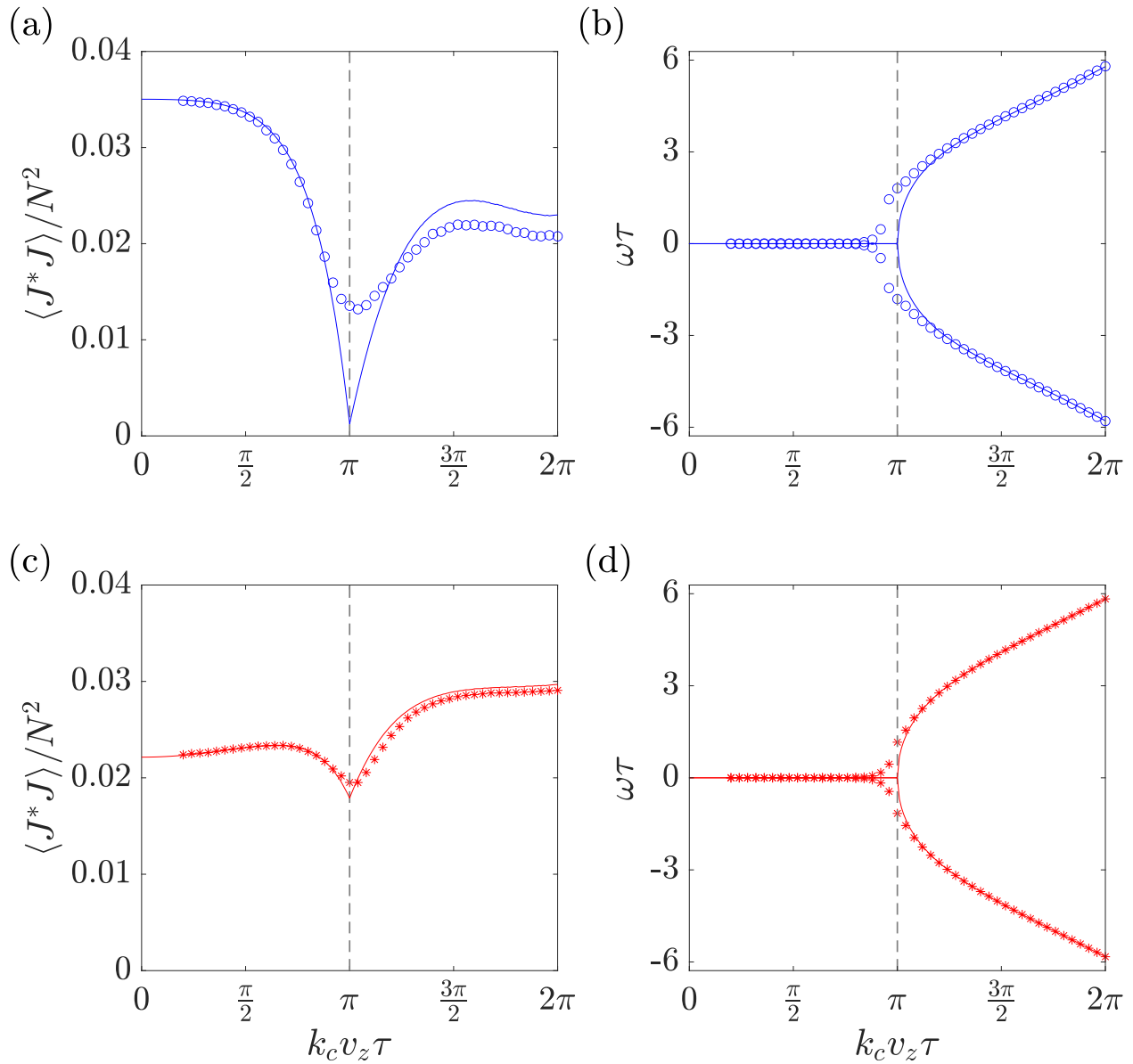


Figure 8.5: The collective dipole $\langle J^* J \rangle / N^2$, subplots (a–c), and the frequency of the light ω in units of $1/\tau$, subplots (b–d), as functions of $k_c v_z \tau$. Subplots (a–b), and (c–d) show results for $N\Gamma_c\tau = 20$ and $N\Gamma_c\tau = 30$, respectively. The circles and stars correspond to numerical simulations of Eqs. (8.5)–(8.8), and the solid lines represent analytical solutions for $N \rightarrow \infty$. The vertical gray dashed lines show the transition from regular SSR to bistable SSR. The numerical values of ω from the simulations in subplots (b) and (d) have been calculated by fitting $g_1(t)$ (Eq. (8.64)) to $\cos(\omega t + \phi_0)e^{-\Gamma t/2}$ and $t_0 = 10\tau$. Here, ω , Γ and ϕ_0 are fitting parameters. The simulations are performed with $N = 800$, an integration time of $t_{\text{sim}} = 100\tau$, and 400 initializations.

point where regular SSR, bistable SSR, and the non-superradiant emission phases meet (tri-critical point is at $N\Gamma_c\tau = 2\pi^2$ and $k_c v_z \tau = \pi$). For the large $k_c v_z \tau$ limit we obtain the asymptotic result $\omega \approx k_c v_z$. The behavior of ω close to the transition is reminiscent of a second order phase transition that is here observed in a highly dissipative setting where neither individual atoms nor individual photons remain in the cavity on a timescale longer than τ . We remark that in both superradiant phases we have broken a U(1) symmetry resulting in a well defined value for the phase of J and corresponding physically to the generation of near-monochromatic light. In the bistable SSR phase we also have a broken time-translation symmetry, which is evident in Eq. (8.38) for $\omega \neq 0$.

As we have pointed out in the previous subsection the system can jump between the two bistable frequencies $\pm\omega$. We now analyze the statistical properties of this effect in more detail using the result of the numerical integration of Eqs. (8.39)–(8.40).

8.4.3 Mode hopping probability

In order to quantitatively analyze the statistical properties of the mode hopping, we calculate the probability for the occurrence of a jump from the negative to the positive frequency. In order to do this, we begin by evaluating $\Delta\varphi(t)$ according to Eq. (8.32). Then, we divide the time interval $[0, t_{\max}]$ of every trajectory of $\Delta\varphi(t)$ into M equal interval time bins $[(m-1)\Delta t, m\Delta t]$ with $m = 1, \dots, M$ and $\Delta t = t_{\max}/M$. Within each time bin we calculate an average frequency

$$\omega(m) = \frac{1}{\Delta t} \int_{(m-1)\Delta t}^{m\Delta t} dt' \frac{d\Delta\varphi(t')}{dt'}. \quad (8.44)$$

From the average frequencies, we can now accumulate statistics on the number of frequency jumps that occur by evaluating whether $\omega(m)\omega(m+1) < 0$ for $m = 1, \dots, M-1$. By counting the total number of jumps from all trajectories, $\mathcal{N}_{\text{jump}}$, and dividing by the maximum number of jumps possible, $\mathcal{N}_{\text{total}} = (M-1) \times \mathcal{T}$, where \mathcal{T} is the number of trajectories, we get

$$P_{\text{jump}} = \frac{\mathcal{N}_{\text{jump}}}{\mathcal{N}_{\text{total}}} \quad (8.45)$$

for the probability of a mode hop.

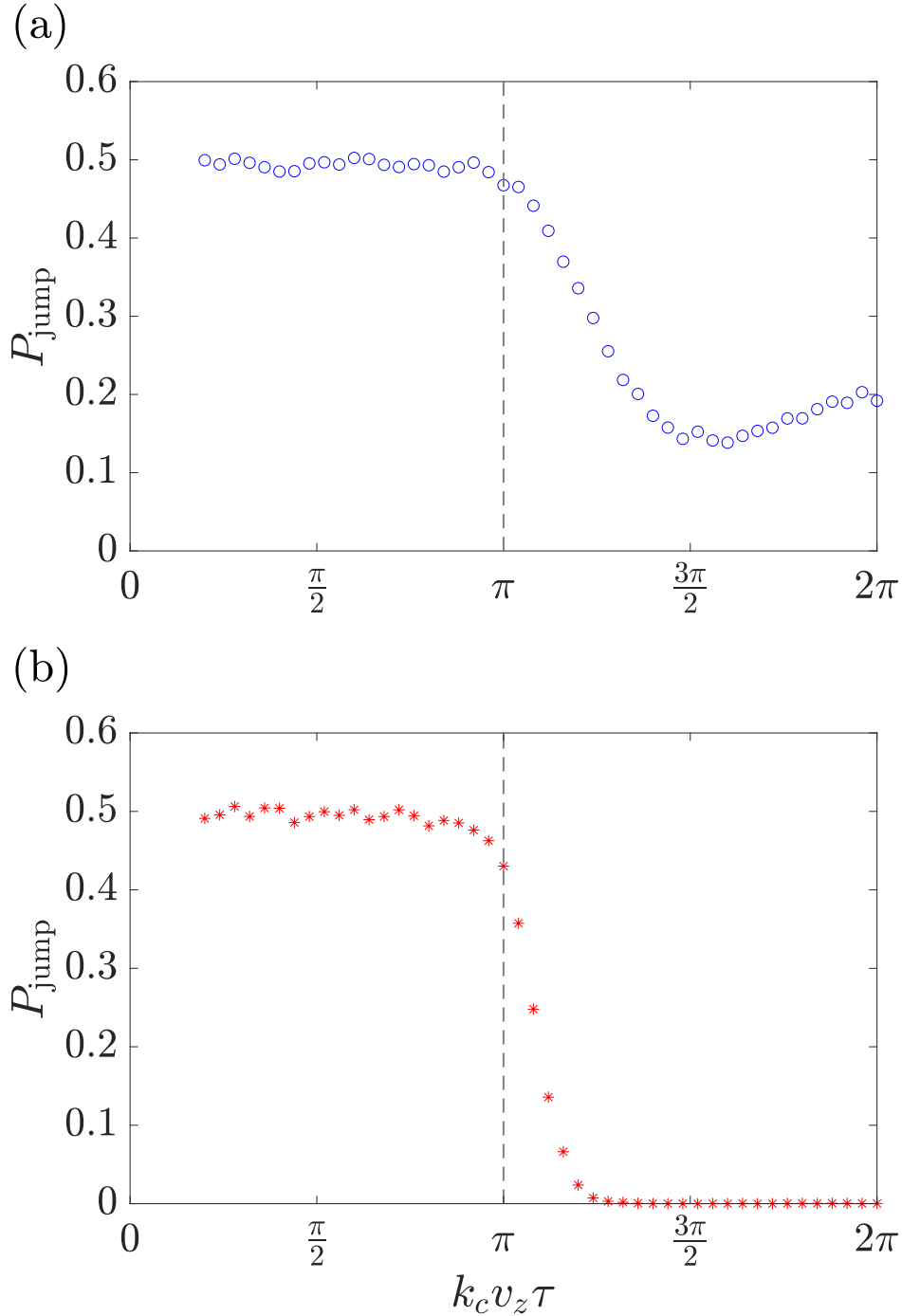


Figure 8.6: The jump probability P_{jump} , defined in Eq. (8.45), for different values of $k_c v_z \tau$ for $N\Gamma_c\tau = 20$ (a) and $N\Gamma_c\tau = 30$ (b). For the simulations we used $t_{\text{sim}} = 100\tau$, $N = 800$, and $\mathcal{T} = 400$ and started the analysis after $t_0 = 10\tau$, after which, to good approximation, the system had reached the stationary state. The value of $\Delta\varphi(t)$ for each trajectory is calculated according to Eq. (8.32) without the time average for $t_1 \rightarrow t_0$. According to the definitions given in the text prior to Eq. (8.45), we have used $t_{\text{max}} = 90\tau$ that we split into $M = 20$ bins. The gray dashed vertical line shows the threshold between the regular SSR and the bistable SSR phases, i.e., $k_c v_z \tau = \pi$.

The jump probability is shown in Fig. 8.6a–b for various values of $k_c v_z \tau$ across the phase transition from regular SSR to bistable SSR and for $N\Gamma_c \tau = 20$ (Fig. 8.6a) and $N\Gamma_c \tau = 30$ (Fig. 8.6b), respectively. The simulations are the same as those shown in Fig. 8.5. We see that P_{jump} is close to $P_{\text{jump}} \approx 0.5$ for both values of $N\Gamma_c \tau$ well inside the regular SSR phase. This can be explained by the fact that $\Delta\varphi$ diffuses. In this case, after every time bin, the total phase gains with probability 0.5 a positive or negative increment. Beyond the transition point, $k_c v_z \tau = \pi$, we observe a decrease of this jump probability in both cases. For $N\Gamma_c \tau = 30$ (Fig. 8.6b), we observe that the jump probability drops to a value very close to $P_{\text{jump}} \approx 0$. This emphasizes that the switch between a negative and a positive frequency becomes very improbable. While we also see a decrease of the jump probability for $N\Gamma_c \tau = 20$ (Fig. 8.6a), after the transition point, a jump is still much more likely than for $N\Gamma_c \tau = 30$. Moreover, we observe that the jump probability shows a local minimum very close to the local maximum of the amplitude of the collective dipole (see Fig. 8.5a). Therefore we propose that the reason for this effect is the more pronounced contribution of noise with respect to the mean value of the collective dipole. For the same reason we expect that the jump probability will decrease in the bistable SSR phase for larger atom number N since the ratio of noise to the mean value of the collective dipole is further reduced.

While deep in the regular SSR phase we have observed a diffusive behavior of the phase $\Delta\varphi$, we have also seen a ballistic behavior inside of the bistable SSR phase (see Eq. (8.38) and Fig. 8.5d). This dynamical phase transition is highlighted in the linewidth of the collectively emitted light as we show now.

8.4.4 The linewidth

Well inside the regular SSR phase we may assume that the system has a macroscopic collective dipole with some arbitrary phase φ in the x - y plane. In that case we can rotate into a frame such that $J_{\parallel} \sim N$ and $J_{\perp} \sim \sqrt{N}$, where \parallel and \perp denote the new x and y axes. The direction corresponding to J_{\parallel} is the direction of the collective dipole while the perpendicular direction J_{\perp} is solely dominated by fluctuations. The dynamics of the dipole component in the perpendicular

direction can be derived from Eqs. (8.10)–(8.12) as

$$\frac{\partial s_{\perp}}{\partial t} + \mathbf{v} \cdot \nabla_{\mathbf{x}} s_{\perp} \approx \frac{\Gamma_c}{2} \eta(\mathbf{x}) J_{\perp} s_{z,\text{st}} + \mathcal{S}_{\perp}, \quad (8.46)$$

where we have dropped second order terms in the fluctuations and noise and are therefore able to substitute the mean-field solution for s_z that reads

$$s_{z,\text{st}} = \frac{N}{2w\lambda} \cos(K(\mathbf{x})). \quad (8.47)$$

Here, K is the solution of Eq. (8.40) for $\omega = 0 = \psi$ in the SSR phase. Equation (8.46) includes cavity noise described by the quantity $\mathcal{S}_{\perp}(\mathbf{x}, t) = \eta(\mathbf{x}) \mathcal{F}_{\perp} s_z$ with $\langle \mathcal{F}_{\perp}(t) \rangle = 0$ and $\langle \mathcal{F}_{\perp}(t) \mathcal{F}_{\perp}(t') \rangle = \Gamma_c \delta(t - t')$. Besides the cavity noise, it also includes the noisy boundary condition that arises from the introduction of new atoms $s_{\perp}(x = -w, z, t) = W_{\perp}(z, t)$, with $\langle W_{\perp}(z, t) \rangle = 0$ and $\langle W_{\perp}(z, t) W_{\perp}(z', t') \rangle = N/(2w\lambda) \delta(z - z') \delta(t - t')/v_x$.

We can integrate Eq. (8.46) to obtain an analytical result for J_{\perp} , which can be used to calculate the linewidth. Furthermore we can use this analytical result to calculate the threshold between the regular SSR and bistable SSR phases.

Using the Laplace transform on Eq. (8.46) we obtain

$$[\nu - \mathcal{L}_0] L[s_{\perp}] - s_{\perp}(\mathbf{x}, 0) = \frac{\Gamma_c}{2} \eta s_{z,\text{st}} L[J_{\perp}] + L[\mathcal{S}_{\perp}]. \quad (8.48)$$

Here we have used the fact that $s_{z,\text{st}}$ is time independent, and included the definition in Eq. (8.20). The initial condition $s_{\perp}(\mathbf{x}, 0)$ arises from the noisy boundary condition that represents atoms entering the cavity. It is given by

$$s_{\perp}(\mathbf{x}, 0) = W_{\perp}(z - v_z t_0(x), -t_0(x)), \quad (8.49)$$

where $t_0(x) = (w + x)/v_x$. Solving now Eq. (8.48) for $L[s_{\perp}]$ we find

$$L[s_{\perp}] = [\nu - \mathcal{L}_0]^{-1} \left[s_{\perp}(\mathbf{x}, 0) + \frac{\Gamma_c}{2} \eta s_{z,\text{st}} L[J_{\perp}] + L[\mathcal{S}_{\perp}] \right]. \quad (8.50)$$

Multiplying by $\eta(\mathbf{x})$ and integrating over the space variable \mathbf{x} , we find an equation for $L[J_{\perp}]$. We solve this equation for $L[J_{\perp}]$ and find the result

$$L[J_{\perp}] = \frac{L[J_{W_{\perp}}] + 2 \frac{1 - D_{\perp}(\nu)}{\Gamma_c} L[\mathcal{S}_{\perp}]}{D_{\perp}(\nu)}, \quad (8.51)$$

where

$$J_{W_{\perp}}(t) = \int d\mathbf{x} \eta(\mathbf{x} + \mathbf{v}t) W_{\perp}(z - v_z t_0(x), -t_0(x)) \quad (8.52)$$

arises from the initial projection noise. In this derivation, we have used Eqs. (8.27)–(8.28) and the change of variables given by $\mathbf{x} \mapsto \mathbf{x} + \mathbf{v}t$.

The function $D_{\perp}(\nu)$ is the dispersion relation of the Goldstone mode of the collective dipole, which reads

$$D_{\perp}(\nu) = 1 - \frac{N\Gamma_c}{4w\lambda} \int d\mathbf{x} \int_0^{\infty} dt e^{-\nu t} \eta(\mathbf{x} + \mathbf{v}t) \eta \cos(K). \quad (8.53)$$

In the regular SSR phase, we can use Eq. (8.41) to rewrite $D_{\perp}(\nu)$ as

$$D_{\perp}(\nu) = 1 - \frac{\int_0^{\infty} dt e^{-\nu t} \int d\mathbf{x} \eta(\mathbf{x} + \mathbf{v}t) \mathbf{v} \cdot \nabla_{\mathbf{x}} s_{\parallel, \text{st}}}{J_{\parallel, \text{st}}},$$

where

$$s_{\parallel, \text{st}} = \frac{N}{2w\lambda} \sin[K(\mathbf{x})], \quad (8.54)$$

and $J_{\parallel, \text{st}} = \int d\mathbf{x} \eta(\mathbf{x}) s_{\parallel, \text{st}}$ has been calculated in Eq. (8.43).

Applying Gauß's theorem and using the fact that the atoms enter in the excited state and that the mode function vanishes at infinity, we get

$$D_{\perp}(\nu) = 1 + \frac{\int_0^{\infty} dt e^{-\nu t} \int d\mathbf{x} \frac{d}{dt} \eta(\mathbf{x} + \mathbf{v}t) s_{\parallel, \text{st}}}{J_{\parallel, \text{st}}}.$$

After another partial integration, we obtain the final form

$$D_{\perp}(\nu) = \nu \frac{\int_0^{\infty} e^{-\nu t} dt \int d\mathbf{x} \eta(\mathbf{x} + \mathbf{v}t) s_{\parallel, \text{st}}(\mathbf{x})}{J_{\parallel, \text{st}}}. \quad (8.55)$$

The zeros of Eq. (8.55) can be used to describe the dynamics of J_{\perp} . In what follows we will assume that $\nu_0 = 0$ is the solution with the largest real part. With this we can argue that the pole at $\nu = 0$ in Eq. (8.51) dictates the long-time behavior of J_{\perp} . To describe this long-time behavior we can use the approximation

$$L[J_{\perp}] \approx \frac{L[J_{W_{\perp}}] + \frac{2}{\Gamma_c} L[\mathcal{S}_{\perp}]}{C_0 \nu}, \quad (8.56)$$

where

$$C_0 = \lim_{\nu \rightarrow 0} \frac{D_{\perp}(\nu)}{\nu} = \frac{\int_0^{\infty} dt \int d\mathbf{x} \eta(\mathbf{x} + \mathbf{v}t) s_{\parallel, \text{st}}(\mathbf{x})}{J_{\parallel, \text{st}}}. \quad (8.57)$$

By inverting the Laplace transform we find now

$$J_{\perp} \approx \frac{\int_0^t dt' [A_1(t') + A_2(t')]}{C_0}, \quad (8.58)$$

with

$$A_1(t') = \int d\mathbf{x} \eta(\mathbf{x} + \mathbf{v}t') W_{\perp}(z - v_z t_0(x), -t_0(x)), \quad (8.59)$$

$$A_2(t') = \frac{2\mathcal{S}_{\perp}(t')}{\Gamma_c}. \quad (8.60)$$

Equation (8.58) describes diffusive dynamics perpendicular to the direction of the collective dipole with length $J_{\parallel, \text{st}}$ that results in phase diffusion. Integrating

$$\frac{d\varphi}{dt} \approx \frac{1}{J_{\parallel, \text{st}}} \frac{dJ_{\perp}}{dt}, \quad (8.61)$$

we obtain

$$\Delta\varphi(t) = \varphi(t) - \varphi(0) \approx \frac{\int_0^t dt' [A_1(t') + A_2(t')]}{C_0 J_{\parallel, \text{st}}}. \quad (8.62)$$

Arguing that the origin of a finite linewidth in the regular SSR phase is phase diffusion, we can calculate the linewidth using

$$\Gamma = \lim_{t \rightarrow \infty} \frac{\langle \Delta\varphi(t)^2 \rangle}{t}. \quad (8.63)$$

To show that our description of Eq. (8.63) is valid we have integrated numerically Eqs. (8.5)–(8.8), calculated the real part of the normalized g_1 function

$$g_1(t) = \frac{\text{Re}(\langle J^*(t+t_0)J(t_0) \rangle)}{\langle |J(t_0)|^2 \rangle}, \quad (8.64)$$

and fitted $\cos(\omega t + \phi_0)e^{-\Gamma t/2}$ where ω , Γ , and ϕ_0 are fitting parameters. In this fit ω is the emission frequency reported in Fig. 8.5 and Γ is the linewidth, visible as circles and stars in Fig. 8.7 for

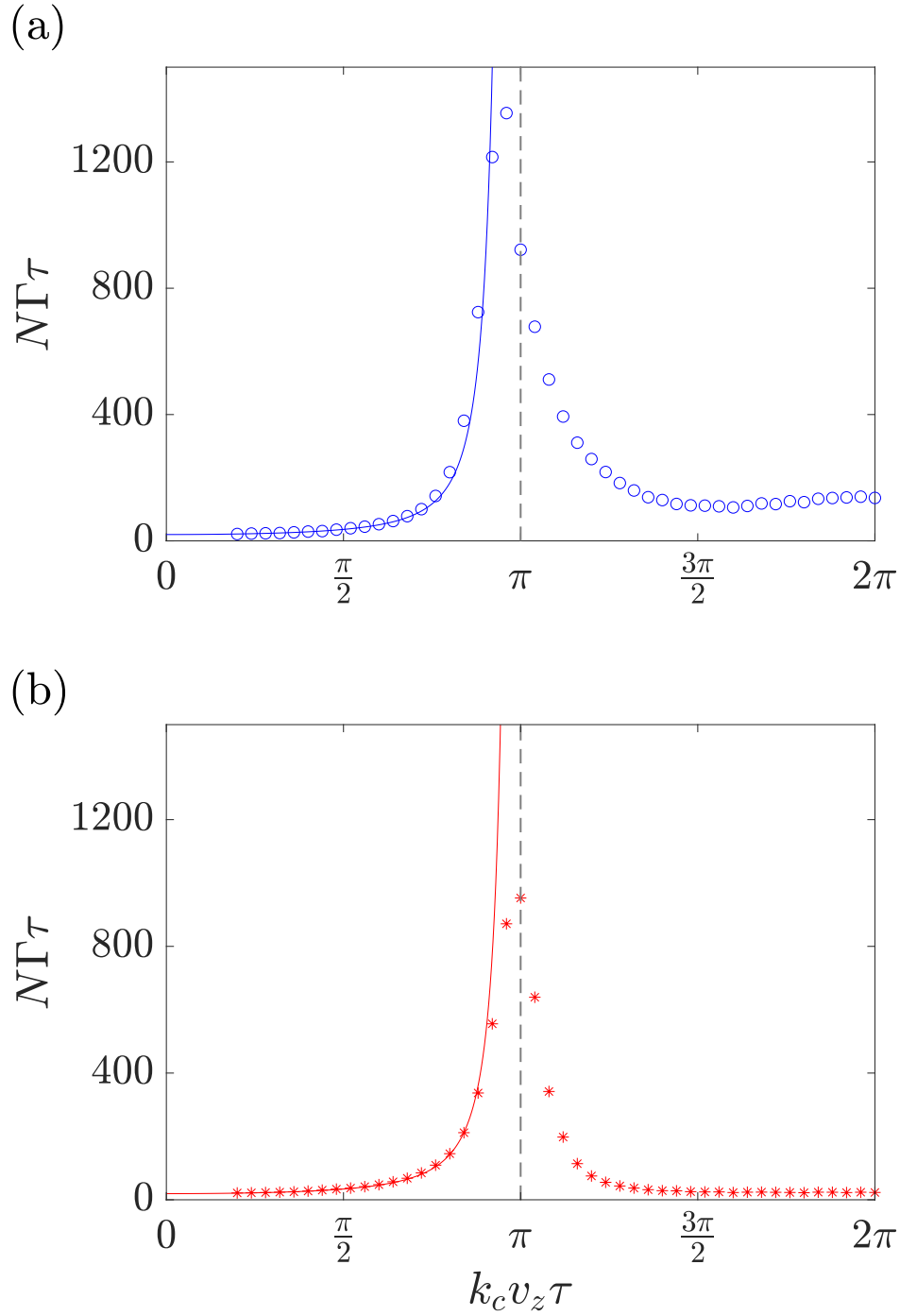


Figure 8.7: The linewidth Γ in units $1/(N\tau)$ as functions of $k_c v_z \tau$ for $N\Gamma_c \tau = 20$ (a) and $N\Gamma_c \tau = 30$ (b). The circles and stars correspond to numerical simulations, and the solid lines represent the result of Eq. (8.63) for $N \rightarrow \infty$. The vertical gray dashed lines show the transition from regular SSR to bistable SSR. The values of Γ have been calculated by fitting g_1 (Eq. (8.64)) with $\cos(\omega t + \phi_0)e^{-\Gamma t/2}$ and $t_0 = 10\tau$. The simulations are performed with $N = 800, 400$ trajectories, and an integration time of $t_{\text{sim}} = 100\tau$.

$N\Gamma_c\tau = 20$ (a) and $N\Gamma_c\tau = 30$ (b). The solid lines in Fig. 8.7 are the calculated linewidth from Eq. (8.63). These curves are in good agreement with the simulations well inside of the regular SSR phase, but predict a diverging linewidth at the critical point.

The origin of this divergence in the analytical result is the break-down of the phase diffusion argument. The diffusive behavior of the phase is a direct result of Eq. (8.56) where we have assumed that $\nu_0 = 0$ is a zero of first order of $D_\perp(\nu)$. However, it breaks down if $C_0 = 0$, which indicates that $\nu_0 = 0$ is a zero of $D_\perp(\nu)$ of higher order than first. This can be used to identify the threshold between the regular SSR and bistable SSR phases. We can solve the integrals in Eq. (8.57) and find

$$C_0 J_{\parallel, \text{st}} = \int_0^\infty dt \int d\mathbf{x} \eta(\mathbf{x} + \mathbf{v}t) s_{\parallel, \text{st}} = \cos\left(\frac{k_c v_z \tau}{2}\right) R, \quad (8.65)$$

with

$$R = 2N \int_0^1 du \frac{\sin\left(\frac{k_c v_z \tau [1-u]}{2}\right) \mathcal{J}_1\left(\frac{\Gamma_c J_{\parallel, \text{st}} \sin\left(\frac{k_c v_z \tau u}{2}\right)}{k_c v_z}\right)}{k_c v_z}, \quad (8.66)$$

where \mathcal{J}_n denotes the Bessel function of order n . For this expression we have used the analytical result of K given by Eq. (8.42). For $k_c v_z \tau = \pi$, we obtain $\cos(\pi/2) = 0$, hence $C_0 = 0$, and the phase diffusion argument breaks down. Therefore $k_c v_z \tau = \pi$ is the threshold between regular SSR and bistable SSR. This phase boundary is shown in Fig. 8.2, 8.5, 8.6, and 8.7 as the vertical dashed lines. At this critical point, we expect that also the numerical result of the linewidth when expressed in units of $1/(N\tau)$ diverges in the large N limit.

In order to support this claim, we plot Γ in units of $1/\tau$ for different values of N in a log-log plot to illustrate the scaling of Γ with the number of atoms, $\Gamma\tau \propto N^\alpha$ (Fig. 8.8). We show the scaling well inside the regular SSR phase for $k_c v_z \tau = \pi/2$ (green crosses), well inside the bistable SSR phase for $k_c v_z \tau = 3\pi/2$ (red stars), and at the theoretically predicted threshold $k_c v_z \tau = \pi$ (blue circles). The values of the exponent α governing the scaling relation $\Gamma\tau \propto N^\alpha$ in the three regimes are extracted using a linear fit and are reported in the caption of Fig. 8.8. For parameters well inside of the regular SSR or bistable SSR phases we obtain an exponent $\alpha \approx -1$. This implies

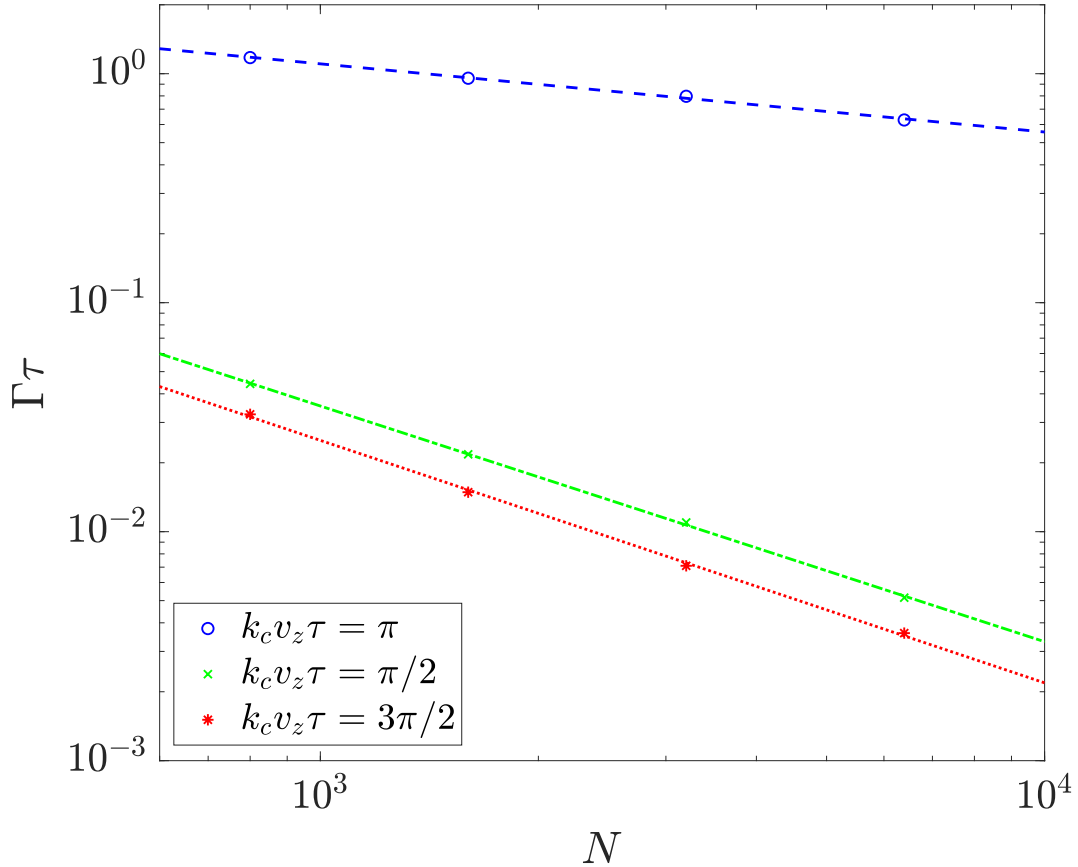


Figure 8.8: The linewidth Γ in units of $1/\tau$ as a function of the intracavity atom number N for $N\Gamma_c\tau = 30$. The blue circles, green crosses, and red stars correspond to different values of $k_c v_z \tau$ (see legend) at the threshold, in the SSR phase, and in the bistable SSR phase. The blue dashed, green dashed-dotted, and red dotted lines are linear fits according to $\Gamma\tau \propto N^\alpha$ with $\alpha = -0.30$, $\alpha = -1.03$, and $\alpha = -1.06$, respectively. For every N we average over $4.8 \times 10^5/N$ trajectories with a simulation time $t_{\text{sim}} = 100\tau$. Every point is calculated using the fit as described in the caption of Fig. 8.7.

that for given values of $k_c v_z \tau$ and $N\Gamma_c \tau$, Γ in units of $1/(N\tau)$ is a constant $\propto \Gamma_c$. This claim is consistent with our theoretical description and also shows that the collective dipole remains stable on timescales that exceed the transit time τ by orders of magnitude.

At the critical point $k_c v_z \tau = \pi$ the phase diffusion argument anticipates a diverging linewidth. Our numerical simulations here show that there exists a critical scaling with an exponent $\alpha \approx -0.3$. Therefore even at the critical point, Γ beats the Fourier limit set by $1/\tau$. In units of $1/(N\tau)$ the linewidth scales as $N^{1+\alpha} \approx N^{0.7} \rightarrow \infty$, supporting our theoretical prediction of a diverging linewidth using the phase diffusion model. This divergence is reminiscent of the quantum critical region [130] that occurs at finite temperature in an equilibrium quantum phase transition where scaling laws provide the potential for extreme sensitivity to model parameters.

Our analytical theory can also give some insight to the relaxation dynamics at the threshold, where we find that $\nu = 0$ is a zero of order two of $D_\perp(\nu)$. Using this we can approximate

$$L[J_\perp] \approx \frac{L[J_{W_\perp}] + \frac{2}{\Gamma_c} L[\mathcal{S}_\perp]}{C_1 \nu^2},$$

where

$$C_1 = \lim_{\nu \rightarrow 0} \frac{D_\perp(\nu)}{\nu^2}. \quad (8.67)$$

This can be used to establish

$$J_\perp \approx \frac{\int_0^t dt' \int_0^{t'} dt'' [A_1(t'') + A_2(t'')]}{C_1}, \quad (8.68)$$

where we have used Eqs. (8.59)–(8.60). Dividing this equation by $J_{\parallel, \text{st}}$ leads to the following equation for the phase

$$\Delta\varphi(t) \approx \frac{\int_0^t dt' \int_0^{t'} dt'' [A_1(t'') + A_2(t'')]}{C_1 J_{\parallel, \text{st}}}. \quad (8.69)$$

With this we find that

$$\langle \Delta\varphi(t)^2 \rangle \propto \frac{t^3}{N}, \quad (8.70)$$

in comparison to t/N inside of the SSR phase. The superdiffusive behavior at the threshold would result in a relaxation timescale $\sim N^{1/3}$. This result is comparable with the timescale $\sim N^{0.3}$ that is given by the inverse of the linewidth at the threshold.

8.5 Discussion and conclusion

A bifurcation in the emission spectrum and a critical scaling of the linewidth has also been reported for a synchronization transition of two atomic ensembles coupled to a lossy cavity [166, 161]. Although the observed features may appear to be remarkably similar, we want to emphasize that the dynamical phase transition discussed here is quite different. In our model, the emission in the regular SSR and bistable SSR phases always appear with a monochromatic but possibly bistable frequency. On the other hand, the unsynchronized phase in Refs. [166, 161] shows a beating of two frequencies that results from simultaneous output. Moreover, the synchronization transition in Refs. [166, 161] appears if the collective linewidth becomes comparable to the frequency splitting of the two ensembles. Here, however, the transition between regular SSR and bistable SSR occurs if the atoms travel exactly half a wavelength during τ , i.e. $k_c v_z \tau = \pi$, independent of $N\Gamma_c$. Therefore the transition from regular SSR to bistable SSR results from the dipole accumulating a phase when it travels through the cavity mode function.

We emphasize that the regular SSR and bistable SSR phases rely on the continuous driving and dissipation of quantum matter, here realized by a beam of preexcited atoms. We provide the tools to analyze such systems and believe that this work will be useful as one of the first stepping stones towards future investigations of collective effects in atomic beams. For the experimental realization of such systems one requires a continuous and dense beam of atoms with a narrow transition that couples to a single cavity mode. The transition between the superradiant phases occurs when $N\Gamma_c\tau > 20$ that is achievable by state-of-the-art cavity setups [115, 116, 87, 50, 136] combined with high phase-space density atomic beams [24].

Future work could investigate the regular SSR and bistable SSR phases in presence of more than just a single velocity. This includes more sophisticated models where for instance the velocity

distribution is broadened. Moreover, we expect that the system is very sensitive to perturbations at the boundary between the regular SSR and bistable SSR phases. Therefore it will be interesting to investigate the potential of this system, in particular in vicinity of the critical region, for metrological applications.

Chapter 9

Summary and Outlook

In this thesis we have developed the theory of a CW superradiant atomic beam laser in the “bad cavity” regime. Our model is intended to be a simple and clear treatment that correctly reproduces the system’s essential features. For various configurations of the model, our framework allows for an analytically tractable mean-field theory, which has been used to study the stable and unstable superradiant phase transitions. A c -number based semiclassical Langevin theory has been used to numerically simulate the time evolution of the system.

To realize a superradiant beam laser, one must choose the beam flux, effusive atom source, and cavity parameters to ensure $\Phi\tau^2\Gamma_c > 8$ and $\delta_D\tau < \pi$. For very narrow linewidths, it may be necessary to reduce δ_D by transverse laser cooling the atomic beam. Furthermore, to realize a given linewidth, cavity pulling must be kept small enough to prevent excessive broadening from environmental noise. If cavity pulling remains minuscule, the linewidth can be narrowed by decreasing the cavity finesse and increasing Φ ; however, the trade-off is that in the limit of extremely small cavity finesse, the laser power vanishes as atoms radiate appreciably into other modes.

Potential future research work includes solving for the output linewidth using exact quantum simulations, investigating optomechanical effects when the collective linewidth is comparable to the recoil frequency [16, 15, 14, 145, 66, 67], and further understanding the dynamical superradiant phases as an analogy to the dissipative time crystals [49, 62, 156, 75]. Our theoretical work in this thesis has provided a comprehensive analysis of the first milestone to realizing a CW superradiant laser with an atomic beam. This system promises to be employed as a potential candidate for

future frequency standards with active optical clocks [25].

Bibliography

- [1] E. Abraham and S. D. Smith. Optical bistability and related devices. Reports on Progress in Physics, 45(8):815–885, 1982.
- [2] M. Abramowitz and I. A. Stegun. Handbook of Mathematical Functions. Dover, New York, 1968.
- [3] J. A. Acebrón, L. L. Bonilla, C. J. Pérez Vicente, F. Ritort, and R. Spigler. The kuramoto model: A simple paradigm for synchronization phenomena. Reviews of Modern Physics, 77(1):137–185, 2005. RMP.
- [4] A. V. Andreev, V. I. Emel’yanov, and Y. A. Il’inskiĭ. Collective spontaneous emission (dicke superradiance). Soviet Physics Uspekhi, 23(8):493–514, 1980.
- [5] A. Angerer, K. Streltsov, T. Astner, S. Putz, H. Sumiya, S. Onoda, J. Isoya, W. J. Munro, K. Nemoto, J. Schmiedmayer, and J. Majer. Superradiant emission from colour centres in diamond. Nature Physics, 14(12):1168–1172, 2018.
- [6] F. T. Arecchi and D. M. Kim. Line shifts in cooperative spontaneous emission. Optics Communications, 2(7):324–328, 1970.
- [7] D. Barberena, R. J. Lewis-Swan, J. K. Thompson, and A. M. Rey. Driven-dissipative quantum dynamics in ultra-long-lived dipoles in an optical cavity. Physical Review A, 99(5):053411, 2019. PRA.
- [8] K. Baumann, C. Guerlin, F. Brennecke, and T. Esslinger. Dicke quantum phase transition with a superfluid gas in an optical cavity. Nature, 464(7293):1301–1306, 2010.
- [9] C. Benkert, M. O. Scully, J. Bergou, L. Davidovich, M. Hillery, and M. Orszag. Role of pumping statistics in laser dynamics: Quantum langevin approach. Physical Review A, 41(5):2756–2765, 1990. PRA.
- [10] A. T. Black, H. W. Chan, and V. Vuletić. Observation of collective friction forces due to spatial self-organization of atoms: From rayleigh to bragg scattering. Physical Review Letters, 91(20):203001, 2003. PRL.
- [11] J. G. Bohnet, Z. Chen, J. M. Weiner, K. C. Cox, and J. K. Thompson. Linear-response theory for superradiant lasers. Physical Review A, 89(1):013806, 2014. PRA.

- [12] J. G. Bohnet, Z. Chen, J. M. Weiner, D. Meiser, M. J. Holland, and J. K. Thompson. A steady-state superradiant laser with less than one intracavity photon. Nature, 484(7392):78–81, 2012.
- [13] R. Bondarescu, A. Schärer, A. Lundgren, G. Hetényi, N. Houlié, P. Jetzer, and M. Bondarescu. Ground-based optical atomic clocks as a tool to monitor vertical surface motion. Geophysical Journal International, 202(3):1770–1774, 2015.
- [14] R. Bonifacio, M. M. Cola, N. Piovella, and G. R. M. Robb. A quantum model for collective recoil lasing. Europhysics Letters (EPL), 69(1):55–60, 2005.
- [15] R. Bonifacio, L. De Salvo, L. M. Narducci, and E. J. D’Angelo. Exponential gain and self-bunching in a collective atomic recoil laser. Physical Review A, 50(2):1716–1724, 1994. PRA.
- [16] R. Bonifacio and L. D. Salvo. Collective atomic recoil laser (carl) optical gain without inversion by collective atomic recoil and self-bunching of two-level atoms. Nuclear Instruments & Methods in Physics Research Section A-accelerators Spectrometers Detectors and Associated Equipment, 341:360–362, 1994.
- [17] R. Bonifacio, P. Schwendimann, and F. Haake. Quantum statistical theory of superradiance. i. Physical Review A, 4(1):302–313, 1971. PRA.
- [18] C. Booker, B. Buča, and D. Jaksch. Non-stationarity and dissipative time crystals: spectral properties and finite-size effects. New Journal of Physics, 22(8):085007, 2020.
- [19] H.-P. Breuer and F. Petruccione. The theory of open quantum systems. Oxford University Press, Oxford [England]; New York, 2010.
- [20] S. M. Brewer, J. S. Chen, A. M. Hankin, E. R. Clements, C. W. Chou, D. J. Wineland, D. B. Hume, and D. R. Leibbrandt. $^{27}\text{Al}^+$ quantum-logic clock with a systematic uncertainty below 10^{-18} . Physical Review Letters, 123(3):033201, 2019. PRL.
- [21] S. C. Burd, R. Srinivas, H. M. Knaack, W. Ge, A. C. Wilson, D. J. Wineland, D. Leibfried, J. J. Bollinger, D. T. C. Allcock, and D. H. Slichter. Quantum amplification of boson-mediated interactions. Nature Physics, 17(8):898–902, 2021.
- [22] A. Campa, T. Dauxois, and S. Ruffo. Statistical mechanics and dynamics of solvable models with long-range interactions. Physics Reports, 480(3):57–159, 2009.
- [23] H. W. Chan, A. T. Black, and V. Vuletić. Observation of collective-emission-induced cooling of atoms in an optical cavity. Physical Review Letters, 90(6):063003, 2003. PRL.
- [24] C.-C. Chen, S. Bennetts, R. G. Escudero, B. Pasquiou, and F. Schreck. Continuous guided strontium beam with high phase-space density. Physical Review Applied, 12(4):044014, 2019. PRAPPLIED.
- [25] J. Chen. Active optical clock. Chinese Science Bulletin, 54(3):348–352, 2009.
- [26] L. Chen, J. L. Hall, J. Ye, T. Yang, E. Zang, and T. Li. Vibration-induced elastic deformation of fabry-perot cavities. Physical Review A, 74(5):053801, 2006. PRA.
- [27] C. Cohen-Tannoudji, J. Dupont-Roc, and G. Grynberg. Photons and Atoms: Introduction to Quantum Electrodynamics. Wiley, New York, 1997.

- [28] C. Cohen-Tannoudji, J. Dupont-Roc, and G. Grynberg. Atom-photon interactions : Basic Processes and Applications. Wiley, New York, 2004.
- [29] K. Debnath, Y. Zhang, and K. Mølmer. Lasing in the superradiant crossover regime. Physical Review A, 98(6):063837, 2018. PRA.
- [30] V. DeGiorgio and M. O. Scully. Analogy between the laser threshold region and a second-order phase transition. Physical Review A, 2(4):1170–1177, 1970. PRA.
- [31] G. Di Domenico, S. Schilt, and P. Thomann. Simple approach to the relation between laser frequency noise and laser line shape. Applied Optics, 49(25):4801–4807, 2010.
- [32] R. H. Dicke. Coherence in spontaneous radiation processes. Physical Review, 93(1):99–110, 1954. PR.
- [33] F. Dimer, B. Estienne, A. S. Parkins, and H. J. Carmichael. Proposed realization of the dicke-model quantum phase transition in an optical cavity qed system. Physical Review A, 75(1):013804, 2007. PRA.
- [34] P. A. M. Dirac. The Principles of Quantum Mechanics. Clarendon Press, 4th edition, 1982.
- [35] P. A. M. Dirac and R. H. Fowler. The fundamental equations of quantum mechanics. Proceedings of the Royal Society of London. Series A, Containing Papers of a Mathematical and Physical Character, 109(752):642–653, 1925.
- [36] N. Dogra, M. Landini, K. Kroeger, L. Hruby, T. Donner, and T. Esslinger. Dissipation-induced structural instability and chiral dynamics in a quantum gas. Science, 366(6472):1496–1499, 2019.
- [37] P. Domokos and H. Ritsch. Collective cooling and self-organization of atoms in a cavity. Physical Review Letters, 89(25):253003, 2002. PRL.
- [38] T. A. Ely, E. A. Burt, J. D. Prestage, J. M. Seubert, and R. L. Tjoelker. Using the deep space atomic clock for navigation and science. IEEE Transactions on Ultrasonics, Ferroelectrics, and Frequency Control, 65(6):950–961, 2018.
- [39] F. Englert and R. Brout. Broken symmetry and the mass of gauge vector mesons. Physical Review Letters, 13(9):321–323, 1964. PRL.
- [40] R. L. Filler. The acceleration sensitivity of quartz crystal oscillators: a review. IEEE Transactions on Ultrasonics, Ferroelectrics, and Frequency Control, 35(3):297–305, 1988.
- [41] R. Friedberg, S. R. Hartmann, and J. T. Manassah. Frequency shifts in emission and absorption by resonant systems of two-level atoms. Physics Reports, 7(3):101–179, 1973.
- [42] C. Gardiner and P. Zoller. Quantum Noise: A Handbook of Markovian and Non-Markovian Quantum Stochastic Methods with Applications to Quantum Optics. Springer, 2004.
- [43] C. W. Gardiner. Handbook of stochastic methods for physics, chemistry, and the natural sciences. Springer, Berlin; New York, 2004.

- [44] C. W. Gardiner and M. J. Collett. Input and output in damped quantum systems: Quantum stochastic differential equations and the master equation. Physical Review A, 31(6):3761–3774, 1985. PRA.
- [45] B. M. Garraway. The dicke model in quantum optics: Dicke model revisited. Philosophical Transactions of the Royal Society A, 369, 2011.
- [46] R. M. Godun, P. B. R. Nisbet-Jones, J. M. Jones, S. A. King, L. A. M. Johnson, H. S. Margolis, K. Szymaniec, S. N. Lea, K. Bongs, and P. Gill. Frequency ratio of two optical clock transitions in $^{171}\text{Yb}^+$ and constraints on the time variation of fundamental constants. Physical Review Letters, 113(21):210801, 2014. PRL.
- [47] J. Goldstone. Field theories with “superconductor” solutions. Il Nuovo Cimento (1955-1965), 19(1):154–164, 1961.
- [48] J. Goldstone, A. Salam, and S. Weinberg. Broken symmetries. Physical Review, 127(3):965–970, 1962. PR.
- [49] Z. Gong, R. Hamazaki, and M. Ueda. Discrete time-crystalline order in cavity and circuit qed systems. Physical Review Letters, 120(4):040404, 2018. PRL.
- [50] H. Gothe, D. Sholokhov, A. Breunig, M. Steinel, and J. Eschner. Continuous-wave virtual-state lasing from cold ytterbium atoms. Physical Review A, 99(1):013415, 2019. PRA.
- [51] R. Graham and H. Haken. Laserlight — first example of a second-order phase transition far away from thermal equilibrium. Zeitschrift für Physik, 237(1):31–46, 1970.
- [52] M. Gross and S. Haroche. Superradiance: An essay on the theory of collective spontaneous emission. Physics Reports, 93(5):301–396, 1982.
- [53] H. Habibian, A. Winter, S. Paganelli, H. Rieger, and G. Morigi. Bose-glass phases of ultracold atoms due to cavity backaction. Physical Review Letters, 110(7):075304, 2013. PRL.
- [54] H. Haken. Laser Theory. Springer Berlin Heidelberg, 1984.
- [55] J. L. Hall, M. S. Taubman, and J. Ye. Laser stabilization, volume IV, book section 27, pages 27.1–27.24. McGraw-Hill Professional, New York, NY, 2010.
- [56] G. Heinrich, M. Ludwig, J. Qian, B. Kubala, and F. Marquardt. Collective dynamics in optomechanical arrays. Physical Review Letters, 107(4):043603, 2011. PRL.
- [57] K. Hepp and E. H. Lieb. On the superradiant phase transition for molecules in a quantized radiation field: the dicke maser model. Annals of Physics, 76:360, 1973.
- [58] P. W. Higgs. Broken symmetries and the masses of gauge bosons. Physical Review Letters, 13(16):508–509, 1964. PRL.
- [59] C. Hotter, D. Plankensteiner, L. Ostermann, and H. Ritsch. Superradiant cooling, trapping, and lasing of dipole-interacting clock atoms. Optics Express, 27(22):31193–31206, 2019.
- [60] N. Huntemann, B. Lipphardt, C. Tamm, V. Gerginov, S. Weyers, and E. Peik. Improved limit on a temporal variation of m_p/m_e from comparisons of yb^+ and cs atomic clocks. Physical Review Letters, 113(21):210802, 2014. PRL.

- [61] S. Häfner, S. Falke, C. Grebing, S. Vogt, T. Legero, M. Merimaa, C. Lisdat, and U. Sterr. 8×10^{-17} fractional laser frequency instability with a long room-temperature cavity. Optics Letters, 40(9):2112–2115, 2015.
- [62] F. Iemini, A. Russomanno, J. Keeling, M. Schirò, M. Dalmonte, and R. Fazio. Boundary time crystals. Physical Review Letters, 121(3):035301, 2018. PRL.
- [63] J. D. Jackson. Classical electrodynamics. Wiley, New York, 1999.
- [64] E. T. Jaynes and F. W. Cummings. Comparison of quantum and semiclassical radiation theories with application to the beam maser. Proceedings of the IEEE, 51(1):89–109, 1963.
- [65] S. B. Jäger. Collective dynamics of driven-dissipative atomic systems in optical cavities. Thesis, 2019.
- [66] S. B. Jäger, J. Cooper, M. J. Holland, and G. Morigi. Dynamical phase transitions to optomechanical superradiance. Physical Review Letters, 123(5):053601, 2019. PRL.
- [67] S. B. Jäger, M. J. Holland, and G. Morigi. Superradiant optomechanical phases of cold atomic gases in optical resonators. Physical Review A, 101(2):023616, 2020. PRA.
- [68] S. B. Jäger, H. Liu, J. Cooper, and M. J. Holland. Collective emission of an atomic beam into an off-resonant cavity mode. Physical Review A, 104(5):053705, 2021. PRA.
- [69] S. B. Jäger, H. Liu, J. Cooper, T. L. Nicholson, and M. J. Holland. Superradiant emission of a thermal atomic beam into an optical cavity. Physical Review A, 104(3):033711, 2021. PRA.
- [70] S. B. Jäger, H. Liu, A. Shankar, J. Cooper, and M. J. Holland. Regular and bistable steady-state superradiant phases of an atomic beam traversing an optical cavity. Physical Review A, 103(1):013720, 2021. PRA.
- [71] J. Keeling. Light-Matter Interactions and Quantum Optics. CreateSpace Independent Publishing Platform, 2014.
- [72] T. Keller, V. Torggler, S. B. Jäger, S. Schütz, H. Ritsch, and G. Morigi. Quenches across the self-organization transition in multimode cavities. New Journal of Physics, 20(2):025004, 2018.
- [73] H. Keßler, J. G. Cosme, C. Georges, L. Mathey, and A. Hemmerich. From a continuous to a discrete time crystal in a dissipative atom-cavity system. New Journal of Physics, 22(8):085002, 2020.
- [74] H. Keßler, J. G. Cosme, M. Hemmerling, L. Mathey, and A. Hemmerich. Emergent limit cycles and time crystal dynamics in an atom-cavity system. Physical Review A, 99(5):053605, 2019. PRA.
- [75] H. Keßler, P. Kongkhambut, C. Georges, L. Mathey, J. G. Cosme, and A. Hemmerich. Observation of a dissipative time crystal. Physical Review Letters, 127(4):043602, 2021. PRL.
- [76] P. E. Kloeden and E. Platen. Numerical solution of stochastic differential equations. Springer-Verlag, Berlin; New York, 1992.

- [77] B. W. S. P. L. Knight. Topical review: The jaynes-cummings model. Journal of Modern Optics, 1993.
- [78] S. Kolkowitz, I. Pikovski, N. Langellier, M. D. Lukin, R. L. Walsworth, and J. Ye. Gravitational wave detection with optical lattice atomic clocks. Physical Review D, 94(12):124043, 2016. PRD.
- [79] R. M. Kroeze, Y. Guo, V. D. Vaidya, J. Keeling, and B. L. Lev. Spinor self-ordering of a quantum gas in a cavity. Physical Review Letters, 121(16):163601, 2018. PRL.
- [80] S. Krämer, L. Ostermann, and H. Ritsch. Optimized geometries for future generation optical lattice clocks. EPL (Europhysics Letters), 114(1):14003, 2016.
- [81] W. E. Lamb and R. C. Retherford. Fine structure of the hydrogen atom by a microwave method. Physical Review, 72(3):241–243, 1947. PR.
- [82] W. E. Lamb, W. P. Schleich, M. O. Scully, and C. H. Townes. Laser physics: Quantum controversy in action. Reviews of Modern Physics, 71(2):S263–S273, 1999. RMP.
- [83] R. Landig, L. Hruby, N. Dogra, M. Landini, R. Mottl, T. Donner, and T. Esslinger. Quantum phases from competing short- and long-range interactions in an optical lattice. Nature, 532(7600):476–479, 2016.
- [84] M. Landini, N. Dogra, K. Kroeger, L. Hruby, T. Donner, and T. Esslinger. Formation of a spin texture in a quantum gas coupled to a cavity. Physical Review Letters, 120(22):223602, 2018. PRL.
- [85] J. Larson, B. Damski, G. Morigi, and M. Lewenstein. Mott-insulator states of ultracold atoms in optical resonators. Physical Review Letters, 100(5):050401, 2008. PRL.
- [86] J. Larson, S. Fernández-Vidal, G. Morigi, and M. Lewenstein. Quantum stability of mott-insulator states of ultracold atoms in optical resonators. New Journal of Physics, 10(4):045002, 2008.
- [87] T. Laske, H. Winter, and A. Hemmerich. Pulse delay time statistics in a superradiant laser with calcium atoms. Physical Review Letters, 123(10):103601, 2019. PRL.
- [88] T. Legero, T. Kessler, and U. Sterr. Tuning the thermal expansion properties of optical reference cavities with fused silica mirrors. Journal of the Optical Society of America B, 27(5):914–919, 2010.
- [89] I. D. Leroux, M. H. Schleier-Smith, and V. Vuletić. Implementation of cavity squeezing of a collective atomic spin. Physical Review Letters, 104(7):073602, 2010. PRL.
- [90] R. J. Lewis-Swan, M. A. Norcia, J. R. K. Cline, J. K. Thompson, and A. M. Rey. Robust spin squeezing via photon-mediated interactions on an optical clock transition. Physical Review Letters, 121(7):070403, 2018. PRL.
- [91] M. Lezius, T. Wilken, C. Deutsch, M. Giunta, O. Mandel, A. Thaller, V. Schkolnik, M. Schiemangk, A. Dinkelaker, A. Kohfeldt, A. Wicht, M. Krutzik, A. Peters, O. Hellmig, H. Duncker, K. Sengstock, P. Windpassinger, K. Lampmann, T. Hülasing, T. W. Hänsch, and R. Holzwarth. Space-borne frequency comb metrology. Optica, 3(12):1381–1387, 2016.

- [92] H. Liu, S. B. Jäger, X. Yu, S. Touzard, A. Shankar, M. J. Holland, and T. L. Nicholson. Rugged mhz-linewidth superradiant laser driven by a hot atomic beam. Physical Review Letters, 125(25):253602, 2020. PRL.
- [93] J. Léonard, A. Morales, P. Zupancic, T. Donner, and T. Esslinger. Monitoring and manipulating higgs and goldstone modes in a supersolid quantum gas. Science, 358(6369):1415–1418, 2017.
- [94] J. Léonard, A. Morales, P. Zupancic, T. Esslinger, and T. Donner. Supersolid formation in a quantum gas breaking a continuous translational symmetry. Nature, 543(7643):87–90, 2017.
- [95] T. Maier, S. Kraemer, L. Ostermann, and H. Ritsch. A superradiant clock laser on a magic wavelength optical lattice. Optics Express, 22(11):13269–13279, 2014.
- [96] D. Manzano. A short introduction to the lindblad master equation. AIP Advances, 10:025106, 2020.
- [97] M. J. Martin and J. Ye. High-precision laser stabilization via optical cavities, book section 237-258. Cambridge University Press, Cambridge, England, 2012.
- [98] W. F. McGrew, X. Zhang, R. J. Fasano, S. A. Schäffer, K. Bely, D. Nicolodi, R. C. Brown, N. Hinkley, G. Milani, M. Schioppo, T. H. Yoon, and A. D. Ludlow. Atomic clock performance enabling geodesy below the centimetre level. Nature, 564(7734):87–90, 2018.
- [99] D. Meiser and M. J. Holland. Intensity fluctuations in steady-state superradiance. Physical Review A, 81(6):063827, 2010. PRA.
- [100] D. Meiser and M. J. Holland. Steady-state superradiance with alkaline-earth-metal atoms. Physical Review A, 81(3):033847, 2010. PRA.
- [101] D. Meiser, J. Ye, D. R. Carlson, and M. J. Holland. Prospects for a millihertz-linewidth laser. Physical Review Letters, 102(16):163601, 2009. PRL.
- [102] A. Messiah and G. M. Temmer. Quantum mechanics. North-Holland Pub. Co. ; Interscience Publishers, Amsterdam; New York, 1961.
- [103] P. Meystre and M. Sargent III. Elements of Quantum Optics. Springer, Berlin, 4th edition, 2007.
- [104] R. Miller, T. E. Northup, K. M. Birnbaum, A. Boca, A. D. Boozer, and H. J. Kimble. Trapped atoms in cavity qed: coupling quantized light and matter. Journal of Physics B: Atomic, Molecular and Optical Physics, 38(9):S551–S565, 2005.
- [105] W. R. Milner, J. M. Robinson, C. J. Kennedy, T. Bothwell, D. Kedar, D. G. Matei, T. Legero, U. Sterr, F. Riehle, H. Leopardi, T. M. Fortier, J. A. Sherman, J. Levine, J. Yao, J. Ye, and E. Oelker. Demonstration of a timescale based on a stable optical carrier. Physical Review Letters, 123(17):173201, 2019. PRL.
- [106] F. Mivehvar, F. Piazza, and H. Ritsch. Disorder-driven density and spin self-ordering of a bose-einstein condensate in a cavity. Physical Review Letters, 119(6):063602, 2017. PRL.
- [107] H. Mori and Y. Kuramoto. Dissipative structures and chaos. Springer, Berlin; New York, 1998.

- [108] J. A. Muniz, D. Barberena, R. J. Lewis-Swan, D. J. Young, J. R. K. Cline, A. M. Rey, and J. K. Thompson. Exploring dynamical phase transitions with cold atoms in an optical cavity. *Nature*, 580(7805):602–607, 2020.
- [109] K. Mølmer, Y. Castin, and J. Dalibard. Monte carlo wave-function method in quantum optics. *Journal of the Optical Society of America B*, 10(3):524–538, 1993.
- [110] D. Nagy, G. Szirmai, and P. Domokos. Self-organization of a bose-einstein condensate in an optical cavity. *The European Physical Journal D*, 48(1):127–137, 2008.
- [111] P. Nataf and C. Ciuti. No-go theorem for superradiant quantum phase transitions in cavity qed and counter-example in circuit qed. *Nature Communications*, 1(1):72, 2010.
- [112] M. A. Nielsen and I. L. Chuang. *Quantum Computation and Quantum Information: 10th Anniversary Edition*. Cambridge University Press, Cambridge, 2010.
- [113] M. A. Norcia, J. R. K. Cline, J. A. Muniz, J. M. Robinson, R. B. Hutson, A. Goban, G. E. Marti, J. Ye, and J. K. Thompson. Frequency measurements of superradiance from the strontium clock transition. *Physical Review X*, 8(2):021036, 2018. PRX.
- [114] M. A. Norcia, R. J. Lewis-Swan, J. R. K. Cline, B. Zhu, A. M. Rey, and J. K. Thompson. Cavity-mediated collective spin-exchange interactions in a strontium superradiant laser. *Science*, 361(6399):259–262, 2018.
- [115] M. A. Norcia and J. K. Thompson. Cold-strontium laser in the superradiant crossover regime. *Physical Review X*, 6(1):011025, 2016. PRX.
- [116] M. A. Norcia, M. N. Winchester, J. R. K. Cline, and J. K. Thompson. Superradiance on the millihertz linewidth strontium clock transition. *Science Advances*, 2(10):e1601231, 2016.
- [117] J. Olson, R. W. Fox, T. M. Fortier, T. F. Sheerin, R. C. Brown, H. Leopardi, R. E. Stoner, C. W. Oates, and A. D. Ludlow. Ramsey-bordé matter-wave interferometry for laser frequency stabilization at 10^{-16} frequency instability and below. *Physical Review Letters*, 123(7):073202, 2019. PRL.
- [118] E. Pedrozo-Peñafiel, S. Colombo, C. Shu, A. F. Adiyatullin, Z. Li, E. Mendez, B. Braverman, A. Kawasaki, D. Akamatsu, Y. Xiao, and V. Vuletić. Entanglement on an optical atomic-clock transition. *Nature*, 588(7838):414–418, 2020.
- [119] L. Pezzè, A. Smerzi, M. K. Oberthaler, R. Schmied, and P. Treutlein. Quantum metrology with nonclassical states of atomic ensembles. *Reviews of Modern Physics*, 90(3):035005, 2018. RMP.
- [120] J. Preskill. Lecture notes for physics 229: Quantum information and computation. *Unpublished*, Pasadena: California Institute of Technology, 1998. <http://theory.caltech.edu/preskill/ph229/>.
- [121] R. R. Puri, T. Asakura, K. H. Brenner, T. W. Hansch, F. Krausz, H. Weber, and W. T. Rhodes. *Mathematical Methods of Quantum Optics*. Springer, 2001.
- [122] A. G. Redfield. *The Theory of Relaxation Processes** *This work was started while the author was at Harvard University, and was then partially supported by Joint Services Contract N5ori-76, Project Order I, volume 1, pages 1–32. Academic Press, 1965.

- [123] G. Rempe, H. Walther, and N. Klein. Observation of quantum collapse and revival in a one-atom maser. Physical Review Letters, 58(4):353–356, 1987. PRL.
- [124] F. Riehle. Frequency Standards: Basics and Applications. Wiley-VCH, New York, 2003.
- [125] H. Ritsch, P. Domokos, F. Brennecke, and T. Esslinger. Cold atoms in cavity-generated dynamical optical potentials. Reviews of Modern Physics, 85(2):553–601, 2013. RMP.
- [126] J. M. Robinson, E. Oelker, W. R. Milner, W. Zhang, T. Legero, D. G. Matei, F. Riehle, U. Sterr, and J. Ye. Crystalline optical cavity at 4 K with thermal-noise-limited instability and ultralow drift. Optica, 6(2):240–243, 2019.
- [127] S. R. K. Rodriguez, A. Amo, I. Sagnes, L. Le Gratiet, E. Galopin, A. Lemaître, and J. Bloch. Interaction-induced hopping phase in driven-dissipative coupled photonic microcavities. Nature Communications, 7(1):11887, 2016.
- [128] M. M. Roses and E. G. Dalla Torre. Dicke model. PLOS ONE, 15(9):e0235197, 2020.
- [129] A. Roth and K. Hammerer. Synchronization of active atomic clocks via quantum and classical channels. Physical Review A, 94(4):043841, 2016. PRA.
- [130] S. Sachdev. Quantum Phase Transitions. Cambridge University Press, Cambridge, 2nd edition, 2011.
- [131] J. J. Sakurai and J. Napolitano. Modern Quantum Mechanics. Cambridge University Press, Cambridge, 2nd edition, 2017.
- [132] C. Sanner, N. Huntemann, R. Lange, C. Tamm, E. Peik, M. S. Safronova, and S. G. Porsev. Optical clock comparison for lorentz symmetry testing. Nature, 567(7747):204–208, 2019.
- [133] J. Schachenmayer, A. Pikovski, and A. M. Rey. Many-body quantum spin dynamics with monte carlo trajectories on a discrete phase space. Physical Review X, 5(1):011022, 2015. PRX.
- [134] M. H. Schleier-Smith, I. D. Leroux, and V. Vuletić. States of an ensemble of two-level atoms with reduced quantum uncertainty. Physical Review Letters, 104(7):073604, 2010. PRL.
- [135] S. A. Schäffer, B. T. R. Christensen, M. R. Henriksen, and J. W. Thomsen. Dynamics of bad-cavity-enhanced interaction with cold sr atoms for laser stabilization. Physical Review A, 96(1):013847, 2017. PRA.
- [136] S. A. Schäffer, M. Tang, M. R. Henriksen, A. A. Jørgensen, B. T. R. Christensen, and J. W. Thomsen. Lasing on a narrow transition in a cold thermal strontium ensemble. Physical Review A, 101(1):013819, 2020. PRA.
- [137] S. Schütz, S. B. Jäger, and G. Morigi. Dissipation-assisted prethermalization in long-range interacting atomic ensembles. Physical Review Letters, 117(8):083001, 2016. PRL.
- [138] S. Schütz and G. Morigi. Prethermalization of atoms due to photon-mediated long-range interactions. Physical Review Letters, 113(20):203002, 2014. PRL.
- [139] M. O. Scully. Collective lamb shift in single photon dicke superradiance. Physical Review Letters, 102(14):143601, 2009. PRL.

- [140] M. O. Scully and W. E. Lamb. Quantum theory of an optical maser. i. general theory. Physical Review, 159(2):208–226, 1967. PR.
- [141] M. O. Scully and M. S. Zubairy. Quantum Optics. Cambridge University Press, Cambridge, 1997.
- [142] A. Shankar, G. P. Greve, B. Wu, J. K. Thompson, and M. Holland. Continuous real-time tracking of a quantum phase below the standard quantum limit. Physical Review Letters, 122(23):233602, 2019. PRL.
- [143] A. Shankar, J. T. Reilly, S. B. Jäger, and M. J. Holland. Subradiant-to-subradiant phase transition in the bad cavity laser. Physical Review Letters, 127(7):073603, 2021. PRL.
- [144] A. Shankar, L. Salvi, M. L. Chiofalo, N. Poli, and M. J. Holland. Squeezed state metrology with bragg interferometers operating in a cavity. Quantum Science and Technology, 4(4):045010, 2019.
- [145] S. Slama, S. Bux, G. Krenz, C. Zimmermann, and P. W. Courteille. Superradiant rayleigh scattering and collective atomic recoil lasing in a ring cavity. Physical Review Letters, 98(5):053603, 2007. PRL.
- [146] I. N. Sneddon. Elements of partial differential equations. McGraw-Hill Kogakusha, Tokyo, 1957.
- [147] D. A. Steck. Quantum and Atom Optics. 2007.
- [148] M. J. Stephen. First-order dispersion forces. The Journal of Chemical Physics, 40(3):669–673, 1964.
- [149] M. Takamoto, I. Ushijima, N. Ohmae, T. Yahagi, K. Kokado, H. Shinkai, and H. Katori. Test of general relativity by a pair of transportable optical lattice clocks. Nature Photonics, 14(7):411–415, 2020.
- [150] M. Tang, S. A. Schäffer, A. A. Jørgensen, M. R. Henriksen, B. T. R. Christensen, J. H. Müller, and J. W. Thomsen. Cavity-immune features in the spectra of superradiant crossover laser pulses. eprint: arXiv:2104.13305, 2021.
- [151] M. Tavis and F. W. Cummings. Exact solution for an n -molecule—radiation-field hamiltonian. Physical Review, 170(2):379–384, 1968. PR.
- [152] M. Tavis and F. W. Cummings. Approximate solutions for an n -molecule-radiation-field hamiltonian. Physical Review, 188(2):692–695, 1969. PR.
- [153] V. V. Temnov. Superradiance and subradiance in the overdamped many-atom micromaser. Physical Review A, 71(5):053818, 2005. PRA.
- [154] V. V. Temnov and U. Woggon. Superradiance and subradiance in an inhomogeneously broadened ensemble of two-level systems coupled to a low- q cavity. Physical Review Letters, 95(24):243602, 2005. PRL.
- [155] D. A. Tieri. Open Quantum Systems with Applications to Precision Measurements. Dissertation, 2015.

- [156] K. Tucker, B. Zhu, R. J. Lewis-Swan, J. Marino, F. Jimenez, J. G. Restrepo, and A. M. Rey. Shattered time: can a dissipative time crystal survive many-body correlations? New Journal of Physics, 20(12):123003, 2018.
- [157] V. D. Vaidya, Y. Guo, R. M. Kroeze, K. E. Ballantine, A. J. Kollár, J. Keeling, and B. L. Lev. Tunable-range, photon-mediated atomic interactions in multimode cavity qed. Physical Review X, 8(1):011002, 2018. PRX.
- [158] D. F. Walls and G. J. Milburn. Quantum Optics. Springer Berlin Heidelberg, 2008.
- [159] Y. K. Wang and F. T. Hioe. Phase transition in the dicke model of superradiance. Physical Review A, 7(3):831–836, 1973. PRA.
- [160] P. Weislo, P. Ablewski, K. Beloy, S. Bilicki, M. Bober, R. Brown, R. Fasano, R. Ciurylo, H. Hachisu, T. Ido, J. Lodewyck, A. Ludlow, W. McGrew, P. Morzyński, D. Nicolodi, M. Schioppo, M. Sekido, R. Le Targat, P. Wolf, X. Zhang, B. Zjawin, and M. Zawada. New bounds on dark matter coupling from a global network of optical atomic clocks. Science Advances, 4(12):eaau4869, 2018.
- [161] J. M. Weiner, K. C. Cox, J. G. Bohnet, and J. K. Thompson. Phase synchronization inside a superradiant laser. Physical Review A, 95(3):033808, 2017. PRA.
- [162] V. Weisskopf and E. Wigner. Berechnung der natürlichen linienbreite auf grund der diracschen lichttheorie. Zeitschrift für Physik, 63(1):54–73, 1930.
- [163] D. J. Wineland, C. Monroe, W. M. Itano, D. Leibfried, B. E. King, and D. M. Meekhof. Experimental issues in coherent quantum-state manipulation of trapped atomic ions. Journal of research of the National Institute of Standards and Technology, 103(3):259–328, 1998.
- [164] M. Xu. Theory of Steady-State Superradiance. Dissertation, 2016.
- [165] M. Xu, S. B. Jäger, S. Schütz, J. Cooper, G. Morigi, and M. J. Holland. Supercooling of atoms in an optical resonator. Physical Review Letters, 116(15):153002, 2016. PRL.
- [166] M. Xu, D. A. Tieri, E. C. Fine, J. K. Thompson, and M. J. Holland. Synchronization of two ensembles of atoms. Physical Review Letters, 113(15):154101, 2014. PRL.
- [167] M. Xu, D. A. Tieri, and M. J. Holland. Simulating open quantum systems by applying $su(4)$ to quantum master equations. Physical Review A, 87(6):062101, 2013. PRA.
- [168] T. Zhang, Y. Wang, X. Zang, W. Zhuang, and J. Chen. Active optical clock based on four-level quantum system. Chinese Science Bulletin, 58(17):2033–2038, 2013.
- [169] Y. Zhang, C. Shan, and K. Mølmer. Ultranarrow superradiant lasing by dark atom-photon dressed states. Physical Review Letters, 126(12):123602, 2021. PRL.
- [170] Y. Zhang, Y.-X. Zhang, and K. Mølmer. Monte-carlo simulations of superradiant lasing. New Journal of Physics, 20(11):112001, 2018.
- [171] B. Zhu, J. Marino, N. Y. Yao, M. D. Lukin, and E. A. Demler. Dicke time crystals in driven-dissipative quantum many-body systems. New Journal of Physics, 21(7):073028, 2019.
- [172] B. Zhu, J. Schachenmayer, M. Xu, F. Herrera, J. G. Restrepo, M. J. Holland, and A. M. Rey. Synchronization of interacting quantum dipoles. New Journal of Physics, 17(8):083063, 2015.

Appendix A

Fourier Series and Fourier Transform

A.1 Fourier series

Consider a function $f : \left[-\frac{L}{2}, \frac{L}{2}\right] \rightarrow \mathbb{C}$. We define its *Fourier series* and find its Fourier coefficients \tilde{f}_k by

$$f(x) = \sum_k \tilde{f}_k e^{ikx}, \quad (\text{A.1a})$$

$$\tilde{f}_k = \frac{1}{L} \int_{-\frac{L}{2}}^{\frac{L}{2}} dx f(x) e^{-ikx}, \quad (\text{A.1b})$$

for $k = \frac{2\pi}{L}n$, $n \in \mathbb{Z}$.

Theorem A.1.1 (Parseval's theorem):

$$\frac{1}{L} \int_{-\frac{L}{2}}^{\frac{L}{2}} |f(x)|^2 dx = \sum_k |\tilde{f}_k|^2. \quad (\text{A.2})$$

Remark A.1.1: Periodic boundary conditions. Consider a function $f_1 : \mathbb{R} \rightarrow \mathbb{C}$ with periodic boundary conditions $f_1(x + mL) = f_1(x)$ for $x \in \left[-\frac{L}{2}, \frac{L}{2}\right]$ and $m \in \mathbb{Z}$. Then f and f_1 have the same Fourier series and coefficients.

Remark A.1.2: Hermitian functions. If $f(x)$ is real, then \tilde{f}_k is Hermitian, i.e., $\tilde{f}_{-k} = \tilde{f}_k^*$.

Remark A.1.3: Rescaling of \tilde{f}_k . The Fourier coefficients \tilde{f}_k defined in Eq. (A.1) can be rescaled by

introducing $h \in \mathbb{C}$ such that

$$f(x) = h \sum_k \tilde{f}_k e^{ikx}, \quad (\text{A.3a})$$

$$\tilde{f}_k = \frac{1}{hL} \int_{-\frac{L}{2}}^{\frac{L}{2}} dx f(x) e^{-ikx}. \quad (\text{A.3b})$$

Notice that this **will** change the prefactors in Parseval's theorem such that

$$\frac{1}{L} \int_{-\frac{L}{2}}^{\frac{L}{2}} |f(x)|^2 dx = |h|^2 \sum_k |\tilde{f}_k|^2. \quad (\text{A.4})$$

We stick to our definitions of Fourier series as in Eq. (A.1) throughout the thesis unless further specified.

Remark A.1.4: Distributions. Tempered distributions defined on Schwartz space can have Fourier series. The Dirac delta function is an example.

A.2 Fourier transform

Consider a function $f : \mathbb{R} \rightarrow \mathbb{C}$. We define its *Fourier transform* and inverse Fourier transform as

$$f(x) = \frac{1}{\sqrt{2\pi}} \int_{-\infty}^{\infty} dk \tilde{f}(k) e^{ikx}, \quad (\text{A.5a})$$

$$\tilde{f}(k) = \frac{1}{\sqrt{2\pi}} \int_{-\infty}^{\infty} dx f(x) e^{-ikx}. \quad (\text{A.5b})$$

Fourier transform is the limit of Fourier series for $L \rightarrow \infty$. Here we have chosen the symmetric prefactors for simplification.

Theorem A.2.1 (Plancherel's theorem):

$$\int_{-\infty}^{\infty} dx |f(x)|^2 = \int_{-\infty}^{\infty} dk |\tilde{f}(k)|^2. \quad (\text{A.6})$$

Theorem A.2.2 (Convolution theorem): The convolution of $f(x)$ and $g(x)$ is the inverse Fourier transform of the product of $\tilde{f}(k)$ and $\tilde{g}(k)$, i.e.,

$$\int_{-\infty}^{\infty} dx' f(x') g(x - x') = \int_{-\infty}^{\infty} dk \tilde{f}(k) \tilde{g}(k) e^{ikx}, \quad (\text{A.7})$$

or equivalently,

$$\tilde{f}(k)\tilde{g}(k) = \frac{1}{2\pi} \int_{-\infty}^{\infty} dx e^{-ikx} \int_{-\infty}^{\infty} dx' f(x')g(x-x'). \quad (\text{A.8})$$

Theorem A.2.3 (Wiener-Khinchin theorem): The autocorrelation function of $f(x)$ is the inverse Fourier transform of its corresponding power spectrum $|\tilde{f}(k)|^2$, i.e.,

$$\int_{-\infty}^{\infty} dx' f^*(x')f(x+x') = \int_{-\infty}^{\infty} dk |\tilde{f}(k)|^2 e^{ikx}, \quad (\text{A.9})$$

or equivalently,

$$|\tilde{f}(k)|^2 = \frac{1}{2\pi} \int_{-\infty}^{\infty} dx e^{-ikx} \int_{-\infty}^{\infty} dx' f^*(x')f(x+x'). \quad (\text{A.10})$$

Notice the similarity between the convolution theorem and the Wiener-Khinchin theorem.

Remark A.2.1: Hermitian functions. If $f(x)$ is real, then $\tilde{f}(k)$ is Hermitian, i.e., $\tilde{f}(-k) = \tilde{f}^*(k)$.

Remark A.2.2: Rescaling of $\tilde{f}(k)$. The Fourier transform $\tilde{f}(k)$ defined in Eq. (A.5) can be rescaled by introducing $h \in \mathbb{C}$ such that

$$f(x) = \frac{h}{\sqrt{2\pi}} \int_{-\infty}^{\infty} dk \tilde{f}(k) e^{ikx}, \quad (\text{A.11a})$$

$$\tilde{f}(k) = \frac{1}{h\sqrt{2\pi}} \int_{-\infty}^{\infty} dx f(x) e^{-ikx}. \quad (\text{A.11b})$$

Notice that this **will** change the prefactors for Plancherel's theorem, the convolution theorem, and the Wiener-Khinchin theorem. We stick to our definitions of Fourier transform as in Eq. (A.5) throughout the thesis unless further specified.

A.3 Kronecker and Dirac delta functions

(1) Let $x \in \left[-\frac{L}{2}, \frac{L}{2}\right]$ and $k = \frac{2\pi n}{L}$, $n \in \mathbb{Z}$. Then we have

$$\delta_{kk'} = \frac{1}{L} \int_{-\frac{L}{2}}^{\frac{L}{2}} dx e^{\pm i(k-k')x}, \quad (\text{A.12})$$

$$\delta(x-x') = \frac{1}{L} \sum_k e^{\pm ik(x-x')}. \quad (\text{A.13})$$

(2) Let $x, k \in \mathbb{R}$. Then we have

$$\delta(k - k') = \frac{1}{2\pi} \int_{-\infty}^{\infty} dx e^{\pm i(k-k')x}, \quad (\text{A.14})$$

$$\delta(x - x') = \frac{1}{2\pi} \int_{-\infty}^{\infty} dk e^{\pm ik(x-x')}. \quad (\text{A.15})$$

Properties (1) and (2) can be used to prove the theorems introduced in this section.

(3) The Fourier transform of a Heaviside step function $\Theta(x)$ is the distribution ¹

$$\tilde{\Theta}(k) = \int_{-\infty}^{\infty} dx e^{-ikx} \Theta(x) = \text{PV} \frac{1}{ik} + \pi \delta(k). \quad (\text{A.16})$$

Thus we obtain

$$\int_0^{\infty} dx e^{-ikx} = \tilde{\Theta}(k) = \text{PV} \frac{1}{ik} + \pi \delta(k), \quad (\text{A.17})$$

which is commonly used in physics.

¹This equation is exact. To match our choice of the Fourier transform in Eq. (A.5) with symmetric prefactors, one needs to multiply $\frac{1}{\sqrt{2\pi}}$ to both sides.

Appendix B

Separation of Center-of-Mass Motion with External Fields

We consider the separation of the center-of-mass motion of an atom with an external field in non-relativistic quantum mechanics.

B.1 Two-body system

Consider a classical system composed of two charged particles. For convenience, we label them by $\{m_1, \mathbf{r}_1, \mathbf{p}_1\}$ and $\{m_2, \mathbf{r}_2, \mathbf{p}_2\}$, where m_j , \mathbf{r}_j , and \mathbf{p}_j represent the mass, position, and momentum of particle j , respectively. Moreover, we let particle 1 carry charge $+e$, and let particle 2 carry charge $-e$ (one can imagine this system as a classical model of a neutral Hydrogen atom).

For a Hamiltonian that has the form

$$H = \frac{\mathbf{p}_1^2}{2m_1} + \frac{\mathbf{p}_2^2}{2m_2} + V(|\mathbf{r}_1 - \mathbf{r}_2|) - e \left(\frac{\mathbf{p}_1}{m_1} - \frac{\mathbf{p}_2}{m_2} \right) \cdot \mathbf{A}, \quad (\text{B.1})$$

where \mathbf{A} is a constant field variable, our task is to separate the center-of-mass motion from H as an external kinetic energy term.

From classical kinetic theory [102], one can check that with the following definitions

$$\left\{ \begin{array}{l} M_1 = m_1 + m_2 \\ \mathbf{R}_1 = \frac{m_1 \mathbf{r}_1 + m_2 \mathbf{r}_2}{M_1} \\ \mathbf{P}_1 = \mathbf{p}_1 + \mathbf{p}_2 \end{array} \right\}, \quad \left\{ \begin{array}{l} \mu_1 = \frac{m_1 m_2}{M_1} \\ \mathcal{R}_1 = \mathbf{r}_1 - \mathbf{r}_2 \\ \mathcal{P}_1 = \frac{m_2 \mathbf{p}_1 - m_1 \mathbf{p}_2}{M_1} \end{array} \right\}, \quad (\text{B.2})$$

where $\{\mu_1, \mathcal{R}_1, \mathcal{P}_1\}$ refers to the first “relative” particle, the properties below hold

$$\frac{\mathbf{p}_1^2}{2m_1} + \frac{\mathbf{p}_2^2}{2m_2} = \frac{\mathbf{P}_1^2}{2M_1} + \frac{\mathcal{P}_1^2}{2\mu_1}, \quad (\text{B.3})$$

$$V(|\mathbf{r}_1 - \mathbf{r}_2|) = V(|\mathcal{R}_1|). \quad (\text{B.4})$$

Here μ_1 is called the reduced mass, and \mathcal{R}_1 and \mathcal{P}_1 are the position and momentum vectors of the relative particle. Moreover, we also observe

$$\frac{\mathcal{P}_1}{\mu_1} = \frac{\mathbf{p}_1}{m_1} - \frac{\mathbf{p}_2}{m_2}. \quad (\text{B.5})$$

Therefore, the two-body Hamiltonian can be rewritten as

$$H = \frac{\mathbf{P}_1^2}{2M_1} + \left[\frac{\mathcal{P}_1^2}{2\mu_1} + V(|\mathcal{R}_1|) \right] - e \frac{\mathcal{P}_1}{\mu_1} \cdot \mathbf{A}, \quad (\text{B.6})$$

where we have separated the Hamiltonian into three parts—the external center-of-mass motion, the internal energy of an particle of mass μ_1 moving in potential V , and the atom-field interaction.

If we now canonically quantize the theory above with the commutation relations

$$\left[(\hat{r}_j)_\alpha, (\hat{p}_k)_\beta \right] = i\hbar \delta_{jk} \delta_{\alpha\beta}, \quad (\text{B.7})$$

for $j, k \in \{1, 2\}$ and $\alpha, \beta \in \{x, y, z\}$, we can check that the new dynamical variables defined in Eq. (B.2) satisfy

$$\left[(\hat{R}_1)_\alpha, (\hat{P}_1)_\beta \right] = \left[(\hat{\mathcal{R}}_1)_\alpha, (\hat{\mathcal{P}}_1)_\beta \right] = i\hbar \delta_{\alpha\beta}, \quad (\text{B.8})$$

for $\alpha, \beta \in \{x, y, z\}$. Notice that no approximation needs to be made for the separation of variables for the two-body system considered above.

B.2 Three-body system

We now consider a classical system composed of three charged particles. We let particle 1 carry charge $+2e$, and particles 2 and 3 carry charge $-e$ (one can imagine this system as a classical model of a neutral Helium atom).

The Hamiltonian is now

$$H = \sum_{j=1}^3 \frac{\mathbf{p}_j^2}{2m_j} + \sum_{l>j}^3 \sum_{j=1}^3 V(|\mathbf{r}_j - \mathbf{r}_l|) - e \left(2 \frac{\mathbf{p}_1}{m_1} - \sum_{j=2}^3 \frac{\mathbf{p}_j}{m_j} \right) \cdot \mathbf{A}, \quad (\text{B.9})$$

We first apply the exactly same approach used for the two-body system in last section on particles $\{m_1, \mathbf{r}_1, \mathbf{p}_1\}$ and $\{m_2, \mathbf{r}_2, \mathbf{p}_2\}$. This replaces them by particles $\{M_1, \mathbf{R}_1, \mathbf{P}_1\}$ and $\{\mu_1, \mathcal{R}_1, \mathcal{P}_1\}$. We then apply the two-body approach once more on particles $\{M_1, \mathbf{R}_1, \mathbf{P}_1\}$ and $\{m_3, \mathbf{r}_3, \mathbf{p}_3\}$. The new particles are labeled as $\{M_2, \mathbf{R}_2, \mathbf{P}_2\}$ and $\{\mu_2, \mathcal{R}_2, \mathcal{P}_2\}$. By definition we have

$$\left\{ \begin{array}{l} M_2 = M_1 + m_3 = \sum_{k=1}^3 m_k \\ \mathbf{R}_2 = \frac{M_1 \mathbf{R}_1 + m_3 \mathbf{r}_3}{M_2} = \frac{\sum_{j=1}^3 m_j \mathbf{r}_j}{M_2} \\ \mathbf{P}_2 = \mathbf{P}_1 + \mathbf{p}_3 = \sum_{j=1}^3 \mathbf{p}_j \end{array} \right\}, \quad \left\{ \begin{array}{l} \mu_2 = \frac{M_1 m_3}{M_1 + m_3} = \frac{(m_1 + m_2) m_3}{m_1 + m_2 + m_3} \\ \mathcal{R}_2 = \mathbf{R}_1 - \mathbf{r}_3 = \frac{m_1(\mathbf{r}_1 - \mathbf{r}_3) + m_2(\mathbf{r}_2 - \mathbf{r}_3)}{m_1 + m_2} \\ \mathcal{P}_2 = \frac{m_3 \mathbf{P}_1 - M_1 \mathbf{p}_3}{M_1 + m_3} = \frac{m_3(\mathbf{p}_1 + \mathbf{p}_2) - (m_1 + m_2) \mathbf{p}_3}{m_1 + m_2 + m_3} \end{array} \right\}. \quad (\text{B.10})$$

One can easily check that the properties

$$\sum_{j=1}^3 \frac{\mathbf{p}_j^2}{2m_j} = \frac{\mathbf{P}_2^2}{2M_2} + \sum_{k=1}^2 \frac{\mathcal{P}_k^2}{2\mu_k}, \quad (\text{B.11})$$

$$\sum_{l>j}^3 \sum_{j=1}^3 V(|\mathbf{r}_j - \mathbf{r}_l|) = \sum_{k=1}^2 V(|\mathcal{R}_k|) \quad (\text{B.12})$$

hold. Eq. (B.12) just means that since from Eq. (B.10) the positions \mathcal{R}_k can be written as a linear combination of the relative positions $\mathbf{r}_j - \mathbf{r}_k$ and vice versa (not linearly independent since the sum of relative positions is $\mathbf{0}$), we can rewrite the potential energy in terms of \mathcal{R}_k .

For the atom-field interaction term, we have

$$\frac{\mathcal{P}_2}{\mu_2} = \frac{\mathbf{P}_1}{M_1} - \frac{\mathbf{p}_3}{m_3} = \frac{\mathbf{p}_1 + \mathbf{p}_2}{m_1 + m_2} - \frac{\mathbf{p}_3}{m_3}. \quad (\text{B.13})$$

Thus

$$\frac{\mathcal{P}_1}{\mu_1} + \frac{\mathcal{P}_2}{\mu_2} = \frac{\mathbf{p}_1}{m_1} - \frac{\mathbf{p}_2}{m_2} + \frac{\mathbf{p}_1 + \mathbf{p}_2}{m_1 + m_2} - \frac{\mathbf{p}_3}{m_3}. \quad (\text{B.14})$$

Recall that we have assigned $+2e$ charge to particle 1. In an atom this means that we actually regard particle 1 as the nucleus, which has a mass m_1 that is far larger than the mass of any other particles, or more specifically, the electrons. With this in mind, we expand Eq. (B.14) on the small parameter $\xi = m_2/m_1$ and get

$$\begin{aligned}
\frac{\mathcal{P}_1}{\mu_1} + \frac{\mathcal{P}_2}{\mu_2} &= \frac{\mathbf{p}_1}{m_1} - \frac{\mathbf{p}_2}{m_2} + \frac{\mathbf{p}_1 + \mathbf{p}_2}{m_1(1 + \xi)} - \frac{\mathbf{p}_3}{m_3} \\
&\approx \frac{\mathbf{p}_1}{m_1} - \frac{\mathbf{p}_2}{m_2} + \frac{\mathbf{p}_1 + \mathbf{p}_2}{m_1}(1 - \xi) - \frac{\mathbf{p}_3}{m_3} \\
&\approx \frac{\mathbf{p}_1}{m_1}(2 - \xi) - \frac{\mathbf{p}_2}{m_2}(1 - \xi) - \frac{\mathbf{p}_3}{m_3} \\
&\approx 2\frac{\mathbf{p}_1}{m_1} - \frac{\mathbf{p}_2}{m_2} - \frac{\mathbf{p}_3}{m_3}.
\end{aligned} \tag{B.15}$$

Therefore for the three-body system, with the condition $\xi \ll 1$ we have

$$H = \frac{\mathbf{P}_2^2}{2M_2} + \left[\sum_{k=1}^2 \frac{\mathcal{P}_k^2}{2\mu_k} + \sum_{k=1}^2 V(|\mathcal{R}_k|) \right] - e \sum_{k=1}^2 \frac{\mathcal{P}_k}{\mu_k} \cdot \mathbf{A}. \tag{B.16}$$

After canonical quantization, the following commutation relations hold

$$\left[\left(\hat{R}_2 \right)_\alpha, \left(\hat{P}_2 \right)_\beta \right] = i\hbar\delta_{\alpha\beta}, \quad \left[\left(\hat{\mathcal{R}}_j \right)_\alpha, \left(\hat{\mathcal{P}}_k \right)_\beta \right] = i\hbar\delta_{jk}\delta_{\alpha\beta}, \tag{B.17}$$

for $j, k \in \{1, 2\}$ and $\alpha, \beta \in \{x, y, z\}$.

B.3 $(N + 1)$ -body system

We now generalize the discussion on three-body systems to an $(N + 1)$ -body system. This corresponds to an atom of atomic number N . We let particle 1 carry charge $+Ne$ being the nucleus, and the other N particles carry charge $-e$ being the electrons.

The Hamiltonian is

$$H = \sum_{j=1}^{N+1} \frac{\mathbf{P}_j^2}{2m_j} + V - e \left(N \frac{\mathbf{p}_1}{m_1} - \sum_{j=2}^{N+1} \frac{\mathbf{p}_j}{m_j} \right) \cdot \mathbf{A}, \tag{B.18}$$

where V refers to the potential that depends on the relative positions of the particles. Our task is to separate the total energy of the $(N + 1)$ particles into an external part that is the center-of-mass

kinetic energy, and an internal part that describes the kinetic and potential energy of the N relative particles. To do this, we define the following sequences of variables

$$\{(M_k, \mathbf{R}_k, \mathbf{P}_k)\}, \quad \{(\mu_k, \mathcal{R}_k, \mathcal{P}_k)\}, \quad (\text{B.19})$$

with $k \in \{1, 2, \dots, N\}$. Here, $(M_k, \mathbf{R}_k, \mathbf{P}_k)$ represents the center of mass of the first $(k+1)$ particles, and $(\mu_k, \mathcal{R}_k, \mathcal{P}_k)$ represents the k th relative particle. Specifically, we define $(M, \mathbf{R}, \mathbf{P})$ to be the center of mass of the atom. Immediately we have $M_N = M$, $\mathbf{R}_N = \mathbf{R}$, and $\mathbf{P}_N = \mathbf{P}$.

We find the expressions of the sequential variables as follows:

(1) Choose the initial conditions as

$$M_0 = m_1, \quad \mathbf{R}_0 = \mathbf{r}_1, \quad \mathbf{P}_0 = \mathbf{p}_1. \quad (\text{B.20})$$

(2) For $k \in \{1, \dots, N\}$, we have

$$\left\{ \begin{array}{l} M_k = M_{k-1} + m_{k+1} = \sum_{j=1}^{k+1} m_j \\ \mathbf{R}_k = \frac{M_{k-1}\mathbf{R}_{k-1} + m_{k+1}\mathbf{r}_{k+1}}{M_k} = \frac{\sum_{j=1}^{k+1} m_j \mathbf{r}_j}{\sum_{j=1}^{k+1} m_j} \\ \mathbf{P}_k = \mathbf{P}_{k-1} + \mathbf{p}_{k+1} = \sum_{j=1}^{k+1} \mathbf{P}_j \end{array} \right. , \quad \left\{ \begin{array}{l} \mu_k = \frac{M_{k-1}m_{k+1}}{M_k} \\ \mathcal{R}_k = \mathbf{R}_{k-1} - \mathbf{r}_{k+1} \\ \mathcal{P}_k = \frac{m_{k+1}\mathbf{P}_{k-1} - M_{k-1}\mathbf{p}_{k+1}}{M_k} \end{array} \right. . \quad (\text{B.21})$$

One can check that the following properties hold

$$\sum_{j=1}^{N+1} \frac{\mathbf{p}_j^2}{2m_j} = \frac{\mathbf{P}^2}{2M} + \sum_{k=1}^N \frac{\mathcal{P}_k^2}{2\mu_k}, \quad (\text{B.22})$$

$$V = \sum_{k=1}^N V(|\mathcal{R}_k|). \quad (\text{B.23})$$

For the atom-field interaction term, we first discuss the small parameter ξ as introduced in the last section. Let $\xi_j = m_j/m_1$ for $j = 2, 3, \dots, N+1$. Since all the particles except for particle 1

are electrons, we actually have $\xi_j = \xi = m_e/m_p \approx 1/2000$ for $j \geq 2$. In the following discussion we start by using ξ_j to label different particles and then use $\xi_j = \xi$ to simplify the expression. Specifically, we claim that in the limit $N\xi \ll 1$,

$$\sum_{k=1}^N \frac{\mathcal{P}_k}{\mu_k} \approx N \frac{\mathbf{p}_1}{m_1} - \sum_{j=2}^{N+1} \frac{\mathbf{p}_j}{m_j}. \quad (\text{B.24})$$

The proof is as follows. From Eq. (B.21),

$$\begin{aligned} \sum_{k=1}^N \frac{\mathcal{P}_k}{\mu_k} &= \sum_{k=1}^N \left(\frac{\mathbf{p}_{k-1}}{M_{k-1}} - \frac{\mathbf{p}_{k+1}}{m_{k+1}} \right) \\ &= \sum_{k=1}^N \left(\frac{\sum_{j=1}^k \mathbf{p}_j}{\sum_{j=1}^k m_j} - \frac{\mathbf{p}_{k+1}}{m_{k+1}} \right) \\ &\approx \sum_{k=1}^N \left[\frac{\sum_{j=1}^k \mathbf{p}_j}{m_1} \left(1 - \sum_{j=2}^k \xi_j \right) - \frac{\mathbf{p}_{k+1}}{m_{k+1}} \right] \\ &\approx \frac{\mathbf{p}_1}{m_1} \sum_{j=2}^{N+1} [1 - (N+1-j)\xi_j] - \sum_{j=2}^{N+1} \frac{\mathbf{p}_j}{m_j} [1 - (N+1-j)\xi_j] \end{aligned} \quad (\text{B.25})$$

If we now substitute $\xi_j = \xi$ for $j \geq 2$, we obtain

$$\sum_{k=1}^N \frac{\mathcal{P}_k}{\mu_k} = N \frac{\mathbf{p}_1}{m_1} \left[1 - \frac{N-1}{2} \xi \right] - \sum_{j=2}^{N+1} \frac{\mathbf{p}_j}{m_j} [1 - (N+1-j)\xi]. \quad (\text{B.26})$$

Thus for $N\xi \ll 1$, we have

$$\sum_{k=1}^N \frac{\mathcal{P}_k}{\mu_k} = N \frac{\mathbf{p}_1}{m_1} - \sum_{j=2}^{N+1} \frac{\mathbf{p}_j}{m_j}. \quad (\text{B.27})$$

The condition $N\xi \ll 1$ is always true if Ne is the charge of the atomic nucleus. Therefore to good approximation, the Hamiltonian can be rewritten as

$$H = \frac{\mathbf{P}^2}{2M} + \sum_{k=1}^N \frac{\mathcal{P}_k^2}{2\mu_k} + \sum_{k=1}^N V(|\mathcal{R}_k|) - e \sum_{k=1}^N \frac{\mathcal{P}_k}{\mu_k} \cdot \mathbf{A}. \quad (\text{B.28})$$

After canonical quantization, the following commutation relations hold

$$\left[\hat{R}_\alpha, \hat{P}_\beta \right] = i\hbar \delta_{\alpha\beta}, \quad \left[\left(\hat{\mathcal{R}}_j \right)_\alpha, \left(\hat{\mathcal{P}}_k \right)_\beta \right] = i\hbar \delta_{jk} \delta_{\alpha\beta}, \quad (\text{B.29})$$

for $j, k \in \{1, 2, \dots, N\}$ and $\alpha, \beta \in \{x, y, z\}$.

Appendix C

Pauli Matrix Relations

We define

$$\sigma^+ = \begin{pmatrix} 0 & 1 \\ 0 & 0 \end{pmatrix}, \quad \sigma^- = \begin{pmatrix} 0 & 0 \\ 1 & 0 \end{pmatrix}, \quad \sigma^z = \begin{pmatrix} 1 & 0 \\ 0 & -1 \end{pmatrix}. \quad (\text{C.1})$$

Then the following matrix relations can be used for convenience;

$$\begin{cases} \sigma^+ \sigma^- + \sigma^- \sigma^+ = 1 \\ \sigma^+ \sigma^- - \sigma^- \sigma^+ = \sigma^z \end{cases}, \quad (\text{C.2})$$

$$\begin{cases} \sigma^z = 2\sigma^+ \sigma^- - 1 \\ \sigma^z = 1 - 2\sigma^- \sigma^+ \end{cases}, \quad \begin{cases} \sigma^+ \sigma^- = (\sigma^+ \sigma^-)^n = \frac{1}{2}(1 + \sigma^z) \\ \sigma^- \sigma^+ = (\sigma^- \sigma^+)^n = \frac{1}{2}(1 - \sigma^z) \end{cases}, \quad n \in \mathbb{Z}^+, \quad (\text{C.3})$$

$$\begin{cases} \sigma^z \sigma^+ = \sigma^+ \\ \sigma^+ \sigma^z = -\sigma^+ \end{cases}, \quad \begin{cases} \sigma^z \sigma^- = -\sigma^- \\ \sigma^- \sigma^z = \sigma^- \end{cases}, \quad (\text{C.4})$$

$$\begin{cases} \sigma^- \sigma^+ \sigma^- = \sigma^- \\ \sigma^+ \sigma^- \sigma^+ = \sigma^+ \end{cases}, \quad \begin{cases} \sigma^+ \sigma^z \sigma^- = -\sigma^+ \sigma^- \\ \sigma^- \sigma^z \sigma^+ = \sigma^- \sigma^+ \end{cases}, \quad (\text{C.5})$$

$$\begin{cases} \sigma^z \sigma^+ \sigma^- = \sigma^+ \sigma^- \\ \sigma^z \sigma^- \sigma^+ = -\sigma^- \sigma^+ \end{cases}, \quad \begin{cases} \sigma^+ \sigma^- \sigma^z = \sigma^+ \sigma^- \\ \sigma^- \sigma^+ \sigma^z = -\sigma^- \sigma^+ \end{cases}. \quad (\text{C.6})$$

Appendix D

Rotating Frames and Interaction Pictures

D.1 Closed systems

We develop a general theory on rotating frames and interaction pictures for closed quantum systems.

D.1.1 Rotating frames

Given a certain closed quantum system, suppose there exist Hermitian operators \hat{H}_1 and \hat{H}_2 ¹ such that the time evolution of the system density matrix $\hat{\rho}$ and any other operator \hat{O} can be expressed by the following equations²

$$\frac{d\hat{\rho}}{dt} = \frac{1}{i\hbar} [\hat{H}_1, \hat{\rho}], \quad (\text{D.1a})$$

$$\frac{d\hat{O}}{dt} = -\frac{1}{i\hbar} [\hat{H}_2, \hat{O}]. \quad (\text{D.1b})$$

Then we can define a *rotating frame* with any unitary operator \hat{U} such that

$$\hat{\rho}^{\text{R}} = \hat{U}^\dagger \hat{\rho} \hat{U}, \quad (\text{D.2a})$$

$$\hat{O}^{\text{R}} = \hat{U}^\dagger \hat{O} \hat{U}, \quad (\text{D.2b})$$

are the density matrix and operator in the new frame, respectively.

¹Operators \hat{H}_1 and \hat{H}_2 can be time-dependent.

²Here, as we will see later, the two equations are none other than the von Neumann equation and Heisenberg equation in an arbitrary rotating frame. For simplicity, we do not consider the cases where \hat{O} is explicitly dependent on time.

The dynamics of $\hat{\rho}^{\text{R}}$ and $\hat{\mathcal{O}}^{\text{R}}$ can be calculated as

$$\begin{aligned}\frac{d\hat{\rho}^{\text{R}}}{dt} &= \frac{d\hat{U}^\dagger}{dt}\hat{\rho}\hat{U} + \hat{U}^\dagger\frac{d\hat{\rho}}{dt}\hat{U} + \hat{U}^\dagger\hat{\rho}\frac{d\hat{U}}{dt} \\ &= \frac{1}{i\hbar}\left[\hat{U}^\dagger\hat{H}_1\hat{U}, \hat{\rho}^{\text{R}}\right] + \frac{d\hat{U}^\dagger}{dt}\hat{U}\hat{\rho}^{\text{R}} - \hat{\rho}^{\text{R}}\frac{d\hat{U}^\dagger}{dt}\hat{U} \\ &= \frac{1}{i\hbar}\left[\hat{U}^\dagger\hat{H}_1\hat{U} + i\hbar\frac{d\hat{U}^\dagger}{dt}\hat{U}, \hat{\rho}^{\text{R}}\right],\end{aligned}\tag{D.3}$$

and

$$\begin{aligned}\frac{d\hat{\mathcal{O}}^{\text{R}}}{dt} &= \frac{d\hat{U}^\dagger}{dt}\hat{\mathcal{O}}\hat{U} + \hat{U}^\dagger\frac{d\hat{\mathcal{O}}}{dt}\hat{U} + \hat{U}^\dagger\hat{\mathcal{O}}\frac{d\hat{U}}{dt} \\ &= -\frac{1}{i\hbar}\left[\hat{U}^\dagger\hat{H}_2\hat{U}, \hat{\mathcal{O}}^{\text{R}}\right] + \frac{d\hat{U}^\dagger}{dt}\hat{U}\hat{\mathcal{O}}^{\text{R}} - \hat{\mathcal{O}}^{\text{R}}\frac{d\hat{U}^\dagger}{dt}\hat{U} \\ &= -\frac{1}{i\hbar}\left[\hat{U}^\dagger\hat{H}_2\hat{U} - i\hbar\frac{d\hat{U}^\dagger}{dt}\hat{U}, \hat{\mathcal{O}}^{\text{R}}\right],\end{aligned}\tag{D.4}$$

where we have used

$$\frac{d(\hat{U}^\dagger\hat{U})}{dt} = \frac{d\hat{U}^\dagger}{dt}\hat{U} + \hat{U}^\dagger\frac{d\hat{U}}{dt} = 0.\tag{D.5}$$

Define

$$\hat{H}_1^{\text{R}} = \hat{U}^\dagger\hat{H}_1\hat{U} + i\hbar\frac{d\hat{U}^\dagger}{dt}\hat{U},\tag{D.6a}$$

$$\hat{H}_2^{\text{R}} = \hat{U}^\dagger\hat{H}_2\hat{U} - i\hbar\frac{d\hat{U}^\dagger}{dt}\hat{U}.\tag{D.6b}$$

Then we recover Eqs. (D.1a)–(D.1b) in the rotating frame, i.e.,

$$\frac{d\hat{\rho}^{\text{R}}}{dt} = \frac{1}{i\hbar}\left[\hat{H}_1^{\text{R}}, \hat{\rho}^{\text{R}}\right],\tag{D.7a}$$

$$\frac{d\hat{\mathcal{O}}^{\text{R}}}{dt} = -\frac{1}{i\hbar}\left[\hat{H}_2^{\text{R}}, \hat{\mathcal{O}}^{\text{R}}\right].\tag{D.7b}$$

Also notice that

$$\hat{H}_1^{\text{R}} + \hat{H}_2^{\text{R}} = \hat{U}^\dagger\left(\hat{H}_1 + \hat{H}_2\right)\hat{U}.\tag{D.8}$$

D.1.2 Interaction pictures

In this section, we apply the formalism developed in Sec.D.1.1 to different scenarios.

Scenario D.1.1: From the Schrödinger picture (SP) to the Heisenberg picture (HP).

Suppose we are in the SP with a Hamiltonian $\hat{H}^S(t)$. Then Eqs. (D.1a)–(D.1b) are true if $\hat{H}_1 = \hat{H}^S(t)$, $\hat{H}_2 = 0$, yielding

$$\frac{d\hat{\rho}^S}{dt} = \frac{1}{i\hbar} [\hat{H}^S(t), \hat{\rho}^S], \quad (\text{D.9a})$$

$$\frac{d\hat{\mathcal{O}}^S}{dt} = 0, \quad (\text{D.9b})$$

Equation (D.9a) is the von Neumann equation, while Eq. (D.9b) means that operators are stationary in the SP.

Let

$$\hat{U} = \hat{U}(t, t_0) = \mathcal{T} \exp \left[-\frac{i}{\hbar} \int_{t_0}^t \hat{H}^S(t') dt' \right], \quad (\text{D.10})$$

where t_0 is some initial time, and \mathcal{T} is the time-ordering operator. Then by Eqs. (D.6a)–(D.6b),

$$\hat{H}_1^R(t) = \hat{U}^\dagger(t, t_0) \hat{H}^S(t) \hat{U}(t, t_0) + i\hbar \frac{d\hat{U}^\dagger}{dt} \hat{U} = 0, \quad (\text{D.11a})$$

$$\hat{H}_2^R(t) = -i\hbar \frac{d\hat{U}^\dagger}{dt} \hat{U} = \hat{U}^\dagger(t, t_0) \hat{H}^S(t) \hat{U}(t, t_0). \quad (\text{D.11b})$$

Therefore, in this rotating frame,

$$\frac{d\hat{\rho}^R}{dt} = 0, \quad (\text{D.12a})$$

$$\frac{d\hat{\mathcal{O}}^R}{dt} = -\frac{1}{i\hbar} [\hat{H}_2^R(t), \hat{\mathcal{O}}^R], \quad (\text{D.12b})$$

and we call the physical picture defined by this rotating frame the Heisenberg picture (HP). Equation (D.12b) is the Heisenberg equation assuming $\hat{\mathcal{O}}^S$ is not explicitly dependent on time.

Scenario D.1.2: From SP to an interaction picture (IP).

Suppose in the SP the Hamiltonian can be written as

$$\hat{H}^S(t) = \hat{H}_0^S + \hat{V}^S(t), \quad (\text{D.13})$$

where \hat{H}_0^S is time-independent and usually describes some known dynamics, and \hat{V}^S is the interaction Hamiltonian that can be time-dependent. Let

$$\hat{U} = \exp\left[-\frac{i}{\hbar}\hat{H}_0^S t\right] \quad (\text{D.14})$$

and thus

$$i\hbar\frac{d\hat{U}^\dagger}{dt}\hat{U} = -\hat{U}^\dagger\hat{H}_0^S\hat{U}. \quad (\text{D.15})$$

Then by Eqs. (D.6a)–(D.6b),

$$\hat{H}_1^R = \hat{U}^\dagger\hat{H}^S\hat{U} - \hat{U}^\dagger\hat{H}_0^S\hat{U} = \hat{U}^\dagger\hat{V}^S\hat{U}, \quad (\text{D.16a})$$

$$\hat{H}_2^R = \hat{U}^\dagger\hat{H}_0^S\hat{U}. \quad (\text{D.16b})$$

Therefore, from Eq. (D.7a), the dynamics of the density matrix $\hat{\rho}^R$ is driven by the interaction Hamiltonian \hat{H}_1^R , i.e.,

$$\frac{d\hat{\rho}^R}{dt} = \frac{1}{i\hbar}[\hat{H}_1^R, \hat{\rho}^R] = \frac{1}{i\hbar}[\hat{U}^\dagger\hat{V}^S\hat{U}, \hat{\rho}^R], \quad (\text{D.17})$$

while the dynamics of the operators is uninteresting. We call this physical picture the *interaction picture* (IP) defined from SP.

Scenario D.1.3: From HP to IP.

In quantum optics, especially for open quantum systems, it is sometimes more convenient to directly study the dynamics of the operators instead of density matrices. Therefore, it is useful to define a rotating frame where the operators evolve with the interesting part of the Hamiltonian (the interaction). We can do this by defining a rotating frame from the HP.

Suppose that we are now in the HP defined in Scenario D.1.1. This is equivalent to saying that $\hat{H}_1 = 0$, $\hat{H}_2 = \hat{H}^H(t)$ in Eqs. (D.1a)–(D.1b), where $\hat{H}^H(t) = \hat{H}_2^R(t)$ found in Eq. (D.11b). Suppose the Hamiltonian in HP can be written as

$$\hat{H}^H(t) = \hat{H}_0^H(t) + \hat{V}^H(t), \quad (\text{D.18})$$

where $\hat{V}^H(t)$ is the interaction. Notice here $\hat{H}_0^H(t)$ is a function of time. Let

$$\hat{U} = \exp\left[\frac{i}{\hbar}\hat{H}_0^H(t)t\right]. \quad (\text{D.19})$$

Then by Sneddon's formula [146, 121]

$$\begin{aligned}
i\hbar \frac{d\hat{U}^\dagger}{dt} \hat{U} &= i\hbar \int_0^1 du e^{-u \frac{i}{\hbar} \hat{H}_0^H t} \left[-\frac{d}{dt} \left(\frac{i}{\hbar} \hat{H}_0^H t \right) \right] e^{(u-1) \frac{i}{\hbar} \hat{H}_0^H t} e^{\frac{i}{\hbar} \hat{H}_0^H t} \\
&= \int_0^1 du e^{-u \frac{i}{\hbar} \hat{H}_0^H t} \left[t \frac{d\hat{H}_0^H}{dt} + \hat{H}_0^H \right] e^{u \frac{i}{\hbar} \hat{H}_0^H t} \\
&= t \int_0^1 du e^{-u \frac{i}{\hbar} \hat{H}_0^H t} \frac{d\hat{H}_0^H}{dt} e^{u \frac{i}{\hbar} \hat{H}_0^H t} + \hat{H}_0^H \\
&= \hat{U}^\dagger \hat{H}_0^H(t) \hat{U} + \hat{C}(t),
\end{aligned} \tag{D.20}$$

where

$$\hat{C}(t) = t \int_0^1 du e^{-u \frac{i}{\hbar} \hat{H}_0^H t} \frac{d\hat{H}_0^H}{dt} e^{u \frac{i}{\hbar} \hat{H}_0^H t}. \tag{D.21}$$

Then by Eqs. (D.6a)–(D.6b),

$$\hat{H}_1^R = \hat{U}^\dagger \hat{H}_0^H \hat{U} + \hat{C}(t), \tag{D.22a}$$

$$\hat{H}_2^R = \hat{U}^\dagger \hat{H}^H \hat{U} - \hat{U}^\dagger \hat{H}_0^H \hat{U} - \hat{C}(t) = \hat{U}^\dagger \hat{V}^H \hat{U} - \hat{C}(t). \tag{D.22b}$$

Therefore, from Eq. (D.7b), the dynamics of the operators is driven by the interaction Hamiltonian \hat{H}_2^R , i.e.,

$$\frac{d\hat{\mathcal{O}}^R}{dt} = -\frac{1}{i\hbar} [\hat{H}_2^R, \hat{\mathcal{O}}^R] = -\frac{1}{i\hbar} [\hat{U}^\dagger \hat{V}^H \hat{U}, \hat{\mathcal{O}}^R] - \frac{1}{i\hbar} [\hat{C}, \hat{\mathcal{O}}^R], \tag{D.23}$$

while the dynamics of the density matrix is uninteresting. We call this physical picture the *interaction picture* (IP) defined from the HP.

Here we give some special cases for $\hat{C}(t)$:

- (1) If $\frac{d\hat{H}_0^H}{dt} = 0$, then $\hat{C}(t) = 0$.
- (2) If $\left[\hat{H}_0^H, \frac{d\hat{H}_0^H}{dt} \right] = 0$, then $\hat{C}(t) = t \frac{d\hat{H}_0^H}{dt}$.
- (3) If $\left[\hat{H}_0^H, \frac{d\hat{H}_0^H}{dt} \right] = \hbar\Omega \frac{d\hat{H}_0^H}{dt}$, then $\hat{C}(t) = \frac{i}{\Omega} (e^{-i\Omega t} - 1) \frac{d\hat{H}_0^H}{dt}$.

As an example, consider the following Hamiltonian in the HP

$$\hat{H}(t) = \hbar\omega\hat{a}^\dagger(t)\hat{a}(t) + \hbar g[\hat{a}^\dagger(t) + \hat{a}(t)], \quad (\text{D.24})$$

where \hat{a} and \hat{a}^\dagger are the bosonic annihilation and creation operators that satisfy $[\hat{a}, \hat{a}^\dagger] = 1$. Let $\hat{H}_0(t) = \hbar\omega\hat{a}^\dagger(t)\hat{a}(t)$ and $\hat{V}(t) = \hbar g[\hat{a}^\dagger(t) + \hat{a}(t)]$. Then in the HP we have

$$\frac{d}{dt}\hat{a}(t) = -\frac{1}{i\hbar}[\hat{H}(t), \hat{a}(t)] = -i\omega\hat{a}(t) - ig, \quad (\text{D.25a})$$

$$\frac{d}{dt}\hat{a}^\dagger(t) = -\frac{1}{i\hbar}[\hat{H}(t), \hat{a}^\dagger(t)] = i\omega\hat{a}^\dagger(t) + ig. \quad (\text{D.25b})$$

Thus

$$\frac{d}{dt}\hat{H}_0(t) = \hbar\omega\frac{d}{dt}[\hat{a}^\dagger(t)\hat{a}(t)] = i\hbar\omega g[\hat{a}(t) - \hat{a}^\dagger(t)]. \quad (\text{D.26})$$

Then

$$\begin{aligned} \hat{C}(t) &= t \int_0^1 du i\hbar\omega g e^{-iu\omega\hat{a}^\dagger\hat{a}t} [\hat{a} - \hat{a}^\dagger] e^{iu\omega\hat{a}^\dagger\hat{a}t} \\ &= t \int_0^1 du i\hbar\omega g [e^{iu\omega t}\hat{a} - e^{-iu\omega t}\hat{a}^\dagger] \\ &= \hbar g(1 - e^{i\omega t})\hat{a}(t) + \hbar g(1 - e^{-i\omega t})\hat{a}^\dagger(t). \end{aligned} \quad (\text{D.27})$$

If we now switch into the IP, then we have

$$\hat{a}^{\text{I}}(t) = \hat{U}^\dagger \hat{a}(t) \hat{U} = e^{i\omega t} \hat{a}(t), \quad (\text{D.28})$$

$$\hat{U}^\dagger \hat{V}^{\text{H}}(t) \hat{U} = \hbar g [(\hat{a}^{\text{I}})^\dagger(t) + \hat{a}^{\text{I}}(t)], \quad (\text{D.29})$$

$$\hat{C}(t) = \hbar g (e^{-i\omega t} - 1) \hat{a}^{\text{I}}(t) + \hbar g (e^{i\omega t} - 1) (\hat{a}^{\text{I}})^\dagger(t). \quad (\text{D.30})$$

By Eq. (D.23) we have

$$\begin{aligned} \frac{d}{dt}\hat{a}^{\text{I}} &= -\frac{1}{i\hbar}\hbar g [(\hat{a}^{\text{I}})^\dagger, \hat{a}^{\text{I}}] - \frac{1}{i\hbar}\hbar g (e^{i\omega t} - 1) [(\hat{a}^{\text{I}})^\dagger, \hat{a}^{\text{I}}] \\ &= -ig - ig(e^{i\omega t} - 1) \\ &= -ige^{i\omega t}. \end{aligned} \quad (\text{D.31})$$

On the other hand, we can directly get from Eqs. (D.25a) and (D.28) that

$$\begin{aligned}
 \frac{d}{dt}\hat{a}^{\text{I}} &= i\omega e^{i\omega t}\hat{a} + e^{i\omega t}\frac{d}{dt}\hat{a} \\
 &= i\omega e^{i\omega t}\hat{a} + e^{i\omega t}(-i\omega\hat{a} - ig) \\
 &= -ige^{i\omega t}.
 \end{aligned}
 \tag{D.32}$$

Therefore our descriptions are consistent.

In the literature, people sometimes refer to Eq. (D.28) as the definition of a rotating frame or an interaction picture when working in the HP. Such transformations, when correctly chosen, will simplify the dynamics of operators as in the case from Eq. (D.25a) to Eq. (D.32). However, such definitions can also be confusing since normally we only talk about an IP when starting from the SP. Here, we see that the IP defined from a HP is much more complicated than that from the SP when $\hat{C} \neq 0$, which originates from the fact that $\hat{H}_0(t)$ is a function of time in the HP, although the construction of rotating frames in Appx. D.1.1 is straightforward and clear. In general, we can define a rotating frame or IP constructed from any picture by choosing the correct unitary. The point is to simplify our calculations by absorbing the global rotating phase into the new variables.

D.2 Open systems

We apply our results on the rotating frames and interaction pictures to open quantum systems.

D.2.1 Master equation

In the derivation of quantum master equation in Sec. 3.1, we have moved into the IP from the SP. However, that rotating frame, or IP, is a construction for the closed system combined of the open system we study and the environment. Here, we consider directly moving into the IP from the SP give a master equation without worrying about the environment.

Suppose we are in the SP defined for the “bigger” system that consists of our open system and the environment. After defining the system density matrix $\hat{\rho}$ as the total density matrix with

the environment traced out and making all the approximations in Sec. 3.1, we have the master equation (3.24), which we copy here as

$$\frac{d}{dt}\hat{\rho} = \frac{1}{i\hbar}[\hat{H}, \hat{\rho}] + \sum_k \Gamma_k \mathcal{L}[\hat{S}_k] \hat{\rho}, \quad (\text{D.33})$$

where we have dropped the S notation since all operators are system operators. Suppose the Hamiltonian \hat{H} can be separated as

$$\hat{H} = \hat{H}_0 + \hat{V}, \quad (\text{D.34})$$

where \hat{H}_0 is time-independent, and \hat{V} usually describes some coherent coupling that can be time-dependent. Let

$$\hat{U} = \exp\left[-\frac{i}{\hbar}\hat{H}_0 t\right] \quad (\text{D.35})$$

and define

$$\hat{\rho}^{\text{I}} = \hat{U}^\dagger \hat{\rho} \hat{U}, \quad (\text{D.36a})$$

$$\hat{\mathcal{O}}^{\text{I}} = \hat{U}^\dagger \hat{\mathcal{O}} \hat{U}, \quad (\text{D.36b})$$

for any system operator $\hat{\mathcal{O}}$. Following similar calculations as Eq. (D.3), we obtain

$$\begin{aligned} \frac{d\hat{\rho}^{\text{I}}}{dt} &= \frac{d\hat{U}^\dagger}{dt} \hat{\rho} \hat{U} + \hat{U}^\dagger \frac{d\hat{\rho}}{dt} \hat{U} + \hat{U}^\dagger \hat{\rho} \frac{d\hat{U}}{dt} \\ &= \frac{1}{i\hbar} \left[\hat{U}^\dagger \hat{H} \hat{U} + i\hbar \frac{d\hat{U}^\dagger}{dt} \hat{U}, \hat{\rho}^{\text{I}} \right] + \sum_k \Gamma_k \mathcal{L}[\hat{S}_k^{\text{I}}] \hat{\rho}^{\text{I}} \\ &= \frac{1}{i\hbar} \left[\hat{U}^\dagger \hat{H} \hat{U} - \hat{U}^\dagger \hat{H}_0 \hat{U}, \hat{\rho}^{\text{I}} \right] + \sum_k \Gamma_k \mathcal{L}[\hat{S}_k^{\text{I}}] \hat{\rho}^{\text{I}} \\ &= \frac{1}{i\hbar} \left[\hat{V}^{\text{I}}, \hat{\rho}^{\text{I}} \right] + \sum_k \Gamma_k \mathcal{L}[\hat{S}_k^{\text{I}}] \hat{\rho}^{\text{I}}, \end{aligned} \quad (\text{D.37})$$

where $\hat{V}^{\text{I}} = \hat{U}^\dagger \hat{V} \hat{U}$. Compared to Eq. (D.17), we see that the frame or picture change is straightforward for a master equation. One just needs to include the Lindbladian superoperator term with operators in the new picture aside from the transformation for closed systems.

As an example, consider the system given in Eq. (3.77)

$$\hat{H} = \frac{\hbar\omega_a}{2} \hat{\sigma}^z + \hbar\omega_c \hat{a}^\dagger \hat{a} + \frac{\hbar g}{2} (\hat{\sigma}^+ \hat{a} + \hat{a}^\dagger \hat{\sigma}^-), \quad (\text{D.38})$$

with a master equation for cavity decay

$$\frac{d}{dt}\hat{\rho} = \frac{1}{i\hbar}[\hat{H}, \hat{\rho}] + \kappa\mathcal{L}[\hat{a}]\hat{\rho}. \quad (\text{D.39})$$

We can define the IP in three ways:

- (1) $\hat{H}_0 = \frac{\hbar\omega_a}{2}\hat{\sigma}^z + \hbar\omega_c\hat{a}^\dagger\hat{a}$. Then we have $\hat{a}^I = \hat{U}^\dagger\hat{a}\hat{U} = e^{-i\omega_c t}\hat{a}$ and $(\hat{\sigma}^-)^I = \hat{U}^\dagger\hat{\sigma}^-\hat{U} = e^{-i\omega_a t}\hat{\sigma}^-$. The master equation is

$$\frac{d}{dt}\hat{\rho}^I = \frac{1}{i\hbar}[\hat{V}^I, \hat{\rho}^I] + \kappa\mathcal{L}[\hat{a}^I]\hat{\rho}^I, \quad (\text{D.40})$$

where

$$\hat{V}^I = \frac{\hbar g}{2} \left[(\hat{\sigma}^+)^I \hat{a}^I + (\hat{a}^\dagger)^I (\hat{\sigma}^-)^I \right] = \frac{\hbar g}{2} \left(\hat{\sigma}^+ \hat{a} e^{-i\Delta t} + \hat{a}^\dagger \hat{\sigma}^- e^{i\Delta t} \right) \quad (\text{D.41})$$

with $\Delta = \omega_c - \omega_a$. Thus we see that with this choice of \hat{H}_0 , the detuning Δ is hidden in the relative phase between atomic pseudospins and the fields.

- (2) $\hat{H}_0 = \frac{\hbar\omega_a}{2}\hat{\sigma}^z + \hbar\omega_c\hat{a}^\dagger\hat{a}$. In this case, operators \hat{a} and $\hat{\sigma}^-$ are eigenoperators of \hat{H}_0 with the same frequency $-\omega_a$. Then we have $\hat{a}^I = e^{-i\omega_a t}\hat{a}$ and $(\hat{\sigma}^-)^I = e^{-i\omega_a t}\hat{\sigma}^-$. The master equation is

$$\frac{d}{dt}\hat{\rho}^I = \frac{1}{i\hbar}[\hat{V}^I, \hat{\rho}^I] + \kappa\mathcal{L}[\hat{a}^I]\hat{\rho}^I, \quad (\text{D.42})$$

where

$$\hat{V}^I = \hbar\Delta(\hat{a}^\dagger)^I(\hat{a})^I + \frac{\hbar g}{2} \left[(\hat{\sigma}^+)^I \hat{a}^I + (\hat{a}^\dagger)^I (\hat{\sigma}^-)^I \right] = \hbar\Delta\hat{a}^\dagger\hat{a} + \frac{\hbar g}{2} (\hat{\sigma}^+ \hat{a} + \hat{a}^\dagger \hat{\sigma}^-). \quad (\text{D.43})$$

Thus with this choice of \hat{H}_0 , the detuning Δ is explicitly shown in the Hamiltonian. People sometimes refer to the rotating frame with this choice of \hat{H}_0 as the frame of the atomic frequency ω_a .

- (3) $\hat{H}_0 = \frac{\hbar\omega_c}{2}\hat{\sigma}^z + \hbar\omega_c\hat{a}^\dagger\hat{a}$. The results are similar to the previous example. People refer to this frame as the rotating frame of the cavity frequency ω_c .

D.2.2 Heisenberg-Langevin equation

Following the similar reasoning as the previous section, one can show that for a Heisenberg-Langevin equation that has the form

$$\frac{d}{dt}\hat{\mathcal{O}} = -\frac{1}{i\hbar}[\hat{H}, \hat{\mathcal{O}}] + \sum_k \Gamma_k \bar{\mathcal{L}}[\hat{S}_k] \hat{\mathcal{O}} + \sum_k \sqrt{\Gamma_k} \left([\hat{S}_k^\dagger, \hat{\mathcal{O}}] \hat{\xi}_k + \hat{\xi}_k^\dagger [\hat{\mathcal{O}}, \hat{S}_k] \right), \quad (\text{D.44})$$

with

$$\begin{cases} \hat{H}(t) = \hat{H}_0(t) + \hat{V}(t) \\ \hat{U}(t) = \exp\left[\frac{i}{\hbar}\hat{H}_0(t)t\right] \end{cases}, \quad \begin{cases} \hat{\mathcal{O}}^I = \hat{U}^\dagger \hat{\mathcal{O}} \hat{U} \\ \hat{\xi}^I = \hat{U}^\dagger \hat{\xi} \hat{U} \end{cases}, \quad (\text{D.45})$$

we have

$$\frac{d}{dt}\hat{\mathcal{O}}^I = -\frac{1}{i\hbar}[\hat{V}^I, \hat{\mathcal{O}}^I] + \sum_k \Gamma_k \bar{\mathcal{L}}[\hat{S}_k^I] \hat{\mathcal{O}}^I + \sum_k \sqrt{\Gamma_k} \left\{ [(\hat{S}_k^\dagger)^I, \hat{\mathcal{O}}^I] \hat{\xi}_k^I + (\hat{\xi}_k^\dagger)^I [\hat{\mathcal{O}}^I, \hat{S}_k^I] \right\} - \hat{C}(t) \quad (\text{D.46})$$

where

$$\hat{V}^I = \hat{U}^\dagger \hat{V} \hat{U}, \quad (\text{D.47})$$

$$\hat{C}(t) = t \int_0^1 du e^{-u\frac{i}{\hbar}\hat{H}_0 t} \frac{d\hat{H}_0}{dt} e^{u\frac{i}{\hbar}\hat{H}_0 t}. \quad (\text{D.48})$$

The formalism above is not always useful, especially when \hat{C} is non-zero. In reality, if the change of frame is straightforward, mostly in the form of Eq. (D.28), then we can define the rotating frame directly without worrying about the \hat{C} operator.

Consider the same system (D.38) as in the last section in the HP. The Heisenberg-Langevin equations for \hat{a} , $\hat{\sigma}^-$, and $\hat{\sigma}^z$ are

$$\frac{d}{dt}\hat{a} = -i\omega_c \hat{a} - \frac{\kappa}{2}\hat{a} - \frac{ig}{2}\hat{\sigma}^- - \sqrt{\kappa}\hat{\xi}, \quad (\text{D.49})$$

$$\frac{d}{dt}\hat{\sigma}^- = -i\omega_a \hat{\sigma}^- + \frac{ig}{2}\hat{\sigma}^z \hat{a}, \quad (\text{D.50})$$

$$\frac{d}{dt}\hat{\sigma}^z = ig(\hat{a}^\dagger \hat{\sigma}^- - \hat{\sigma}^+ \hat{a}). \quad (\text{D.51})$$

We now define a rotating frame in the atomic frequency ω_a by letting

$$\hat{a}^{\text{I}} = e^{i\omega_a t} \hat{a}, \quad (\text{D.52})$$

$$(\hat{\sigma}^-)^{\text{I}} = e^{i\omega_a t} \hat{\sigma}^-, \quad (\text{D.53})$$

$$\hat{\xi}^{\text{I}} = e^{i\omega_a t} \hat{\xi}, \quad (\text{D.54})$$

Then the Heisenberg-Langevin equations become

$$\frac{d}{dt} \hat{a}^{\text{I}} = -i\Delta \hat{a}^{\text{I}} - \frac{\kappa}{2} \hat{a}^{\text{I}} - \frac{ig}{2} (\hat{\sigma}^-)^{\text{I}} - \sqrt{\kappa} \hat{\xi}^{\text{I}}, \quad (\text{D.55})$$

$$\frac{d}{dt} (\hat{\sigma}^-)^{\text{I}} = \frac{ig}{2} \hat{\sigma}^z \hat{a}^{\text{I}}, \quad (\text{D.56})$$

$$\frac{d}{dt} \hat{\sigma}^z = ig \left[(\hat{a}^\dagger)^{\text{I}} (\hat{\sigma}^-)^{\text{I}} - (\hat{\sigma}^+)^{\text{I}} \hat{a}^{\text{I}} \right]. \quad (\text{D.57})$$

Notice that the definitions of \hat{a}^{I} and $(\hat{\sigma}^-)^{\text{I}}$ are the same if we choose $\hat{H}_0 = \frac{\hbar\omega_a}{2} \hat{\sigma}^z + \hbar\omega_a \hat{a}^\dagger \hat{a}$ in Eq. (D.45). Therefore Eqs. (D.55)–(D.57) should be consistent with the result we get from our formalism but much easier. Likewise one can define a rotating frame in the cavity frequency ω_c . Again the point of changing into a rotating frame is to get rid of the fast rotating global phase $e^{i\omega_a t}$ or $e^{i\omega_c t}$ and simplify the equations as much as possible.

Appendix E

Derivation of Lindblad Master Equation

The Redfield master equation (3.13) given in Sec. 3.1 has the form

$$\frac{d}{dt}\hat{\rho}_S^I(t) = -\frac{1}{\hbar^2} \int_0^\infty ds \operatorname{Tr}_E \left[\hat{V}^I(t), \left[\hat{V}^I(t-s), \hat{\rho}_S^I(t) \otimes \hat{\rho}_E \right] \right]. \quad (\text{E.1})$$

Expanding Eq. (E.1) yields

$$\begin{aligned} \frac{d}{dt}\hat{\rho}_S^I(t) = -\frac{1}{\hbar^2} \int_0^\infty ds \left\{ \operatorname{Tr}_E \left[\hat{V}^I(t)\hat{V}^I(t-s)\hat{\rho}_S^I(t)\hat{\rho}_E \right] \right. \\ - \operatorname{Tr}_E \left[\hat{V}^I(t-s)\hat{\rho}_S^I(t)\hat{\rho}_E\hat{V}^I(t) \right] \\ + \operatorname{Tr}_E \left[\hat{\rho}_S^I(t)\hat{\rho}_E\hat{V}^I(t-s)\hat{V}^I(t) \right] \\ \left. - \operatorname{Tr}_E \left[\hat{V}^I(t)\hat{\rho}_S^I(t)\hat{\rho}_E\hat{V}^I(t-s) \right] \right\}. \quad (\text{E.2}) \end{aligned}$$

From Eq. (3.18), we have the form of interaction Hamiltonian $\hat{V}^I(t)$ as

$$\hat{V}^I(t) = \hbar \sum_k \Omega_k e^{-i\omega_k t} \hat{S}_k \otimes \hat{E}_k^{I,\dagger}(t) + \Omega_k^* e^{i\omega_k t} \hat{S}_k^\dagger \otimes \hat{E}_k^I(t). \quad (\text{E.3})$$

We now substitute Eq. (E.3) into Eq. (E.2) and calculate the four terms in Eq. (E.2) one by one.

We obtain

$$\begin{aligned}
1^{\text{st}} \text{ term} &= -\frac{1}{\hbar^2} \int_0^\infty ds \text{Tr}_E \left[\hat{V}^I(t) \hat{V}^I(t-s) \hat{\rho}_S^I(t) \hat{\rho}_E \right] \\
&= -\sum_{k,l} \text{Tr}_E \int_0^\infty ds \left[\Omega_k e^{-i\omega_k t} \hat{S}_k \hat{E}_k^{I,\dagger}(t) + \Omega_k^* e^{i\omega_k t} \hat{S}_k^\dagger \hat{E}_k^I(t) \right] \\
&\quad \times \left[\Omega_l e^{-i\omega_l(t-s)} \hat{S}_l \hat{E}_l^{I,\dagger}(t-s) + \Omega_l^* e^{i\omega_l(t-s)} \hat{S}_l^\dagger \hat{E}_l^I(t-s) \right] \hat{\rho}_S^I(t) \hat{\rho}_E \\
&\approx -\sum_{k,l} \Omega_k \Omega_l^* e^{i(\omega_l - \omega_k)t} \hat{S}_k \hat{S}_l^\dagger \hat{\rho}_S^I(t) \int_0^\infty ds e^{-i\omega_l s} \text{Tr}_E \left[\hat{E}_k^{I,\dagger}(t) \hat{E}_l^I(t-s) \hat{\rho}_E \right] \\
&\quad - \sum_{k,l} \Omega_k^* \Omega_l e^{i(\omega_k - \omega_l)t} \hat{S}_k^\dagger \hat{S}_l \hat{\rho}_S^I(t) \int_0^\infty ds e^{i\omega_l s} \text{Tr}_E \left[\hat{E}_k^I(t) \hat{E}_l^{I,\dagger}(t-s) \hat{\rho}_E \right], \tag{E.4}
\end{aligned}$$

where we have ignored $\hat{E} \hat{E}$ and $\hat{E}^\dagger \hat{E}^\dagger$ correlation terms. These correlation terms are usually assumed to be zero if we consider a heat bath at thermal state.¹

At this point, we assume the heat bath is stationary, which means that the correlation of environment operators is only a function of s , and not a function of t anymore, i.e.,

$$\text{Tr}_E \left[\hat{E}_k^{I,\dagger}(t) \hat{E}_l^I(t-s) \hat{\rho}_E \right] = \text{Tr}_E \left[\hat{E}_k^{I,\dagger}(s) \hat{E}_l^I(0) \hat{\rho}_E \right] = \left\langle \hat{E}_k^{I,\dagger}(s) \hat{E}_l \right\rangle, \tag{E.5}$$

etc., where we have used $\hat{E}_l \equiv \hat{E}_l(0) = \hat{E}_l^I(0)$ to represent operators at $t = 0$. Therefore we can ignore rapid oscillations when $\omega_k \neq \omega_l$ and only keep the stationary solutions with $k = l$. Thus the first term becomes

$$\begin{aligned}
1^{\text{st}} \text{ term} &= -\sum_k \hat{S}_k \hat{S}_k^\dagger \hat{\rho}_S^I(t) |\Omega_k|^2 \int_0^\infty ds e^{-i\omega_k s} \left\langle \hat{E}_k^{I,\dagger}(s) \hat{E}_k \right\rangle \\
&\quad - \sum_k \hat{S}_k^\dagger \hat{S}_k \hat{\rho}_S^I(t) |\Omega_k|^2 \int_0^\infty ds e^{i\omega_k s} \left\langle \hat{E}_k^I(s) \hat{E}_k^\dagger \right\rangle. \tag{E.6}
\end{aligned}$$

If we define

$$|\Omega_k|^2 \int_0^\infty ds e^{-i\omega_k s} \left\langle \hat{E}_k^{I,\dagger}(s) \hat{E}_k \right\rangle = \frac{1}{2} G_k + i\epsilon_k, \tag{E.7a}$$

$$|\Omega_k|^2 \int_0^\infty ds e^{i\omega_k s} \left\langle \hat{E}_k^I(s) \hat{E}_k^\dagger \right\rangle = \frac{1}{2} \Gamma_k + i\delta_k, \tag{E.7b}$$

¹They are nonzero if the bath is squeezed. See Ref. [42].

where the real parts are

$$G_k = |\Omega_k|^2 \int_{-\infty}^{\infty} ds e^{-i\omega_k s} \langle \hat{E}_k^{\text{I},\dagger}(s) \hat{E}_k \rangle, \quad (\text{E.8a})$$

$$\Gamma_k = |\Omega_k|^2 \int_{-\infty}^{\infty} ds e^{-i\omega_k s} \langle \hat{E}_k^{\text{I}}(s) \hat{E}_k^\dagger \rangle, \quad (\text{E.8b})$$

then we have the final form of the first term as

$$1^{\text{st}} \text{ term} = - \sum_k \left[\left(\frac{1}{2} G_k + i\epsilon_k \right) \hat{S}_k \hat{S}_k^\dagger \hat{\rho}_S^{\text{I}} + \left(\frac{1}{2} \Gamma_k + i\delta_k \right) \hat{S}_k^\dagger \hat{S}_k \hat{\rho}_S^{\text{I}} \right]. \quad (\text{E.9})$$

From Eqs. (E.8a)–(E.8b) it is obvious that the real parts G_k and Γ_k are the power spectra of the coupling corresponding to the normal ordering and anti-normal ordering of the environment operators, respectively. The physical meanings of the imaginary parts ϵ_k and δ_k are more subtle. Below we give an example to help understand them.

Equations. (E.7a)–(E.7b) do not assume any specific form of the heat bath. Suppose we now consider a heat bath with Hamiltonian \hat{H}_E composed of harmonic oscillators of multiple frequencies, such as the one considered in Eq. (3.34). Moreover, assume that the operators \hat{E}_k are all eigenoperators of \hat{H}_E such that $[\hat{H}_E, \hat{E}_k] = -\omega'_k \hat{E}_k$ and $[\hat{H}_E, \hat{E}_k^\dagger] = \omega'_k \hat{E}_k^\dagger$.² Then in the IP, we have $\hat{E}_k^{\text{I}}(s) = e^{-i\omega'_k s} \hat{E}_k$. Immediately, we obtain from Eqs. (E.7a)–(E.7b)

$$\begin{aligned} \frac{1}{2} G_k + i\epsilon_k &= |\Omega_k|^2 \int_0^{\infty} ds e^{-i\omega_k s} \langle \hat{E}_k^{\text{I},\dagger}(s) \hat{E}_k \rangle \\ &= |\Omega_k|^2 \langle \hat{E}_k^\dagger \hat{E}_k \rangle \int_0^{\infty} ds e^{-i(\omega_k - \omega'_k)s}, \\ &= |\Omega_k|^2 \bar{N}_k \left[\pi \delta(\omega_k - \omega'_k) - i \text{PV} \frac{1}{\omega_k - \omega'_k} \right] \end{aligned} \quad (\text{E.10a})$$

$$\begin{aligned} \frac{1}{2} \Gamma_k + i\delta_k &= |\Omega_k|^2 \int_0^{\infty} ds e^{i\omega_k s} \langle \hat{E}_k^{\text{I}}(s) \hat{E}_k^\dagger \rangle \\ &= |\Omega_k|^2 \langle \hat{E}_k \hat{E}_k^\dagger \rangle \int_0^{\infty} ds e^{-i(\omega'_k - \omega_k)s} \\ &= |\Omega_k|^2 (\bar{N}_k + 1) \left[\pi \delta(\omega_k - \omega'_k) + i \text{PV} \frac{1}{\omega_k - \omega'_k} \right], \end{aligned} \quad (\text{E.10b})$$

²If operators \hat{E}_k are not eigenoperators of \hat{H}_E , all we need to do is decomposing \hat{E}_k into its complete eigenbasis and then rearranging the summation over k in Eq. (3.18) to include the extra summation.

and therefore

$$\left\{ \begin{array}{l} G_k = |\Omega_k|^2 \bar{N}_k 2\pi\delta(\omega_k - \omega'_k) \\ \epsilon_k = -\text{PV} \frac{|\Omega_k|^2 \bar{N}_k}{\omega_k - \omega'_k} \end{array} \right\}, \quad \left\{ \begin{array}{l} \Gamma_k = |\Omega_k|^2 (\bar{N}_k + 1) 2\pi\delta(\omega_k - \omega'_k) \\ \delta_k = \text{PV} \frac{|\Omega_k|^2 (\bar{N}_k + 1)}{\omega_k - \omega'_k} \end{array} \right\}. \quad (\text{E.11})$$

Here we have used $\bar{N}_k = \langle \hat{E}_k^\dagger \hat{E}_k \rangle$ which is the occupation number of the heat bath with eigenfrequency ω'_k . The symbol PV represents the Cauchy principal value.³ In vacuum, we would expect $\bar{N}_k \rightarrow 0$, resulting in $G_k \rightarrow 0$ and $\epsilon_k \rightarrow 0$. However, due to the bosonic commutation relation, we see that $\Gamma_k \neq 0$, leading to the dissipation due to vacuum fluctuation, and $\delta_k \neq 0$, leading to the vacuum Lamb shift. When $\bar{N}_k \neq 0$, the extra terms proportional to \bar{N}_k give the Stark shift. Due to taking the principal values, both ϵ_k and δ_k terms are small and usually ignored.

Equation (E.9) gives the general form of the first term in Eq. (E.2). Likewise, we obtain

$$\begin{aligned} 2^{\text{nd}} \text{ term} &= \frac{1}{\hbar^2} \int_0^\infty ds \text{Tr}_E \left[\hat{V}^I(t-s) \hat{\rho}_S^I(t) \hat{\rho}_E \hat{V}^I(t) \right] \\ &= \sum_{k,l} \text{Tr}_E \int_0^\infty ds \left[\Omega_l e^{-i\omega_l(t-s)} \hat{S}_l \hat{E}_l^{\text{I},\dagger}(t-s) + \Omega_l^* e^{i\omega_l(t-s)} \hat{S}_l^\dagger \hat{E}_l^{\text{I}}(t-s) \right] \hat{\rho}_S^I(t) \hat{\rho}_E \\ &\quad \times \left[\Omega_k e^{-i\omega_k t} \hat{S}_k \hat{E}_k^{\text{I},\dagger}(t) + \Omega_k^* e^{i\omega_k t} \hat{S}_k^\dagger \hat{E}_k^{\text{I}}(t) \right] \\ &\approx \sum_k \hat{S}_k \hat{\rho}_S^I \hat{S}_k^\dagger |\Omega_k|^2 \int_0^\infty ds e^{i\omega_k s} \langle \hat{E}_k^{\text{I},\dagger}(s) \hat{E}_k^{\text{I},\dagger} \rangle + \sum_k \hat{S}_k^\dagger \hat{\rho}_S^I \hat{S}_k |\Omega_k|^2 \int_0^\infty ds e^{-i\omega_k s} \langle \hat{E}_k^{\text{I},\dagger}(s) \hat{E}_k^{\text{I}} \rangle \\ &= \sum_k \left[\left(\frac{1}{2} \Gamma_k + i\delta_k \right) \hat{S}_k \hat{\rho}_S^I \hat{S}_k^\dagger + \left(\frac{1}{2} G_k + i\epsilon_k \right) \hat{S}_k^\dagger \hat{\rho}_S^I \hat{S}_k \right]. \end{aligned} \quad (\text{E.12})$$

$$\begin{aligned} 3^{\text{rd}} \text{ term} &= -\frac{1}{\hbar^2} \int_0^\infty ds \text{Tr}_E \left[\hat{\rho}_S^I(t) \hat{\rho}_E \hat{V}^I(t-s) \hat{V}^I(t) \right] \\ &= -\sum_{k,l} \text{Tr}_E \int_0^\infty ds \hat{\rho}_S^I(t) \hat{\rho}_E \left[\Omega_l e^{-i\omega_l(t-s)} \hat{S}_l \hat{E}_l^{\text{I},\dagger}(t-s) + \Omega_l^* e^{i\omega_l(t-s)} \hat{S}_l^\dagger \hat{E}_l^{\text{I}}(t-s) \right] \\ &\quad \times \left[\Omega_k e^{-i\omega_k t} \hat{S}_k \hat{E}_k^{\text{I},\dagger}(t) + \Omega_k^* e^{i\omega_k t} \hat{S}_k^\dagger \hat{E}_k^{\text{I}}(t) \right] \\ &\approx -\sum_k \hat{\rho}_S^I \hat{S}_k \hat{S}_k^\dagger |\Omega_k|^2 \int_0^\infty ds e^{i\omega_k s} \langle \hat{E}_k^{\text{I},\dagger} \hat{E}_k^{\text{I}}(s) \rangle - \sum_k \hat{\rho}_S^I \hat{S}_k^\dagger \hat{S}_k |\Omega_k|^2 \int_0^\infty ds e^{-i\omega_k s} \langle \hat{E}_k \hat{E}_k^{\text{I},\dagger}(s) \rangle \\ &= -\sum_k \left[\left(\frac{1}{2} G_k - i\epsilon_k \right) \hat{\rho}_S^I \hat{S}_k \hat{S}_k^\dagger + \left(\frac{1}{2} \Gamma_k - i\delta_k \right) \hat{\rho}_S^I \hat{S}_k^\dagger \hat{S}_k \right]. \end{aligned} \quad (\text{E.13})$$

³See Appx. A.3.

$$\begin{aligned}
4^{\text{th}} \text{ term} &= \frac{1}{\hbar^2} \int_0^\infty ds \text{Tr}_{\text{E}} \left[\hat{V}^{\text{I}}(t) \hat{\rho}_{\text{S}}^{\text{I}} \hat{\rho}_{\text{E}} \hat{V}^{\text{I}}(t-s) \right] \\
&= \sum_{k,l} \text{Tr}_{\text{E}} \int_0^\infty ds \left[\Omega_k e^{-i\omega_k t} \hat{S}_k \hat{E}_k^{\text{I}\dagger}(t) + \Omega_k^* e^{i\omega_k t} \hat{S}_k^\dagger \hat{E}_k^{\text{I}}(t) \right] \hat{\rho}_{\text{S}}^{\text{I}} \hat{\rho}_{\text{E}} \\
&\quad \times \left[\Omega_l e^{-i\omega_l(t-s)} \hat{S}_l \hat{E}_l^{\text{I}\dagger}(t-s) + \Omega_l^* e^{i\omega_l(t-s)} \hat{S}_l^\dagger \hat{E}_l^{\text{I}}(t-s) \right] \\
&\approx \sum_k \hat{S}_k \hat{\rho}_{\text{S}}^{\text{I}} \hat{S}_k^\dagger |\Omega_k|^2 \int_0^\infty ds e^{-i\omega_k s} \langle \hat{E}_k \hat{E}_k^{\text{I}\dagger}(s) \rangle + \sum_k \hat{S}_k^\dagger \hat{\rho}_{\text{S}}^{\text{I}} \hat{S}_k |\Omega_k|^2 \int_0^\infty ds e^{i\omega_k s} \langle \hat{E}_k^\dagger \hat{E}_k^{\text{I}}(s) \rangle \\
&= \sum_k \left[\left(\frac{1}{2} \Gamma_k - i\delta_k \right) \hat{S}_k \hat{\rho}_{\text{S}}^{\text{I}} \hat{S}_k^\dagger + \left(\frac{1}{2} G_k - i\epsilon_k \right) \hat{S}_k^\dagger \hat{\rho}_{\text{S}}^{\text{I}} \hat{S}_k \right]. \tag{E.14}
\end{aligned}$$

Therefore Eq. (E.2) becomes

$$\begin{aligned}
\frac{d}{dt} \hat{\rho}_{\text{S}}^{\text{I}} &= - \sum_k \left[\left(\frac{1}{2} G_k + i\epsilon_k \right) \hat{S}_k \hat{S}_k^\dagger \hat{\rho}_{\text{S}}^{\text{I}} + \left(\frac{1}{2} \Gamma_k + i\delta_k \right) \hat{S}_k^\dagger \hat{S}_k \hat{\rho}_{\text{S}}^{\text{I}} \right] \\
&\quad + \sum_k \left[\left(\frac{1}{2} \Gamma_k + i\delta_k \right) \hat{S}_k \hat{\rho}_{\text{S}}^{\text{I}} \hat{S}_k^\dagger + \left(\frac{1}{2} G_k + i\epsilon_k \right) \hat{S}_k^\dagger \hat{\rho}_{\text{S}}^{\text{I}} \hat{S}_k \right] \\
&\quad - \sum_k \left[\left(\frac{1}{2} G_k - i\epsilon_k \right) \hat{\rho}_{\text{S}}^{\text{I}} \hat{S}_k \hat{S}_k^\dagger + \left(\frac{1}{2} \Gamma_k - i\delta_k \right) \hat{\rho}_{\text{S}}^{\text{I}} \hat{S}_k^\dagger \hat{S}_k \right] \\
&\quad + \sum_k \left[\left(\frac{1}{2} \Gamma_k - i\delta_k \right) \hat{S}_k \hat{\rho}_{\text{S}}^{\text{I}} \hat{S}_k^\dagger + \left(\frac{1}{2} G_k - i\epsilon_k \right) \hat{S}_k^\dagger \hat{\rho}_{\text{S}}^{\text{I}} \hat{S}_k \right] \\
&= \sum_k \frac{G_k}{2} \left(2 \hat{S}_k^\dagger \hat{\rho}_{\text{S}}^{\text{I}} \hat{S}_k - \hat{S}_k \hat{S}_k^\dagger \hat{\rho}_{\text{S}}^{\text{I}} - \hat{\rho}_{\text{S}}^{\text{I}} \hat{S}_k \hat{S}_k^\dagger \right) \\
&\quad + \sum_k \frac{\Gamma_k}{2} \left(2 \hat{S}_k \hat{\rho}_{\text{S}}^{\text{I}} \hat{S}_k^\dagger - \hat{S}_k^\dagger \hat{S}_k \hat{\rho}_{\text{S}}^{\text{I}} - \hat{\rho}_{\text{S}}^{\text{I}} \hat{S}_k^\dagger \hat{S}_k \right) \\
&\quad - i \sum_k \left[\epsilon_k \hat{S}_k \hat{S}_k^\dagger + \delta_k \hat{S}_k^\dagger \hat{S}_k, \hat{\rho}_{\text{S}}^{\text{I}} \right] \\
&= \sum_k \Gamma_k \mathcal{L} \left[\hat{S}_k \right] \hat{\rho}_{\text{S}}^{\text{I}} + \sum_k G_k \mathcal{L} \left[\hat{S}_k^\dagger \right] \hat{\rho}_{\text{S}}^{\text{I}} - i \sum_k \left[\epsilon_k \hat{S}_k \hat{S}_k^\dagger + \delta_k \hat{S}_k^\dagger \hat{S}_k, \hat{\rho}_{\text{S}}^{\text{I}} \right], \tag{E.15}
\end{aligned}$$

where we have defined the Lindbladian superoperator

$$\mathcal{L} \left[\hat{\mathcal{O}} \right] \hat{\rho} = \frac{1}{2} \left(2 \hat{\mathcal{O}} \hat{\rho} \hat{\mathcal{O}}^\dagger - \hat{\mathcal{O}}^\dagger \hat{\mathcal{O}} \hat{\rho} - \hat{\rho} \hat{\mathcal{O}}^\dagger \hat{\mathcal{O}} \right) \tag{E.16}$$

for arbitrary operator $\hat{\mathcal{O}}$ and density matrix $\hat{\rho}$. The ϵ_k and δ_k terms give the Stark and Lamb shifts due to the interaction with the heat bath.

Appendix F

Einstein Relation

Consider the Heisenberg-Langevin equations of two operators \hat{O}_μ and \hat{O}_ν as defined in Eq. (3.55),

$$\frac{d}{dt}\hat{O}_\mu = -\frac{1}{i\hbar}[\hat{H}, \hat{O}_\mu] + \hat{D}_\mu(t) + \hat{F}_\mu(t), \quad (\text{F.1})$$

$$\frac{d}{dt}\hat{O}_\nu = -\frac{1}{i\hbar}[\hat{H}, \hat{O}_\nu] + \hat{D}_\nu(t) + \hat{F}_\nu(t). \quad (\text{F.2})$$

where we have assumed only one noise source. The diffusion matrix defined in Eq. (3.61) satisfies

$$2M_{\mu\nu}\delta(t-t') = \langle \hat{F}_\mu(t)\hat{F}_\nu(t') \rangle. \quad (\text{F.3})$$

By writing $\hat{O}_\mu(t)$ as

$$\hat{O}_\mu(t) = \hat{O}_\mu(t-\Delta t) + \int_{t-\Delta t}^t dt' \frac{d\hat{O}_\mu(t')}{dt'}, \quad (\text{F.4})$$

we obtain

$$\begin{aligned} \langle \hat{O}_\mu(t)\hat{F}_\nu(t) \rangle &= \langle \hat{O}_\mu(t-\Delta t)\hat{F}_\nu(t) \rangle + \int_{t-\Delta t}^t dt' \left\langle \frac{d\hat{O}_\mu(t')}{dt'} \hat{F}_\nu(t) \right\rangle \\ &= \int_{t-\Delta t}^t dt' \langle \hat{F}_\mu(t)\hat{F}_\nu(t') \rangle \\ &= \int_{t-\Delta t}^t dt' 2M_{\mu\nu}\delta(t'-t) \\ &= \frac{1}{2} \int_{-\infty}^{\infty} dt' 2M_{\mu\nu}\delta(t'-t) \\ &= M_{\mu\nu}(t), \end{aligned} \quad (\text{F.5})$$

which is a result of causality and the Markov approximation. Similarly,

$$\langle \hat{F}_\mu(t) \hat{O}_\nu(t) \rangle = M_{\mu\nu}(t), \quad (\text{F.6})$$

Using Eqs. (F.5) and (F.6), from Eqs. (F.1) and (F.1) we obtain

$$\begin{aligned} \left\langle \frac{d}{dt} (\hat{O}_\mu \hat{O}_\nu) \right\rangle &= \left\langle \frac{d\hat{O}_\mu}{dt} \hat{O}_\nu \right\rangle + \left\langle \hat{O}_\mu \frac{d\hat{O}_\nu}{dt} \right\rangle \\ &= -\frac{1}{i\hbar} \langle [\hat{H}, \hat{O}_\mu] \hat{O}_\nu \rangle + \langle \hat{D}_\mu \hat{O}_\nu \rangle + \langle \hat{F}_\mu \hat{O}_\nu \rangle \\ &\quad - \frac{1}{i\hbar} \langle \hat{O}_\mu [\hat{H}, \hat{O}_\nu] \rangle + \langle \hat{O}_\mu \hat{D}_\nu \rangle + \langle \hat{O}_\mu \hat{F}_\nu \rangle \\ &= -\frac{1}{i\hbar} \langle [\hat{H}, \hat{O}_\mu \hat{O}_\nu] \rangle + \langle \hat{D}_\mu \hat{O}_\nu \rangle + \langle \hat{O}_\mu \hat{D}_\nu \rangle + 2M_{\mu\nu}. \end{aligned} \quad (\text{F.7})$$

As a result, we have derived the Einstein relation

$$2M_{\mu\nu}(t) = \left\langle \frac{d}{dt} (\hat{O}_\mu \hat{O}_\nu) \right\rangle + \frac{1}{i\hbar} \langle [\hat{H}, \hat{O}_\mu \hat{O}_\nu] \rangle - \langle \hat{D}_\mu \hat{O}_\nu \rangle - \langle \hat{O}_\mu \hat{D}_\nu \rangle. \quad (\text{F.8})$$

The Einstein relation (F.8) relates the diffusion matrix to the corresponding drift terms, thus comprising a quantum fluctuation-dissipation theorem [103].